THE ELECTROCHEMICAL OXIDATION
OF HYDROGEN PEROXIDE
ON NICKEL ELECTRODES
IN PHOSPHATE BUFFER SOLUTIONS

A thesis presented in partial fulfilment of the requirements for

the degree of Master of Science in Chemistry

at Massey University, Palmerston North, New Zealand

Justin John Nairn

2000

ABSTRACT

The electrochemical oxidation of hydrogen peroxide was studied at nickel electrodes in phosphate buffer solutions. This reaction is of interest because of its possible use in the construction of devices for the electrochemical detection of hydrogen peroxide. The devices developed could be advantageous in many industrial and medical processes.

Using the electrochemical technique, staircase potentiometry, the activity of the nickel electrode in catalysing hydrogen peroxide oxidation was evaluated over a range of bulk hydrogen peroxide concentrations, rotation rates, electrode potentials, temperatures, buffer concentrations and pH.

A mechanism was developed to account for the observed activity. This was based on a previous model developed for the electrochemical oxidation of hydrogen peroxide at platinum electrodes [1-6]. The mechanism involved H_2O_2 interaction with binding sites on the surface of the electrode. These were initially identified as a nickel phase oxide, $Ni(OH)_2$. Later, the involvement of buffer phosphate species HPO_4^- was identified. Hydrogen peroxide is adsorbed onto the binding site to form the complex $Ni_{BS} \cdot H_2O_2$. This complex then undergoes an internal charge transfer to form a reduced nickel site, liberating the products water and oxygen. The binding site regenerates electrochemically to give rise to an amperometric signal with the release of protons. A side reaction was proposed which involved an interaction between the binding sites and dioxygen. This interaction competitively inhibited the binding of H_2O_2.

A rate equation was derived to account for all the surface sites involved in the proposed reaction mechanism. The kinetic, equilibrium and thermodynamic constants of the resulting model were optimised by a SIMPLEX procedure. These constants were in turn used in conjunction with the rate equation to produce synthetic responses, which were then compared to the observed steady-state response. A satisfactory fit was found over the entire range of conditions studied. This supported the proposition that the mechanism was appropriate.

The equilibrium constants were found to be potential invariant, with $K_1 = 4.43 \times 10^{-3}$ and $K_4 = 0.360$ m^3 mol^{-1} at 20°C. The former, K_1, was exothermic, with $\Delta H = -28.32$ kJ K^{-1} between 5 and 25°C, and became significantly more exothermic, with $\Delta H = -198.33$ kJ K^{-1}

between 25 and 35°C. In contrast, K_4 was slightly endothermic, with $\Delta H = -16.5$ kJ K^{-1} over the temperature range. One rate constant could be approximated to be potential invariant, $k_3N = 7.99 \times 10^{-4}$ mol m^{-2} s^{-1} at 20°C. Whereas, the other, k_2N, varied with potential. Both rate constants were endothermic with pseudo-activation energies for k_3N being 24.3 kJ mol^{-1} and for k_2N ranging between 130–80 kJ mol^{-1} (depending on electrode potential).

An optimum pH region for the study of H_2O_2 oxidation at nickel was found to be between pH 4 and 9. Above and below these bounds competitive reactions occurred that were not attributable to hydrogen peroxide and insignificant rates of reaction for electrochemical measurement were found.

The phosphate species HPO_4^{-2} was identified as being involved in the oxidative mechanism. The nature of this involvement was complex, with HPO_4^{-2} both inhibiting and facilitating H_2O_2 oxidation, depending on surface concentration. To accommodate this, the proposed mechanism was further modified to include this involvement. It was proposed that HPO_4^{-2} was required to form the H_2O_2 binding site from a nickel precursor site on the electrode surface. However, the complexation of a second HPO_4^{-2} to this site would inhibit H_2O_2 binding.

The work presented in this thesis represents a fundamental study into the electrochemical behaviour of hydrogen peroxide at nickel electrodes. This behaviour has been clearly identified over a range of temperatures, hydrodynamic conditions, buffer compositions and concentrations. This enabled a new and comprehensive mechanism, for the oxidation of hydrogen peroxide at nickel electrode, to be developed.

ACKNOWLEDGEMENTS

First I would like to acknowledge the supreme efforts of Simon without whom this work would have been impossible. I would like to thank him for his time, patience, guidance, and humour in teaching me an area of chemistry in which I had no prior experience. You always made time for the most inane of questions and seldom lived up to your middle initial - one could not ask for a better supervisor.

To my co-workers and friends Giovanna, Ant, Emad, and Michael you made an inspired lab. Emad (the father figure) - your help and guidance were greatly appreciated, I loved our talks. Michael (lunch!!) you contributed so much to the humour of the lab. G and Ant I could not ask for better friends, you most of all made doing Masters a blast. Thanks.

To Gav, Jo (meeeow), tall Paul, Sonya, Rekha, big Paul, Steve, Ester, Adrian, Andrew, Wayne, Garf, farmer Jim, G (respect my authoritar), Ant & Bec, Clem, Dave, and Beccy (I hope I didn't miss anyone). Thank you for being social and getting involved, Viva Viagara, need I say more? Your fantastic friendship and humour has made my life so much more colourful (in a good way). Beccy, despite my complaints, your gentle nagging and all that you have given me are greatly appreciated. To the other chemistry students, staff (esp. Dave, Andy and Emily), and other affiliated members your easy going friendly attitude made life so much better.

Last but certainly not least I wish to acknowledge my family. Mum, Dad, Charles & Shelley, Granny, Lek and all the cousins, uncles, and aunts who have given me so much love, never held me back, for always encouraging me and letting me believe I can do anything. It makes it so much easier knowing you are always there. I am always thinking of you.

I have had so much fun and have many wonderful memories it saddens me that I have to finish.

TABLE OF CONTENTS

LIST OF FIGURES

LIST OF TABLES

LIST OF SYMBOLS

Symbol	Description	Unit
a_i	hydrodynamic radii for species i	$m^2\,s^{-1}$
c	concentration	$mol\,L^{-1}$
d_{av}	average deviation	$mA\,cm^{-2}$
D	diffusion coefficient	$m^2\,s^{-1}$
D_i	diffusion coefficients for species i	$m^2\,s^{-1}$
e^-	electron	
E	electrode potential	mV
E^o	standard electrode potential	mV
F	Faraday constant	$C\,mol^{-1}$
ΔH_{DBE}	dissociative bond energies	$kJ\,mol^{-1}$
ΔH	enthalpy change	$kJ\,mol^{-1}$
ΔH°	enthalpy of formation	$kJ\,mol^{-1}$
$\Delta H^\ddagger$	activation energy	$kJ\,mol^{-1}$
i	current density	$mA\,cm^{-2}$
i_a	anodic current density	mA
i_c	cathodic current density	mA
i_{obs}	current density observed	$mA\,cm^{-2}$
i_L	limiting current density	$mA\,cm^{-2}$
i_k	kinetic current density	$mA\,cm^{-2}$
i_{calc}	current density calculated	$mA\,cm^{-2}$
I	current	mA
j	flux or rate of diffusion	$mol\,m^{-2}\,s^{-1}$
k_2	heterogeneous rate constant	$m\,s^{-1}$
k_3	heterogeneous rate constant	$m\,s^{-1}$
k_D	diffusion constant	$(m^2\,s^{-1})^{1/6}$
k_f	heterogeneous electron transfer rate constant	$m\,s\,C^{-1}$
K_N	equilibrium constant	$m^3\,mol^{-1}$

K_1	equilibrium constant	$m^3 \, mol^{-1}$
K_4	equilibrium constant	$m^3 \, mol^{-1}$
K_5	equilibrium constant	$m^3 \, mol^{-1}$
l	length	m
$\overline{m}$	molarity	$mol \, Kg^{-1}$
M	molarlity	$mol \, L^{-1}$
n	number of electrons	
n_p	number of data points	
N	number of binding sites	
N^*	number of precursor sites	
r	radius	m
r_s	sum of residuals	
R_1/R_2	roots of a quadratic	
Re	Reynolds number	
γ	mean activity coefficient	
η	Absolute viscosity	$kg \, m^{-1} \, s^{-1}$
θ	surface coverage	
$\lambda_1/\lambda_2/\lambda_3$	roots of a 3rd order polynomial	
ν	kinematic viscosity	$m^2 \, s^{-1}$
ρ	density	$g \, ml^{-1}$
υ	characteristic velocity	$m^2 \, s^{-1}$
ω	angular velocity	$rad \, s^{-1}$

LIST OF ABBREVIATIONS

BAS	Bioanalytical Systems
CE	counter electrode
CPE	carbon paste electrode
CV	cyclic voltammetry
DNA	deoxyribose nucleic acid
ECE	electron-transfer/chemical/electron-transfer mechanism
FIA	flow-injection analysis
GOD	glucose oxidase
H_2O_2	hydrogen peroxide
IFS	Institute of Fundamental Sciences
NADH	nicotinamide adenine dinucliotide hydride
NEXFAS	near edge x-ray adsorption fine structure
ppm	parts per million
RDE	rotating disc electrode
RE	reference electrode
rpm	revolutions per minute
SAM	self-assembled monolayers
SCE	saturated calomel electrode
SCP	staircase potentiometry
SHE	standard hydrogen electrode
WE	working electrode
wt/wt	weight by weight

CHAPTER 1

INTRODUCTION

1.1   Introduction

Hydrogen peroxide, H_2O_2, is a strong oxidising agent with many industrial and medical applications. The reaction of hydrogen peroxide at electrodes is of interest for the development of hydrogen peroxide detection instruments, which would be of potential use in any application where hydrogen peroxide is involved. The area of biosensors, in particular, is foreseen as a major growth area for hydrogen peroxide detectors. The nickel electrode may be at the leading edge of this evolution providing a cheap, durable, easily synthesised electrode material for the accurate measure of H_2O_2.

The anodic oxidation of hydrogen peroxide at nickel electrodes is the major emphasis of this study. This was investigated under phosphate buffer conditions chosen due to their widespread use in biosensors currently developed. A previous study by Khudaish [1-6] on the electrochemical oxidation of hydrogen peroxide at platinum electrodes forms the platform upon which this thesis is built.

This chapter gives a brief overview of hydrogen peroxide and its commercial uses, and outlines the current knowledge on H_2O_2 oxidation at nickel electrodes and electrodes in general.

1.2   Hydrogen Peroxide

1.2.1 *Production*

Historically, hydrogen peroxide was mass produced from the hydrolysis of a solution containing the persulphate ion, which in turn is produced from ammonium bisulphate by the process of electrolysis.

$$2NH_4HSO_4 \longrightarrow (NH_4)_2S_2O_8 + H_2 \tag{1.1}$$

$$(NH_4)_2S_2O_8 + 2H_2O \longrightarrow 2NH_4HSO_4 + H_2O_2 \tag{1.2}$$
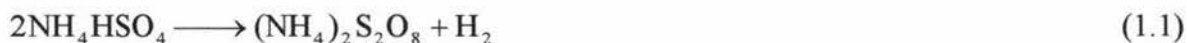
The overall reaction is 80 – 85% current efficient. The concentration of H_2O_2 produced in this process is 30 to 40% *wt/wt* and may be further concentrated by fractional distillation. Anhydrous H_2O_2 may be produced through this process. Commercially, hydrolysis of ammonium persulphate, persulphuric acid and potassium persulphate have all been used to produce H_2O_2 by the process described above.

The modern chemical method for H_2O_2 manufacture was initially developed in Germany during World War II. This method is an organic autoxidation process in which a suitable organic compound (usually a hydroquinone) is oxidised to the quinone form with the concurrent formation of H_2O_2.

$$\text{hydroquinone} + O_2 \longrightarrow \text{quinone} + H_2O_2 \tag{1.3}$$

The hydrogen peroxide is removed and the quinone can be reduced catalytically and reused. This reaction process produces 25% *wt/wt* H_2O_2 which may also be purified by fractional distillation.

Another common commercial production involves the oxidation of isopropyl alcohol to yield two useful products, acetone and hydrogen peroxide.

$$CH_3CH(OH)CH_3 + O_2 \longrightarrow CH_3COCH_3 + H_2O_2 \tag{1.4}$$
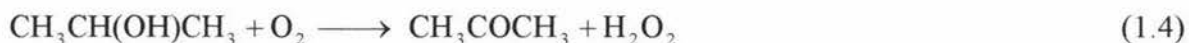
This process yields 25% *wt/wt* H_2O_2 [7].

1.2.2 *Structure and Properties*

Pure hydrogen peroxide is a colourless viscous liquid, which is miscible with water in all proportions. Hydrogen peroxide, which boils at 155.5°C and freezes at –0.461°C, has a specific gravity of 1.438 g ml^{-1} at 20°C.

Hydrogen peroxide has a H–O–O–H structure with OOH bond angles of 100°. The internal rotation about the O–O bond is quite labile having a small energy barrier. The most common conformation has 120° rotation between the two terminal protons when viewed down the O–O axis. Hydrogen peroxide forms strong hydrogen bonds, O–H----O at 2.8 Å (*c.f.* 2.76 Å in H_2O), due to this the structure previously described may vary due to crystal packing forces in the solid state.

Contact of concentrated H_2O_2 with organic substances may cause spontaneous combustion. This reactivity is primarily due to its unique bond energies which allow low energy

rearrangements to give hydroxide and oxo radicals. In acetonitrile H_2O_2 is oxidised to O_2 via an electron-transfer/chemical/electron-transfer (ECE) mechanism [8].

$$H_2O_2 \xrightarrow{\;-e^-\;} [H_2O_2]^+ \xrightarrow{\;+H_2O\;} HOO\cdot + H_3O^+ \qquad E^{\circ} = +2.0 \text{ V vs SHE} \qquad (1.5)$$

$$HOO\cdot \xrightarrow{\;+H_2O\; -e^-\;} O_2 + H_3O^+ \qquad\qquad E^{\circ} = +0.6 \text{ V vs SHE} \qquad (1.6)$$
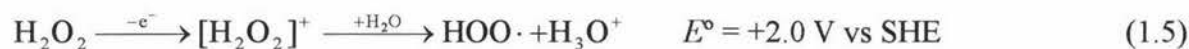
Gas Phase dissociative bond energies ΔH_{DBE} are given in Table 1.1 for hydrogen peroxide, with those for water and dioxygen included for comparison. Hydrogen peroxide is naturally unstable and its decomposition is accelerated by contamination especially by metals ions. The presence of 1 ppm of iron or 0.05 ppm of copper can cause rapid decomposition [9].

$$H_2O_2 \longrightarrow 2H_2O + O_2 \qquad\qquad \Delta H = -99 \text{ kJ mol}^{-1} \qquad (1.7)$$

The activation of this reaction by reduced transition metals, known as Fenton chemistry, has been known for almost 100 years. Hydrogen peroxide is so susceptible to decomposition it can only be contained and transported in a few inert materials such as glass, quartz, some plastics, and high purity (97%+) aluminium. Even then stabilisers such as tin species or chelating ligands are often added [7,8].

Hydrogen peroxide is a strong oxidising agent – a property that makes it highly prized for many industrial processes. The redox chemistry of H_2O_2 in aqueous solutions is described by the following half equations.

$$O_2 + 2H^+ + 2e^- \rightleftharpoons H_2O_2 \qquad\qquad E^{\circ} = 177 \text{ mV vs SHE} \qquad (1.8)$$

$$H_2O_2 + 2H^+ + 2e^- \rightleftharpoons 2H_2O \qquad\qquad E^{\circ} = 68 \text{ mV vs SHE} \qquad (1.9)$$

$$HO_2^- + 2H_2O + 2e^- \rightleftharpoons 3OH^- \qquad\qquad E^{\circ} = 87 \text{ mV vs SHE} \qquad (1.10)$$
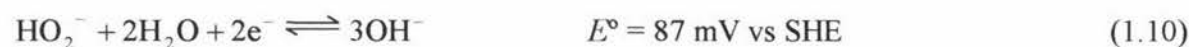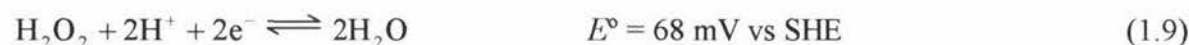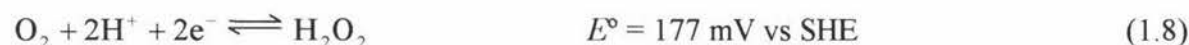
1.2.3 *Commercial Uses for Hydrogen Peroxide*

The uses developed for H_2O_2 mainly arise from its strong oxidising properties. In addition, the products from decomposition of H_2O_2 are non-toxic, being water and oxygen gas. This makes it invaluable for use at an industrial scale. Initially, the major user of H_2O_2 was the military, who along with the aerospace industry remain the only big users of high grade 90%+ *wt/wt* H_2O_2. It is a primary oxidant for hydroxylamine in rocket propulsion. During the latter stages of World War II, the German air force employed the vigorous reaction

Bond	$\dfrac{\Delta H_{\text{DBE}}{}^{\text{a}}}{\text{kJ mol}^{-1}}$
H-OOH	372.6
H-OH	464.0
HO-OH	213.5
O=O	498.2
$HOOH \rightarrow HOH + O$	163.3
$HOH \rightarrow H_2 + O$	489.9

a [Ref. 81]

Table 1.1 Gas phase dissociative bond energies for hydrogen peroxide, water and dioxygen.

between H_2O_2 and hydrazine to propel Komet fighters. For laboratories and other uses less than 30% *wt/wt* is usually sufficient. One of the larger modern H_2O_2 consumer is the textile and paper pulp industry which uses H_2O_2 as a bleaching agent in place of chloride since it is capable of producing good whiteness but without compromising fibre strength and does not produce dioxins. It is used in many chemical applications such as in the epoxidation of oils and fatty acid esters and the manufacture of peracids and glycerin [7].

The discovery of the anti-bacterial properties of H_2O_2 has provided many other applications in medicines and cosmetics in dilute concentrations. Since chlorine is an irritant to mucus membranes and eyes and also has an unpleasant odour, H_2O_2 is an alternative to chlorine in swimming pool hygiene. Hydrogen peroxide use in wastewater treatment has been advantageous since, anti-bacterial properties aside, it controls noisome hydrogen sulphide odours as well as oxygenating the water. It was initially thought that anti-bacterial properties arose from the oxygen produced from decomposition. It is now recognised that it is the undecomposed H_2O_2, which is effective [9].

Hydrogen peroxide is now widely used in the dairy industry as a milk germicide. Schrodt first exploited this property of H_2O_2 in milk preservation in 1883. Hydrogen peroxide is ideal for this role since the concentrations required for significant inhibition of bacterial growth are small. Hydrogen peroxide is very easily removed by enzymatic treatment and breaks down into non-toxic products which are to all intents and purposes undetectable.

The use of H_2O_2 in milk was discussed by representatives of many different countries at the Food and Agriculture Organisation of the United Nations in 1957. Their report stipulated that the use of H_2O_2 should be permitted only when the availability of tested and approved grades of H_2O_2 can be ensured. Also, when any residue preservative can be adequately tested and removed from milk destined for human consumption. This should in no circumstances exceed 0.80g of H_2O_2 per litre of milk and preferably lie between 0.01% *wt/wt* and 0.04% *wt/wt* per litre.

1.3   Oxidation of H_2O_2 at Nickel electrodes

The research presented here has no further goal than to build comprehensive knowledge of the fundamental electrochemical behaviour of H_2O_2 at nickel electrodes. This study is of

interest, however, in the construction of H_2O_2 detection devices employing a nickel electrode. Many processes have been used to determine H_2O_2 concentrations. These include titration, spectrophotometery, chemiluminescence, and fluorometry. All these methods suffer from a range of interferences are time consuming and require expensive reagents [1]. Electrochemical determination using a nickel electrode could potentially avoid these deficiencies while providing further advantages. Electrochemical determination might offer rapid detection with high accuracy, lower detection limits, decreased interference, with the minimum of reagents.

There is an obvious niche for an accurate H_2O_2 detector in the dairy industry to meet the quality control regulations imposed by the Food and Agriculture Organisation of the United Nations. One of the current methods of detection involves potassium iodide-starch paper. The milk sample is diluted 1 to 1 with HCl, a drop of weak formalin added, the mixture warmed to 60°C and then tested on the paper. This method is touted to detect 0.001% by weight H_2O_2. Munday used 1% vanadium pentoxide in 6% dilute sulphuric acid, which on addition to milk turns a red colour in the presence of H_2O_2. This method is less sensitive with a detection limit of 0.008% by weight H_2O_2 [9]. These methods give simple positive or negative results. An electrochemical device employing a nickel electrode, on the other hand, would give qualitative data over a range of H_2O_2 concentrations, use little or no reagents and require very small sample sizes, thereby minimising waste.

In fact in all the industries described in Section 1.2.3 that use or produce H_2O_2, a quick, accurate, cheap measure of H_2O_2 would be invaluable. Possible uses abound in the field of quality control and in any process where the addition of H_2O_2 is required. Gaining knowledge of the exact H_2O_2 concentration might prevent excessive industrial wastage and reduce production costs. Testing the H_2O_2 concentration just prior to use is particularly important since it is so unstable and liable to decompose.

One of the major growth areas for electrochemical detection of H_2O_2 is in biosensors. The field of biosensors has received significant attention in recent years from both the scientific and medical community. Recently, with the advent of professional sport the sports medicine industry has developed significantly. The use of biosensors in this area is of interest to monitor stresses exerted on muscles during exercise, which would give researchers the

means to aid athletes in recuperation and developing greater muscle efficiency. The simultaneous detection of numerous metabolites might permit the successful identification and control of many disorders and diseases that effect the human body.

It is proposed that the toxicity of many drugs and chemicals arise from the generation of superoxide and hydrogen peroxide to levels that are beyond the cell ability to efficiently control. These species are toxic to cells due to their oxidising effects on many cellular structures in particular proteins and DNA. Therefore, the accurate measurement of these species at the cellular level would be of great interest to therapeutic drug designers.

Biosensors for glucose detection provide perhaps the most tangible and useful application for the detection of H_2O_2. Hence, the requirement that biosensors operate under physiological conditions has influenced the buffer and pH range selected for study during this thesis. Many studies of possible biosensor systems have reflected this decision [1, 10-17].

Millions of people worldwide suffer from diabetes mellitus, which can be controlled by monitoring glucose levels in blood and injecting accordingly the required dose of insulin. Diabetes arises from many causes but all involve the inability of the body to assimilate glucose at a normal rate. The oral glucose tolerance test is used to diagnose diabetes mellitus. This test is a measure of an individual's ability to assimilate a glucose load. In normal cases blood sugar levels rise substantially within the first hour of the test and begin to decline by the end of two hours. Since the diabetic is unable to metabolise glucose at a normal rate their blood glucose level will rise much higher and return more slowly. This test gives an obvious application for a glucose biosensor.

Two systems of insulin therapy for diabetes have been developed. One is an open-loop system whereby a fixed dose of insulin is taken regularly. The other, which is of more interest, is the closed-loop where blood glucose levels are measured via a biosensor and the required dose of insulin applied. The problem of the closed-circuit system is the time lag between detection of damaging hyperglycaemia and insulin lowering glucose levels [18]. Therefore, development of a quick detection method is imperative. Amperometric glucose biosensors provide rapid response times and are candidates for this role. While *in vivo* biosensors would serve perfectly well, *in vitro* biosensors would provided many additional

benefits, not in the least patient comfort. Consequently, this field is beginning to attract a great deal of interest [16-21]. Electrochemical biosensors are, once again, ideal since they are easily miniaturised, reliable, unaffected by sample colour or turbidity, and as analyte consumption is minimal, bio-feed-back problems are minimised [19]. Implantable electrochemical glucose sensors would require a long lifetime and need to be free of reagent addition. Alleviating these concerns has become the source of much research, especially in developing better electrodes. Glassy carbon pasted with nickel hydroxide has been viewed as a possible electrode material for these biosensors. However, they perform satisfactorily for less than seven days [15]. This may make a pure nickel electrode superior since it has the potential to have a half-life significantly longer than this.

Glucose can be electrochemically detected directly by oxidisation at the electrode (for example activated platinum [19]) to gluconic acid.

$$\beta - \text{D glucose} \xrightarrow{\text{activated Pt}} \text{gluconic acid} + 2\text{H}^+ + 2\text{e}^- \tag{1.11}$$

However, this method is fraught with problems especially in clinical applications. Due to lack of selectivity, with other chemical species also giving an amperometric response, and poisoning of the electrode surface by adsorption [14].

The current method in favour is the indirect detection of glucose by measuring the H_2O_2 liberated from the enzymatic oxidation of glucose. These enzymatic biosensors avoid the lack of sensitivity exhibited by the direct methods by making use of the highly selective properties of enzymes. Clark and Guilbault, in 1973, were the first to exploit the production of H_2O_2 by the glucose oxidase (GOD) catalysed reaction.

$$\beta - \text{D glucose} \xrightarrow{\text{GOD}} \text{gluconolactone} + \text{H}_2\text{O}_2 \tag{1.12}$$
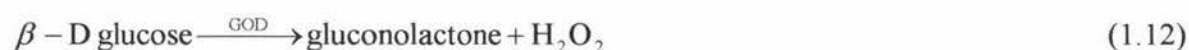
This used a Pt electrode to reduce H_2O_2. These electrodes are frequently referred to as Clark-type biosensors [22]. Since this discovery, considerable research has been put into these enzymatic biosensor systems that use GOD, in an effort to make a viable glucose sensor [10, 13, 14, 16, 17, 19-22].

A promising amperometric enzyme-based (GOD) glucose sensor has been developed and used as a detector in flow injection analysis (FIA) of diabetic patients blood glucose levels. GOD was immobilised by a glutaraldehyde/bovine serum albumin crosslinking procedure on the surface of a thin film of nickel hexacyanoferrate, which was electrocrystallised onto a

nickel electrode. This electrode was used to reduce the H_2O_2 produced by the biocatalytic action of GOD on glucose. This sensor was found to have good sensitivity over a reasonable range of glucose concentration, good stability and shows no interference by the common blood constituents [14].

Presently, researchers in the field of biosensors are active in pursuing the development of amperometric sensors, which are devoid of mediators. Such approaches pave the way for alternate and less complex methods for the construction of biosensors. The term reagentless biosensor has been coined to define an amperometric enzyme electrode which provides a substrate proportional current signal without being dependent on a mediator or coenzyme [15].

Many other enzymatic biosensors have been studied to detect metabolites other than glucose. These biosensors use similar H_2O_2 dependent electrodes but employ a different enzyme (usually an oxidase) that liberates H_2O_2 in the process of oxidising the target metabolite. Lactic acid is one such metabolite, which has drawn significant interest. Lactic acid is produced as a by-product of glycolysis, the body's system of producing usable energy from glucose. Muscles require energy and hence produce significant quantities of lactic acid. It may accumulate in muscles under conditions of high stress, especially in periods of anaerobic work, and will eventually inhibit the muscle operation. The rapid and reliable monitoring of lactate is therefore of great interest in the areas of clinical diagnosis, sports medicine, and biotechnology. Here, lactate oxidase is employed to catalyse the production of reaction H_2O_2.

$$L - \text{Lactate} + O_2 \xrightarrow{\text{Lactate oxidase}} \text{pyruvate} + H_2O_2 \tag{1.13}$$

Lactate dehydrogenase biosensors which liberate NADH have also proven useful [15, 22].

An alcohol biosensor employing alcohol oxidase has also received some attention [22].

$$\text{alcohol} + O_2 \xrightarrow{\text{alcohol oxidase}} \text{acetaldehyde} + H_2O_2 \tag{1.14}$$
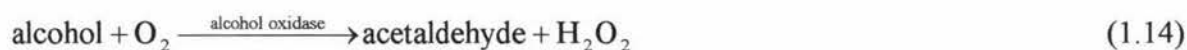
These have not been very successful due to low enzymatic activity and short enzyme lifetimes.

A nickel electrode used for the detection of H_2O_2 could most certainly be useful in all the applications described, whether to detect H_2O_2 levels for industrial, military, dairy or medicinal purposes. Electrochemical detection is capable of providing an easy, rapid, test

with minimal cost and waste. A nickel electrode would provide a cheaper alternative to many of the other electrode materials currently used such as platinum, gold, and electrodes produced from metal complexes.

1.4 Electrochemical Oxidation of Hydrogen Peroxide at Nickel Electrodes

After an exhaustive literature search only two minor references to the electrochemical oxidation of H_2O_2 on pure nickel metal electrodes were found [23, 24]. Both these papers were primarily concerned with the electroreduction of dioxygen and H_2O_2 at nickel electrodes. These studies were both extended to give a cursory examination of the electroxidation of H_2O_2. The findings of these two studies are discussed in Sections 1.5.2 and 1.5.3.

Otherwise, this is apparently an unresearched area, which is somewhat surprising given the potential interest. The majority of correspondence is concerned with the reduction of H_2O_2 [25-30]. Another major field evident in the literature was the spontaneous decomposition of H_2O_2, which does not take place under electrochemically controlled conditions. In electrochemistry, the reactions involved occur at the solution/electrode phase boundary and are driven by the potential applied to the electrode. It is therefore unlikely that dissociation studies will significantly aid the understanding of the electrochemical reactions. Where electrochemical H_2O_2 oxidation was reported in the literature it was on electrodes other than nickel [1-6, 13, 31-34]. When nickel was involved in the electrode composition it was as part of a complex or amalgam of metals [13, 31, 32, 34]. Many of these other studies were also performed under different buffer conditions, which further distances them from the present study. The hydrogen peroxide behaviour at these other electrode systems may, however, give some small insight into the behaviour at pure nickel electrodes in phosphate buffers under physiological conditions.

The nearest system to that studied in this thesis is the electrochemical oxidation of H_2O_2 on platinum electrodes studied by Khudaish [1-6]. This research was also performed with the Massey University electrode research group. Indeed, this research formed the platform for the study of the reaction at nickel electrodes. Many methods and analytical techniques developed Khudaish have been adopted in this study. A null hypothesis is that the

electrochemical oxidation of H_2O_2 on nickel electrodes will occur in an identical manner to that on platinum electrodes. Being of the same periodic group this is a naive but not entirely unreasonable expectation since elements in the same periodic group often have similar properties.

1.5   Relevant Literature

1.5.1   *Oxidation of Hydrogen Peroxide on Platinum Electrode Surfaces*

Hall *et al.* have recently publish a comprehensive series of papers [2-5] based upon Khudaish's doctoral research [1] on the study of the "Electrochemical Oxidation of Hydrogen Peroxide on Platinum Electrode Surfaces in Phosphate Buffer Solutions". The oxidation was studied over a range of bulk H_2O_2 concentration, rotation rates, potentials, temperatures, buffer concentrations and pH. It was found that there was not a simple relationship between the steady-state responses attributed to the oxidation and the parameters studied. These non-linear responses versus bulk H_2O_2 concentration were not inconsistent with a previous study on platinum [22]. Earlier, less complex models developed for electrode kinetics were found to be insufficient to describe the responses observed. These deficient models include the Levich model for mass transport control, and the Koutecty-Levich model, a more complicated model permitting control by both mass transport and electron transfer processes. Therefore, a complex mechanistic model for this reaction was developed using Micheals-Menten kinetics modified to incorporate mass transport.

The Khudaish model involved binding sites at the surface of the electrode that were based on some form of hydrous platinum oxide, initially identified as $Pt(OH)_2$. The model involved a series of cascading reactions of which the net effect yields

$$H_2O_2 \longrightarrow O_2 + 2H^+ + 2e^- \tag{1.15}$$

This net reaction, Eqn. 1.15, was not inconsistent with the pH data from another study on the same electrode system [35].

The proposed reaction mechanism commences with H_2O_2 adsorbing on to an active platinum-binding site to form the complex $Pt(OH)_2 \cdot H_2O_2$.

$$Pt(OH)_2 + H_2O_2 \overset{K_1}{\rightleftharpoons} Pt(OH)_2 \cdot H_2O_2 \qquad (1.16)$$

The complex then undergoes an internal electron transfer reducing the binding site and releasing the products water and oxygen.

$$Pt(OH)_2 \cdot H_2O_2 \overset{k_2}{\longrightarrow} Pt^{\circ} + 2H_2O + O_2 \qquad (1.17)$$

The reduced site then regenerates electrochemically with the release of protons. This gives rise to an amperometric signal.

$$Pt^{\circ} + 2H_2O \overset{k_3}{\longrightarrow} Pt(OH)_2 + 2H^+ + 2e^- \qquad (1.18)$$

Two side reactions were proposed, the first involved a competitive inhibition of the binding site by oxygen

$$Pt(OH)_2 + O_2 \overset{K_4}{\rightleftharpoons} Pt(OH)_2 \cdot O_2 \qquad (1.19)$$
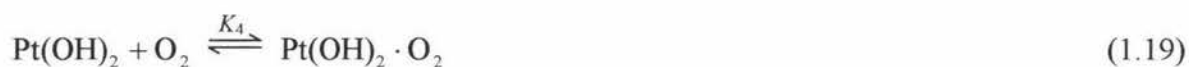
The second involved a non-competitive inhibition of $Pt(OH)_2 \cdot H_2O_2$ by protons

$$Pt(OH)_2 \cdot H_2O_2 + H^+ \overset{K_5}{\rightleftharpoons} Pt(OH)_2 \cdot H_2O_2 \cdot H^+ \qquad (1.20)$$
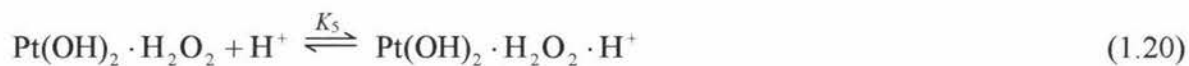
A rate equation was derived to account for all electrode sites involved in the proposed mechanism, with kinetic parameters for electrode reactions.

$$j = \frac{k_2 N K_1 [H_2O_2]}{1 + K_4 [O_2] + K_1 [H_2O_2](1 + K_5 [H^+] + k_2/k_3)} \qquad (1.21)$$

The kinetic and equilibrium constants of this model were optimised using a SIMPLEX procedure. The equilibrium constants were potential- and temperature-invariant ($K_1 = 6.38 \times 10^{-3}$ m^3 mol^{-1}, $K_4 = 0.128$ m^3 mol^{-1} and $K_5 = 0.053$ m^3 mol^{-1}). The rate constants, $k_2 N$ and $k_3 N$ were found to vary with both potential and temperature, and potential-dependent pseudo-activation energies for k_2 were found to range from 40 - 70 kJ mol^{-1}. Obtaining pseudo-activation energies for k_3 was not considered feasible.

The model was further developed to account for the formation of the platinum binding sites from precursor sites. Experiments with a range of buffer compositions showed that the steady-state responses for the oxidation of H_2O_2 were dependent on the phosphate concentration. In the absence of phosphate an alternate binding mechanism was evident. The pH-dependence studies suggested that $H_2PO_4^-$ was the species involved in the formation of platinum binding sites (now identified as Pt_{BS}) from precursor sites Pt_{PS}.

$$Pt_{PS} + H_2PO_4^- \overset{K_{BS}}{\rightleftharpoons} Pt_{BS} \tag{1.22}$$

1.5.2 *Nature of the Catalytic Surface*

Electrode catalysis occurs at the surface/solution interface. While most reactions are thought to occur on the surface in some cases the atoms from the electrode may dissociate to catalysis the reaction in solution before depositing back on the electrode surface. This mode of catalysis alters the physical structure of the electrode surface. This mode is not believed to be occurring at platinum or nickel but does highlight the intimate nature of the electrodes role in catalysis and hence why the behaviour of each type of electrode may be quite individual. The catalytic mechanism developed by Khudaish [1-6] to account for the electrochemical data was based on binding site theory as will also the mechanism established in this thesis. This theory asserts that the electrode surface is not completely homogeneous. There are sites at which the electrochemical reaction occurs where the electroactive solution species are involved in a shuttle system between these sites and the solution interface. These sites may be visualised in a similar manner to nuclei required for crystal nucleation. For the reaction to take place the site has to be in a critical conformation to allow the electroactive solution species to bind to the surface and react. The number of binding sites per unit area can not be quantitatively measured but may be estimated qualitatively from total response at the electrode (assuming reaction kinetics at each specific site). The observation that different electrodes have quite different rate characteristics to specific electrochemical reactions may well be due to the relative surface concentration and catalytic ability of the active sites. Should the concentration of active sites on an electrode be low and should these sites be of such a conformation that only slow catalysis could occur, then the electrode would not yield high rates.

The nickel and platinum electrode surfaces have been nominally referred to as Ni° and Pt°. However, it is widely recognised that the metal surfaces are readily oxidised at anodic potentials. Anson and Lingane [36] established through chemical analysis that both PtO and PtO_2 are formed on an anodic platinum electrode. Bulk growth of cupric (I) oxide/hydroxide films was clearly seen for potentials more positive than $-0.6V$ on copper-nickel alloys. These films were recognised as being important in H_2O_2 reduction kinetics [27]. Studies of passive

iron electrodes indicate that iron oxide films can be formed. These are, however, poor catalysts for H_2O_2 oxidation [37].

It is well documented that nickel forms phase oxides under anodic conditions. The nickel surface becomes more oxidised from oxidation states. II, III to IV as the potential is made more anodic [23, 38]. The composition of the nickel layer at 1.5 V is predominantly β-NiOOH [23]. In oxygen ionisation studies on nickel in alkaline conditions it was observed that above *ca.* −0.15 V vs SHE oxygen begins to adsorb and above +0.1 V a phase oxide such as $Ni(OH)_2$ is probably formed [39].

The K-Edge near edge x-ray adsorption fine structure (NEXAFS) technique showed that surface metal atoms on a charged nickel electrode, were coordinated to six oxygen atoms, together with Ni coordinated to two and four oxygen atoms, giving an average oxidation state of 3.5. Many structural phases were cited including α and β-$Ni(OH)_2$ and β and γ-NiOOH [40]. A nickel electrode that was electrochemically pretreated in a similar manner to that used in this thesis showed evidence of α-$Ni(OH)_2$, β-$Ni(OH)_2$ and NiOOH formation. The α-$Ni(OH)_2$ has a more open conformation than β-$Ni(OH)_2$. The pretreatment process involved cycling between −0.96 V and +0.69 V for one hour, left at open circuit potential for a further hour before being held for 10 minutes anodically at +0.34 V [41].

The rate of oxygen reduction at Nickel rotating disc electrodes (RDE) in alkaline solutions was found to be significantly diminished by surface nickel oxidation. Nickel was found to be highly oxidisable, with formation of oxides and possible oxygen penetration deep into the layers near the surface. The rate of non-electronic H_2O_2 decomposition at nickel was very low 4.4×10^{-11} mol s^{-1} cm^{-2}, when compared to the rate at platinum or silver. This is attributed to the presence of poorly conducting phase oxides near the steady-state potential [24]. The nickel oxide layers formed at $E > -0.8V$ are very slow to electrochemically reduced back to nickel metal [27].

Khudaish initially proposed that the active site on a platinum electrode, for the catalysis of H_2O_2 oxidation, was in the oxidised form $Pt(OH)_2$. In the face of the evidence presented above, an analogous hypothesis was subsequently adopted for this thesis. The catalysis of H_2O_2 oxidation on a nickel electrode is likely to occur at an active site in the form $Ni(OH)_2$. In a perfunctory study into the oxidation region of H_2O_2 some evidence was found for

oxidation occurring on nickel phase oxides [24]. Tseung *et al*. stated that the kinetics of the oxygen evolution reaction (H_2O_2 oxidation) on nickel electrodes in alkaline solutions depends on the physicochemical and structural characteristics of the oxo-hydroxide nickel layer [42]. Chang *et al*. found that "the catalytic action of the nickel surface in alkaline media appears to be associated with the formation of a higher oxide, commonly termed NiOOH, from the Ni(OH)$_2$" [43].

1.5.3 *Reactions of Hydrogen Peroxide and Oxygen on Oxidised Surfaces*

Care must be taken to avoid confusing electrochemically obtained electroactive surfaces and surfaces obtained by other means. There are strong differences between a nickel oxide surface obtained by electrochemically means and those obtained by calcination [44] or by directly crystallising nickel oxo/hydroxide salts onto the electrode surface [15, 23]. Despite this, these may perhaps provide the best insight into how H_2O_2 might react on pure nickel electrodes.

Carbonio, Macagno and Arvia [23] found that the potential at which H_2O_2 oxidation occurs is dependent on the nature of the electrode. The reaction begins at significantly lower anodic potentials on vitreous carbon electrodes (*ca.* +0.1V) compared to carbon electrodes precipitated with Ni(OH)$_2$ (*ca.* +0.8V). Hydrogen peroxide electroxidation was observed to take place at a potential lower than that of the Ni(II)/Ni(III) couple. Thus adding to the proposition that Ni(OH)$_2$ is the electroactive species. However, it should be noted that the catalytic activity of electrodes prepared by precipitation of nickel hydroxide on a range of conducting substrates, for O_2 evolution, were found to depend on the presence of nickel (III) oxide species (NiOOH) [23].

A glassy carbon electrode modified with Ni(OH)$_2$ was used to detect biologically important compounds such as glucose, hydrogen peroxide, lactate and ascorbate. The nickel oxide species involved was believed to be NiOOH since the oxidation of glucose, lactate and ascorbate occurred at the potential of the Ni(OH)$_2$/NiOOH redox couple. However, catalysis of hydrogen peroxide on glassy carbon pasted with Ni(OH)$_2$ produces substantial currents at a lower potential than the Ni(OH)$_2$/NiOOH redox couple. On bare glassy carbon

electrodes oxidation of H_2O_2 did not proceed at an appreciable rate up to +1.0 V vs SCE and beyond +1.0 V the background currents became large [15].

Where oxide surfaces were obtained by calcination it was found that all the phase oxides were energetically comparable with the catalytic activity depending on the concentration of the active sites and not on its nature [44].

1.5.4 *Assorted Studies of Hydrogen Peroxide Oxidation*

The electrochemical oxidation of hydrogen peroxide at electrode systems other than nickel may yield some insight into what may occur on nickel so it is prudent to briefly examine these other systems. However, one must bear in mind each system is unique and correlation between these reactions and those at pure nickel electrodes may well be tenuous at best. For instance, the electroreduction of H_2O_2 at a pure nickel electrode produces a markedly different potentiogram to that on a copper-nickel alloy [27]. However, the authors did appear satisfied that there were significant analogies between the electrocatalytic activities of copper-nickel alloy electrodes and those of gold electrodes. It was also found that the Levich model could satisfactorily account for the electrochemical oxidation of H_2O_2 at silver electrodes [45]. This was not found to be the case for this reaction studied by Khudaish at platinum electrodes where a markedly more complicated model was required [1-6].

A glassy carbon electrode showed an electrochemical process, at $E > +0.2$ V vs SHE, occurring at pH 11.72 [33]. This anodic wave, which was not observed below pH 10, was attributed to the superhydroxide reaction

$$OH_2^- + OH^- \rightleftharpoons O_2 + H_2O + 2e^- \tag{1.24}$$

The support for this reaction appears weakened by an unresolved reaction order with respect to OH^-. This wave, somewhat unusually, showed little to no rotation rate dependence. This limited mass transport control, which would not be expected from a solution species, is perhaps more indicative of the presence of surface oxide species. The formation of surface oxides at this potential has been well observed on other electrodes [27] and the propensity of carbon to be oxidised to surface hydroxides, aldehydes, ketones and carboxylic acids is recognised. The conclusion is therefore reasonably dubious and a more apparent explanation would evolve from the oxidation of the carbon surface in highly basic conditions. The

authors note that this anodic wave was not observed in other similar studies on Pt, Pd, Au, Ag, Graphite and Fe electrodes [33]. This further highlights the dangers or comparing one system to another.

The suggestion that oxidation of H_2O_2 proceeds through a superhydroxide pathway is reasonably common in the literature [23, 31, 33, 37, 46-48] especially at high solution pH. However, none rule out the involvement of H_2O_2. Non electrochemical decomposition studies [34, 49] on metal complexes have indicated that superhydroxide is a more reactive species which may be reflected in electrochemical oxidation. On pyrolytic graphite electrodes it was found that the enhanced rate, at pH > 9 indicated that the H_2O_2 oxidation mechanism proceeded via the superhydroxide ion. However, this study lacked reproducibility, which prevented a defined mechanistic proposal [47]. Carbonio, Macagno and Arvia [23] subscribe to the theory that the H_2O_2 oxidation proceeds through the superhydroxide pathway on electrodes pasted with $Ni(OH)_2$ when NaOH is the electrolyte. Only one reference appeared to suggest that for the metal complexes studied the superhydroxide pathway

$$H_2O_2 \rightleftharpoons HO_2^- + H^+ \tag{1.24}$$

$$HO_2^- + M^{3+} \longrightarrow HO_2^{\bullet} + M^{2+} \tag{1.25}$$

$$2HO_2^{\bullet} \longrightarrow H_2O_2 + O_2 \tag{1.26}$$

$$\text{or } HO_2^{\bullet} \longrightarrow O_2 + H^+ \tag{1.27}$$

$$\text{or } HO_2^{\bullet} + M^{3+} \longrightarrow O_2 + M^{2+} + H^+ \tag{1.28}$$
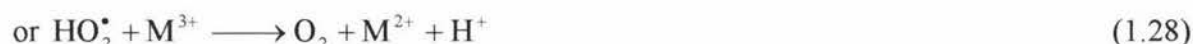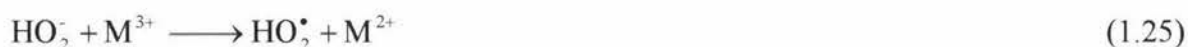
is the dominant mode of H_2O_2 oxidation to pH as low as pH 2 [31].

Studies of H_2O_2 oxidation at passive iron electrodes, in buffers from pH 9.8 to 13.8, show that superhydroxide is the most likely electroactive species. The reaction order for H_2O_2 is 0.5. This suggested the novel mechanism

$$OH_2^- \rightleftharpoons HO_2^-(ads) \tag{1.29}$$

$$HO_2^-(ads) \longrightarrow HO_2^{\bullet}(ads) + e^- \tag{1.30}$$

$$HO_2^{\bullet}(ads) + OH^- \rightleftharpoons H_2O + O_2^- \tag{1.31}$$

$$O_2^-(ads) \rightleftharpoons O_2 + e^- \qquad\qquad (1.32)$$
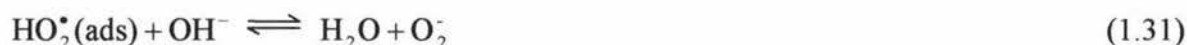
The authors recognised, however, that their data did not refute another mechanism that was previously proposed by Zurilla *et al.* [91]

$$HO_2^- + O_2 + OH^- \rightleftharpoons H_2O + 2O_2^-(ads) \qquad\qquad (1.33)$$

$$O_2^-(ads) \rightleftharpoons O_2 + e^- \qquad\qquad (1.32)$$

An interesting finding from this study [37] was that the current was almost independent of rotation rate for a significant range of electrode potential. The rate was also unaffected by N_2 or O_2 in solution which is surprising given the two proposed mechanisms.

Preliminary studies of H_2O_2 oxidation on a bare gold electrode surface found no electrocataylic oxidation in 0.1 M Na_2SO_4 solutions. In $NaNO_3$ solutions a higher capacitive current is observed so there is inconclusive evidence of H_2O_2 oxidation. This would indicate to some definite buffer involvement in the electrochemical behaviour of the bare gold electrode [50].

Hydrogen peroxide oxidation at self-assembled monolayers (SAM) of Nickel (II) pentazamacrocyclic complexes on gold electrodes have been studied in pH 2.7 Na_2SO_4 and $NaNO_3$ solutions. H_2O_2 oxidation on the SAM proceeding through an inner sphere reaction that requires free coordination sites. The voltammogram developed from this reaction was quite unique, especially in $NaNO_3$ buffers where a sharp peak was observed in the cathodic scan in a similar manner to that on the anodic scan. Such unique behaviour is expected to reflect the mechanistic details of the catalytic oxidation of H_2O_2 by the SAM. This would therefore not be expected to be analogous to nickel or any other electrode system with the possible exception of SAMs. That the rate of H_2O_2 oxidation was so dependent on $[NO_3^-]$ was attributed to NO_3^- anions stabilising the intermediates in the rate-determining step [50, 51]. Although this mechanism of buffer involvement is not available for bare metal electrodes it does highlight that solvent effects should not be ignored. Since H_2O_2 oxidation at the SAM is so unique, it is doubtful any analogies between this and pure nickel electrodes might be found.

1.6   Scope of Research

The primary aim of this thesis was to investigate the electrochemical reaction of H_2O_2 oxidation at nickel electrodes in phosphate buffer solutions under physiological conditions. This was with the goal of developing a mechanistic model to account for the faradaic currents yielded from this reaction over a range of conditions. The mechanistic model developed would then be used to quantitatively evaluate the kinetic and thermodynamic parameters.

The mechanism proposed was a modification of that developed by Khudaish [1-6] to describe the H_2O_2 oxidation at platinum electrodes over a similar range of conditions. The electrochemical oxidation was investigated, in reference to the mechanism developed, to gain understanding of the effects of varying the parameters:

i)   potential, rotation rate, hydrogen peroxide concentration [Chapter 3]

ii)   temperature [Chapter 4]

iii)   and buffer composition, to both pH and phosphate concentration [Chapter 5].

The electrochemical technique staircase potentiometry was primarily used in this investigation. SIMPLEX optimisation techniques were used to determine the appropriateness of the mechanistic model and to obtain the kinetic and thermodynamic parameters.

CHAPTER 2

EXPERIMENTAL METHODS

2.1   Introduction

In this thesis a number of electrochemical techniques including cyclic voltammetry and potential staircase were employed to explore the oxidation of hydrogen peroxide in phosphate buffer solutions. The reaction was studied over a range of conditions for buffer temperature, phosphate concentration and pH.

This chapter provides details of the methods and techniques utilised during the course of this thesis, including the underlying theories and concepts upon which these are based. The chapter includes details of equipment (both electrochemical and mechanical), software, reagents and procedures for the preparation of the buffer solutions.

2.2   Electrochemical Equipment

2.2.1   *Components of the Electrochemical Cell*

The electrochemical cell consisted of three electrodes as shown in Fig. 2.1. Either a nickel rotating disc working electrode (RDE), surface area 0.07069 cm^2, (custom made to Massey University specifications by Bioanalytical Systems Inc, Indiana, USA) or a static nickel working electrode (nickel purchased from Johnson Mathey 99.997%, assembled in PEEK plastic housing by IFS workshop, Massey University, NZ). A Pt coiled wire as a counter electrode and for the reference electrode, a silver/silver chloride gel electrode (3M NaCl) with potential of + 197 mV vs SHE (Bioanalytical Systems Inc., Indiana, USA).

All the electrodes were held in a phosphate buffer solution contained within a 250 ml thermostated water jacket (IFS Glassblowing Workshop, Massey University, NZ). This buffer was maintained at the desired temperature by a circulating water bath (Colora, Messtecknik, GmbH, Germany) which pumped water through the water jacket. The temperature of the phosphate buffer solutions was constantly monitored by a calibrated
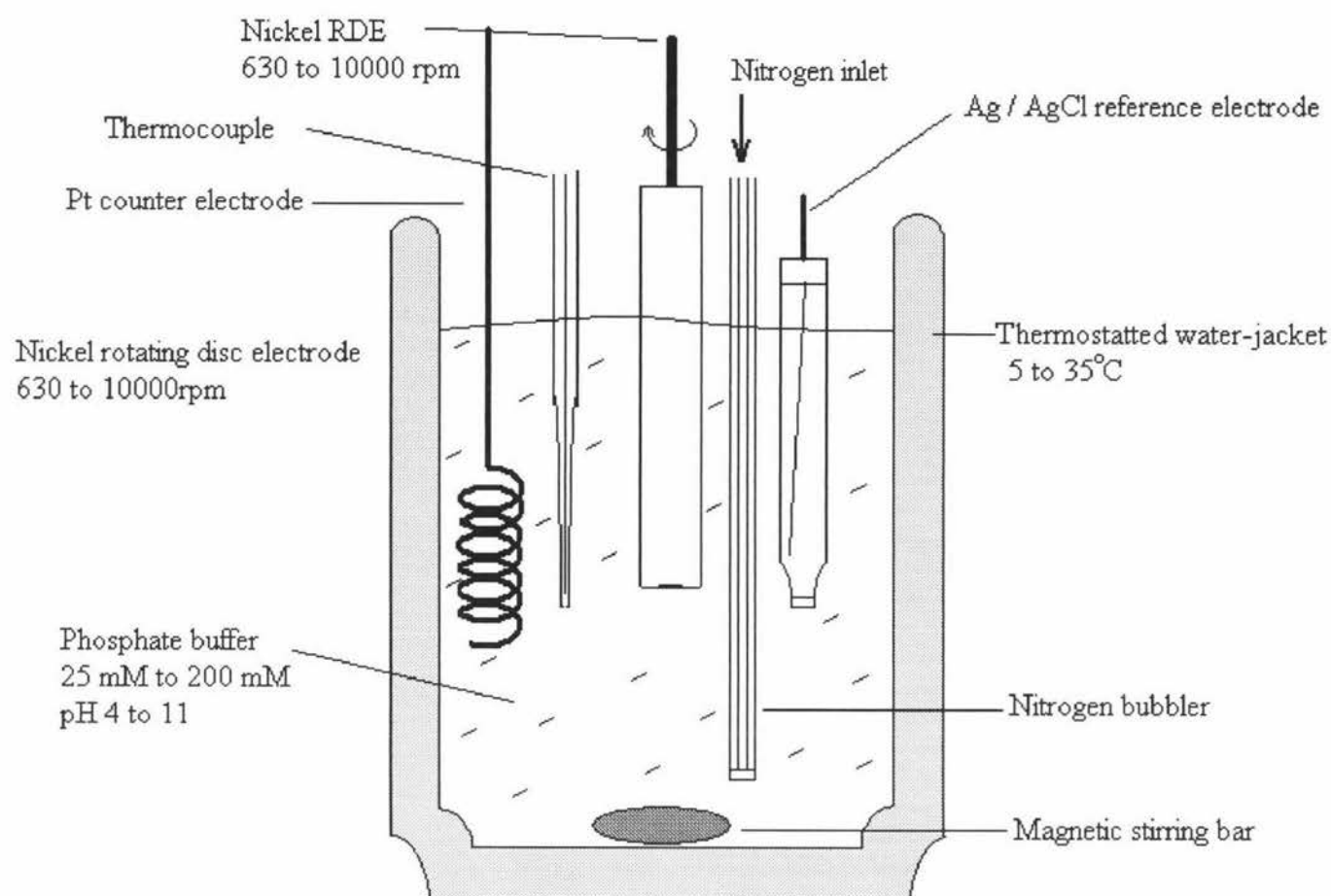
Fig. 2.1   A schematic diagram of the electrochemical cell.

thermocouple (Barrant 115, Taiwan) placed at the same depth as the inverted face of the working electrode. A stirrer bar was used for re-establishing homogeneous conditions after addition of aliquots of concentrated H_2O_2 stock solutions to the cell.

2.2.2   *The Rotating Disc Electrode System*

The nickel rotating disc electrode consists of a cylindrical nickel rod with a diameter of 0.30 cm and a surface area of 0.07069 cm^2 encased within a Kel-F type plastic cylinder, of diameter 0.65 cm. This was mounted vertically onto the shaft of a synchronous digitally-controlled motor in the RDE-1 device (Bioanalytical Systems Inc, Indiana, USA) and rotated at a constant speed (rad s^{-1}) in a direction perpendicular to the plane of the electrode disc.

Both the nickel RDE and the static nickel working electrodes were preconditioned before every experiment unless otherwise stated. Preconditioning involved the nickel surface being polished on a buffing pad (PK-4 microcloth, Bioanalytical Systems Inc, Indiana, USA) with 0.05 μm alumna past (Bioanalytical Systems Inc, Indiana, USA) for 3 min. If corrosion was visually evident then a new surface was rendered using a coarse nylon pad and 1 μm diamond paste (Bioanalytical Systems Inc, Indiana, USA), then polished for 3 min with 0.05 μm alumna past as before. After polishing the electrode was rinsed and then electrochemically cycled from 0 to +1000 mV vs Ag/AgCl at 100 mVs^{-1} for 20 cycles terminating at the anodic potential of 0 mV at the end of the final cycle. An example preconditioning cycle taken for the 25°C series of experiments in the primary 0.1 M phosphate buffer at pH 7.28 is shown in Fig. 2.2. This is believed to increase activity by coating the nickel surface with a uniform film of Ni(OH)$_2$ and avoids the growth of a higher oxidation state oxide film, which may decrease the activity of the electrode [1-6, 23, 24, 27, 41, 42]. This preconditioning was carried out in the appropriate phosphate medium for subsequent sequences of experiments.

2.2.3   *Calibrating the Rotation Disc Electrode*

The RDE was calibrated using a Digital Photo/Contact Tachometer (EXTECH Instruments, Taiwan) to ensure that the RDE settings were achieving the rotation rate reported by the RDE-1 display panel. Calibration proceeded by affixing a small reflective strip to
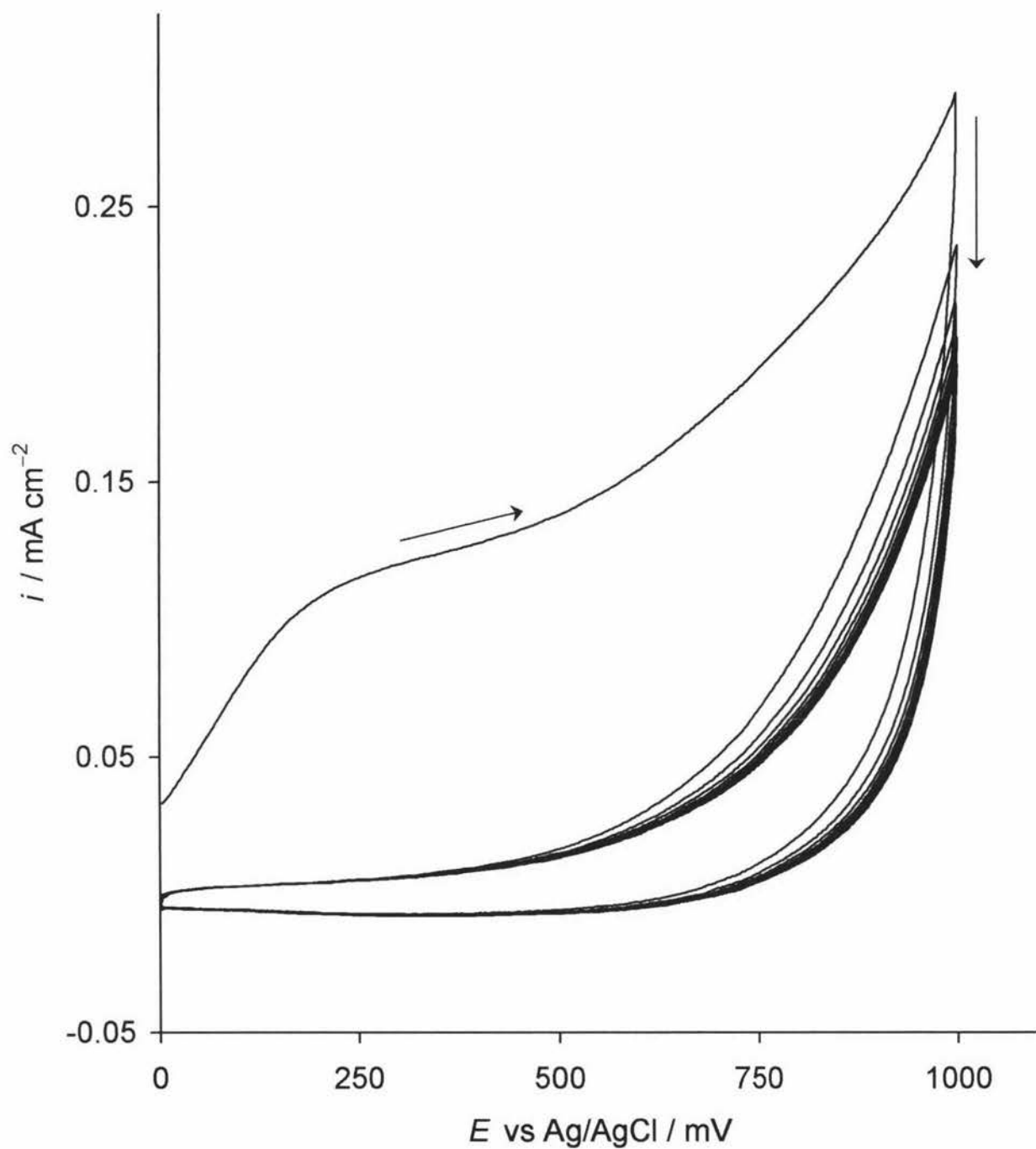
Fig. 2.2   A sample preconditioning cycle taken from the 25°C experiment run in the primary 0.100 mol L^{-1} pH 7.28 phosphate buffer. This was cycled for 10 cycles over the 0 to +1000 mV potential range at a sweep rate of 100 μV s^{-1}.

the shaft of the electrode. The Tachometer set in Photometric mode projects a light which when held 50 mm to 150 mm will return a signal every time the reflective strip passes the sensor. The Tachometer samples the number of signals (strip revolutions) continuously and reports the rotation rate in revolutions per minute. The Tachometer manufacturers claim ±0.05% accuracy or to the last digit over the range of 5 to 99999 rpm [52] well within the range of rotation rates employed in this thesis. The Tachometer confirmed that the rotation rates used in this thesis were indeed accurate as shown by a set of typical results listed in Table 2.1. There is in fact a 100% correlation between the RDE setting and the recorded rotation rate for a wider range of rotation rates (Fig. 2.3).

2.2.4 *Electrolyte Pumping Activity of the RDE*

As the RDE rotates a centrifugal force, in a direction parallel to the surface and towards the electrode's rim, impinges on every point on the electrode surface. Solution molecules near the electrode surface will also be effected by the centrifugal force. The solution, which is mobile, will therefore flow from the centre towards the rim (Fig. 2.4(a)). The bulk solution will be drawn in to replace this surface solution. This replenishing solution originates from the bulk solution at an angle perpendicular to the surface of the electrode (Fig. 2.4(b)). Thus, the rotation of the RDE acts as a pump drawing solution in from the bulk and across the surface of the electrode. It is recognised as a very useful method of obtaining efficient mass transport in a highly reproducible and predictable manner [53].

2.2.5 *Mass Transport and Electrode Rotation Rate*

When the rotating disc electrode is rotating the linear velocity of points on the surface increases with increasing distance from the centre of the electrode. However, the rate of mass transport to the surface is uniform since the mass transport is dependent upon the supply of solution to the surface and, as described in Section 2.2.4, above this is independent of the velocity of any one point on the surface. The faster the RDE is rotated, the more rapidly the solution is "pumped" over the surface. However, this has a limit at the point where the solution flowing over the electrode surface changes from lamina to

The RDEs setting rpm	Digital Tachometer reading rpm
630	629.6
1000	1000
1585	1585
2500	2500
4000	4000
6300	6300
10000	10000

Table 2.1   Digital Tachometer confirmation of the seven rotation rates used during the course of this thesis.
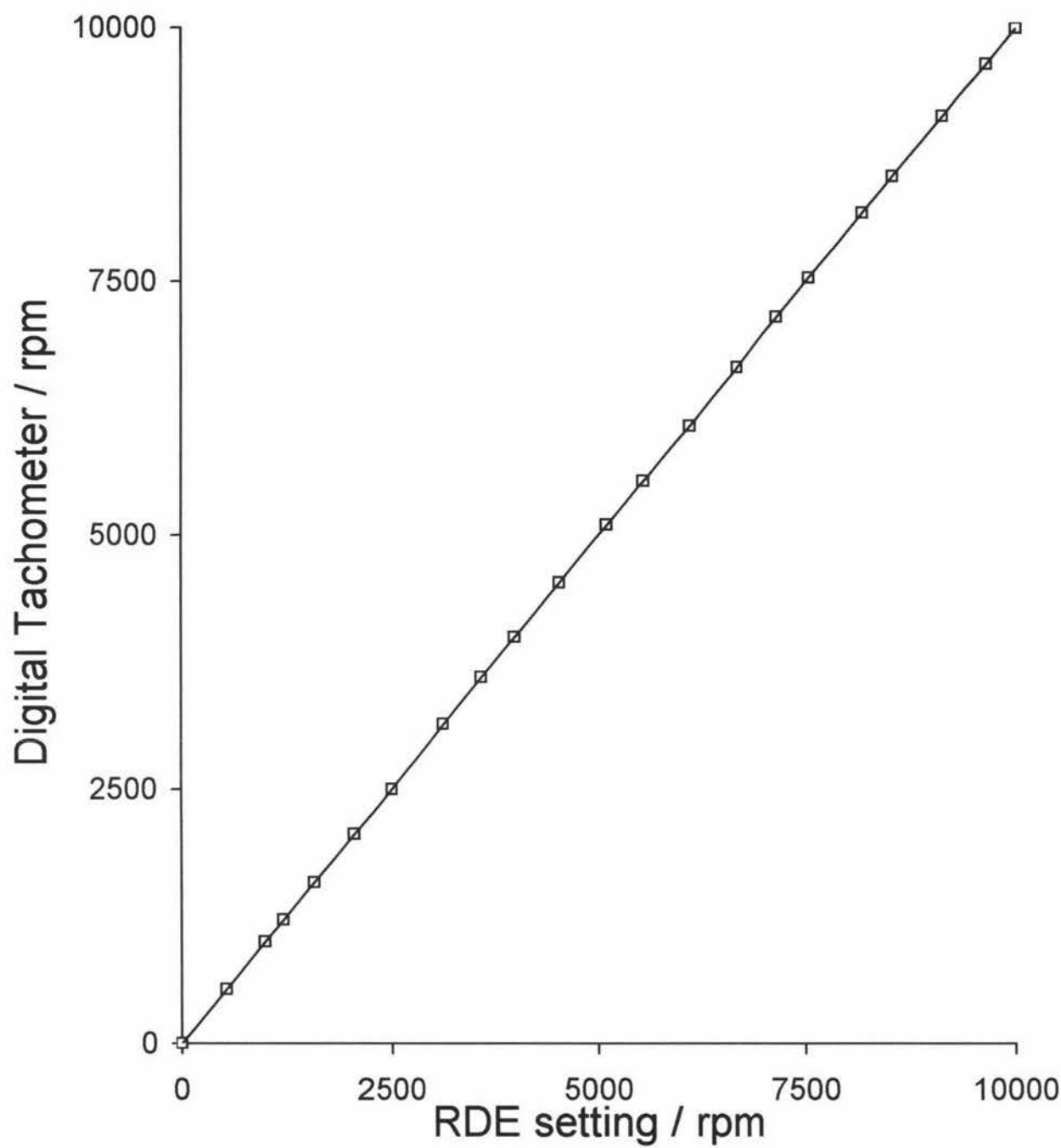
Fig. 2.3   Calibration line for the rotation rates settings of the RDE-1 device using a Digital Tachometer for a range of selected rotation rates over the 0–10000 rpm range
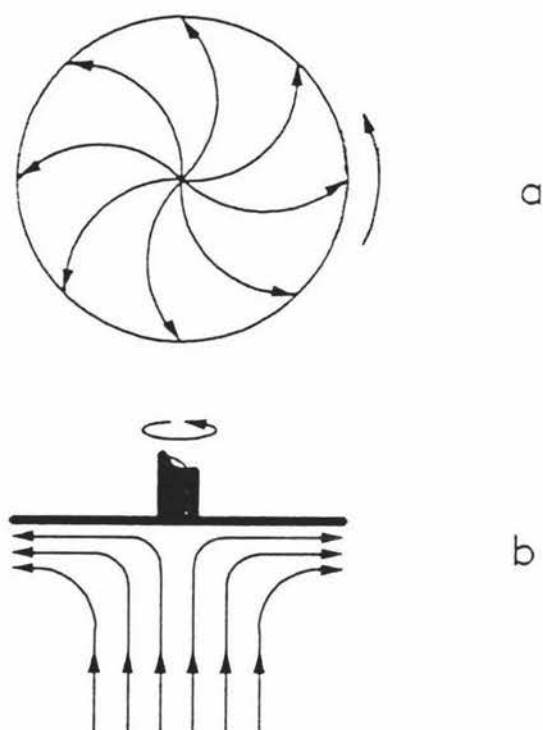
Fig. 2.4(a) A schematic diagram of solution flow across the surface of a rotating disc electrode

    (b) Flow of bulk solution "pumped" towards the rotating disc electrode.

turbulent flow. If turbulent flow were to occur, the mass transport relationships discussed in the following section become inappropriate. In turbulent flow random eddies and ripples cause transient concentration profiles over the surface in an entirely unpredictable manner and consequently is of little use for electrochemical studies. The transition from laminar to turbulent flow is described by the Reynolds equation.

$$Re = \frac{vl}{\upsilon}$$
(2.1)

where Re is the Reynolds number, l is the characteristic length of the flow in this case the radius of the rotating disc electrode, υ is the kinematic viscosity (defined as viscosity multiplied by the density) and v represents the characteristic velocity, which in this case is the linear velocity of the outer edge of the disc. This linear velocity is given by Eqn.2.2.

$$v = \omega r$$
(2.2)

Where ω is the angular velocity in rad s^{-1}. Substitution of Eqn. 2.1 into Eqn. 2.2 affords the Reynolds equation for a rotating disc electrode.

$$Re = \frac{\omega r^2}{\upsilon}$$
(2.3)

The Reynolds number is a dimensionless number provided r and υ are both measured with the same dimensions for length (i.e. cm for r and cm^2 s^{-1} for υ). The critical value for Re is 1×10^5. Above this, turbulent flow is expected to predominate. This value is set assuming an ideally smooth electrode surface perpendicular to rotation. Since this can not be achieved in practice the critical Reynolds value will be lower than 1×10^5. Using a viscosity of 0.02 cm^2 s^{-1} for a dilute aqueous solution, a Reynolds number of 4720 is obtained. This is significantly lower than the critical Reynolds value of 1×10^5 for an ideally smooth surface. In an ideal situation the maximum rotation rate that can be used before flow becomes turbulent is approximately 22200 rpm. This is somewhat higher than the maximum rotation rate of the RDE-1 equipment.

The lower limit for RDE rotation rate occurs when the rotation rate is so slow that the limiting current density is not significantly larger than what one would obtain when the electrode is stationary and mass transport is due to natural convection. This lower limit is approximately 400 rpm and can only be extended lower in carefully controlled experiments [53]. In this thesis, the lowest rotation rate used is 630 rpm. Therefore, both the highest and lowest rotation rates employed in this thesis are well within the recognised limits for a rotating disc electrode system. This, combined with the precision electrodes and electrode shaft provides confidence that the solution flow along the surface of the electrode is laminar in character and is giving uniform mass transport of H_2O_2 over the electrode surface.

In such cases and where mass-transport is the only limiting parameter the Levich equation can be used to calculate the limiting current density, i_L.

$$i_L = 0.62nFD^{2/3}v^{-1/6}\omega^{1/2}c_{bulk} \qquad (2.4)$$

where F is the faraday constant (96484.6 C mol^{-1}), n represents the number of electrons that take part in the overall reaction. D is the diffusion coefficient for hydrogen peroxide, ω is the rotation rate of the RDE and c_{bulk} represents the hydrogen peroxide concentration of the bulk solution.

2.2.6   *Problems of Gas Bubbles*

Gas bubbles may cause problems by adhering to the inverted surface of the nickel RDE since these reduce the surface area of the electrode exposed to the solution. This will decrease the amount of H_2O_2 oxidation and therefore the observed current. Bubbles will also alter the hydrodynamic flow across the electrode surface by causing turbulence. Since these bubbles do not form in a regular and consistent manner, they cause inaccurate and inconsistent results which can not be later accounted for during data processing.

There are two gases which may form bubbles in the system under study. The first is oxygen created as a by-product of the H_2O_2 oxidation. The other is nitrogen gas, which is bubbled to deoxygenate the solution as described in Section 2.2.8. The technique employed to prevent gas bubbles adhering to the inverted surface of the nickel RDE was to rapidly pulse the RDE revolutions to the maximum possible (10000 rpm), by application of an external

analogue signal to the rotation rate input of the RDE–1 device. This spins the bubbles from the surface of the RDE. If any bubbles persist then the RDE was raised out of the solution and pulsed to 10000rpm before being immersed back into the buffer solution. This technique was applied before every experiment and after any bubbling of nitrogen gas through the solution.

2.2.7 *Chronological Effects*

A single series of experiments by necessity takes a significant period of time (~13 hours). The electrode is only mechanically polished prior to this series. Preliminary experiments showed that the electrode exhibits a time-based change in character to become slowly more catalytic (observed as an increase in current) possibly attributable to an enlargement of electrode surface area. Figure 2.5 shows SCP experiments conducted at 0.010 mol L^{-1} [H$_2$O$_2$]$_{bulk}$, $\omega = 4000$ rpm and from +332 mV to +1100 mV vs Ag/AgCl over a 1 hour period. From Fig. 2.5 the electrode can be seen to become more catalytic with time however after the initial surge the relative change in electrode character slows significantly. Over one hour the current increased by *ca.* 0.010 mA cm^{-2} with strong indications that it did not increase significantly further. This increase is insignificant when considering the changes in response due to varying other solution parameters studied in this thesis. Each SCP series are chronologically only five minutes apart from each other so any change with time would be dispersed. For these reasons time based effects are considered insignificant and are henceforth ignored. In any case the preconditioning time described in Section 2.2.2 exceeded the time period for this chosen activity.

2.2.8 *General Set Up Procedure for a Potential Step Experiment*

The thermostated water jacket was filled with 250 ml of the relevant phosphate buffer, which was then heated or cooled to the desired temperature by heated water pumped though the water jacket by the circulating temperature controlled water bath. The phosphate buffer solution was deoxygenated by bubbling oxygen free nitrogen gas through the solution for half an hour. The nickel RDE (working electrode) was polished for three minutes on a buffing pad with fine 1 μm aluminium paste, then thoroughly cleaned with methanol then
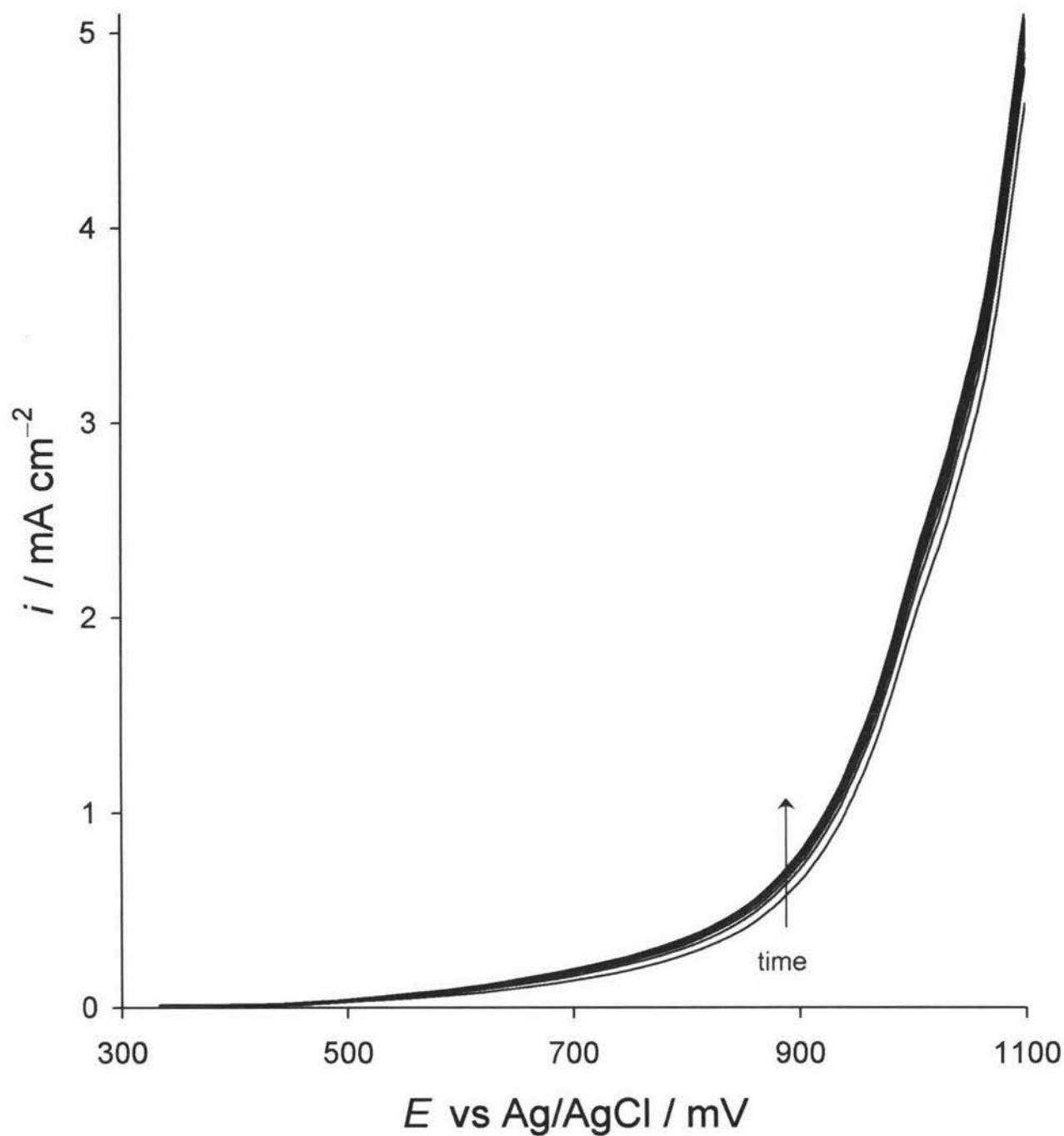
Fig 2.5   Steady-state responses after 0, 4, 8, 12, 16, 20, 32, and 60 minutes for $[H_2O_2]_{bulk} = 0.010$ mol L^{-1} at $\omega = 4000$ rpm and $E = +332$ mV to $+1100$ mV vs Ag/AgCl. Change over time indicated by the arrow.

Millipore water before being immersed in the phosphate buffer solution. The Ag/AgCl reference and Pt counter electrodes were both thoroughly cleaned with Millipore water and inserted into the buffer solution to the same depth as the working electrode. Both electrodes were both taped to the RDE-1 device to prevent movement. Similarly, the thermocouple used to measure the buffer temperature during the experiment was placed at the same depth as the working electrode (see Fig. 2.1). All bubbles adhering to the electrodes were removed in the manner described in Section 2.2.5. After removing the bubbles the RDE-1 device was set to 630 rpm for the preconditioning cycle.

2.3   Reagents

2.3.1   *Chemicals*

All chemicals used during the course of this thesis were AR grade. All solutions were prepared in Millipore water (Nanopure II, Barnstead, Newton, Massachusetts, USA). The chemicals used to make the phosphate buffer solutions included di-potassium Hydrogen ortho-phosphate (Univar, Australia), tri-potassium phosphate-1-hydrate (Riedel-de Haën, Seelze-Hannover), potassium di-hydrogen phosphate (Riedel-de Haën, Seelze-Hannover), and orthophosphoric acid (Univar, Australia).

The concentration of hydrogen peroxide (30% wt/wt Prolabo, France) used for experimental work was calibrated prior to use (Section 2.3.1). Chemicals used for this includes $KMnO_4$ (Univar, Australia) and potassium oxalate (Merck, Germany).

2.3.2   *Preparation of Hydrogen Peroxide Solutions*

Due to hydrogen peroxide decomposing over time the concentration of the pure hydrogen peroxide used for experimental work had to be continuously measured. This was achieved by titrating against $KMnO_4$ which in turn was standardised using the primary standard oxalate. The concentration of the 30% wt/wt hydrogen peroxide was determined in this manner before commencing a run of experiments and checked regularly thereafter. The bottle was replaced when the concentration dropped by more than 5% below the quoted concentration as stated by the supplier. Although wasteful, this procedure was adopted since experience showed that should the concentration drop much lower than the 5%

threshold the concentration was liable to rapidly fall with time. This may be due to introduction of particulate impurities into the bottle from successive openings, which catalyse the decomposition of hydrogen peroxide, reaching sufficient levels to cause significant concentration change. This rapid decline in concentration would give no confidence that the measured concentration will be accurate for any length of time.

For the stock hydrogen peroxide was the mixed with an equal amount of phosphate buffer made to twice the concentration of the experimental buffer. This was done so that the double strength buffer is diluted by the pure hydrogen peroxide to be the same phosphate concentration as the experimental buffer. Therefore, as the buffer diluted hydrogen peroxide was added to the vessel, the total buffer concentration was not altered.

The buffer diluted hydrogen peroxide was added to the bulk experimental buffer, with a calibrated auto-pipette, in 440 µL aliquots. After each addition the solution was thoroughly homogenised using a magnetic flea and the RDE-1 device set to 10000 rpm. During stirring the solution was also deoxygenated by bubbling pure nitrogen through the buffer. The solution is stirred and deoxygenated for four minutes. Finally, the working electrodes again had bubbles removed immediately prior to the next set of potential step experiments.

2.4 Preparation of Phosphate Buffer Solutions

Unless otherwise stated, all experiments were carried out in the primary phosphate buffer solution, 0.100 mol L^{-1} phosphate and pH 7.28. This primary phosphate buffer was the buffer to which all experiments are compared.

2.4.1 *Phosphate Buffer Solutions of Varying Concentrations*

Phosphate buffer solutions of varying concentrations were prepared, according to the methods described by Khudaish (composition shown in Table 2.2). The pH was maintained as close as possible to 7.28 to permit comparisons to be made with the primary solution.

2.4.2 *Phosphate Buffer Solutions of Varying pH*

Phosphate buffer solutions of varying pH were prepared, according the methods described by Khudaish (preparations shown in Table 2.3). These preparations were designed to maintain the concentration of phosphate at 0.1 mol L^{-1} allowing the effect of changing the

$\dfrac{[PO_4^{-3}]_{Nominal}}{mol\ L^{-1}}$	$\dfrac{K_2HPO_4}{mol\ L^{-1}}$	$\dfrac{KH_2PO_4}{mol\ L^{-1}}$	pH
0.025	0.017	0.008	7.29
0.050	0.036	0.014	7.32
0.075	0.054	0.021	7.29
0.100	0.075	0.025	7.28
0.150	0.110	0.040	7.26
0.200	0.146	0.054	7.23

Table 2.2   Preparations following Khudaish [1,5] for phosphate buffer solutions of varying concentrations at the approximate pH of ~7.28 over the range of 25 to 200 mM together with the measured pH.

$\dfrac{K_3PO_4}{mol\ L^{-1}}$	$\dfrac{K_2HPO_4}{mol\ L^{-1}}$	$\dfrac{KH_2PO_4}{mol\ L^{-1}}$	$\dfrac{H_3PO_4}{mol\ L^{-1}}$	$\dfrac{E_{glass}}{mV}$	pH
—	—	0.09700	0.00300	174.7	4.07
—	0.0025	0.09750	—	107.7	5.35
—	0.0125	0.08750	—	85.7	6.09
—	0.0750	0.02500	—	7.19	7.28
—	0.0960	0.00400	—	−46.0	8.20
0.00025	—	0.09975	—	−90.0	9.14
0.05275	—	0.04725	—	−163.3	10.28
0.06245	—	0.03755	—	−232.4	11.51

Table 2.3   Preparations following Khudaish [1,5] for phosphate buffer solutions of varying pH for the constant concentration of 0.100 mol L^{-1} together with the measured glass electrode potential and corresponding pH.

pH on the electrochemical oxidation of hydrogen peroxide to be studied. These solutions will be compared to the primary 0.1 mol L^{-1} pH 7.28 buffer.

The pH of each phosphate buffer solution was measured before each run using a high impedance pH-meter (Model 50, Denver Instrument Company, USA). The pH-meter was fitted with a pH – Ag/AgCl combination glass membrane (Denver Instrument Company, USA) in which the reference compartment was filled with 4 mol L^{-1} KCl saturated with AgCl.

The pH of the solution measured was calculated using the Nernst relationship

$$E_{glass} = E_{glass}^{\circ} - (2.303RT / nF)\text{pH} \tag{2.5}$$

where E_{glass} is the measured potential for the solution and E°_{glass} is the standard potential of the glass electrode with respect to the internal Ag/AgCl reference electrode. Equation 2.5 describes an ideal system, however, electrodes are seldom ideal. Therefore the pH-meter Ag/AgCl combination glass electrode was calibrated at 20°C against standard solutions prepared from pH 4 to 11 (preparations taken from [54], see Table 2.4) before every pH measurement to account for any change in the electrode character between experiments. Using Eqn. 2.6 a more accurate value for the slope can be obtained and, therefore, a more accurate pH can be determined.

$$E_{glass} = \text{intercept} - \text{slope} \times \text{pH} \tag{2.6}$$

where the slope and intercept are the equivalents of 2.303 RT/nF and E°_{glass} respectively. The average value obtained for the slope was –52.192 mV decade^{-1}, which is different but in reasonably close agreement with the calculated slope of 58.175 mV decade^{-1} at 20°C for an ideal situation. Plotting the measured E_{glass} potential against the expected pH of the standard buffer solutions gives the straight line shown in Fig. 2.6. Also plotted in this figure are E_{glass} potentials created using the slope calculated above in Eqn. 2.6.

pH	Standard buffer compositions	$\dfrac{E_{glass}}{mV}$
4.0	50 ml of 0.1 mol L^{-1} ($KHC_8H_4O_4$) 0.1 ml of 0.1 mol L^{-1} (HCl)	177.3
5.0	50 ml of 0.1 mol L^{-1} ($KHC_8H_4O_4$) 22.6 ml of 0.1 mol L^{-1} (NaOH)	117.0
6.0	50 ml of 0.1 mol L^{-1} (KH_2PO_4) 5.6 ml of 0.1 mol L^{-1} (NaOH)	88.2
7.0	50 ml of 0.1 mol L^{-1} (KH_2PO_4) 29.1 ml of 0.1 mol L^{-1} (NaOH)	23.4
8.0	50 ml of 0.1 mol L^{-1} (KH_2PO_4) 46.7 ml of 0.1 mol L^{-1} (NaOH)	−56.7
9.0	50 ml of 0.1 mol L^{-1} ($H_2NC(CH_2OH)_3$) 0.1 ml of 0.1 mol L^{-1} (HCl)	−108.8
10.0	50 ml of 0.05 mol L^{-1} (Na_2CO_3) 10.7 ml of 0.1 mol L^{-1} (NaOH)	−154.4
11.0	50 ml of 0.05 mol L^{-1} (Na_2CO_3) 22.7 ml of 0.1 mol L^{-1} (NaOH)	−193.0

Table 2.4   Preparations for pH standard buffer solutions from pH 4 to pH 11 [54] and the corresponding measured E_{glass} potential.

2.5   Instrumentation and Electrochemical Techniques

2.5.1   *Potentiostat Equipment*

One potentiostat was used during the course of this research – a BAS 100B/W Electrochemical analyser and accompanying BAS 100B/W version 2.0 software (Bioanalytical Systems Inc, West Lafayette, Indiana, USA). The potentiostat works by applying a set potential between the working and counter electrodes. This causes a faradic process to occur on or near the surface of the working electrode. At the counter electrode a similar faradic process as at the working electrode will occur but in the opposite direction. This effectively allows the current to pass through the solution completing the potentiostat circuit. These processes can be described by the Nernst equation for the reversible couple.

$$Ox + ne^- \rightleftharpoons Rd \tag{2.7}$$

$$E = E^\circ_{Ox,Rd} + \left(\frac{2.303RT}{nF}\right)\log\left(\frac{c^s_{Ox}}{c^s_{Rd}}\right) - E_{ref} \tag{2.8}$$

Where E is the potential applied to the cell, in volts (V), $E^\circ_{Ox,Rd}$ the formal reduction potential of the Ox/Rd couple, (V vs SHE), n equals the number of electrons transferred per molecule, c^s_{Ox} and c^s_{Rd} are the surface concentrations of the oxidised (Ox) and reduced (Rd) species respectively, E_{ref} refers to the half-cell potential of reference electrode, (V vs SHE.).

In practice, when E is sufficiently negative, Ox can be reduced to Rd on the working electrode. Similarly Rd can be oxidised to Ox by making E sufficiently positive. Analogous reactions occur on the counter electrode but in the opposite direction (i.e. a significantly negative E, the Rd species will be oxidised to Ox on the counter electrode surface). The reactions that occur on the counter electrode are not usually of interest so long as it does not affect the electrochemistry at the working electrode. At the relatively low currents these experiments exhibit we can be confident that products produced at the counter will have no effect on the working electrode and can be safely be ignored.
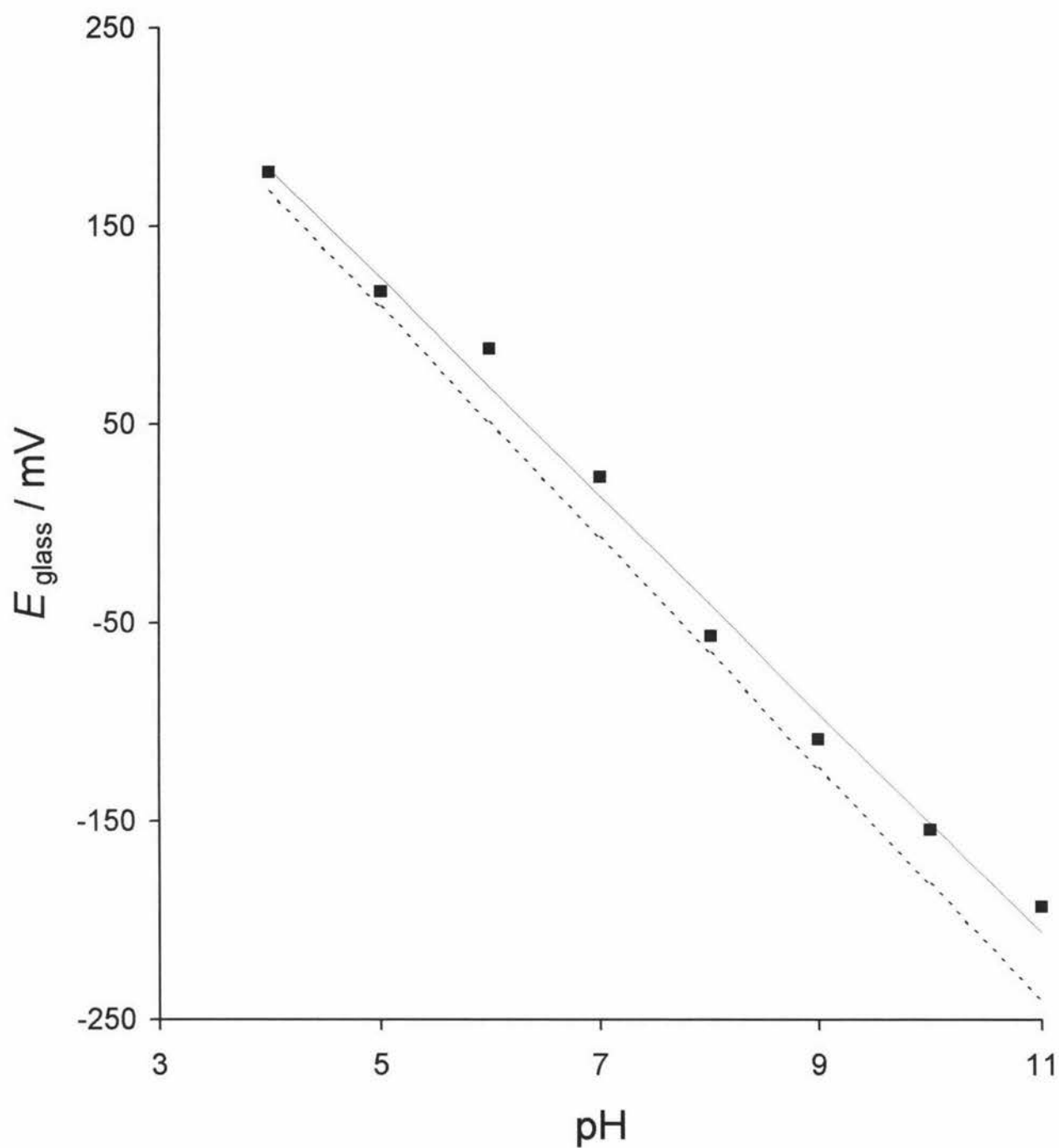
Fig. 2.6 The E_{glass} potential measured from the pH standard buffers (■) compared to the E_{glass} potential calculated from ideal conditions (---).

The potential applied by the potentiostat is controlled by a feedback loop. In this the potential between the working (nickel RDE) and the reference (Ag/AgCl) electrodes are compared to an externally set value. The difference is then amplified and a current passed between the working and the counter electrodes (Pt coiled wire) of such a magnitude and sign as to make that difference close to zero [53].

Figure 2.7 shows the manner in which current versus potential responses are displayed in this thesis. It should be noted that the current axis has an opposite sign to the American convention.

2.5.2 Electrochemical Techniques

Two electrochemical techniques were employed during this thesis, Cyclic Voltammetry (CV) and Sampled Current Polarography (SCP). In CV a triangular potential waveform is applied, an example of which is shown in Fig. 2.8. The faradaic current produced from this technique is dependent on the kinetics and transportation of the electroactive species. A plot of the resulting response curve is known as a voltammogram. Important parameters for this technique are the initial potential, the initial sweep direction, sweep rate, maximum and minimum potentials, and the number of segments [55]. In the example (Fig. 2.8) potential was varied between -1500 mV and $+1500$ mV vs Ag/AgCl at a sweep rate of 100 mV s^{-1} for four segments beginning and ending at -1500 mV.

SCP, first proposed by Barker [56], utilises a time based staircase potential waveform, pictorially represented in Fig. 2.9, to monitor the faradaic current. Important parameters for this technique include the initial potential, the direction of potential change, step height (pulse amplitude), step width (pulse width) and sample time. The step parameters in Fig. 2.9 are that which were applied in the majority of experiments explored in this thesis. The potential was, for reasons discussed in Chapter 4, stepped from $+332$ mV to $+1100$ vs Ag/AgCl. The other parameters were kept identical to those established by Khudaish [1-6], including a step height of 32 mV and width of 8 seconds with the last 17 milliseconds measured, as shown in Fig 2.9, to give the responses reported in this thesis. Thus, the results reported for this technique consists of a series of discrete currents for a range of discrete potentials.

i_a Anodic current

OXIDATION

The currents plotted above the line indicates a negative charge flow towards the electrode

As the potential is increased in the negative direction, the electrode becomes a stronger "Reducing agent"

E (−) volts

E (+) volts

REDUCTION

The current below the line indicates a negative charge flow from the electrode

As the potential is increased in the positive direction, the electrode becomes a stronger "Oxidizing agent"

i_c Cathodic current

Fig. 2.7   Sign convention typically used to display response versus potential data.
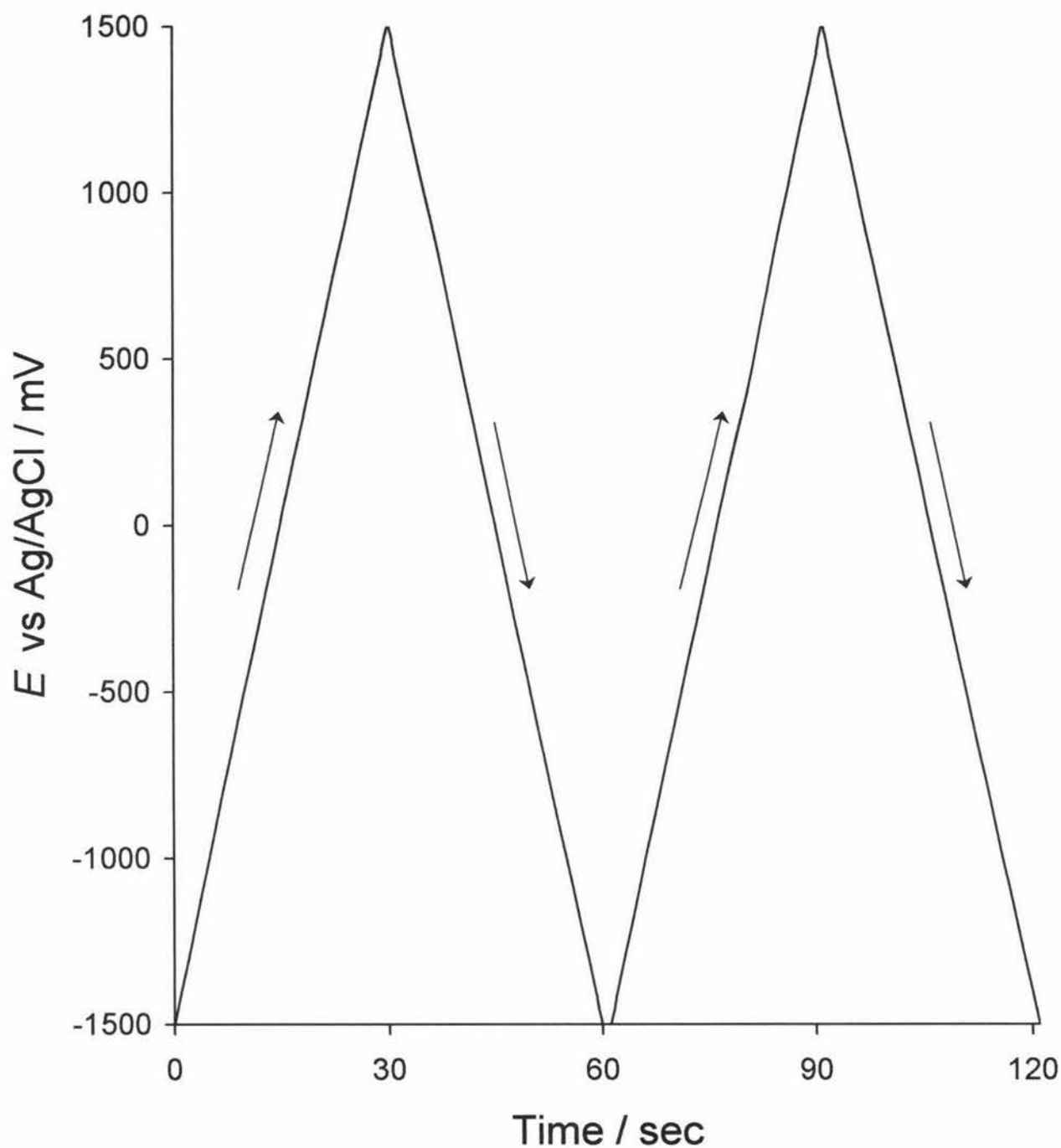
Fig. 2.8 The triangle potential waveform applied by the Cyclic Voltammetry technique over the potential range −1500 mV to +1500 mV vs Ag/AgCl at a sweep rate of 100 mV s^{-1} for four segments beginning and ending at −1500 mV.
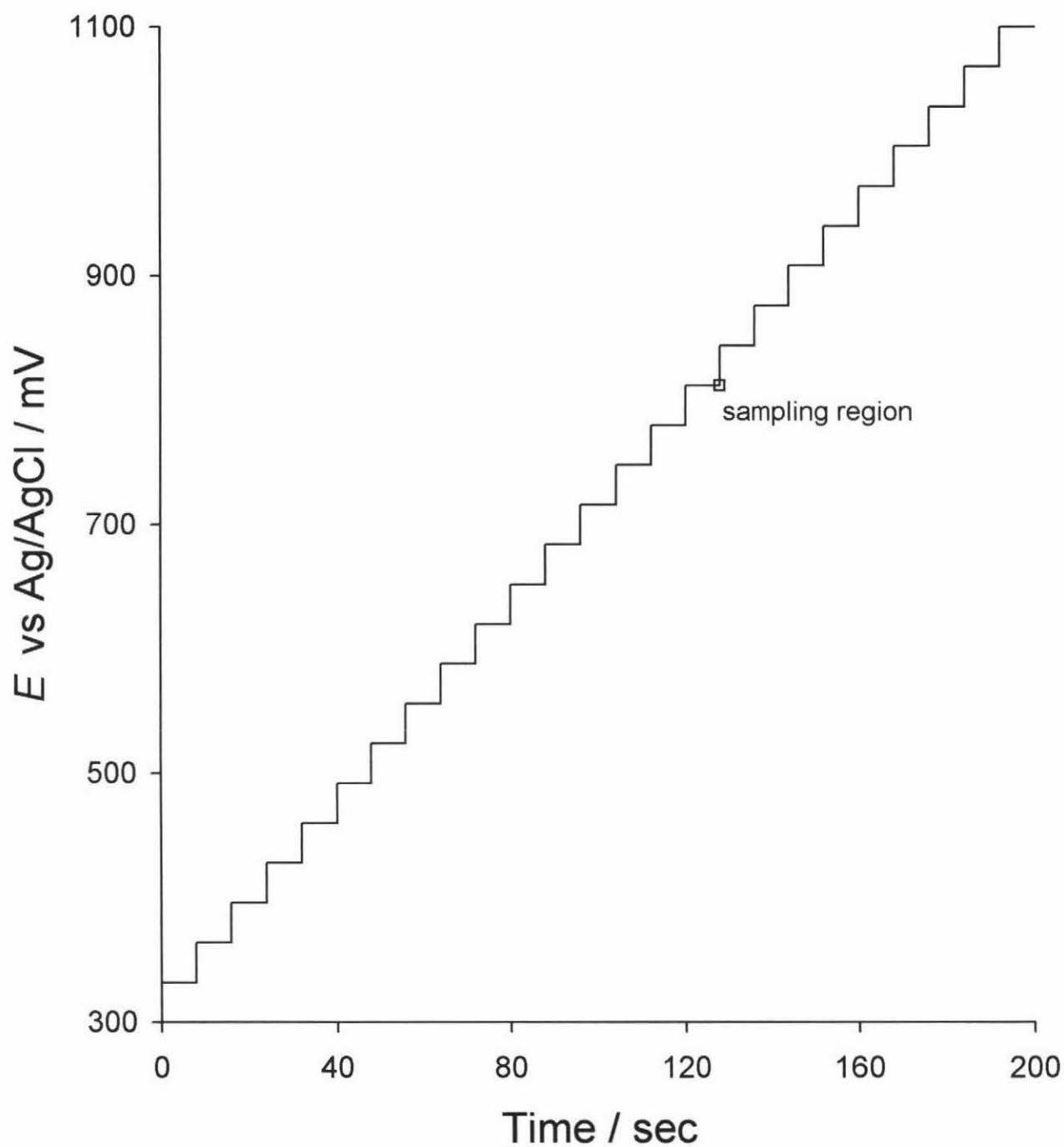
Fig. 2.9   The staircase potential waveform applied by the Sampled Current Polarography technique over the potential range +332 mV to +1100 mV vs Ag/AgCl. With a step height of +32 mV, step width of 8 seconds, and a sampling time of 17 milliseconds at the end of each step.

The advantage of SCP is that potential is held constant for sufficient time to establish steady-state conditions before the response is measured, this requires 4 seconds. Steady-state conditions can be defined as those at which the electrochemical reactions have all reached stable rates. Once the response is measured the potential is stepped to the next level causing the position of the equilibria change by Le Chatiers principle. The CV technique, on the other hand, measures the response when the reaction is in a continual state of flux so the response is dependent on the sweep rate and the speed at which the reactions can follow the changing conditions.

2.6   Software

2.6.1   *General Information*

Some commercial software packages utilised during this thesis have already been discussed such as those required to operate and view the experimental data obtained by the BAS 100B/W potentiostat. Other software packages employed included Microsoft® Word (97) used for word processing, Microsoft® Excel (97) spreadsheets to view, manipulate and graph the experimental data. Spreadsheets were also used to develop simple curves of best fit and for comparing the experimental to the model calculated data.

 Some software developed by the project supervisor S. B. Hall, using the programming language Turbo Pascal (version 7.0) on an IBM PC type computer, was also employed. The software developed can be divided into two distinct types. The first, was software to collate the experimental data, merge many files into one, transform and assemble the data into the appropriate form. The second type of software was developed to optimise the kinetic and thermodynamic parameters that were identified in a series of models.

2.6.2   *Data Collation Software*

The software used to harvest the appropriate from the BAS software files was SCPAV. This piece of software is an extension of the ESTEPAV program used and described by Khudaish [1-6]. SCPAV collates staircase potentiometry files generated by the BAS 100B/W software (Chapter 3) and provides two forms of output. One, which is similar to the two dimensional array created by ESTEPAV, where one file is created for each

potential step listing the currents as a function of rotation rate at each peroxide concentration in the correct format for the optimisation programs described in Section 2.6.3. The second function of this program is to produce two-dimensional arrays for Excel spreadsheets to allow the data to be viewed, graphed and manipulated.

2.6.3   *Optimisation Software*

The optimisation program makes use of a SIMPLEX algorithm [57, 58] to perform the optimisation of kinetic and thermodynamic parameters. The SIMPLEX algorithm was initially developed by Box and Wilson [59] and allows numerous parameters to be optimised until the lowest possible sum for the square of differences between the observed and model calculated data is found.

$$\sum \text{res} = \sum (i_{obs} - i_{calc})^2 \tag{2.9}$$

where i_{obs} in this case is the experimental current density and i_{calc} is the current density predicted by the model.

This goal seeking was further refined by Spendly *et al.* [60] and by Nedler and Mead [61]. The core of the optimisation programs code was written by A. Kucernak in 1986 (whilst studying as a postgraduate student at Auckland university, now lecturing at the Imperial College of London). This code has been progressively modified over the last decade by the project supervisor S. B. Hall to enable the optimisation of a diverse range of physiochemical systems including pharmaceutical formulations [62] and binding of pyridyl ligands to zinc porphrins [63].

2.6.4   *An Example Optimisation*

To illustrate the method that the software for optimisation uses in goal seeking a simple model may be considered. The model chosen is the basic quadratic (shown below), having only two parameters *a* and *b*.

$$y = a + bx^2 \tag{2.10}$$

The observed data that this quadratic model describes was obtained from Eqn. 2.11 for *x* given by the integers 0 to 25 (i.e. 0, 1, 2, 3.....25).

$$y = 2 + 0.2x^2 \tag{2.11}$$

Hence, the optimisation software should find the parameters as $a = 2$, and $b = 0.2$. The software works by setting initial estimated values for a and b, placing these in the model and then comparing the model output to the observed data to get the sum of residuals. The better the model fit to the observed data the lower the sum of residuals. Should the model be perfect, the sum of residuals will be zero. A perfect fit of model to the observed data is usually impossible, since a model cannot possibly account for all random indeterminate errors in real situations. Consequently, the optimisation software has a threshold where the sum of residuals is considered sufficiently close to zero to terminate. This can be illustrated by considering a model of putting in golf where we could include the power of the stroke, the speed of the green, and the slope of the green. However, the perfect solution would include the humidity, the wind, the dirt on the ball, the gravitational pull of the moon, and many more factors. In this case the putting model just has to be sufficiently close to perfect to sink the putt. The golf ball does not have to hit the hole exactly at the centre. The program may also be set to terminate after a set number of iterations so that if the requirements are not met the program will not run forever.

The goal seeking of the optimisation software is shown in Fig. 2.10. The program is seeded by the programmer by setting the initial values, in the case of Eqn. 2.10, for a and b. Usually the programmer will set the parameters close to the anticipated outcome thereby ensuring that the program will begin searching in the right ballpark and return a viable answer. In this case, both parameters were set to one. The first iteration begins by changing both parameters, the initial change also set by the programmer. In this case, both parameters were increased by approximately 0.26 this change made the model fit worse (increasing the sum of residuals). The software now begins its goal seeking. First it takes the parameter (a) whose change had the most effect and randomly changes it, while keeping the other parameter (b) constant. Parameter a was increased to 2.23. However, since this change also increased the sum of residuals, a was returned to its initial value. Now the software begins changing b, which was increased to 1.97. This change significantly increased the sum of residuals. By the fourth iteration the program has found the correct direction to change both parameters so that a was increased to 1.92 and b decreased to 1.44. This reduced the sum of residuals. To determine which change had the most significant effect, a was kept constant and b was returned to 1.97. This significantly
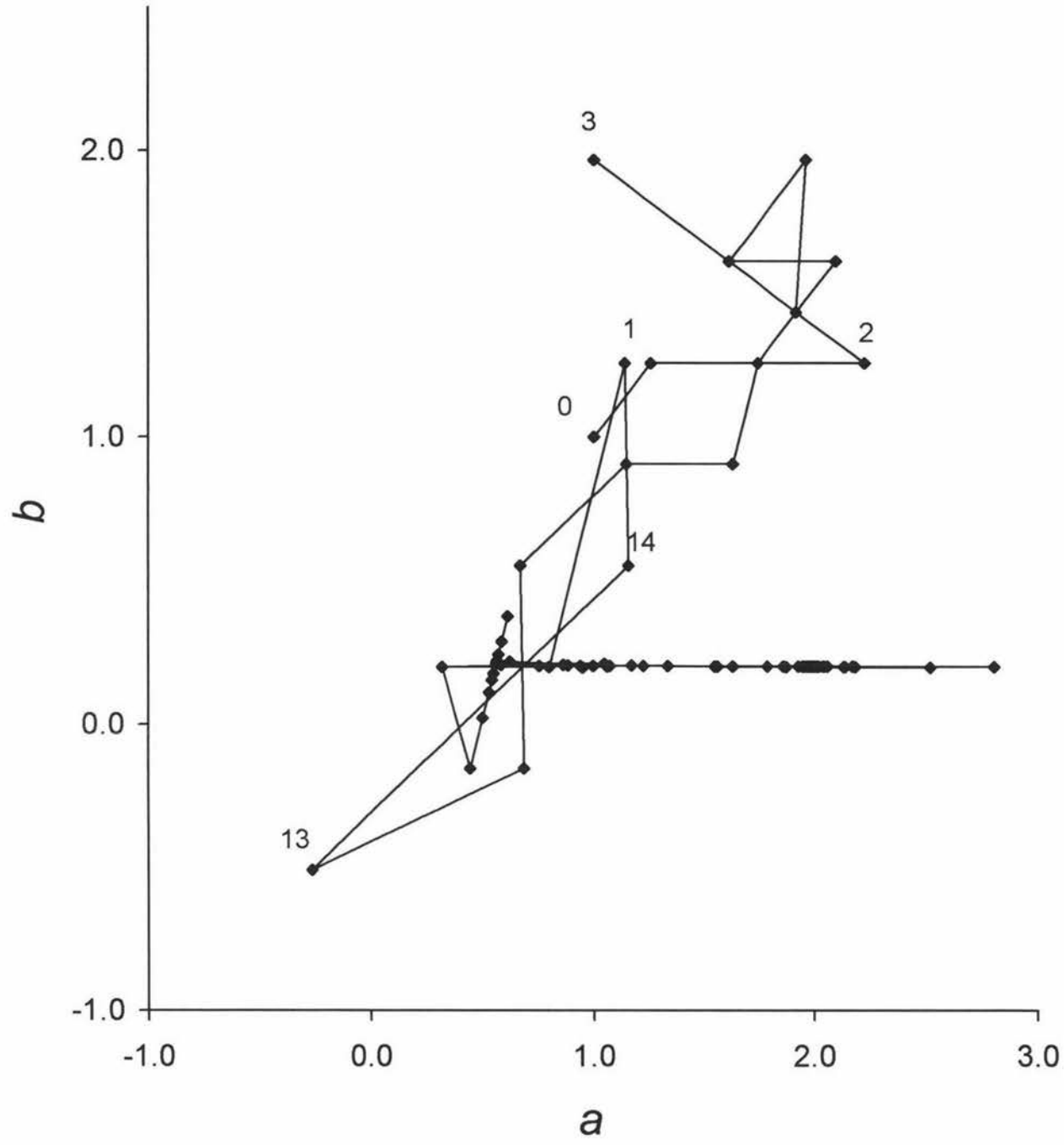
Fig. 2.10 150 iterations in the optimisation of the parameters a and b for Eqn. 2.10. Optimisation starting at $a = 1$ and $b = 1$, and finishing with $a = 2$ and $b = 0.2$.

increased the sum of residuals. So it was established that reducing b had the most significant effect. Over the next few iterations both parameters were lowered in relatively large steps. Upon reaching the 13th iteration both parameters were negative and were found to be too low. Since parameter b had the larger effect on the model it was first to be optimised to the detriment of parameter a. By the 25th iteration b cycled above and below its optimum value 0.2 slowly homing in – varying only slightly as parameter a was optimised. The program now focused on the less significant parameter a which was only 0.57 at that stage, by the 50th iteration a was close to 2. Both parameters were fully optimised by the 150th iteration with minor fluctuations above and below the optimum. The natural log of the sum of residuals reached -21.2 which equates to parameters a and b being 2×10^{-6} and 1×10^{-8} away from the perfect values of 2 and 0.2 respectively. Figure 2.11 shows how the goal seeking of the optimisation software reduced the natural log of the sum of residuals to focus on the best fit for the model data.

It is possible with this mode of optimisation that there might be two or more equally viable values for the parameters. A problem with this software is that the program may find local minima in the sum of residuals, which will give inaccurate values for the parameters. This would usually be picked up by the sum of residuals not reducing down to a satisfactory level. Local minima can be avoided by reseeding the program with different starting parameters, one would expect the optimised result to be the same if it was the primary minima. The optimisation just described has the problem in that it is entirely possible that the program could consider negative parameters. For kinetic rate and equilibrium parameters a negative value is an impossibility. To avoid this problem the program can be modified so that the software optimises the natural log of the parameters. Using the same model as before the optimisation software would instead optimise the equation.

$$y = \exp[\ln(a)] + \exp[\ln(b)]x^2 \tag{2.12}$$

The goal seeking of this modified model can be seen by Fig. 2.12. As before, the parameters $\exp[\ln(a)]$ and $\exp[\ln(b)]$ were set at one. In the first iteration both parameters were increased by 0.295 a similar increase as seen before. From there on the optimisation continues in almost the exact same manner, though an idiosyncrasy of the log function is that it causes small changes in the parameter to be amplified, so the program makes slightly larger steps than seen previously. However, this similarity between the two models ends

Fig. 2.11   The natural log of the sum of residuals showing how the optimisation software seeks the lowest possible sum of residuals by changing the parameters a and b for Eqn. 2.11.
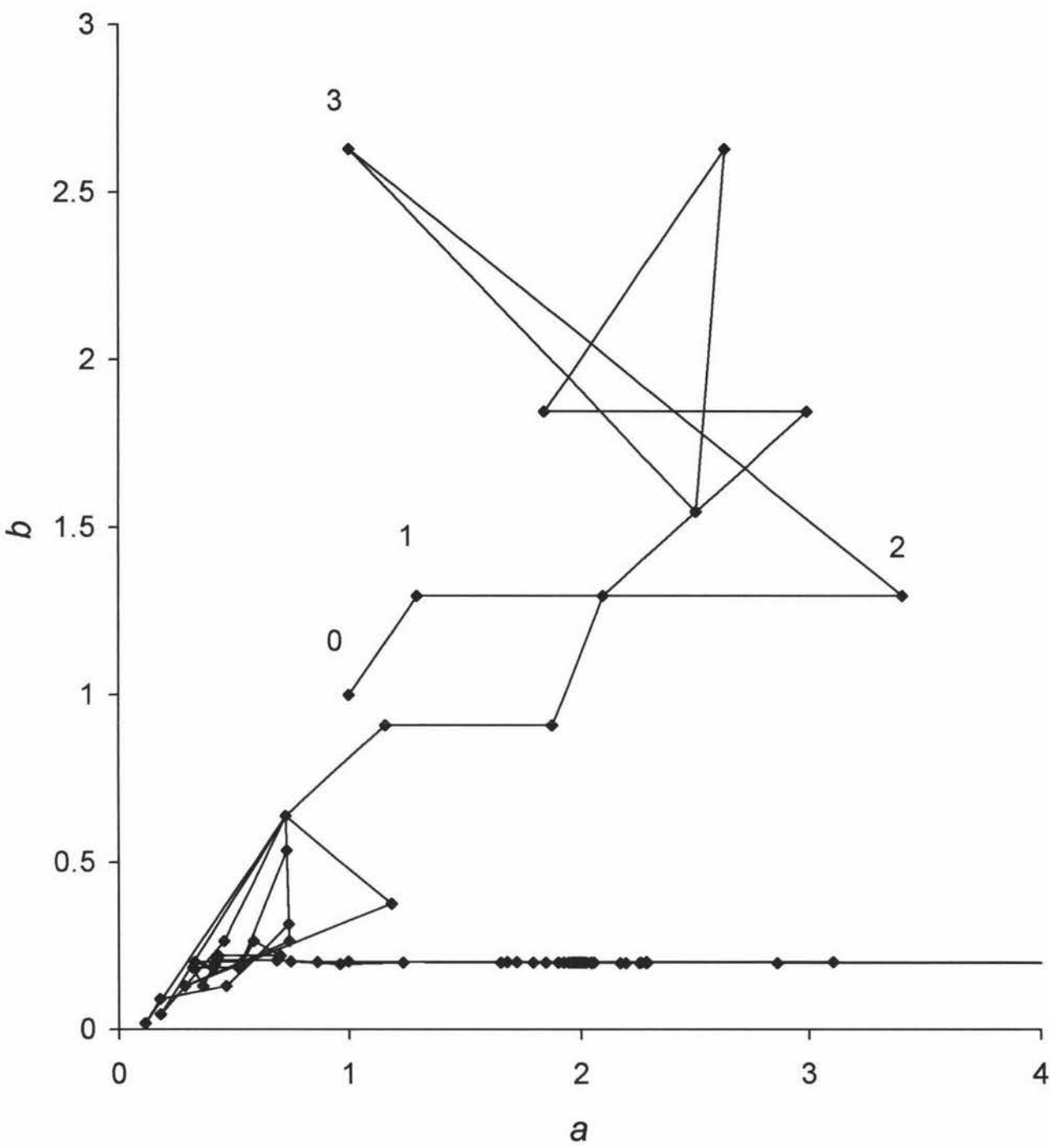
Fig. 2.12   150 iterations in the optimisation of the natural log of the parameters a and b for Eqn. 2.11. Optimisation starting at $\exp[\ln(a)] = 1$ and $\exp[\ln(b)] = 1$, and finishing with $a = 2$ and $b = 0.2$.

around the 13th iteration because when both parameters in the previous example went into the negative values this program retains these as positive values.

By optimising the log of the parameters we have removed three quadrants, effectively leaving only 25% of the available possibilities. This accelerates the optimisation which is invaluable in more complicated models. In this simple case the parameters are ultimately optimised, down to a lower natural log of the sum of residuals of –23.2, after 140 iterations with infinitesimal changes in the later iterations as shown in Fig. 2.13. This is only slightly faster than the previous optimisation. Although this program did reach the same sum of residuals, as the linear program achieved after 150 iterations, this occurred in only 125 iterations.

The value of the optimisation software developed is that it can optimise many parameters simultaneously in the manner shown by the simple examples above. The model actually used to model the electrochemical oxidation of hydrogen peroxide was significantly more complicated, since it optimises for up to four potential invariant and up to two potential varying parameters at any one time. The simple examples shown can easily be viewed in the two-dimensional graph format. Three parameters are also relatively easy to display in three dimensions. However, the multidimensional system involving the six parameters optimised in this study can not be readily visualised.
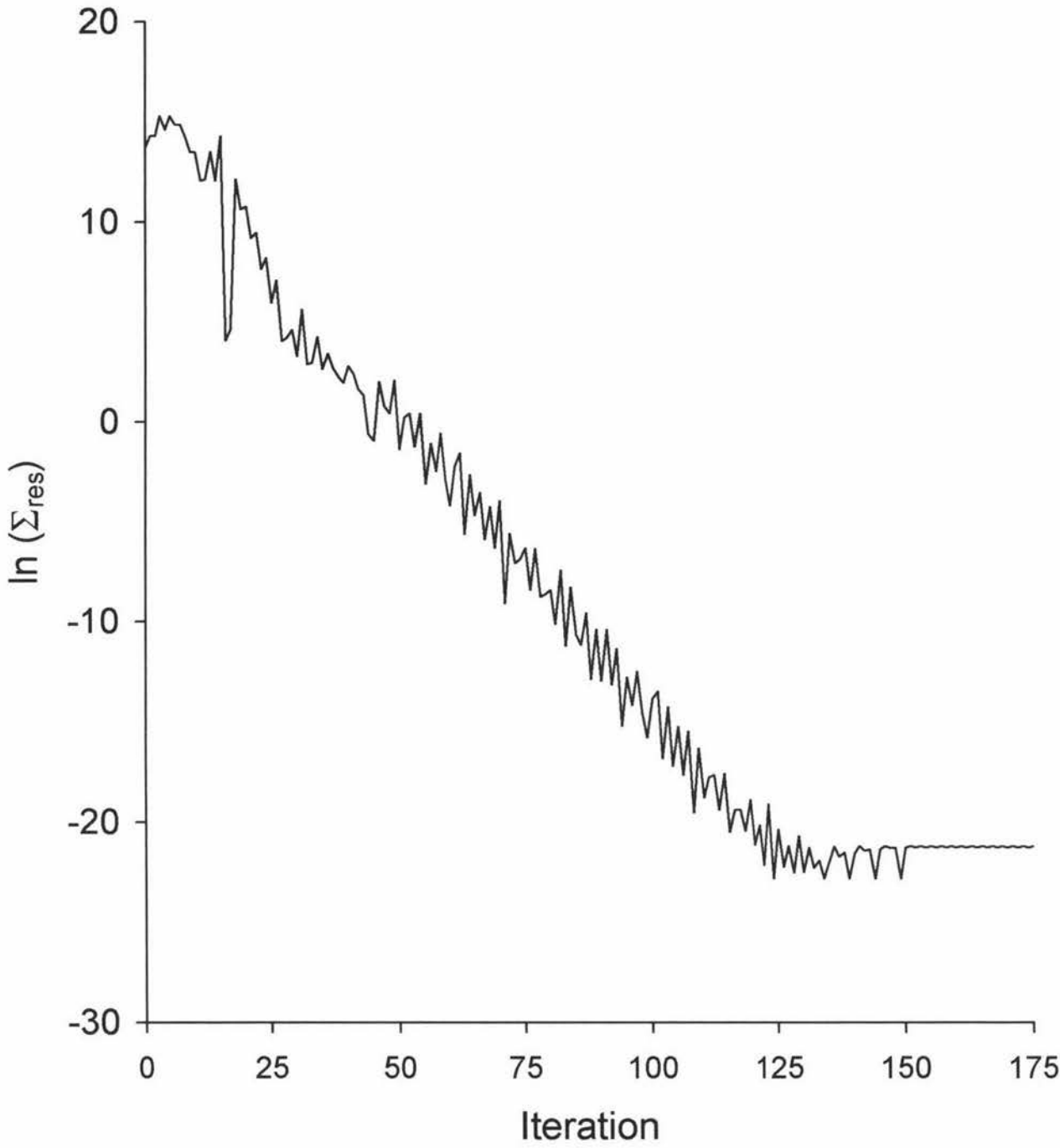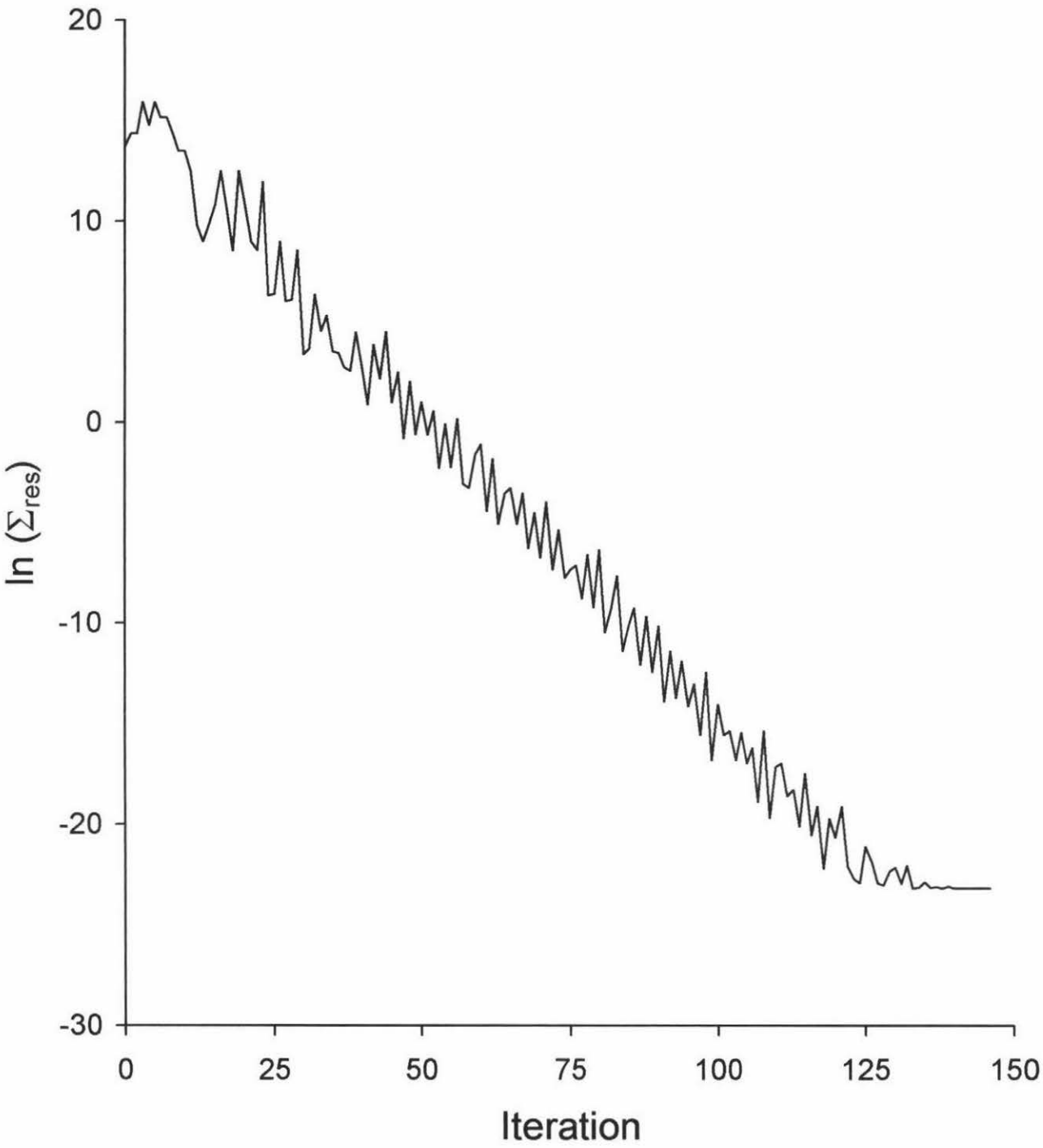
Fig. 2.13 The natural log of the sum of residuals showing how the optimisation software seeks the lowest possible sum of residuals by changing the parameters $\exp[\ln(a)]$ and $\exp[\ln(b)]$ for Eqn. 2.12.

CHAPTER 3

POTENTIAL, ROTATION RATE AND HYDROGEN PEROXIDE CONCENTRATION DEPENDENCE

3.1   Introduction

To use a nickel electrode for the electrochemical detection of hydrogen peroxide it is imperative that a robust mathematical model be developed, to allow complete understanding of the electrochemical oxidation of hydrogen peroxide on the electrode surface.

This chapter studies dependence of the electrochemical oxidation of hydrogen peroxide on the rotation rate, potential and bulk hydrogen peroxide concentration. Seven rotation rates from 630 to 10000 rpm, 24 potentials from +332 to +1100 mV and hydrogen peroxide concentrations from 0 to 130 mM were studied.

A series of models were developed and were used to account for the responses over the range of these conditions. These models were based upon the product-inhibited Michaelis-Menten mechanism developed by Khudaish [1-6] for the electrochemical oxidation of hydrogen peroxide on a platinum electrode surface (Chapter 1). The model parameters were optimised, using the optimisation software described in Section 2.6, and these are used to predict the response expected under defined conditions. Surface and bulk concentrations of species are differentiated in the text. For example $[H_2O_2]_{bulk}$ denotes the concentration in the bulk solution and $[H_2O_2]$ the surface concentration.

3.2   Experimental Conditions

3.2.1   *Reagent and Electrodes*

All chemicals, reagents, electrodes and electrochemical equipment used during the experiments described in the proceeding sections are outlined in Chapter 2.

3.2.2 *Electrochemical Technique*

Sampled Current Polarography is the only electrochemical technique employed for studying the electrochemical oxidation of H_2O_2 in this chapter (described in Chapter 2, Section 2.5.2). This technique was utilised for studying the potential range +332 mV to +1100 mV chosen for reasons outlined later in Section 3.3. All electrochemical measurements were made over the 0–130 mM $[H_2O_2]_{bulk}$ range and for the seven rotation rates 630, 1000, 1585, 2500, 4000, 6300, and 10000 rpm. All experiments discussed in this chapter were conducted at a constant temperature of 20°C. Experiments were also conducted in the primary 0.1 M buffer with pH 7.28. Whilst all the experiments were conducted over all seven rotation rates to avoid unnecessary complication, most graphs will be displayed at the moderate rotation rate of 4000 rpm unless otherwise stated.

3.3 Potential Dependence

Potential is the most important parameter in electrochemical experiments. The potential determines which charge transfer reactions occur and the rate of these reactions on the surface of the electrode. Section 2.5.1 explains, and Fig. 2.11 shows, how when the potential is negative reduction reactions begin to occur on the surface. The majority of this thesis is concerned with the oxidation reactions of H_2O_2.

Two studies with and without the presence of H_2O_2 were done using the Cyclic Voltammetry technique to identify the oxidation region for H_2O_2 on a nickel RDE. Figure 3.1 shows the current-potential wave for the primary 7.28 0.100 mol L^{-1} phosphate buffer in the absence and in the presence of 0.120 mol L^{-1} $[H_2O_2]_{bulk}$ the potential was cycled from +1300 to −1300 mV vs Ag/AgCl and back again at a sweep rate of 0.1 V s^{-1}. This figure shows that there is a significant oxidation wave occurring only in the presence of H_2O_2, with the current deviating from that at the open circuit potential and rising rapidly above +300 mV vs Ag/AgCl. There are some indications of a solvent oxidation wave occurring at +1100 mV vs Ag/AgCl easily observed in the absence of H_2O_2. This rise in response beyond +300 mV with 0.120 mol L^{-1} $[H_2O_2]_{bulk}$ can only be attributed to the electrochemical oxidation of H_2O_2 on the nickel electrode. The optimal potential range for studying the
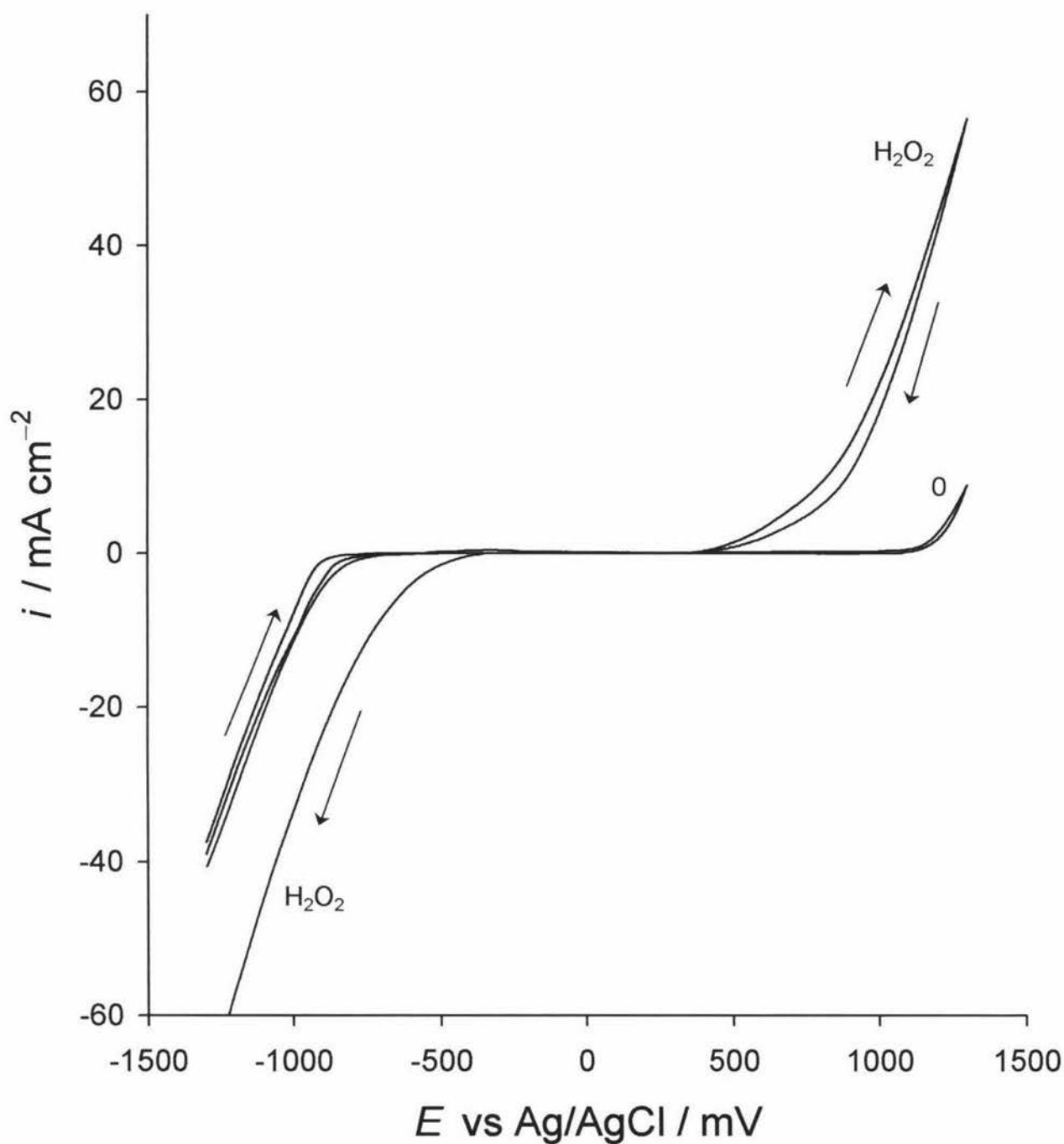
Fig. 3.1 A Cyclic Voltammetric plot of the steady-state responses with the potential beginning at −1300 mV sweeping anodically to +1300 mV and cathodically back −1300 mV vs Ag/AgCl in the presence (H_2O_2) and absence (0) of 0.120 mol L^{-1} [H_2O_2]$_{bulk}$ at 20°C and ω = 4000 rpm.

electrochemical oxidation of H_2O_2 on the nickel electrode can, therefore, be identified as being between +300 and +1100 mV vs Ag/AgCl. More cathodic than this region and no significant oxidation occurs. At more anodic potentials competitive oxidation of the solvent starts to develop and hinder the study of H_2O_2. The majority of graphs involving potential will be displayed at +1036 mV this was selected since this potential was believed to be sufficiently anodic to give significant currents and was sufficiently cathodic to avoid any competitive oxidation of the solvent.

It is working to note in passing the reduction region shown in Fig. 3.1. It shows that significant reduction currents are observed in the absence of H_2O_2 below −800 mV vs Ag/AgCl. In the presence of H_2O_2 reduction currents due to H_2O_2 occur only after prior oxidation (i.e. on the return sweep). In this case, the electrochemical reduction of an oxidised H_2O_2 species on a nickel electrode surface commences at −400 mV vs Ag/AgCl. This shows that the study of the reduction region would not be a simple matter due to competitive solvent reduction and would require the previous study of the oxidation region for H_2O_2 to establish what species remains to be reduced.

The steady-state responses for the oxidation of a range of $[H_2O_2]_{bulk}$ and over a series of anodic potentials at a single rotation rate, 4000 rpm, are shown in Fig. 3.2. Represented in this figure is only a $1/7^{th}$ of the rotation rate data collected for a single series of experiments. In addition only 8 of 18 representative $[H_2O_2]_{bulk}$ covering the entire 0 to 130 mM range are displayed (others excluded for clarity). The potential is increased from +332 mV to +1100 mV vs Ag/AgCl in twenty-four 32 mV steps giving rise to an exponential increase in current in the presence of H_2O_2. In all studies of this type the background current was measured before the addition of H_2O_2. These yielded currents several orders of magnitude smaller, once again, proving that the steady-state responses observed may only be attributed to H_2O_2 oxidation. The exponential change in current is not consistent over the entire range of $[H_2O_2]_{bulk}$. At low concentrations the current deviates from linearity at higher potentials and the relative current increase with potential was not as pronounced as that at the higher concentrations. The deviation between the currents observed at each $[H_2O_2]_{bulk}$ are less pronounced at higher concentrations since a limiting current is approached (where the
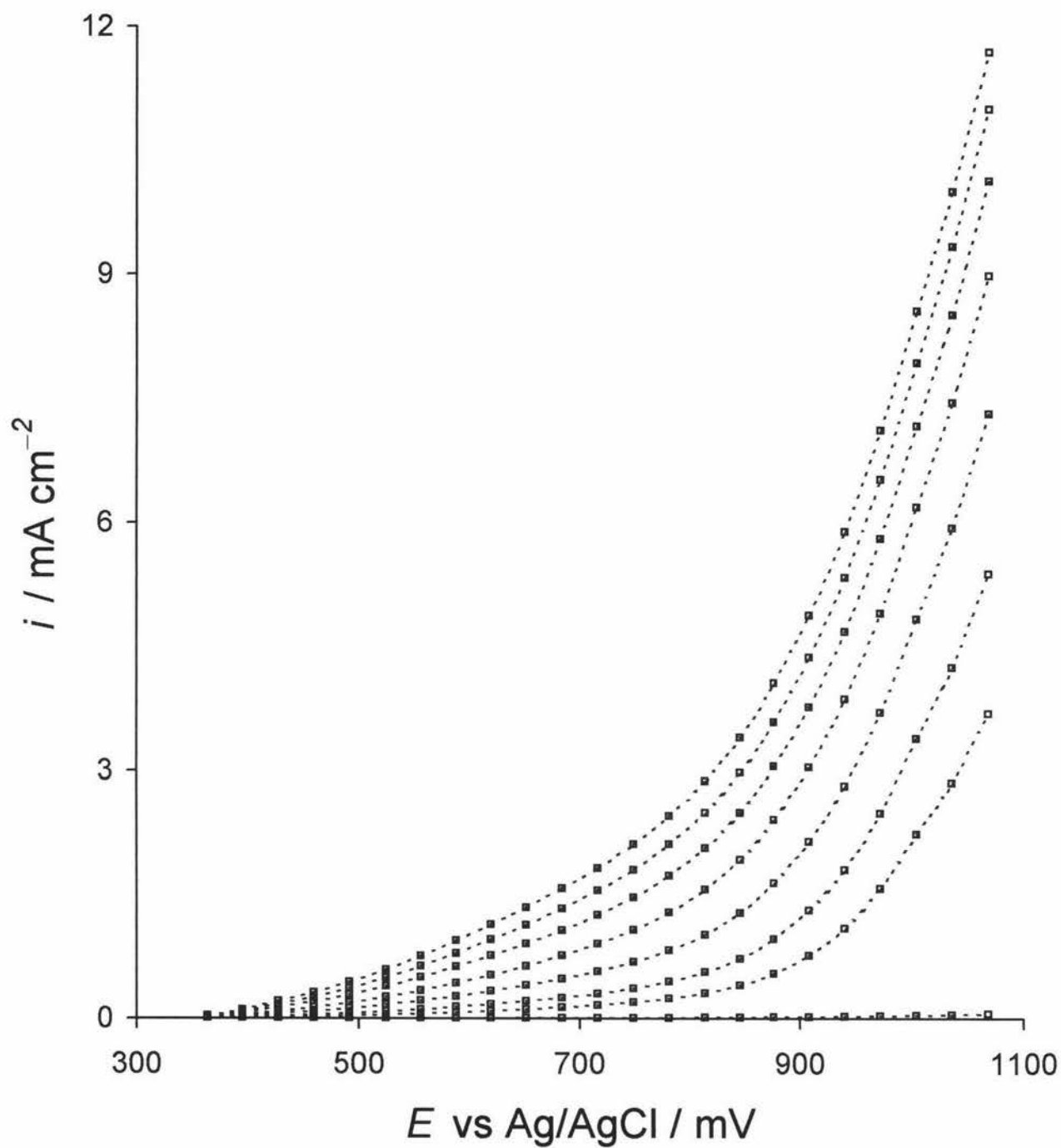
Fig. 3.2 Seven representative hydrogen peroxide concentrations 0, 7.8, 15.5, 31.0, 53.9, 76.7, 99.2, and 121.5 mM are displayed (others not shown for clarity) over the E range +332 to +1100 mV vs Ag/AgCl at 20°C.

current begins to plateau). The rise in response at low $[H_2O_2]_{bulk}$ is more significant at higher potentials.

3.4 Hydrogen Peroxide Concentration and Rotation Rate Dependence

The currents that are observed in the SCP experiments arise from the electrochemical oxidation of H_2O_2. Therefore, a reasonable prediction would be a simple linear relationship between the currents observed and the $[H_2O_2]_{bulk}$. However, this is not the case as shown in Fig. 3.3. This figure presents the steady-state responses for a selection of potentials (others not shown for clarity) over the $[H_2O_2]_{bulk}$ range $0 - 130$ mM. The response profile initially rises rapidly and begins to plateau at higher $[H_2O_2]_{bulk}$ as the limiting current density is approached. This is more pronounced at the higher potentials.

Figure 3.4 presents the observed steady-state responses for the 0 to 130 mM range of $[H_2O_2]_{bulk}$ at rotations rates of 630, 1000, 1585, 2500, 4000, 6300, and 10000 rpm. It is compiled from the experimental data collected at the standard temperature of 20°C and displayed at a sufficiently anodic potential of +1036 mV so that a high current is observed. The response trends observed previously remain at each rotation rate, that of increasing response with increasing $[H_2O_2]_{bulk}$. As before a limiting current density is approached, a higher limit with increasing rotation rate.

Increasing the rotation of the RDE causes the bulk solution to be pumped faster towards the electrode surface (discussed in Section 2.2.4). This solution flow improves the mass transportation of H_2O_2 and effectively raises the surface concentration of hydrogen peroxide. Reduction or oxidation reactions occur on or near the surface of the electrode. Therefore, it is useful to consider the surfaces concentrations of hydrogen peroxide and the products of its oxidation. When H_2O_2 is oxidised it dissociates to a dioxygen molecule and two free hydrogen ions [1-6, 8, 35]

$$H_2O_2 \longrightarrow O_2 + 2H^+ + 2e^- \tag{1.15}$$

An increase in the $[H_2O_2]_{bulk}$ generally corresponds to an increase in the surface concentration. However, surface reactions consume the surface H_2O_2 so that the
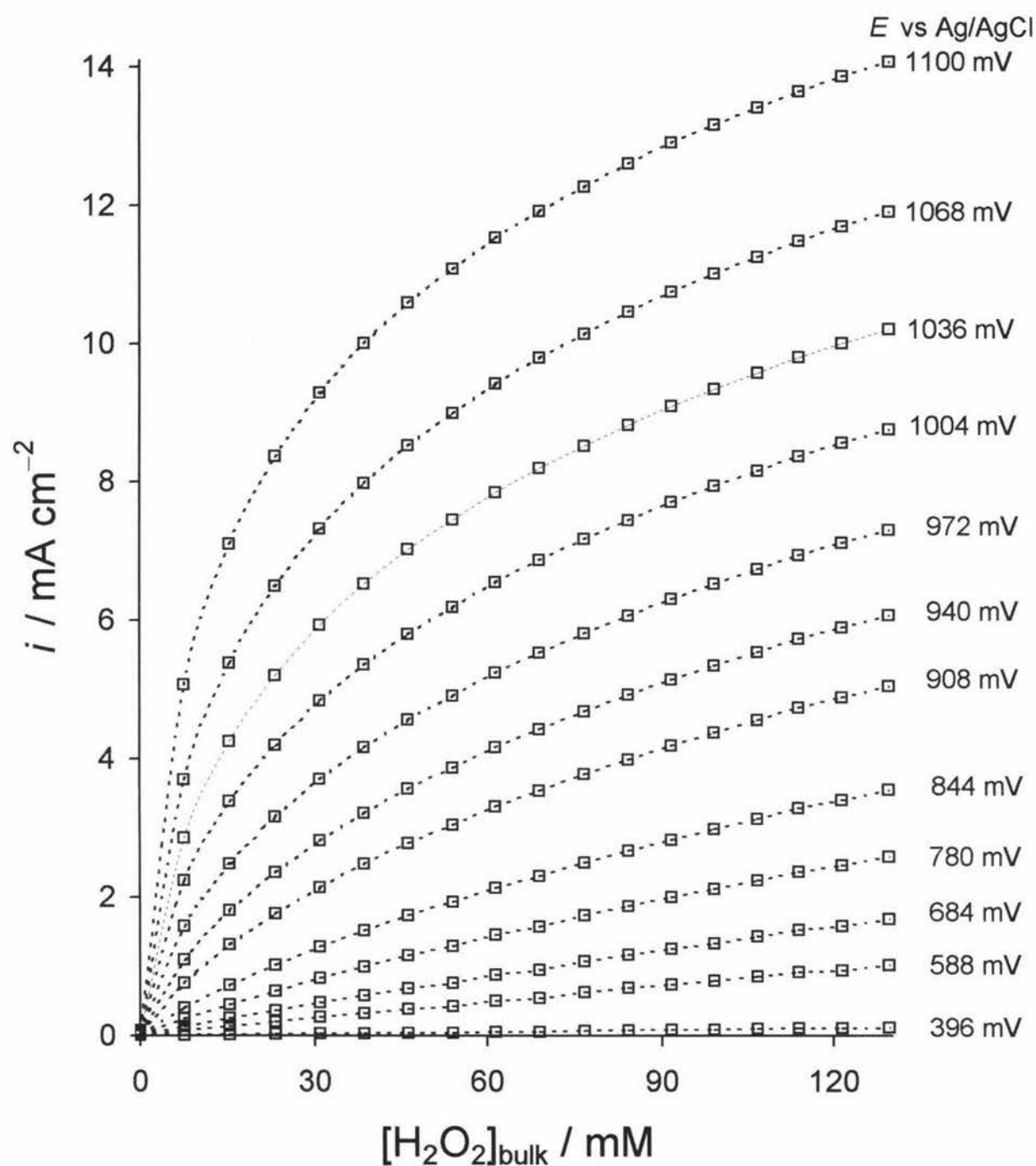
Fig. 3.3   Steady-state responses from a representative selection of potentials spanning +396 to +1100 mV vs Ag/AgCl as a function of $[H_2O_2]_{bulk}$ at 20°C and ω = 4000 rpm.
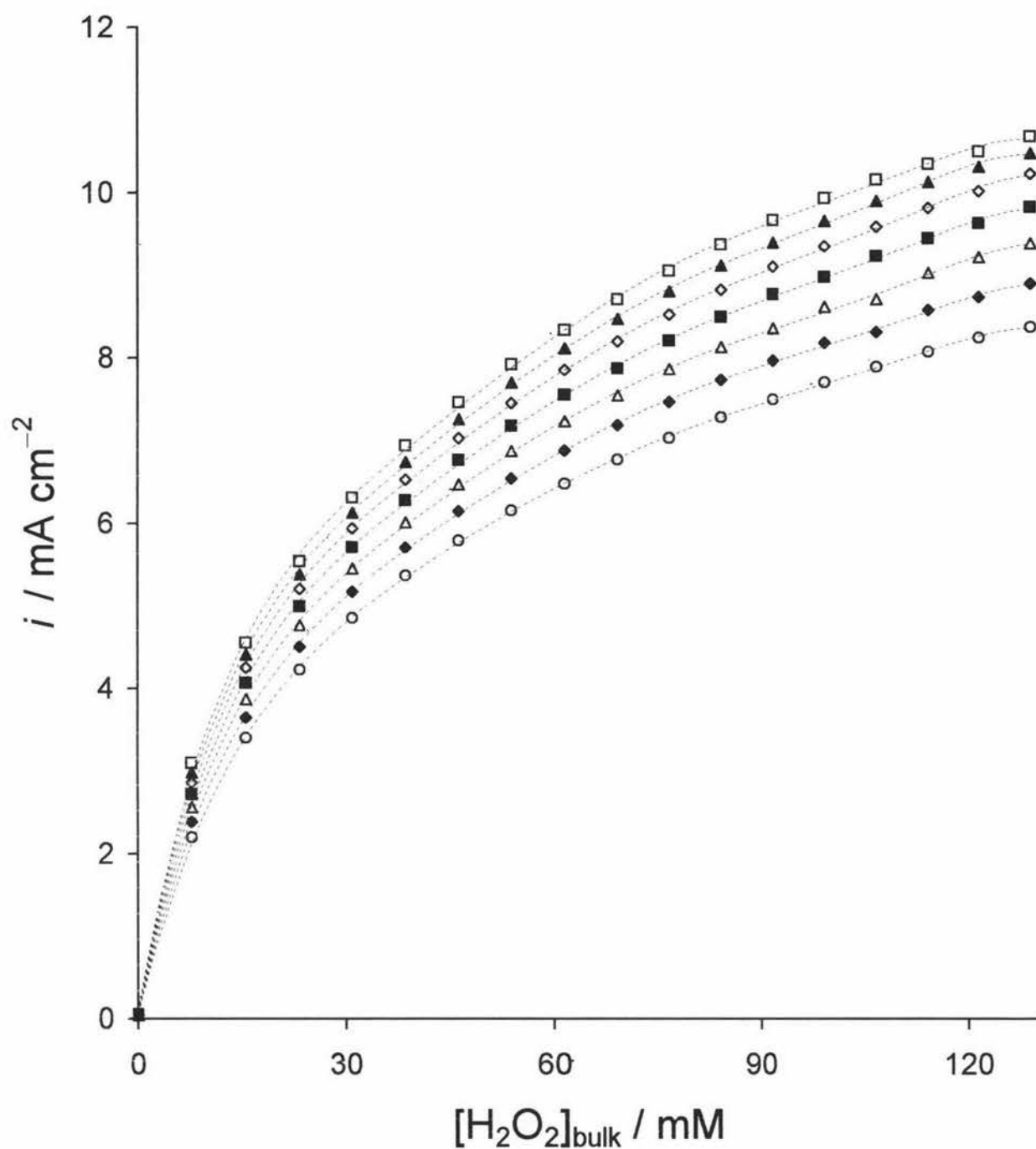
Fig. 3.4 Steady-state responses for seven rotation rates, ω = 630 ($\circ$), 1000 ($\blacklozenge$), 1585 ($\triangle$), 2500 ($\blacksquare$), 4000 ($\diamond$), 6300 ($\blacktriangle$), and 10000 ($\square$) rpm, at E = +1036 mV vs Ag/AgCl as a function of $[H_2O_2]_{bulk}$ at 20°C.

surface concentration is always less than the $[H_2O_2]_{bulk}$ and becomes dependent on the diffusion of H_2O_2 from the bulk. Therefore, under steady state conditions, the surface concentrations of a species can be related to the bulk concentration by considering the diffusion layer thickness, the rate, j, at which the species is consumed or produced at the surface, and by application of Fick's first law of diffusion.

Thus, the surface concentrations of hydrogen peroxide, dioxygen, and hydrogen ions are given by

$$[H_2O_2] = [H_2O_2]_{bulk} - jk_D D_{H_2O_2}^{-2/3} \omega^{-1/2} \tag{3.1}$$

$$[O_2] = [O_2]_{bulk} + jk_D D_{O_2}^{-2/3} \omega^{-1/2} \tag{3.2}$$

$$[H^+] = [H^+]_{bulk} + 2jk_D D_{H^+}^{-2/3} \omega^{-1/2} \tag{3.3}$$

where k_D is given by

$$k_D = 1.61\nu^{1/6} \tag{3.4}$$

and $[H_2O_2]_{bulk}$, $[O_2]_{bulk}$, and $[H^+]_{bulk}$ refer to the bulk concentrations of hydrogen peroxide, dioxygen, and hydrogen ions respectively. The diffusion coefficients for each species, i, are indicated by the symbols D_i. Of these $D_{H_2O_2} = 0.63 \times 10^9$ m^2 s^{-1} at 20°C was that which was optimised by Khudaish in identical buffer conditions. $D_{O_2} = 1.67 \times 10^9$ m^2 s^{-1} and $D_{H^+} = 8.06 \times 10^9$ m^2 s^{-1} at 20°C were calculated using the Stokes-Einstein equation.

$$D_i = \frac{kT}{6\pi\eta a_i} \tag{3.5}$$

where η is the absolute viscosity at 20°C. The hydrodynamic radii (a_i) were calculated using the reported diffusion coefficients of dioxygen and hydrogen ions at 25°C [64,65]. The bulk dioxygen concentration can be considered zero since the buffer solutions where rigorously degassed with nitrogen gas to achieve this (Section 2.2.8). Therefore the only source of surface dioxygen that formed is as a product of the oxidation of H_2O_2.

Figure 3.5 shows the surface concentrations of the hydrogen peroxide, dioxygen and hydrogen ion species, calculated from Eqns. 3.1, 3.2 and 3.3 respectively, as a function of $[H_2O_2]_{bulk}$ for a single potential and rotation rate. The lowest rotation rate was selected to present the most pronounced effect since raising the rotation rate would improve the mass transportation of H_2O_2 from the bulk, therefore, reducing its surface perturbation from the

bulk. Higher rotation rates will also improve the mass transportation of the oxidation products into the bulk making these surface concentrations approach zero. Figure 3.5 shows the surface concentration of H_2O_2 to be scarcely different to the bulk concentration. However, at low concentrations there is a marked deviation from the bulk, surface concentration being *ca.* 50% lower. However, above 20mM bulk concentration the bulk/surface relationship is approximately linear only slightly diverging from each other, so that the surface concentration is uniformly 12 mM lower than the bulk over the 20 mM to 130 mM $[H_2O_2]_{bulk}$ range. The surface concentrations of dioxygen and hydrogen ion are small in comparison, and slowly increase with the $[H_2O_2]_{bulk}$ to reach maximum concentrations of 5.6 mM and 3.9 mM respectively, with the proton concentration consistently being approximately 70% of the dioxygen concentration. Due to the low rate there is only small surface deviation of H_2O_2 from the bulk this indicates that the system is not significantly limited by mass transport. This makes optimisation of $D_{H_2O_2}$ from this data next to impossible, and for this reason, the $D_{H_2O_2}$ used was that optimised by Khudaish on a platinum electrode under significantly higher rates.

3.5   Development of a Model

3.5.1   *Model I: A Product Inhibited Michaelis-Menten Mechanism*

The primary model employed by Khudaish [1-6] in the study of the electrochemical oxidation of H_2O_2 on a platinum rotating disc electrode was outlined in Section 1.5.1. The null hypothesis in this study is that the electrochemical oxidation of H_2O_2 on a nickel rotating disc electrode will proceed in an identical manner to that found by Khudaish. The Khudaish model (Eqns. 1.16-1.20) may be interpreted in terms of nickel species expected for the oxidation of H_2O_2 to give Model I. First H_2O_2 binds to an active nickel-binding site, $Ni(OH)_2$, to form the complex $Ni(OH)_2 \cdot H_2O_2$.

$$Ni(OH)_2 + H_2O_2 \underset{}{\overset{K_1}{\rightleftharpoons}} Ni(OH)_2 \cdot H_2O_2 \tag{3.6}$$
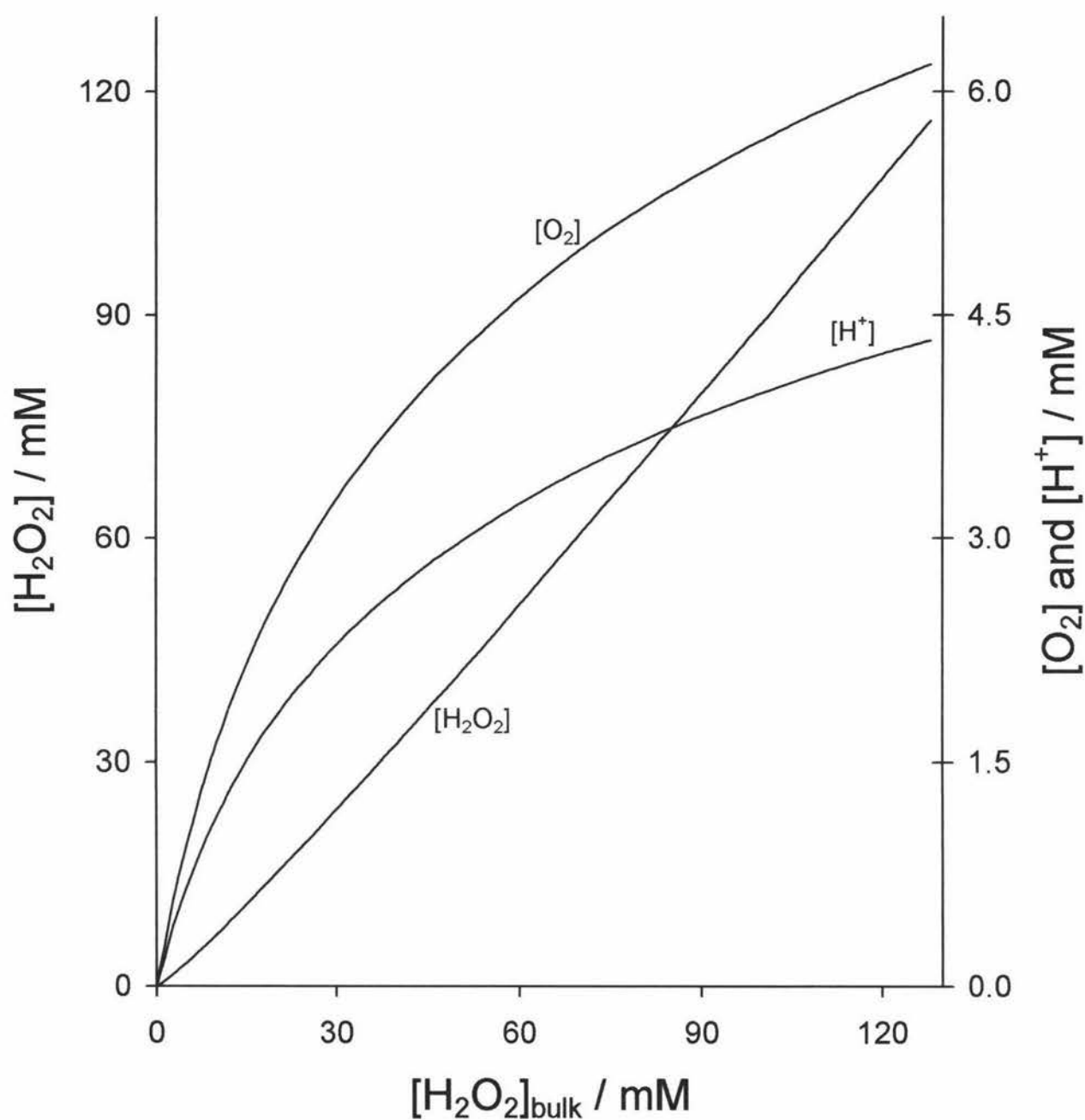
Fig. 3.5 Calculated surface concentrations of H_2O_2, O_2, and H^+ as a function of $[H_2O_2]_{bulk}$ at $\omega = 630$ rpm, $+1036$ mV vs Ag/AgCl and 20°C. $[H_2O_2]$ is significantly larger, therefore, is plotted individually versus the left hand axis, O_2 and H^+ are plotted versus the smaller right hand axis.

Then the complex undergoes an internal electron transfer reducing the binding site and releasing the products water and oxygen. Here it is assumed that the active site comprises nickel in a +II oxidation state.

$$Ni(OH)_2 \cdot H_2O_2 \xrightarrow{k_2} Ni^\circ + 2H_2O + O_2 \tag{3.7}$$

The reduced site then regenerates electrochemically with the release of protons. This gives rise to the amperometic signal.

$$Ni^\circ + 2H_2O \xrightarrow{k_3} Ni(OH)_2 + 2H^+ + 2e^- \tag{3.8}$$

The net effect of reactions Eqns. 3.6 – 3.8 is the oxidative catalytic cycle

$$H_2O_2 \longrightarrow O_2 + 2H^+ + 2e^- \tag{1.15}$$

The inhibition of the dioxygen and proton by-products on the unbound nickel active site and the H_2O_2 /nickel site complex respectively are given below

$$Ni(OH)_2 + O_2 \underset{}{\overset{K_4}{\rightleftharpoons}} Ni(OH)_2 \cdot O_2 \tag{3.9}$$

$$Ni(OH)_2 \cdot H_2O_2 + H^+ \underset{}{\overset{K_5}{\rightleftharpoons}} Ni(OH)_2 \cdot H_2O_2 \cdot H^+ \tag{3.10}$$
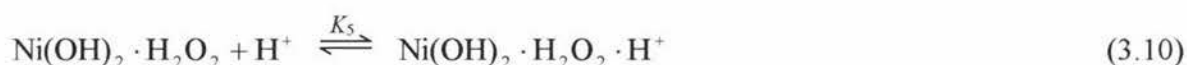
The rate equation was developed using Michaelis-Menten kinetics and by considering the surface coverage of the electroactive species (derivation given in Appendix 1), and shown to be

$$j = \frac{k_2 N K_1 [H_2O_2]}{1 + K_4[O_2] + K_1[H_2O_2](1 + K_5[H^+] + k_2/k_3)} \tag{3.11}$$

The electrochemical oxidation of hydrogen peroxide occurs on or at the surface of the nickel electrode therefore the concentration terms $[H^+]$, $[O_2]$ and $[H_2O_2]$ in the rate equation (Eqn. 3.11) refer to the surface concentrations of these species. In Section 3.4 it was shown that under steady state conditions the surface concentrations of a species can be related to the bulk concentration by Eqns. 3.1, 3.2 and 3.3. Substitution of these rate and diffusion dependent expressions into the product inhibited Michaelis-Menten rate Eqn. 3.11 yields the third order polynomial.

$$0 = xj^3 + aj^2 + bj + c \tag{3.13}$$

where the polynomial coefficients are given by

$$x = -2K_1 K_5 k_D{}^2 D_{H_2O_2}^{-2/3} D_{H^+}^{-2/3} \omega^{-1/2} \tag{3.14}$$

$$a = K_4 k_D D_{O_2}^{-2/3} \omega^{-1/2} + 2K_1 K_5 [H_2O_2]_{bulk} k_D D_{H^+}^{-2/3} \omega^{-1/2}$$
$$- K_1 k_D D_{H_2O_2}^{-2/3} \omega^{-1/2} \left(1 + K_5 [H^+]_{bulk} + \frac{k_2}{k_3} \right) \tag{3.15}$$

$$b = 1 + K_4 [O_2]_{bulk} + k_2 N K_1 k_D D_{H_2O_2}^{-2/3} \omega^{-1/2}$$
$$+ K_1 [H_2O_2]_{bulk} \left(1 + K_5 [H^+]_{bulk} + \frac{k_2}{k_3} \right) \tag{3.16}$$

$$c = -k_2 N K_1 [H_2O_2]_{bulk} \tag{3.17}$$

These coefficients are expressed in terms of the bulk concentrations of the reactants and products used in the mechanism proposed.

Ascertaining the validity of the mechanism and evaluating the kinetic parameters requires the comparison of the roots of the polynomial, Eqn.3.13, with the experimental data. The roots of a third order polynomial can be obtain using Viéte's method [1-6] in terms of an angle, ϕ, and calculated by

$$\phi = \cos^{-1} \left(\frac{2a^3 - 9ab + 27c}{2(a^2 - 3ab)^{3/2}} \right) \tag{3.18}$$

where the three roots λ_1, λ_2, and λ_3 are given by

$$\lambda_1 = -2 \left(\frac{a^2 - 3b}{9} \right)^{1/2} \cos \left(\frac{\phi}{3} \right) - \frac{a}{3} \tag{3.19}$$

$$\lambda_2 = -2 \left(\frac{a^2 - 3b}{9} \right)^{1/2} \cos \left(\frac{\phi + 2\pi}{3} \right) - \frac{a}{3} \tag{3.20}$$

$$\lambda_3 = -2 \left(\frac{a^2 - 3b}{9} \right)^{1/2} \cos \left(\frac{\phi + 4\pi}{3} \right) - \frac{a}{3} \tag{3.21}$$

This operation was encoded in a purpose written program employing SIMPLEX optimisation to compare the roots of Eqn. 3.13 to the experimental data gathered as described in Section 2.6. Equations 3.13 to 3.17 reveal that the kinetic parameters that were optimised by this program are K_1, K_4, K_5 the product k_2N and the k_2/k_3 ratio. The values used for the diffusion constants D_{H^+}, D_{O_2}, and $D_{H_2O_2}$ were the same as that used by Khudaish. The two former constants were obtained from the literature and taken to be 9.31×10^{-9} m^2 s^{-1} [65] and 1.93×10^{-9} m^2 s^{-1} [64] respectively. Due to the low response

observed, in this study, the diffusion of H_2O_2 was not a limiting factor making its optimisation unfeasible. Therefore the latter was taken to be 0.66×10^{-9} m^2 s^{-1} as optimised by Khudaish [1-6].

The SIMPLEX program was forced to deal with positive values of the kinetic and binding constant parameters though optimisation of the natural logarithm of each parameter. The SIMPLEX procedure was primed with values similar to that optimised by Khudaish for the electrochemical oxidation of H_2O_2 on a platinum electrode[1,3]. Only one root, λ_3, affords the positive real values for j. The kinetic parameters were optimised using the minimum sum of residuals (r_s) method (Section 2.6) with 400 iterations where r_s is given by

$$r_s = \Sigma(j - \lambda_3) \tag{3.22}$$

where λ_3 is the positive root of the third order polynomial, Eqn. 3.21. The average deviation between the model and the experimental data, d_{av} was calculated by

$$d_{av} = nF \sqrt{\frac{r_s}{n_p}} \tag{3.23}$$

where n_p is the number of data points optimised $n_p = 2737$ (7 rotation rates $\times$ 17 $[H_2O_2]_{bulk} \times$ 23 potentials).

This Khudaish model adjusted for nickel, Model I, was used to predict steady-state currents occurring at 20°C, in the primary pH 7.28, 0.1 M phosphate buffer over the $[H_2O_2]_{bulk}$ range 0 to 130 mM. It can be seen from Fig. 3.6 that the model exhibits systematic errors fluctuating from predicting responses which are too low, too high, and then too low again across the $[H_2O_2]_{bulk}$ range. Therefore, although the data fit can only be considered fair, the predicted shape is not yet correct. Inspection of Fig. 3.7, which displays the fractional surface coverage for each species, show that the species $Ni(OH)_2 \cdot H_2O_2 \cdot H^+$ remains effectively zero at all concentrations. This is also the case at the other rotation rates and potentials. The main source of inhibiting protons is as a by-product of the reoxidation of the reduced nickel sites, which are in turn produced by the electrochemical oxidation of H_2O_2. With the relatively low rate of oxidation there is significantly less reduced sites to reoxidise producing protons to cause inhibition when compared to the rates observed by Khudaish on platinum in acidic [1-6]. The rate of reduced site replenishment is slow (covered in Section 3.5.3), therefore, the production of protons will also be comparatively low.
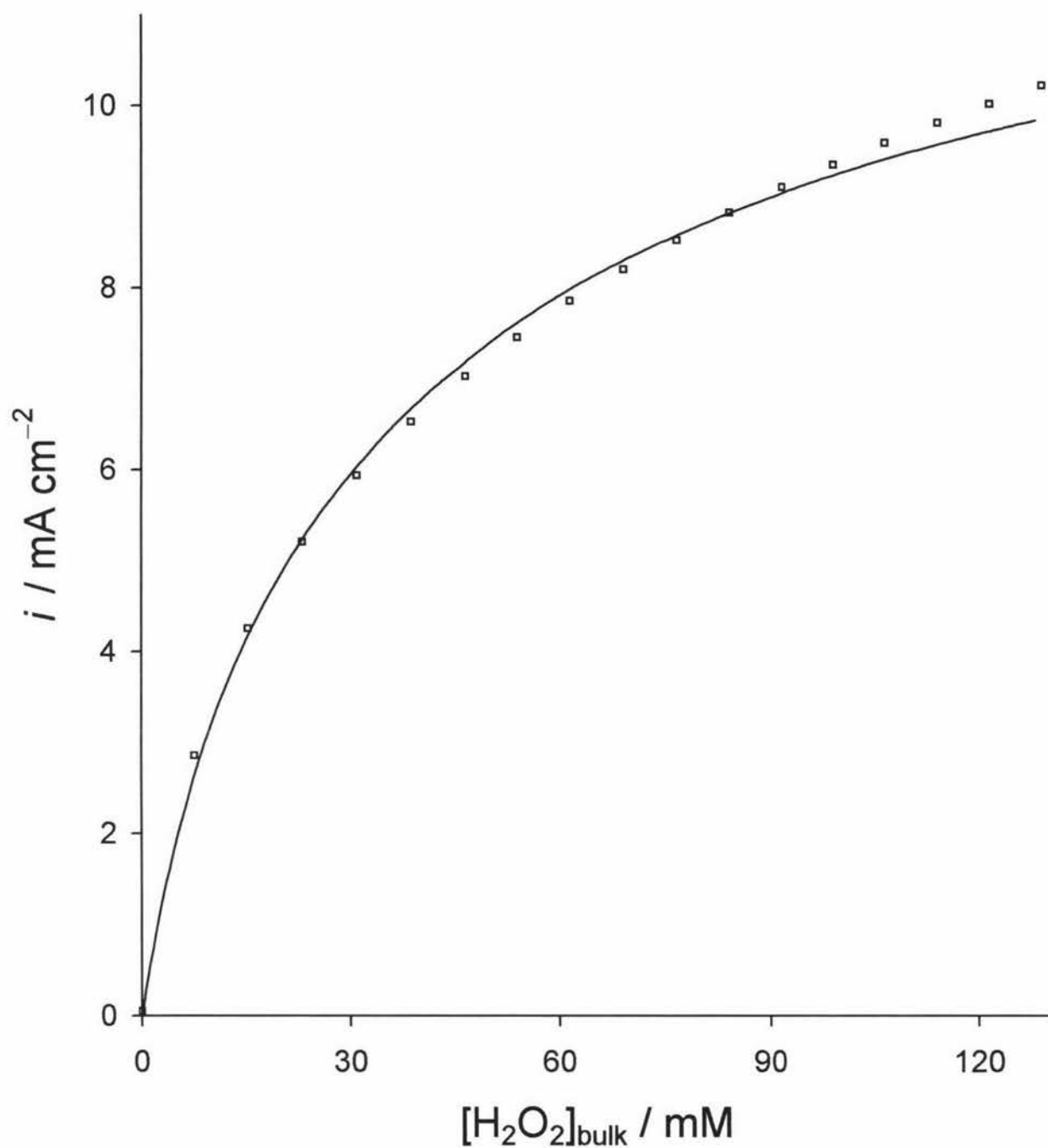
Fig. 3.6 Steady-state responses (□) at E = +1036 mV vs Ag/AgCl and ω = 4000 rpm as a function of $[H_2O_2]_{bulk}$ at in the primary pH 7.28 0.100 mol L^{-1} phosphate buffer at 20°C. Smooth curves are the synthetic responses calculated using the parameters optimised in Model I.
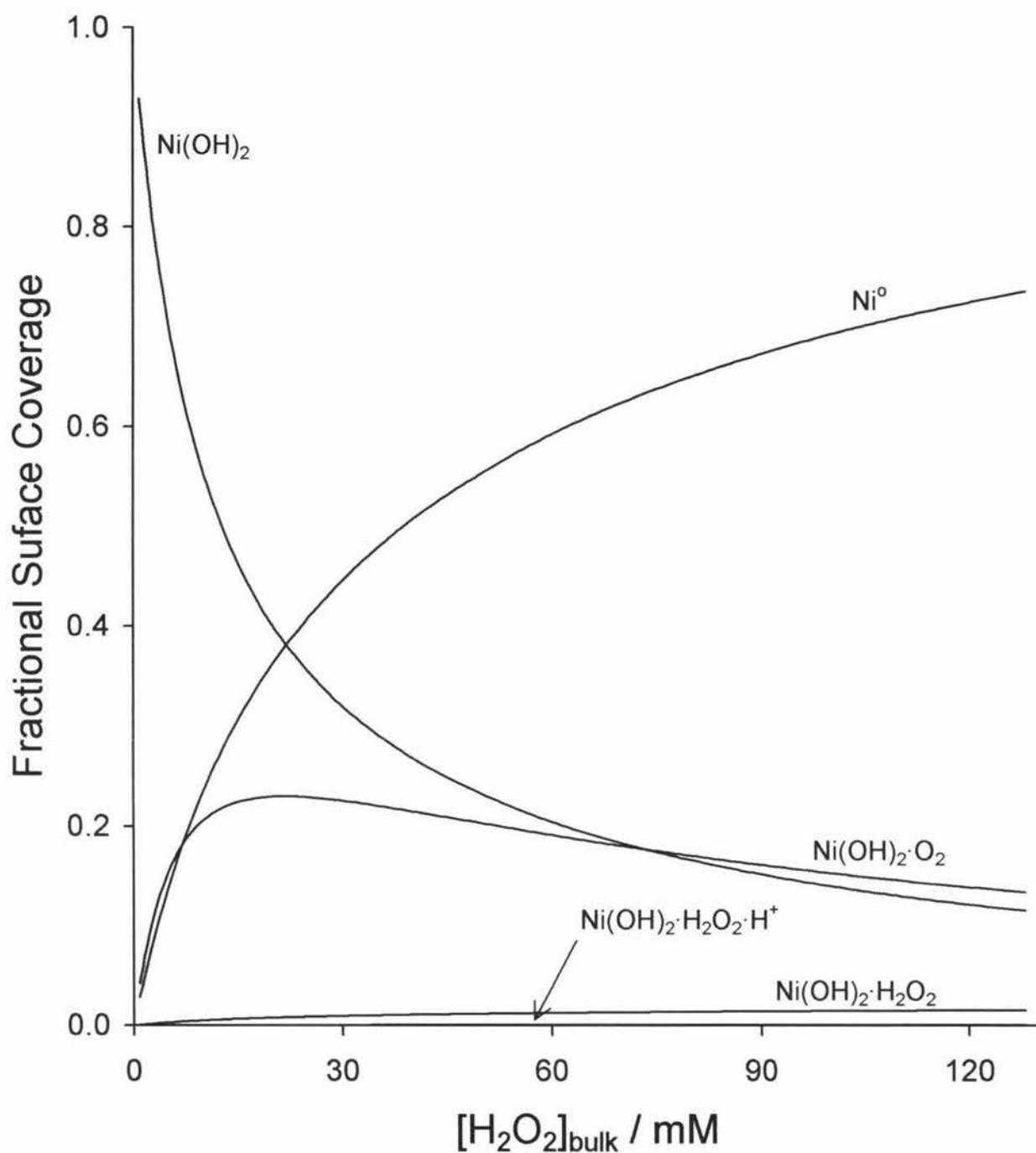
Fig. 3.7 The relative fractional surface coverage of the nickel species $Ni(OH)_2$, $Ni(OH)_2 \cdot O_2$, $Ni(OH)_2 \cdot H_2O_2$, $Ni(OH)_2 \cdot H_2O_2 \cdot H^+$ and Ni^o on the nickel RDE, $E = +1036$ mV vs Ag/AgCl, and $\omega = 4000$ rpm, in the primary pH 7.28 0.100 mol L^{-1} phosphate buffer at 20°C. Surface coverage of $Ni(OH)_2 \cdot H_2O_2 \cdot H^+$ is not discernible against the X-axis.

3.5.2 *Model II*

The observations above, for Model I, strongly suggest that the Khudaish model may be refined for nickel electrodes by removing the K_5 term altogether (i.e. discounting Eqn. 3.10) to give Model II. The rate equation of the simplified model, Model II, is

$$j = \frac{k_2 N K_1 [H_2 O_2]}{1 + K_4 [O_2] + K_1 [H_2 O_2](1 + k_2/k_3)} \tag{3.24}$$

Again, the rate and diffusion dependent expressions, Eqns 3.1, .3.2 and 3.3, need to be substituted into rate equation, Eqn. 3.24. This yielded a much simpler second order polynomial expression for the rate in terms of the bulk concentrations of the reactants and products of the mechanism.

$$0 = aj^2 + bj + c \tag{3.25}$$

where the polynomial coefficients are given by

$$a = K_4 k_D D_{O_2}^{-2/3} \omega^{-1/2} - K_1 k_D D_{H_2 O_2}^{-2/3} \omega^{-1/2} \left(1 + \frac{k_2}{k_3}\right) \tag{3.26}$$

$$b = 1 + K_1 [H_2 O_2]_{bulk} \left(1 + \frac{k_2}{k_3}\right) + k_2 N K_1 k_D D_{H_2 O_2}^{-2/3} \omega^{-1/2} \tag{3.27}$$

$$c = k_2 N K_1 [H_2 O_2]_{bulk} \tag{3.28}$$

Once again, ascertaining the validity of the mechanism and evaluating the kinetic parameters requires the comparison of the roots of the polynomial with the experimental data. The roots, R_1 and R_2, of the second order polynomial can be obtained by solving the quadratic equation

$$j = \frac{-b \pm \sqrt{b^2 + 4ac}}{2a} \tag{3.29}$$

This operation was encoded in the SIMPLEX optimisation program comparing the roots of Eqn. 3.25 to the experimental data gathered as described in Section 2.6. As before only one of the roots, R_1, affords real positive values for j. Therefore, the minimum sum of residuals for Model II was given by

$$r_s = \Sigma(j - R_1) \tag{3.30}$$

Model II was used to predict the steady-state responses observed at 20°C, in the primary pH 7.28, 0.1 M phosphate buffer over the $[H_2 O_2]_{bulk}$ range 0 to 130 mM. Comparison of the

predicted rates to the experimental data collected under the same conditions is shown in Fig. 3.8 for the selected rotation rate and potential. Although this model still shows some systematic error, it is evident that removing K_5 improves the models data fit.

3.5.3 *Development of Model III*

A number of parameters of Model II (Eqn. 3.12) are potential-invariant (binding constants K_1 and K_4, and the diffusion coefficients $D_{H_2O_2}$ and D_{O_2}) since it is likely the potential only influences charge transfer reactions. The heterogeneous rate constants k_2 and k_3 describe charge transfer reactions, in the model, so are expected to vary with potential. These terms, in the k_2/k_3 ratio, are inseparable from each other in the same manner as k_2N. However, k_3N may be evaluated from k_2/k_3 and k_2N. The potential variation of the optimised heterogeneous rate constants for Model II are plotted logarithmically in Fig. 3.9. From this figure k_2N can be seen to change exponentially with the potential. However, k_3N can be seen to fluctuate wildly at lower potentials until $+780\,mV$ when it appears to adopt a constant and low value of about 8.0×10^{-4}. This is in contrast to the expected potential dependence. If the oxidation of the reduced site back to the active surface species was an electron transfer reaction one might expect the heterogeneous rate constant k_3N to increase with potential. This parameter would not be expected to be very high and oscillating wildly at low potentials only to drop to a constant value of similar magnitude to k_2N at higher potentials. Therefore, it is likely that k_3N is in fact constant as observed at higher potentials and the unusual behaviour at low potentials is an artefact during optimisation of the root R_1 at low rates. An explanation for the potential invariance of k_3N is that this reoxidation process is limited by some slow step not involving electron transfer. The possibility that some phosphate species from the buffer may also be involved in this reaction will be discussed later in Chapter 5.

Consequently, an additional restraint was imposed upon the optimisation to give Model III so that k_3N is treated as a potential invariant parameter together with K_1 and K_4. A comparison between each of the Models I, II and III is shown in Table 3.1. The d_{av} shows that all of these models show a comparable fit to the Khudaish model for platinum [1-6].

Fig. 3.8   Steady-state responses (□) at E = +1036 mV vs Ag/AgCl as a function of $[H_2O_2]_{bulk}$ at ω = 4000 rpm in the primary pH 7.28 0.100 mol L^{-1} phosphate buffer at 20°C. Smooth curves are the synthetic responses calculated using the parameters optimised in Model II.
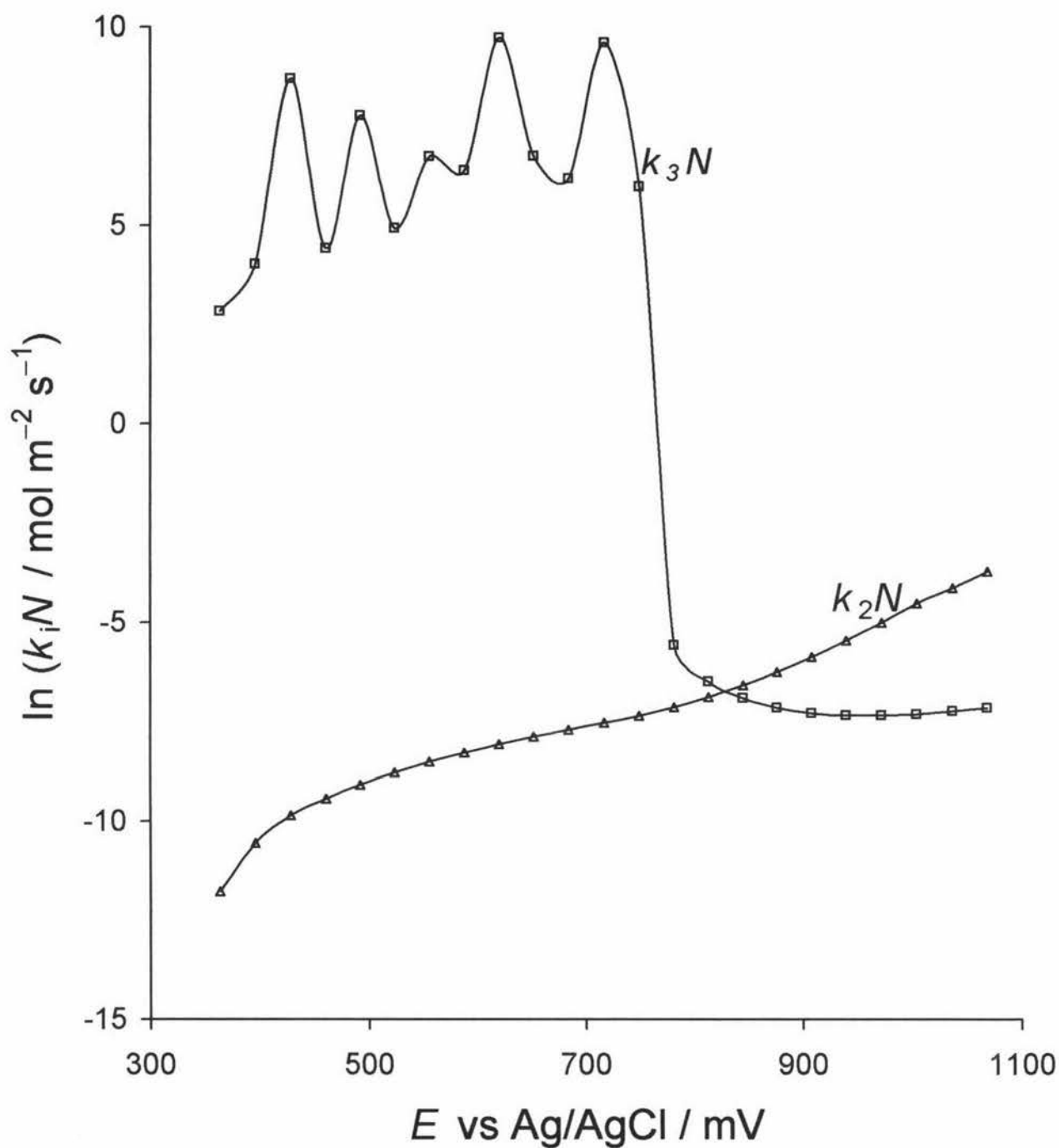
Fig. 3.9 Logarithmic plot of the heterogeneous rate constants, k_2N ($\triangle$) and k_3N ($\square$), varying with potential. Plotted over the +332 mV to +1100 mV potential range, at 20°C.

Model	I	II	III
k_3N / mol m^{-2} s^{-1}	E variant	E variant	constant
K_5 / m^3 mol^{-1}	0.01321	—	—
K_1 / m^3 mol^{-1}	0.00380	0.00209	0.00443
K_4 / m^3 mol^{-1}	0.39689	0.40857	0.35982
r_s / 10^{-8} (mol m^{-2} s^{-1})^2	5.89	4.11	6.15
d_{av} / mA cm^{-2}	0.087	0.073	0.089

Table 3.1   Optimised equilibrium parameters together with r_s and d_{av} to access the relative quality of Models I, II, and III describing the electrochemical oxidation of hydrogen peroxide on a nickel electrode surface.

The model is significantly improved by discounting the proton inhibition, K_5, indicated by a large decrease in the sum of residuals and the average deviation between the model and the experimental data. These indicators suggest that the model is not improved by preventing k_3N to vary with potential. Indeed, it makes Model III slightly worse that Model I, leaving Model II as the statistically superior model. However, Model II incorporates an extra parameter which would be expected to improve the fit, it is interpreted here that the improvement in fit is not sufficient to warrant inclusion of k_3N as a potential variant parameter in light of the values it adopts. Furthermore, Model II offers seemingly non-sensical variation of k_3N with potential. Consequently, the final Model III is used in all subsequent sections and chapters.

3.6   The Quality of Model III Fit to Experimental Data

The fit of Model III to the experimentally observed steady-state responses, for the data given in Fig. 3.4, for ω = 4000 rpm and E = +1036 mV vs Ag/AgCl, over the 0 to 130 mM $[H_2O_2]_{bulk}$, is shown in Fig. 3.10. This demonstrates that while Model III has not completely lost the systematic error observed in the earlier models it affords a very respectable fit across the $[H_2O_2]_{bulk}$ range at E = +1036 mV.

It is useful at this point to consider the change in the relative surface coverage θ_i of each nickel species i with the increase of $[H_2O_2]_{bulk}$ and how this pertains to Model III (Fig. 3.11). Figure 3.11 shows that with increasing $[H_2O_2]_{bulk}$ the number of unoccupied $Ni(OH)_2$ sites for possible electrochemical oxidation decreases. A coinciding increase in reduced sites (having oxidised the surface H_2O_2 producing current) and sites with H_2O_2 transiently bound before oxidation was observed. With the increased H_2O_2 oxidation (and current) there was also a corresponding increase in the surface dioxygen levels generated as a by-product of the oxidation.

This increase of H_2O_2 oxidation accounts for the large initial increase in dioxygen bound sites, up to a $[H_2O_2]_{bulk}$ of 20mM, following the increase in oxidation (reduced sites). It must be noted that the dioxygen has a much larger binding constant than hydrogen peroxide to the unoccupied nickel site, as shown in Table 3.1. Consequently, although the surface
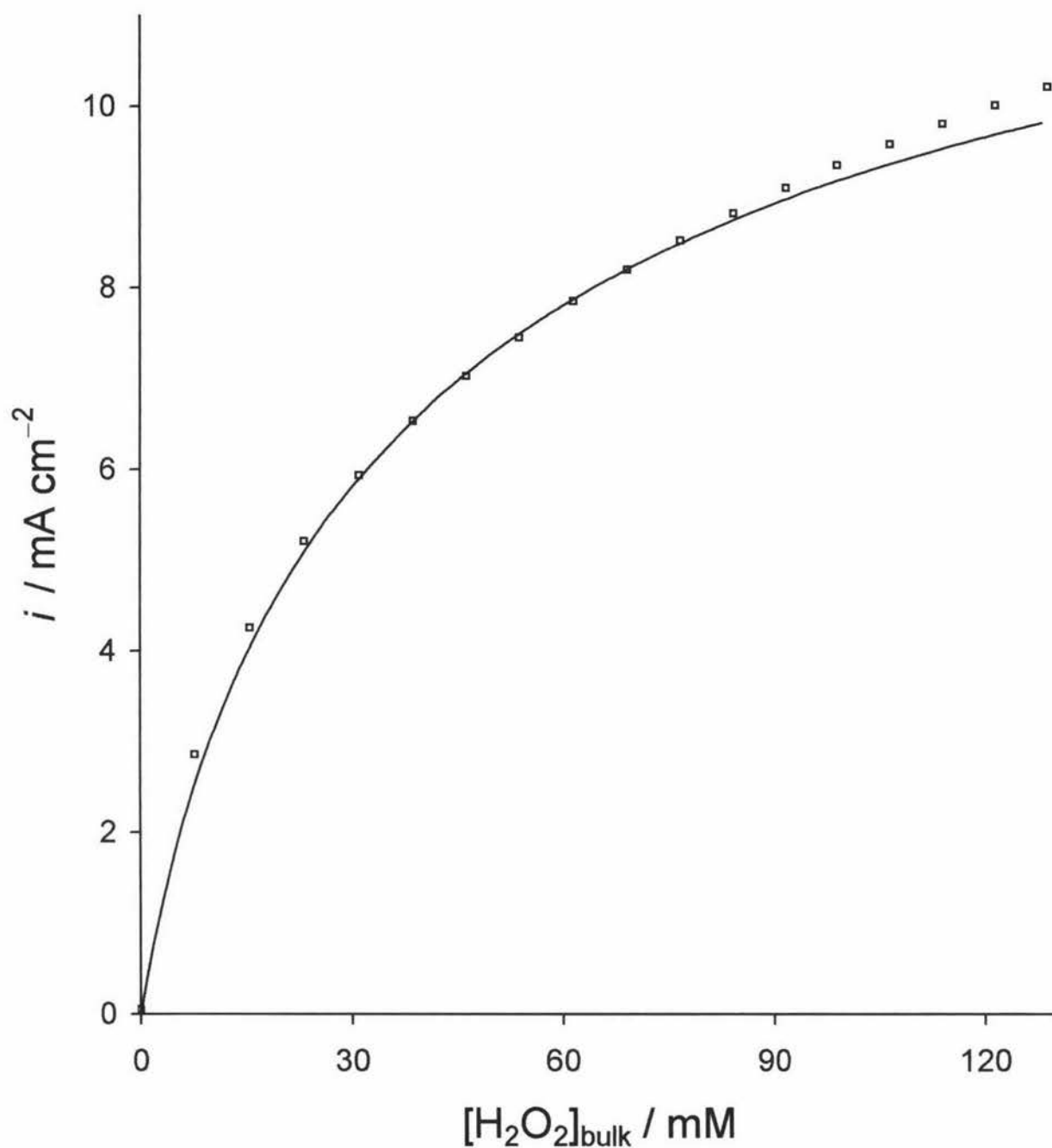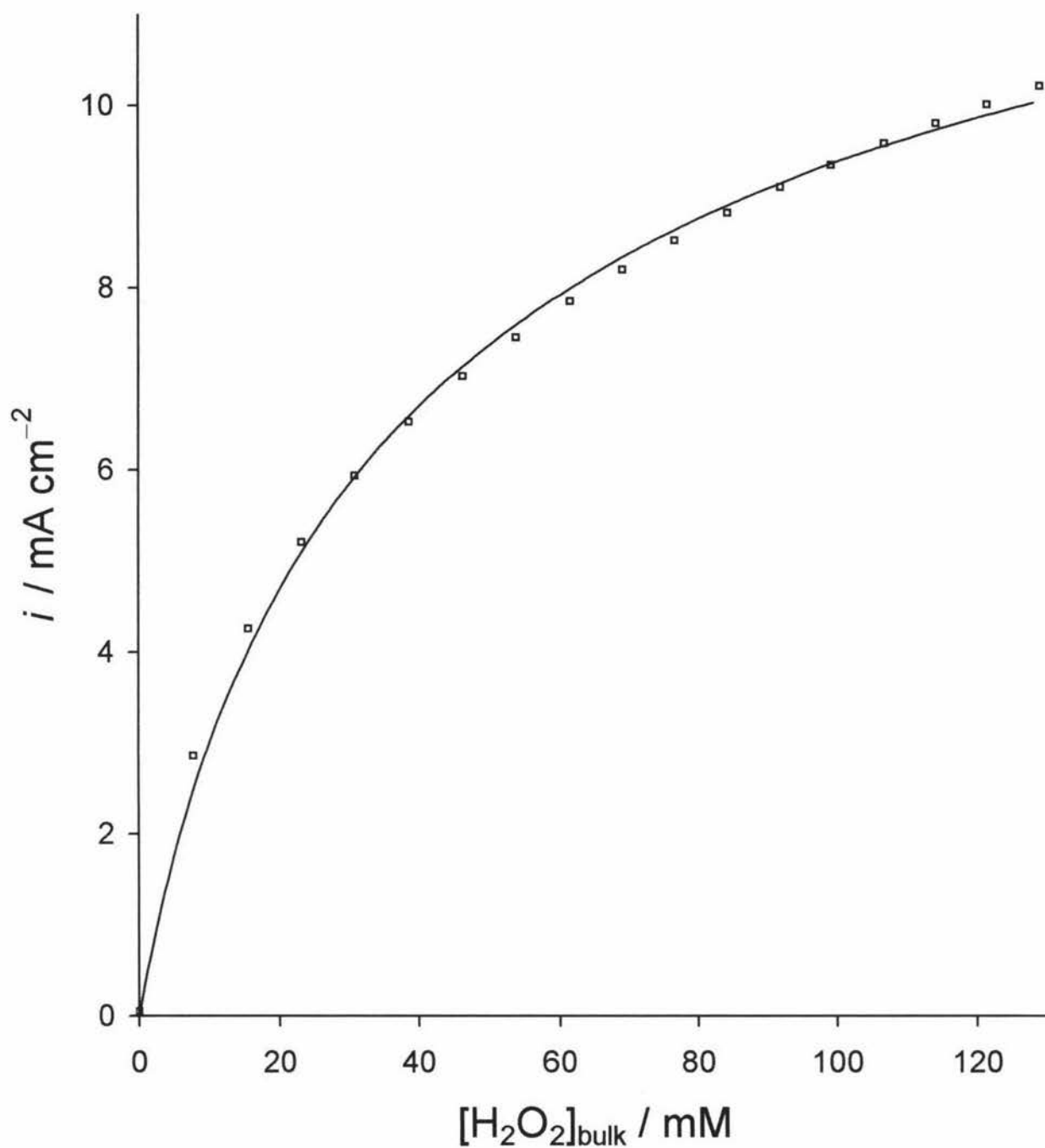
Fig. 3.10 Steady-state responses (□) at $E = +1036$ mV vs Ag/AgCl as a function of [H$_2$O$_2$]$_{bulk}$ at $\omega = 4000$ rpm in the primary pH 7.28 0.100 mol L^{-1} phosphate buffer at 20°C. The parameters optimised in Model III are used to generate the synthetic response plotted as a smooth curve.
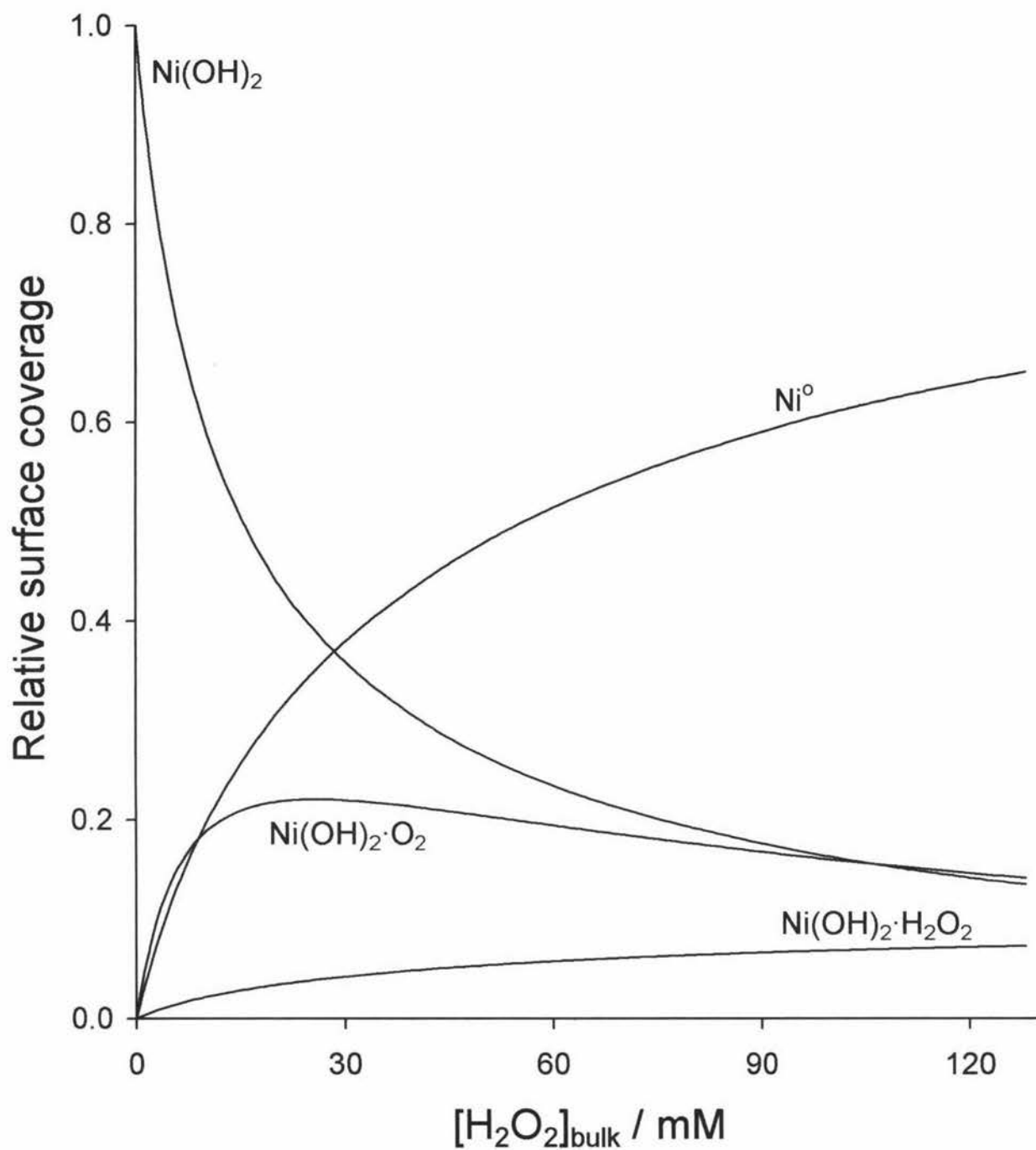
Fig. 3.11 The relative fractional surface coverage of the nickel species $Ni(OH)_2$, $Ni(OH)_2 \cdot O_2$, $Ni(OH)_2 \cdot H_2O_2$, and Ni° on the nickel RDE surface at $+1036$ mV vs Ag/AgCl and $\omega = 4000$ rpm at $20°C$. Calculated from parameters optimised in Model III.

concentration of hydrogen peroxide is much larger than dioxygen, as shown by Fig. 3.5, dioxygen occupies proportionately considerably more sites as seen in Fig. 3.11. Dioxygen competes with hydrogen peroxide for the unbound $Ni(OH)_2$ sites. Therefore, it will become slightly less significant at higher $[H_2O_2]_{bulk}$. Although more dioxygen is produced by increased oxidation there is noticeably more hydrogen peroxide available to appropriate the unbound sites. This is well illustrated by Fig. 3.11 where, once past the dioxygen peak at 20 mM $[H_2O_2]_{bulk}$, the dioxygen decline is evenly matched by the increase of unoxidised H_2O_2 bound sites.

At higher $[H_2O_2]_{bulk}$ the current is limited by mass transportation of H_2O_2 to the electrode surface (see Section 2.2.4). Due to the reliability of the rotation disc electrode pump the mass transport to the surface of the electrode can be easily modelled shown by the excellent fit of the model line to the observed data points (Fig. 3.10). Mass transport limitations may be a cause of the current beginning to plateau at higher $[H_2O_2]_{bulk}$ observed in Fig. 3.3. A finite number of sites available for H_2O_2 oxidation can also cause the current plateau observed. When all the sites are saturated (factional surface coverage of $Ni(OH)_2$ drops to approximately zero), the rate of oxidation in that case will be limited by the rate of site replenishment, no longer by the quantity of H_2O_2 molecules near the electrode surface. The plateau effect is not as significant as described by Khudaish [1-6] in the platinum study even at near to twice the $[H_2O_2]_{bulk}$.

3.6.1 *Rotation Rate Variation*

The steady-state responses, used to give Fig. 3.4, at $E = +1036$ mV vs Ag/AgCl over the 0 to 130 mM $[H_2O_2]_{bulk}$ for all seven rotation rates $\omega = 630$, 1000, 1585, 2500, 4000, 6300, and 10000 rpm are given in Fig. 3.12, plotted with predicted responses of Model III. From Fig. 3.12 the models predicted response profile with rotation rate could be seen to fit the experimental data admirably. However, this model slightly deviates from the observed data at lower $[H_2O_2]_{bulk}$ where there was less current and slight separation between rotation rates. At higher $[H_2O_2]_{bulk}$ and higher currents the model fits excellently. This inconsistency may be due to the nature of the optimisation technique in that the regions of higher current have more influence over the optimisation than regions of low current. For example, regions with
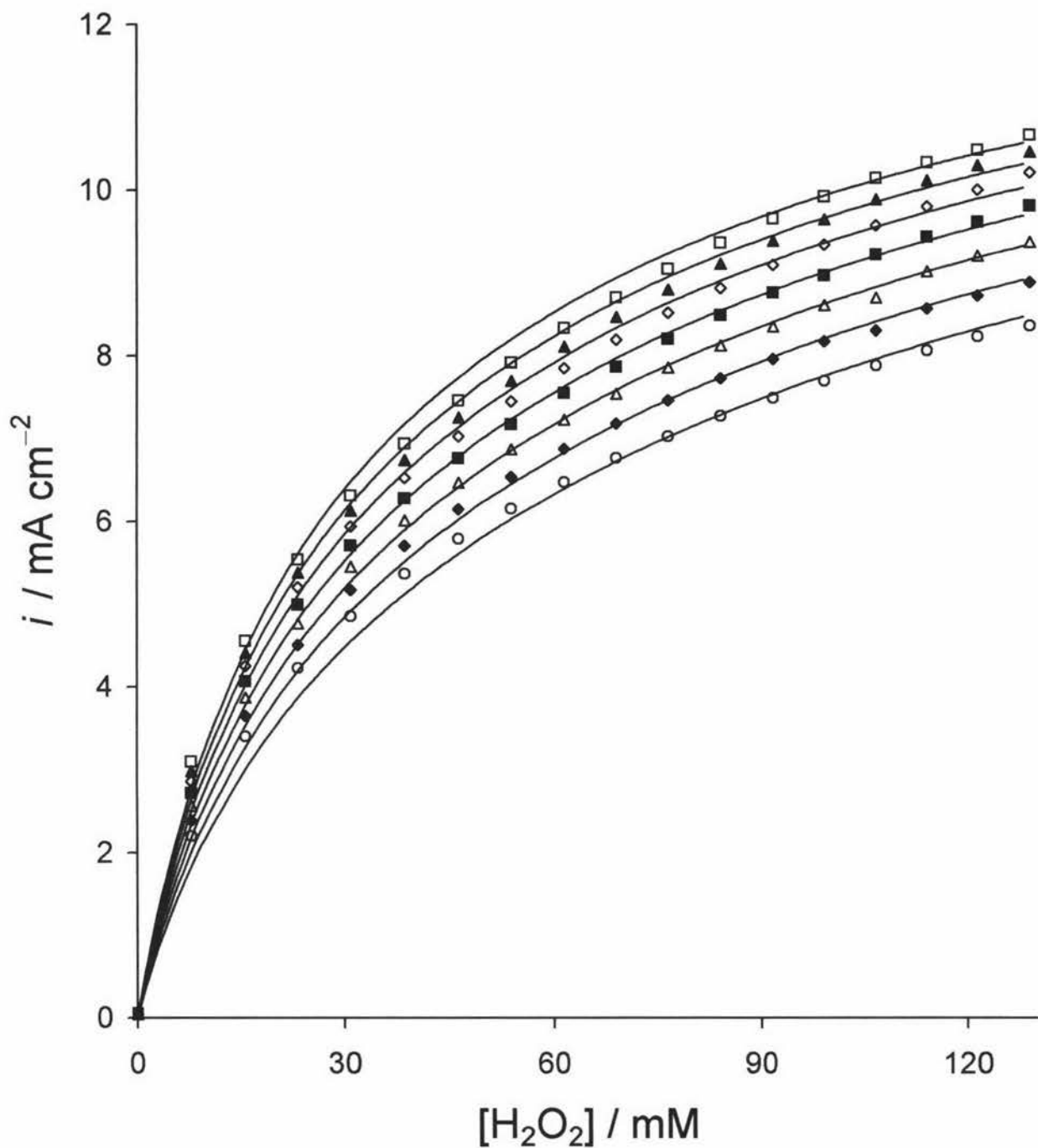
Fig. 3.12 Steady-state responses of seven rotation rates, ω = 630 ($\bigcirc$), 1000 ($\blacklozenge$), 1585 ($\triangle$), 2500 ($\blacksquare$), 4000 ($\diamond$), 6300 ($\blacktriangle$), and 10000 ($\square$) rpm, at E = +1036 mV vs Ag/AgCl as a function of $[H_2O_2]_{bulk.}$. Smooth curves are the synthetic responses calculated using the parameters optimised in Model III.

twice the current will have four times the influence over the optimisation of the model parameters given that the sum of residuals is being minimised. In low $[H_2O_2]_{bulk}$ regions where rotation rate is not as significant, other factors exert some influence on determining the current observed. In low $[H_2O_2]_{bulk}$ regions the model's projection simulates an ideal situation in which the rotation rate has a stronger influence as predicted in the higher $[H_2O_2]_{bulk}$ region. The model's fit in the low $[H_2O_2]_{bulk}$ region is still a reasonably accurate facsimile and the differences, which are mainly seen at the lowest rotation rate (630 rpm) and low in current conditions, could be attributed to random fluctuations in data gathering which can not be modelled.

The effect of the rotation rate can be readily displayed by considering the fractional surface coverage of each nickel species at the rotation rate extremes 630 rpm (Fig 3.13) and 10000 rpm (Fig 3.14). Comparing these two figures we can see that the most notable effect of changing from 630 rpm to 10000 rpm is that the number of active sites blocked by the dioxygen is reduced by a third. This is a logical consequence of increasing the rotation rate, since at very low rotation rates mass transport is quite minimal. Therefore, at low rotation rates there will be a lower surface concentration of H_2O_2 similarly there is a high surface concentration of oxidation by-products. Mass transport at high rotation rates is improved so the by-products are removed with much more efficiency. At higher rotation rates more bulk H_2O_2 is transported to the surface this competes with dioxygen for the unoccupied sites. All of this reduces the surface coverage of dioxygen at higher rotation rates. Now that 17% less surface is covered by the dioxygen species there is a small 2% increase in the surface coverage by both the unoccupied site $Ni(OH)_2$, and the hydrogen peroxide bound site $Ni(OH)_2 \cdot H_2O_2$. The reduced site Ni^o covers the remaining 13% of the available surface. The regeneration of the binding site is the rate limiting reaction. Therefore, at higher rotation rates the number of reduced sites accumulate since more H_2O_2 binds and reduces the recently unoccupied sites faster than they are replenished. So reduction in the dioxygen bound sites directly equates to an increase in the rate of electrochemical oxidation of hydrogen peroxide and hence, the higher current that was observed.
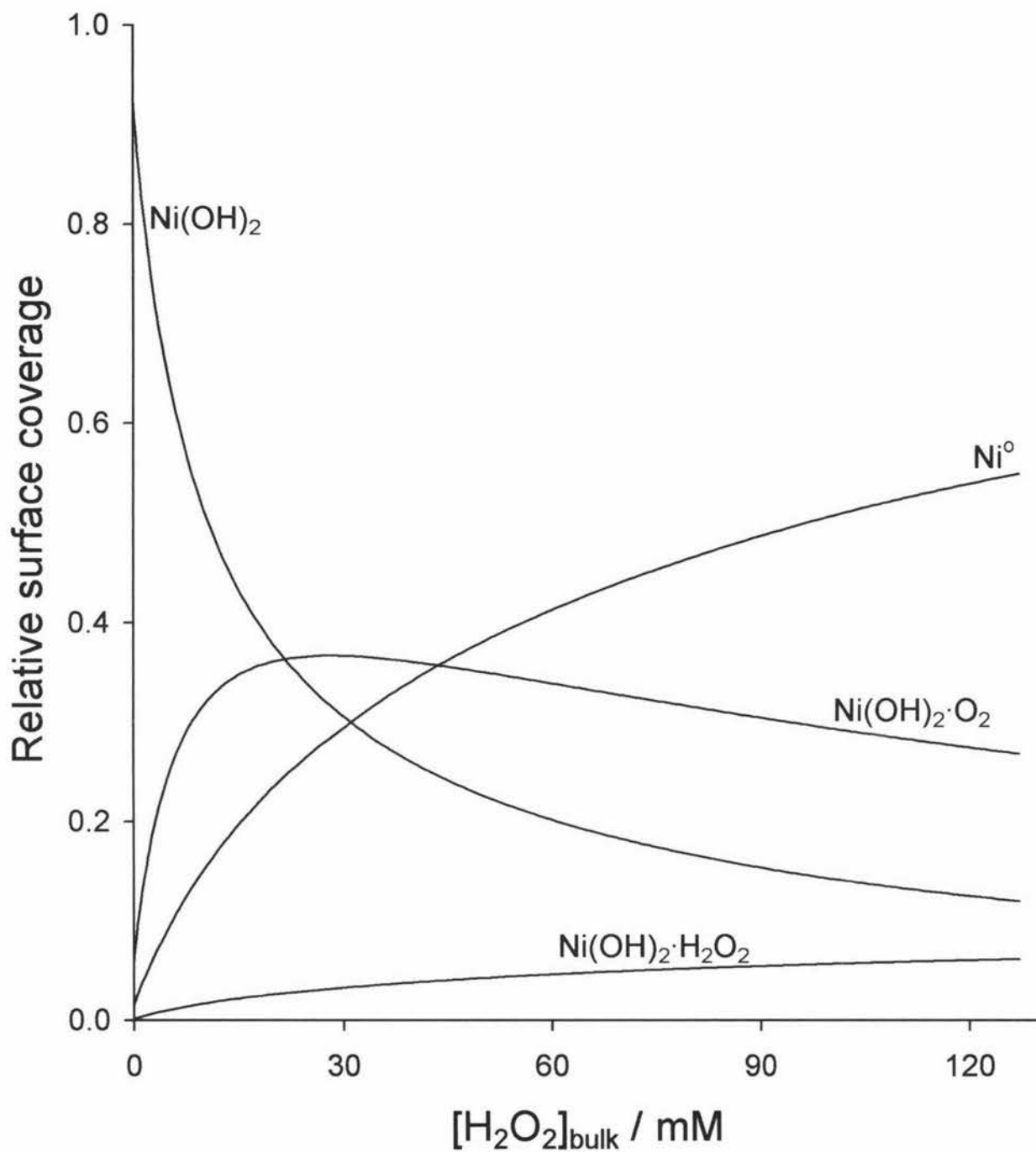
Fig. 3.13   The relative fractional surface coverage of the nickel species $Ni(OH)_2$, $Ni(OH)_2 \cdot O_2$, $Ni(OH)_2 \cdot H_2O_2$, and Ni^o on the nickel RDE surface at a low rotation rate of $\omega = 630$ rpm displayed at +1036 mV at 20°C calculated from parameters optimised in Model III.
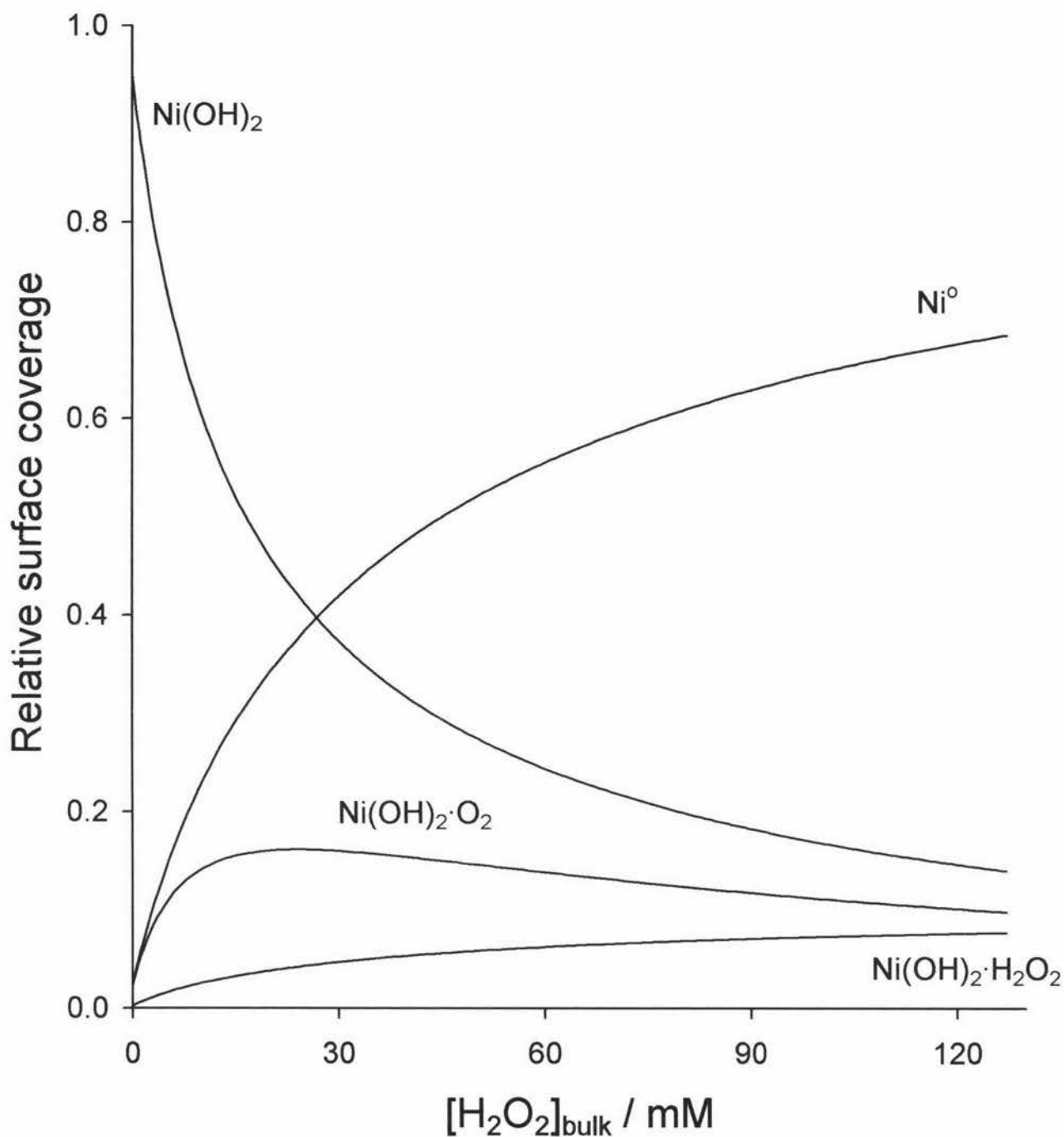
Fig. 3.14 The relative fractional surface coverage of the nickel species $Ni(OH)_2$, $Ni(OH)_2 \cdot O_2$, $Ni(OH)_2 \cdot H_2O_2$, and Ni° on the nickel RDE surface at a high rotation rate of $\omega = 10000$ rpm displayed at $+1036$ mV vs Ag/AgCl at 20°C calculated from parameters optimised in Model III.

3.6.2 *Potential Variation*

The steady-state responses, used to give Fig. 3.2, for a selected range of $[H_2O_2]_{bulk}$ over the potential range +332 to +1100 mV vs Ag/AgCl at one representative rotation rate ($\omega = 4000$ rpm) are plotted with the predicted responses of Model III in Fig 3.15. Model III predicted responses, given in Fig 3.15, are not at the exact $[H_2O_2]_{bulk}$ at which the experimental data was collected and are displayed. Therefore, the small systematic shifts between the model and experimental data is an artefact. However, what may be appreciated from this figure is that the response profiles with potential variation are very similar. Figure 3.15 shows that the model generated predictions adequately describe the observed data's variation with potential.

Considering how the model fits over the entire range of $[H_2O_2]_{bulk}$ at low potentials such as +428 mV, displayed in Fig. 3.16, we can see that Model III is not completely successful in describing this region. The observed data shows a reasonably linear increase in current with $[H_2O_2]_{bulk}$ whereas Model III predicts a curve, in which the increase with concentration begins to curtail at higher concentrations. This difficulty arises because +428 mV is at the very beginning of H_2O_2 oxidation and the currents are minimal, several orders of magnitude lower than the currents at +1036 mV. This is shown by Fig. 3.17 where most of the available sites remain unoccupied and the only other significant surface species is the H_2O_2 bound site. This indicates that the rate of reaction is so slow that these sites remain unoxidised and their concentration levels build up. With such a low rate of reaction there are few reduced sites and insufficient dioxygen is produced to compete with the H_2O_2 binding. This highlights a small but unavoidable deficiency that when trying to optimise model parameters for the electrochemical oxidation of H_2O_2 the software is more influenced by the larger currents at higher potentials where much more oxidation occurs. If more emphases is placed on the optimisation of the low potential region we risk optimising parameters that poorly describe the high potential region where the majority of oxidation occurs. So the present optimisation technique is to the detriment of the low potential region, where little oxidation occurs. Therefore, the model predicts a current/$[H_2O_2]_{bulk}$ relationship in this region that would only occur when higher rates of oxidation are attained. It should be noted that in these low current conditions, whilst the model predicts a current/$[H_2O_2]_{bulk}$ profile that
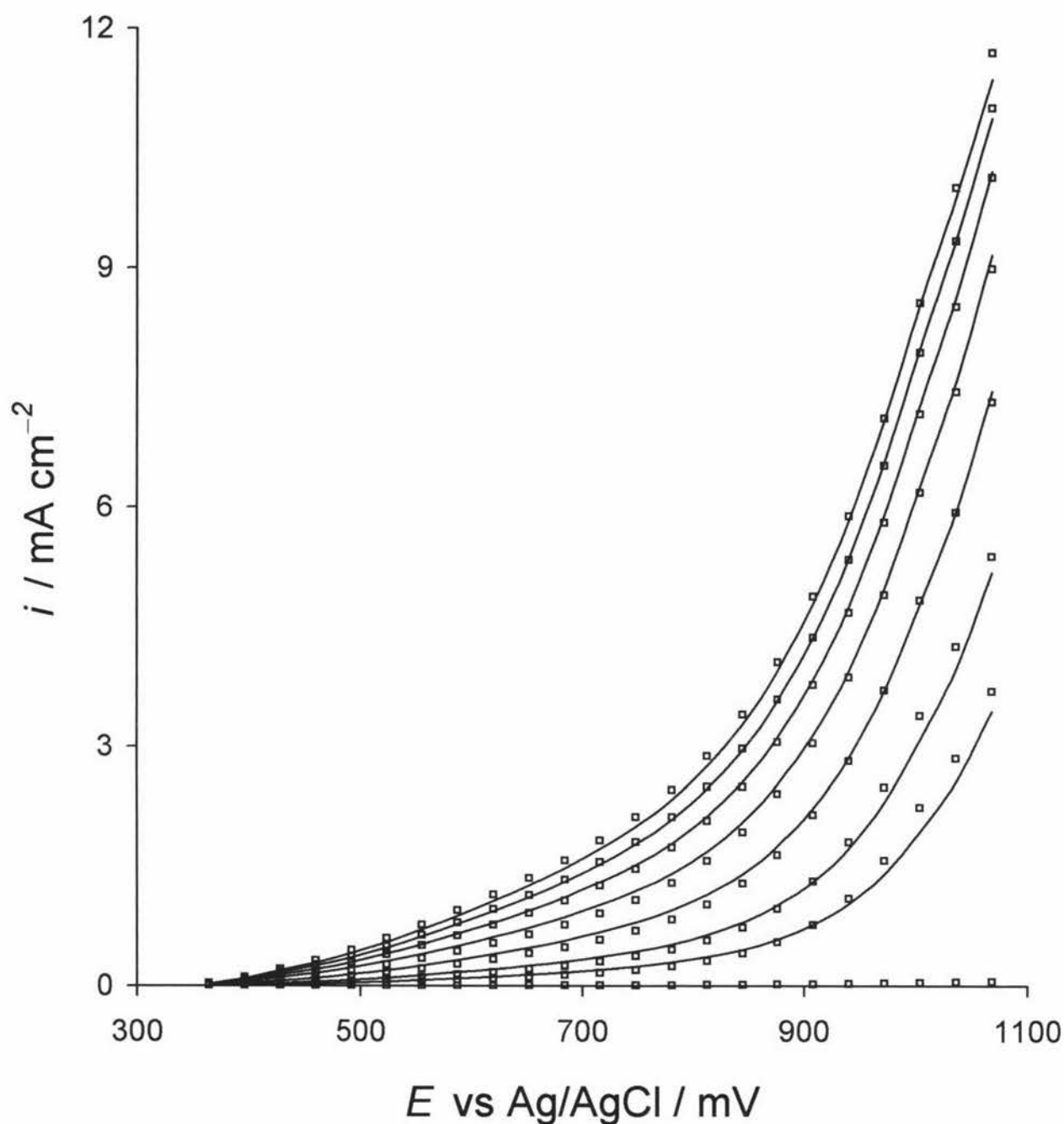
Fig. 3.15 Seven representative hydrogen peroxide concentrations (similar to Fig. 3.2) 0, 7.8, 15.5, 31.0, 53.9, 76.7, 99.2, and 121.5 mM are displayed over the range $E = +332$ to $+1100$ mV vs Ag/AgCl at 20°C. Smooth lines are predicted from Model III at approximately the same concentrations of 0, 8, 15.2, 31.2, 53.6, 76.8, 99.2, and 121.6 mM $[H_2O_2]_{bulk}$.
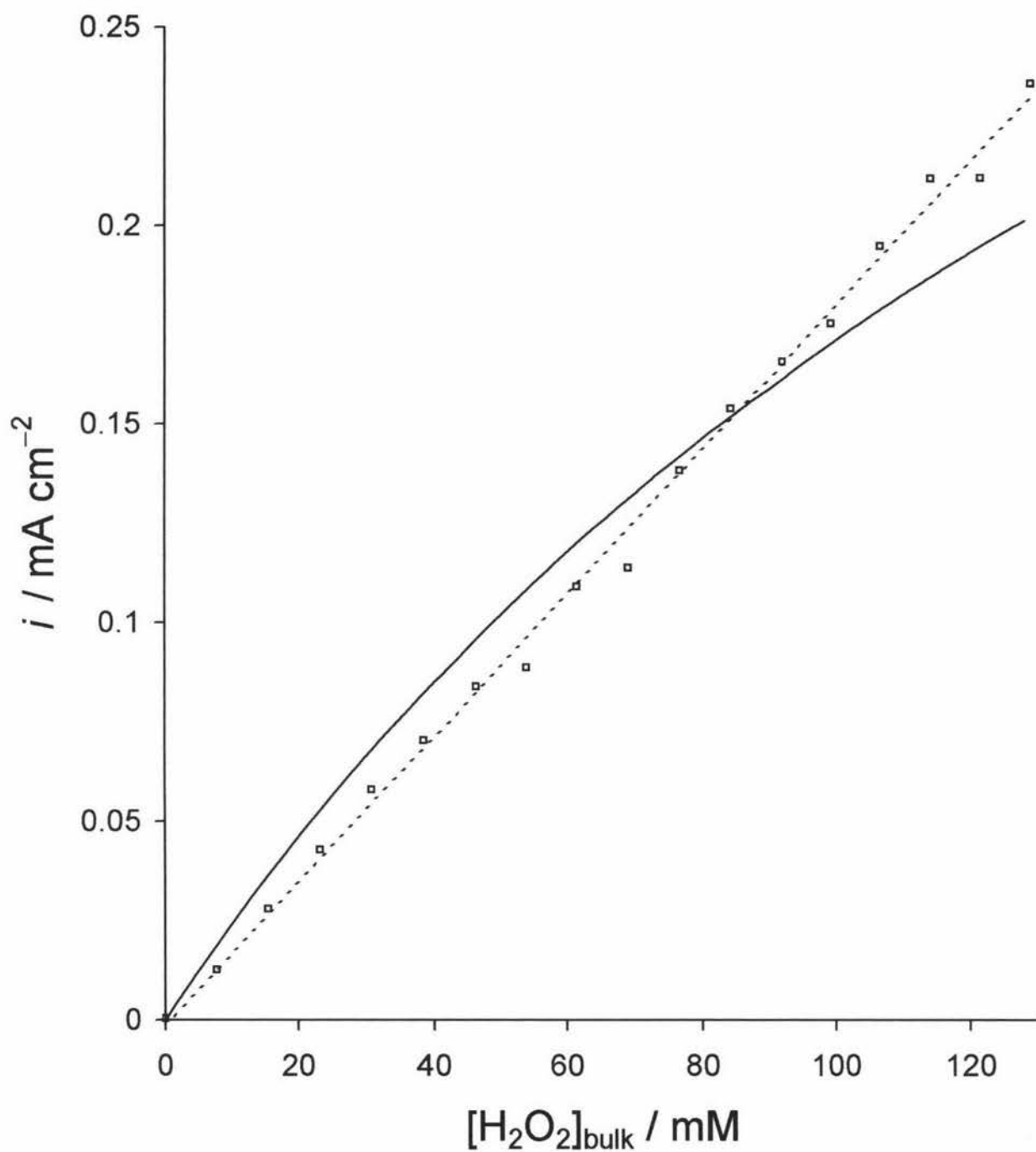
Fig. 3.16 The steady-state responses of the observed data (□) at $E = +428$ mV vs Ag/AgCl overlaid by a simple linear fit (---) as a function of $[H_2O_2]_{bulk}$ at $\omega = 4000$ rpm at 20°C. The smooth curve is the synthetic response calculated using the parameters optimised in Model III.
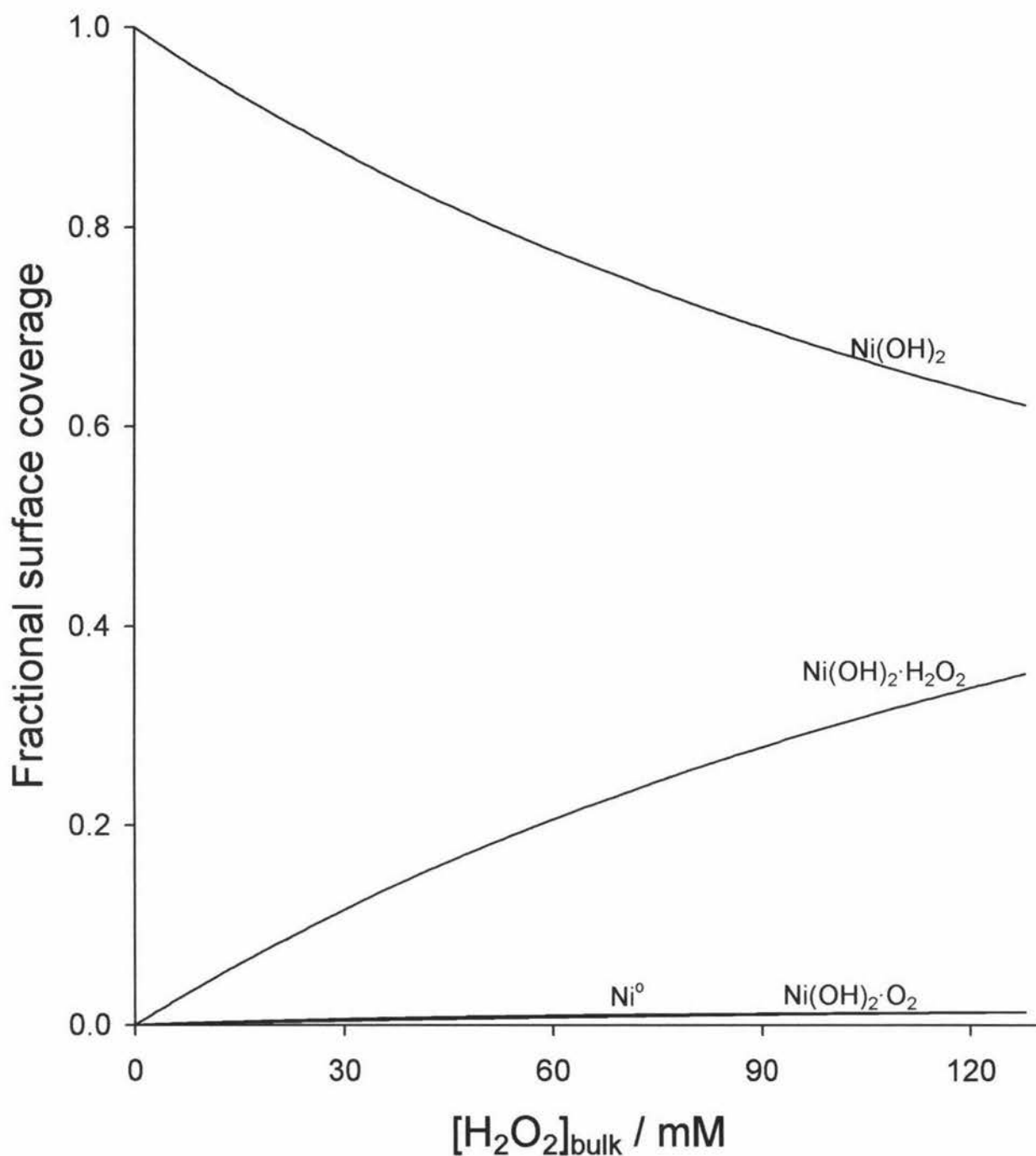
Fig. 3.17 The relative fractional surface coverage of the nickel species $Ni(OH)_2$, $Ni(OH)_2 \cdot O_2$, $Ni(OH)_2 \cdot H_2O_2$, and Ni^o on the nickel RDE surface at a low potential of $E = +428$ mV vs Ag/AgCl displayed at $\omega = 4000$ rpm at 20°C. In this plot species $Ni(OH)_2 \cdot O_2$, and Ni^o are superimposed the former slightly higher.

is only seen at higher potentials, the currents predicted are still very close to the currents observed.

If we now consider the mid potential region round +844 mV (Fig. 3.18) we can now see that the model fit is significantly improved although yet again the increase in current with $[H_2O_2]_{bulk}$ is slightly more linear than the model prediction. Previously it could be seen, in Fig. 3.10, that the model fits the +1036 mV data almost perfectly in comparison to that observed in Figs. 3.16 and 3.18, for +428 mV and +844 mV respectively. Furthermore, it can also be noted that only at the highest potential does the limiting current density get approached, as indicated by the current beginning to plateau at higher $[H_2O_2]_{bulk}$. The current/$[H_2O_2]_{bulk}$ relationship in the middle to low potential regions is tending towards a more linear relationship, which the model adequately reflects. Comparing the fractional surface coverage of the middle to high regions (ignoring the low potentials where little oxidation occurs), shown in Figs. 3.19 and 3.11, at +844 mV there are the symptoms of a low rate. There was a high coverage of the unoccupied site $Ni(OH)_2$, and the concentration of the H_2O_2 occupied site was still quite high due to not immediately been converted to the reduced site. The coverage of the reduced site, not surprisingly, follows that of the observed current, described earlier, being significantly more linear with respect to the $[H_2O_2]_{bulk}$ than the high potential region. The surface concentration of dioxygen, which is intrinsically linked to the rate, is also low. However, as alluded to earlier, dioxygen has disproportionately higher binding constant to the unoccupied site compared to hydrogen peroxide. This is graphically shown in Fig. 3.19 where, although there is little dioxygen produced at +844 mV indicated by the low surface coverage of the reduced nickel site (Ni° the other oxidation product), the amount of bound dioxygen is comparable to that observed in Fig. 3.11, at +1036 mV, above 60 mM $[H_2O_2]_{bulk}$.

3.6.3 *Heterogeneous Rate Constant k_2N Variation with Potential*

With k_3N being considered potential invariant, in Model III, the heterogeneous rate constant k_2N remains as the only potential variant parameter. This implies that changes in k_2N are the sole source of current variation with potential whether this be attributable to a changing of the heterogeneous rate constant k_2 or due to increasing numbers of available sites N, or more
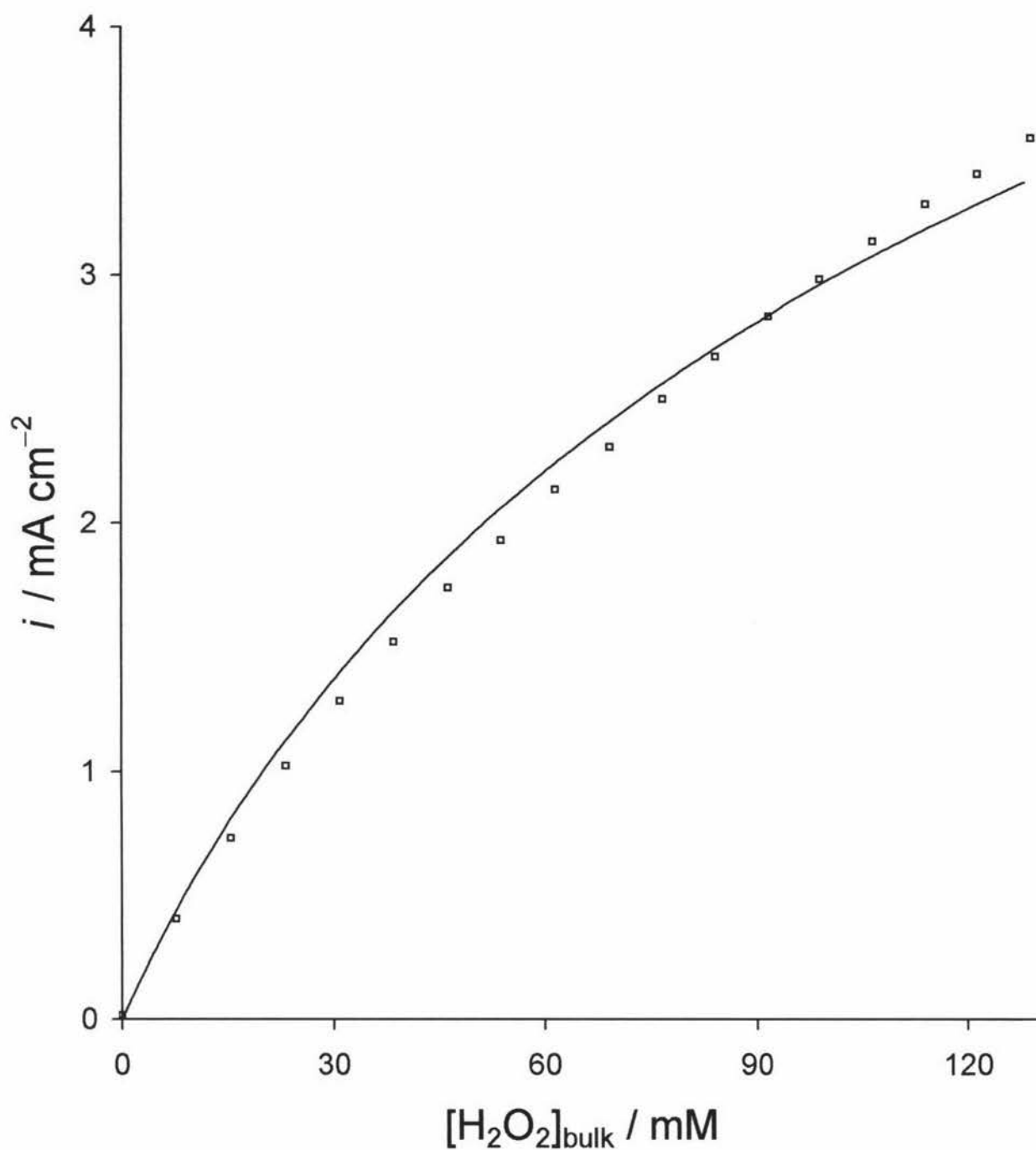
Fig. 3.18 The steady-state responses, at a medium potential of $E = +844$ mV, of the observed data (□) overlaid by a smooth line of the synthetic responses calculated from the parameters optimised from Model III as a function $[H_2O_2]_{bulk}$, at $\omega = 4000$ rpm at 20°C.
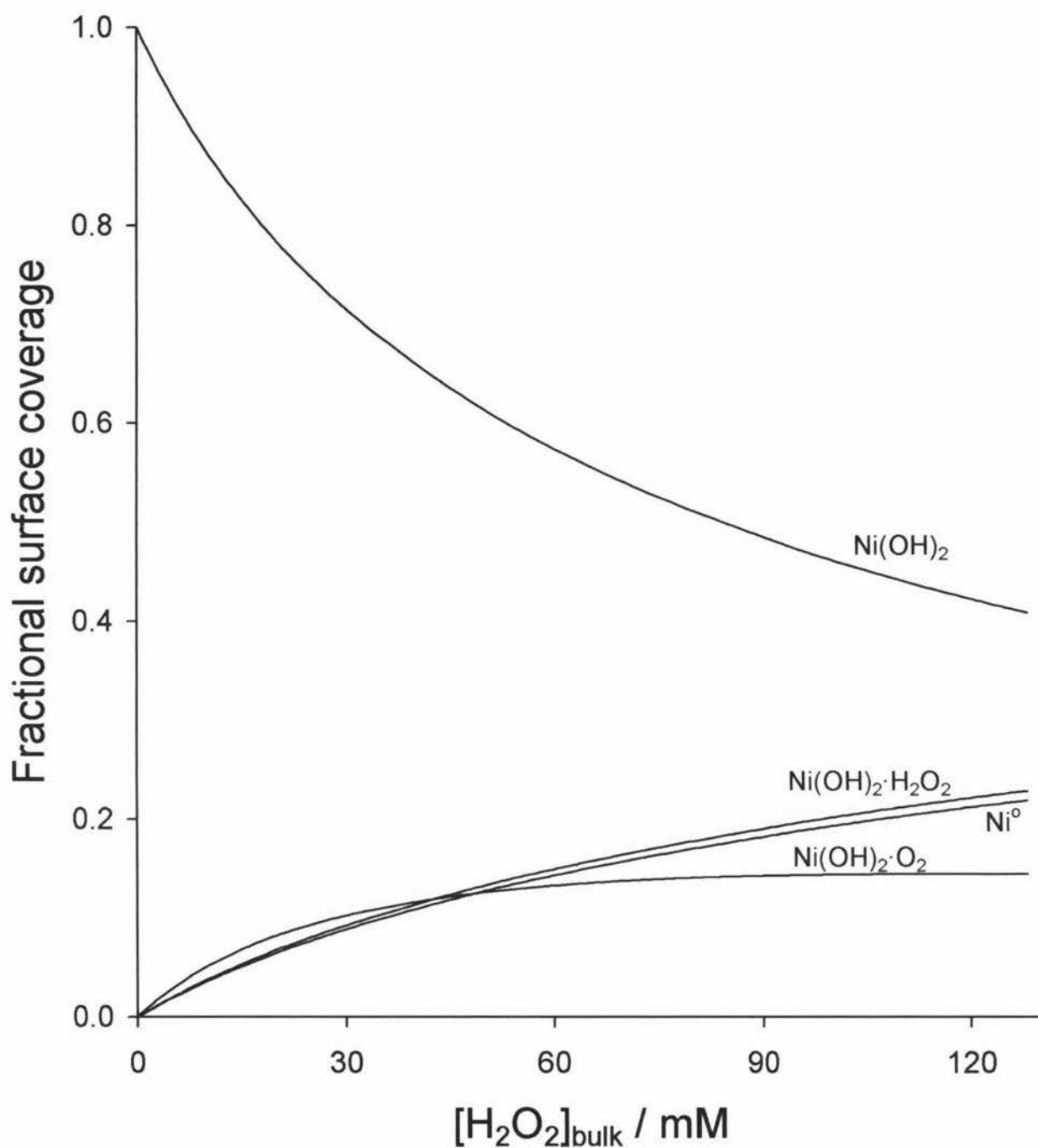
Fig. 3.19 The relative fractional surface coverage of the nickel species $Ni(OH)_2$, $Ni(OH)_2 \cdot O_2$, $Ni(OH)_2 \cdot H_2O_2$, and Ni^o on the nickel RDE surface at a medium potential of $E = +844$ mV vs Ag/AgCl, displayed at $\omega = 4000$ rpm at 20°C.

likely a combination of the two. Figure 3.20 demonstrates how the heterogeneous rate constant k_2N (displayed as a natural logarithm) increases exponentially with potential when k_3N is held constant. The change of k_2N with potential is adequately described by the equation given below.

$$\ln(k_2 N) = -7.549 \times 10^{-11} E^4 + 2.604 \times 10^{-7} E^3 - 3.197 \times 10^{-4} E^2 + 0.174E - 44.231 \qquad (3.31)$$

where E represents the potential applied in mV vs Ag/AgCl. k_2N only surpasses k_3N at potentials above +844 mV vs Ag/AgCl. This supports the surface coverage plots, shown earlier, where the reduced site reached high concentrations at potentials greater than +844 mV. This demonstrates that the replenishment of the reduced site is a major limiting factor to the electrochemical oxidation of H_2O_2 on a nickel electrode. This slow reoxidation does not significantly curtail the current at potentials higher than +844 mV since even at +1036 mV all the available sites are not fully saturated.

The sharp increase in the k_2N constant at very low potentials may be attributed to a number of factors. One possibility is that at anodic potentials so close to the open circuit potential, there may be competition from a simultaneous reduction processes. The competition is such that the k_2N values displayed in Fig. 3.20 are actually a composition of the true oxidation, k_2N, less the simultaneous reduction. Consequently, at slightly higher potentials the reduction drops off markedly giving rise to the observed escalation in k_2N. The second interpretation is that at low potentials the number of available sites for H_2O_2 oxidation changes. The escalation in k_2N being attributed to the increase in N is implausible in the present model since both rate constants are ultimately linked to the N term and in the main model k_3N is forced to remain constant throughout the potential range. Therefore, changes in the number of available sites would have to be exactly matched by the k_3 term for k_3N to remain constant. However, when the k_3N term was allowed to vary and optimise, Model I and II, it was found that in the low current regions of low potentials k_3N fluctuated wildly, this may possibly be associated with changes in N. Model III fixes k_3N as constant. This does not allow N to change which may be a cause of the poor fit of the model to the data observed at low potentials commented in the preceding sections. Khudaish proposed that on platinum electrodes at potentials between +200 mV to +600 mV vs Ag/AgCl the number of binding sites increases rapidly making the electrode surface more catalytic [1,3]. These
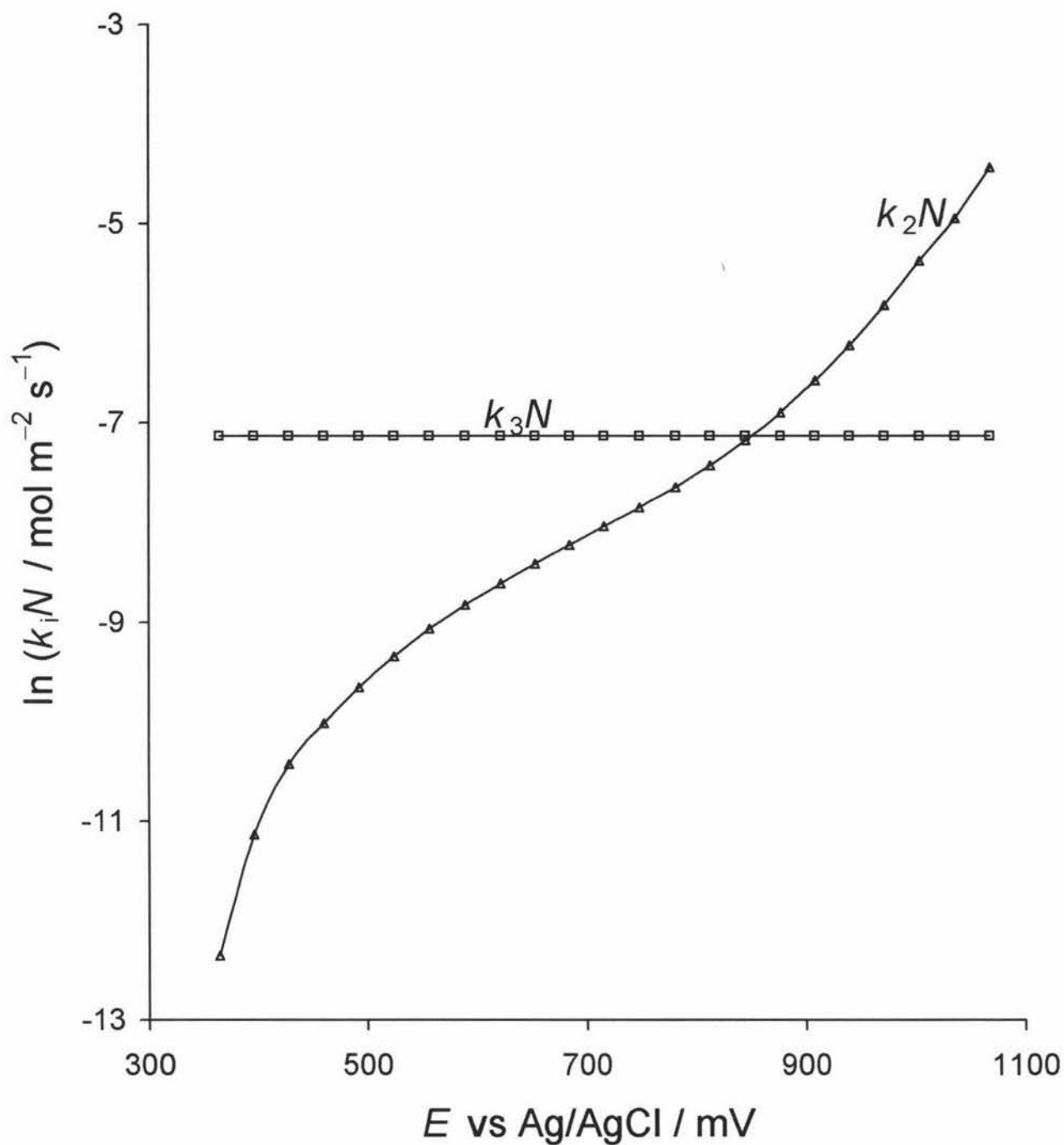
Fig. 3.20 A logarithmic plot of the heterogeneous rate constant k_2N ($\triangle$) and varying with potential, and k_3N ($\square$), invariant ($\ln(k_3N) = -7.13$ mol m^{-2} s^{-1}) at 20°C, as optimised by Model III.

findings indicate that the number of available sites on a nickel electrode may indeed change at low potentials.

3.7   Conclusions

Model III, based on a product inhibited Michaelis-Menten mechanism (Eqns. 3.6 to 3.9), when mass transport is taken into account, can reliably predict the response. There is effectively no inhibition caused by protonation of the H_2O_2 bound complex. The replenishment of the reduced site is slow and can be considered potential independent. The model performs adequately over the measured range of rotation rates (630 to 10000 rpm), $[H_2O_2]_{bulk}$ (0 to 130 mM) and potentials (+332 to +1100 mV). A minor failing of the model and its optimised parameters was that in very low current conditions, such as those found at anodic potentials close to the open circuit potential or at low $[H_2O_2]_{bulk}$, the predicted response, while of the correct magnitude, has a profile shape which is only observed in higher currents conditions. This deficiency has been attributed to an unavoidable consequence of the optimisation process. Contributing factors may arise from the k_3N term been affixed as constant where in the low potential region N may be changing.

Due to the relatively low currents, produced from the electrochemical oxidation of hydrogen peroxide on a nickel electrode, the surface H_2O_2 concentrations do not vary significantly from the $[H_2O_2]_{bulk}$. The current does not increase linearly with $[H_2O_2]_{bulk}$ but appears to approach a limiting current.

The rotation rate exerts more influence over the current observed at higher $[H_2O_2]_{bulk}$. Dioxygen, which competes with hydrogen peroxide for the available unbound nickel active sites, has a larger binding constant than that for hydrogen peroxide. The increase in current with rotation rate can be attributed to the more efficient removal of dioxygen, which reduces the competition for hydrogen peroxide binding.

The currents observed increase exponentially with potential. Increasing the potential speeds the electrochemical oxidation of H_2O_2, this is shown by k_2N increasing exponentially with potential. The reoxidation of the reduced site becomes a limiting factor at potentials greater than +844 mV since above this potential the reoxidation of the reduced site is significantly slower than the reduction of the H_2O_2 bound site.

CHAPTER 4

TEMPERATURE DEPENDENCE

4.1   Introduction

In the previous chapter a model, Model III, was developed to account for the electrochemical oxidation of hydrogen peroxide during conditions of E = +332 to +1100 mV vs Ag/AgCl, 0 – 130 mM $[H_2O_2]_{bulk}$ and at rotation rates of ω = 630, 1000, 1585, 2500, 4000, 6300, and 10000 rpm. This model was a modification of an earlier model developed by Khudaish [1-6] and incorporates product inhibited Michaelis-Menten mechanism and mass transport, to account for the saturation kinetics. The mechanism involved the reversible binding of H_2O_2 to the active nickel binding site.

$$Ni(OH)_2 + H_2O_2 \overset{K_1}{\rightleftharpoons} Ni(OH)_2 \cdot H_2O_2 \tag{3.6}$$

Followed by an internal electron transfer reducing the nickel binding site and simultaneously oxidising the bound H_2O_2.
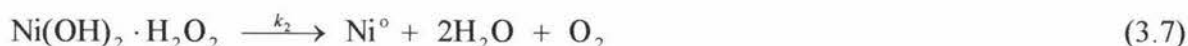
$$Ni(OH)_2 \cdot H_2O_2 \overset{k_2}{\longrightarrow} Ni^\circ + 2H_2O + O_2 \tag{3.7}$$

Followed by the regeneration of the active binding state to complete the catalytic cycle.

$$Ni^\circ + 2H_2O \overset{k_3}{\longrightarrow} Ni(OH)_2 + 2H^+ + 2e^- \tag{3.8}$$
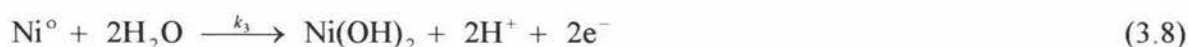
The mechanism is inhibited by the reversible binding of the product dioxygen to the active nickel-binding site.

$$Ni(OH)_2 + O_2 \overset{K_4}{\rightleftharpoons} Ni(OH)_2 \cdot O_2 \tag{3.9}$$

This mechanism yields a rate equation expressed in terms of the surface concentrations of solution species $[H_2O_2]$ and $[O_2]$.

$$j = \frac{k_2 N.K_1[H_2O_2]}{1 + K_4[O_2] + K_1[H_2O_2](1 + k_2/k_3)} \tag{3.24}$$

The parameters K_1, K_4, k_2N and k_2/k_3 were determined using SIMPLEX optimisation (Chapter 2, Section 2.6) of the positive root of the quadratic which includes mass transport features

$$0 = aj^2 + bj + c \tag{3.25}$$

where the polynomial coefficients are given by

$$a = K_4 k_D D_{O_2}^{-2/3} \omega^{-1/2} - K_1 k_D D_{H_2O_2}^{-2/3} \omega^{-1/2} \left(1 + k_2/k_3\right) \tag{3.26}$$

$$b = 1 + K_1[H_2O_2]_{bulk}\left(1 + k_2/k_3\right) + k_2 N K_1 k_D D_{H_2O_2}^{-2/3} \omega^{-1/2} \tag{3.27}$$

$$c = k_2 N K_1 [H_2O_2]_{bulk} \tag{3.28}$$

It was established that the three potential invariant parameters, K_1, K_4, and unexpectedly $k_3 N$, combined with the only potential dependent parameter, $k_2 N$, can satisfactorily account for the steady-state responses over the potential, $[H_2O_2]_{bulk}$, and rotation rate ranges.

In this chapter, the temperature dependence of the electrochemical oxidation of hydrogen peroxide on a nickel RDE is examined. The robustness of the model, developed previously for data collected at 20°C, to temperature variation is evaluated. The kinetic and thermodynamic parameters were optimised for data collected over the temperature range 5 – 35°C. The model includes mass transport considerations of both reactants and products. These will fluctuate with temperature since these are dependent on the diffusion coefficients and electrolyte viscosity.

4.2 Experimental Conditions

4.2.1 Reagents and Electrodes

All chemicals, reagents, electrodes and electrochemical equipment used during the experiments described in the proceeding sections are outlined in Chapter 2.

4.2.2 Electrochemical Methodology

The primary 0.1 mol L^{-1} pH 7.28 phosphate buffer was maintained at the desired temperature by a circulating water bath, pumping temperature-controlled water through the electrochemical cell water jacket. The temperature of the buffer solutions contained within the water jacket were monitored using a calibrated thermocouple placed at the same depth as the inverted face of the working electrode (Sections 2.2.1 and 2.2.8). Sampled Current Polarography was the only electrochemical technique employed in this chapter to study the

electrochemical oxidation of hydrogen peroxide (described in Section 2.5.2). Electrochemical steady-state measurements ($n_p = 20286$) were made over the potential range +332 mV to +1100 mV vs Ag/AgCl (at the stated temperature) in 32 mV steps; 0 – 130 mM [H$_2$O$_2$]$_{bulk}$; at rotation rates of 630, 1000, 1585, 2500, 4000, 6300, and 10000 rpm. This combination of potential, rotation rate and [H$_2$O$_2$]$_{bulk}$ was repeated at seven different temperatures 5°C, 10°C, 15°C, 20°C, 25°C, 30°C, and 35°C. Whilst all the experiments were conducted over the fore-mentioned conditions where appropriate, for reasons of brevity, only a representative selection of data are presented.

4.2.3 *Temperature Dependence of the Reference Electrode*

Not only does the temperature alter the rate of the reactions at the working electrode, but also the equilibrium occurring at the reference electrode [66, 67]. These changes in the reference electrode must be accounted for when analysing the observed data. The temperature dependence of the 3 M NaCl Ag/AgCl reference electrode can be established using the Nernst equation.

$$E_{Ag/AgCl,T} = E^\circ_{Ag/AgCl,T} - \frac{RT}{nF}\ln(m_{NaCl}\gamma_{\pm NaCl}) \tag{4.1}$$

Khudaish [1,4] determined the potentials for this reference electrode at each temperature, $E_{Ag/AgCl,T}$, using the formal potentials, $E^\circ_{Ag/AgCl,T}$, reported by Harned and Owen [68]. These potentials were reinforced by work from Harned and Ehlers, Bates and Bower, and Harned and Paxton [69–71], all reporting very similar values. Khudaish interpolated the mean activity coefficients, $\gamma_{\pm NaCl}$, using the cubic spline function of Mathcad, as a function of molality, m_{NaCl}, from data reported by Robinson for 5, 10, 15, 20, 30, and 35°C [72] and by Harned and Nims for 25°C [73]. Conversion from molarity, $\overline{m}$, (3 M NaCl at 25°C) to molality, m, was accomplished by using the lowest root for m in the quadratic

$$\overline{m} = m\rho - Am^2 \tag{4.2}$$

where ρ, the density of water in g L^{-1}, and the constant A as a function of temperature were taken from the literature [54 and 74 respectively]. The relevant data and calculated reference electrode potentials are tabulated at each temperature in Table 4.1.

$\dfrac{T}{°C}$	$\dfrac{E°_{Ag/AgCl} \text{ vs SHE}}{V}$	$\gamma_{\pm NaCl}$	$\dfrac{E_{Ag/AgCl} \text{ vs SHE}}{V}$
5	0.23392	0.687	0.2175
10	0.23126	0.702	0.2141
15	0.22847	0.714	0.2107
20	0.22551	0.724	0.2071
25	0.22239	0.731	0.2035
30	0.21912	0.736	0.1997
35	0.21563	0.738	0.1958

Table 4.1   Formal potentials, $E°_{Ag/AgCl}$, and reduction potentials, $E_{Ag/AgCl}$, for the Ag/AgCl 3M NaCl reference electrode ($m = 3.197$ mol kg^{-1}) as a function of temperature as calculated by Khudaish [1,4]. Activity coefficients were interpolated from published data [72, 73], and formal potentials from those reported by Harned and Owen [68].

4.2.4   *Viscosity, Density and Diffusion Coefficients*

The viscosity and density of the primary 0.100 mol L^{-1} pH 7.28 phosphate buffer as a function of temperature have been previously established by Khudaish [1,4]. These parameters, as well as the diffusion coefficients for the electroactive species, are integral to the understanding of the effect of temperature on the electrochemical oxidation of hydrogen peroxide in a phosphate electrolyte and hence, development of the model describing this process.

The values for the viscosity, density and diffusion coefficients, $D_{H_2O_2}$ and D_{O_2}, are tabulated at each temperature in Table 4.2. The diffusion coefficients at each temperature for H$_2$O$_2$ were optimised by Khudaish [1,4], whereas the diffusion coefficients for dioxygen were developed using the Stokes-Einstein equation.

$$D_i = \frac{kT}{6\pi\eta a_i} \tag{3.5}$$

where η is the absolute viscosity at each temperature (also included in Table 4.2) and using the reported diffusion coefficient of dioxygen at 25°C [64] to calculate the effective hydrodynamic radii which was $a_{O_2} = 1.23$ pm. This approach relies upon the assumption that the hydrodynamic radius for dioxygen does not alter with temperature.

The diffusion coefficient for H$_2$O$_2$, as optimised by Khudaish, is lower than other values reported in the literature [75-77] and does not follow an obvious trend over the temperature range studied. The diffusion coefficient increases almost linearly with temperature in the 20°C to 35°C range. Below 20°C no obvious trend is apparent, with $D_{H_2O_2}$ adopting a relatively constant value of *ca.* 0.6 × 10^{-9} m^2 s^{-1} in the 10°C to 20°C region and increasing to 0.7 × 10^{-9} m^2 s^{-1} at 5°C. These optimised coefficients do not obey the Stokes-Einstein equation (Eqn. 4.3) for a single fixed hydrodynamic radius. Khudaish attributed this lack of adherence to the Stokes-Einstein equation to changes in the effective hydrodynamic radii changing with temperature to reach a maximum of 325 pm at 20°C decreasing above and below this temperature (175 pm and 250 pm at 5°C and 35°C respectively).

T	$D_{H_2O_2} \times 10^9$	$D_{O_2} \times 10^9$	$\nu_{buffer} \times 10^6$	$\rho_{buffer} \times 10^{-3}$	$\eta_{buffer} \times 10^3$
°C	$m^2\,s^{-1}$	$m^2\,s^{-1}$	$m^2\,s^{-1}$	$kg\,m^{-3}$	$kg\,m^{-1}\,s^{-1}$
5	0.70	1.05	1.5456	1.01338	1.5663
10	0.60	1.24	1.3369	1.01299	1.3543
15	0.64	1.45	1.11662	1.01216	1.1804
20	0.63	1.67	1.0304	1.01135	1.0421
25	0.83	1.93	0.9082	1.00997[*]	0.9173
30	1.02	2.17	0.8242	1.00819	0.8310
35	1.17	2.45	0.7787	1.00660	0.7839

[*] value was verified at 25°C by an Anton Paar vibrating-tube density meter, where the measured value was $\rho_{25} = 1.00994 \times 10^{-3}\ kg\,m^{-3}$.

Table 4.2   Temperature variation of diffusion coefficients and properties (kinematic viscosity, density and absolute viscosity) of the 0.100 mol L^{-1} pH 7.28 primary phosphate buffer. The diffusion coefficients for H_2O_2 were optimised and those for O_2 were calculated using the Stokes-Einstein equation, by Khudaish [1,4].

4.3   Temperature Effects on Mass Transportation

To consider the effect of temperature on the mass transport Figs. 4.1 and 4.2 show the steady state current responses of a nickel rotating disc at +1036 mV vs Ag/AgCl over a range of $[H_2O_2]_{bulk}$ as a function of rotation rate, at the temperature extremes of 5°C and 35°C respectively. The current densities for both temperatures, as seen previously, increase with $[H_2O_2]_{bulk}$ to approach a limiting current. The figures show rotation rate dependence indicating the electrochemical oxidation of H_2O_2 is still diffusion limited at both temperature extremes. One of the most apparent features to be seen is that there is a four-fold increase in the response observed over the 5°C to 35°C temperature change.

The diffusion coefficient for H_2O_2, as optimised by Khudaish [1,4] listed in (Table 4.2), increases with temperature whilst the viscosity of the supporting electrolyte decreases. The combination of these two parameters will help to enhance the mass transport of H_2O_2 to the electrode surface. The diffusion coefficient for dioxygen also increases with temperature according to the Stokes-Einstein relationship. This combined with lower viscosity dictates that the mass transport of dioxygen away from the electrode surface will also be more rapid. Both of these mass transportation effects, one delivering more H_2O_2 to the electrode surface to bind and the other removing the inhibiting oxidation product, serve to increase the rate of electrochemical oxidation which is reflected in the observed response.

4.4   The Effect of Temperature on the Rate of Electrochemical Oxidation

A representative sample of steady-state responses for the electrochemical oxidation of hydrogen peroxide on a nickel electrode surface, is shown in Fig. 4.3. The rotation rate and potential dependence of this system was established in Chapter 3. This represents only $1/230^{th}$ of the data collected in this temperature study (seven rotation rates and 23 potentials over seven temperatures). Other data subsets at fixed rotation rates and potentials showed similar temperature dependence.

Inspection of Model III proposed in Chapter 4 suggest two equilibrium reactions (Eqns. 3.6 and 3.9) which could reasonably be expected to vary with temperature. Inspection of the rate equation for this model (Eqn. 3.24) permits the prediction that if K_1, describing the binding of H_2O_2 to the active nickel-binding site, should increase with temperature (i.e. be
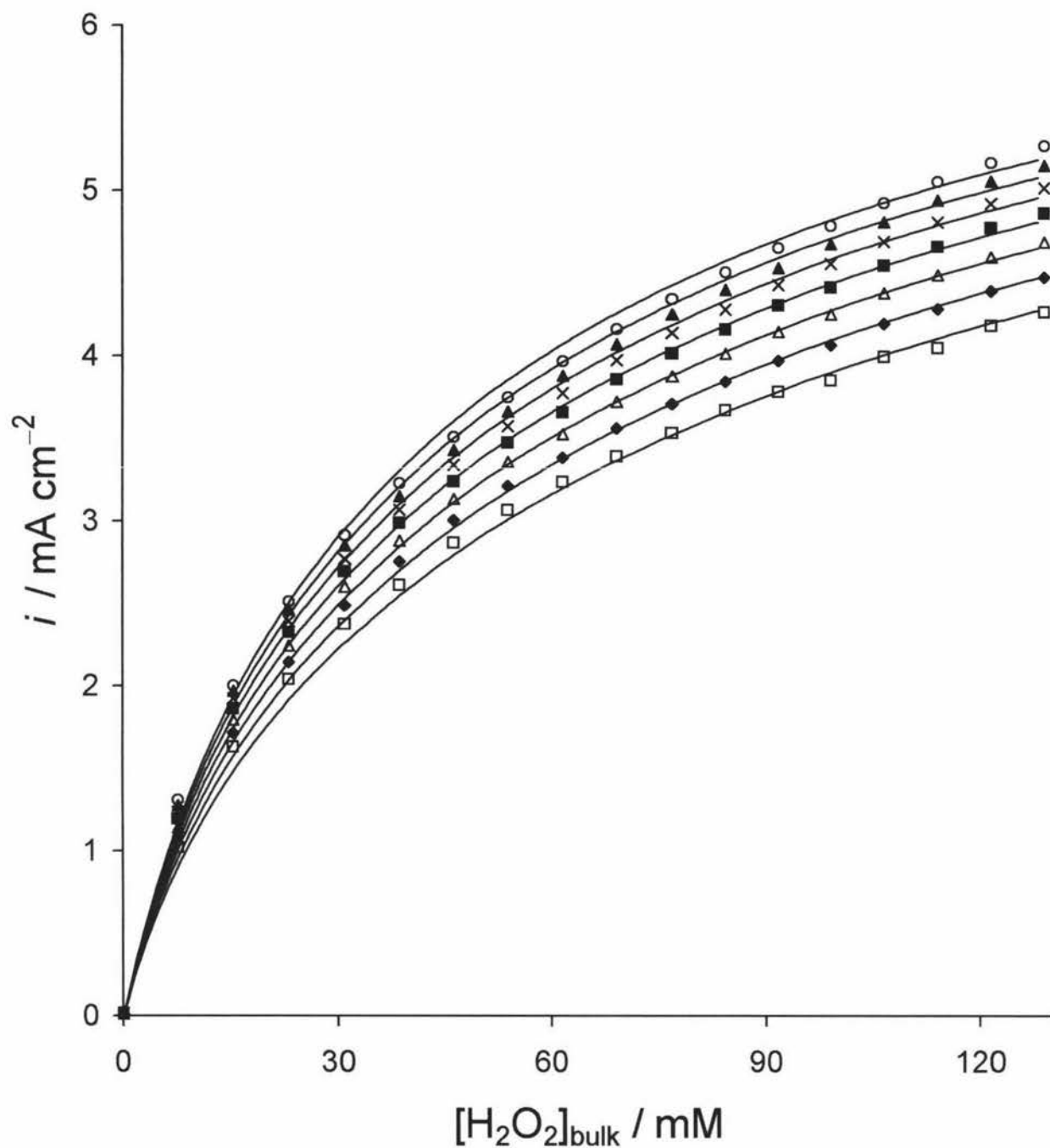
Fig. 4.1 Steady-state responses at +1036 mV vs Ag/AgCl as a function of $[H_2O_2]_{bulk}$ at 5°C for a range of rotation rates; □ 630, ◆ 1000, △ 1585, ■ 2500, × 4000, ▲ 6300, and ○ 10000 rpm. Smooth curves, (—), are the model predicted response using the parameters developed in this study.
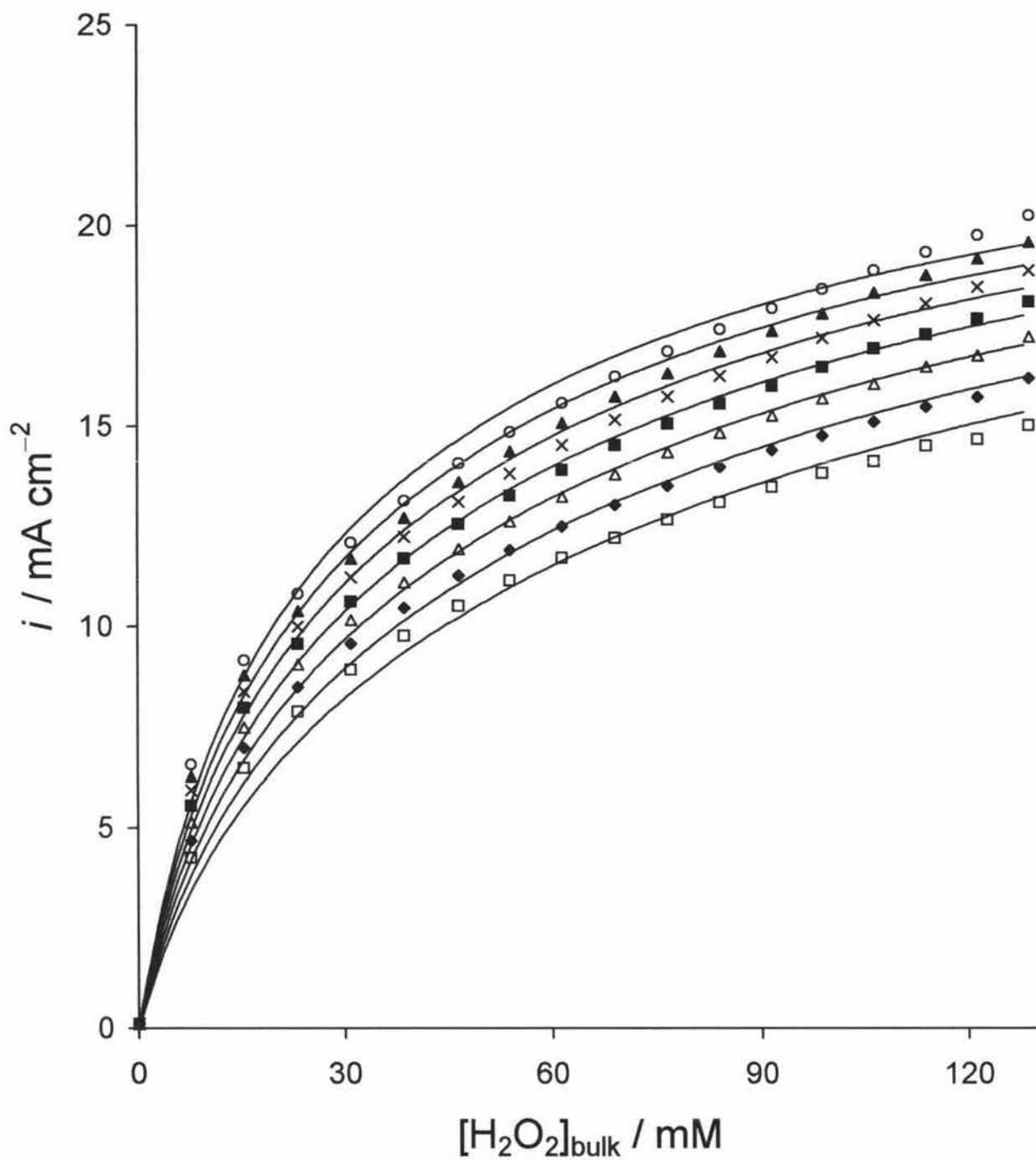
Fig. 4.2   Steady-state responses at +1036 mV vs Ag/AgCl as a function of $[H_2O_2]_{bulk}$ at 35°C for a range of rotation rates; □ 630, ◆ 1000, △ 1585, ■ 2500, × 4000, ▲ 6300, and ○ 10000 rpm. Smooth curves, (—), are the model predicted response using the parameters developed in this study.
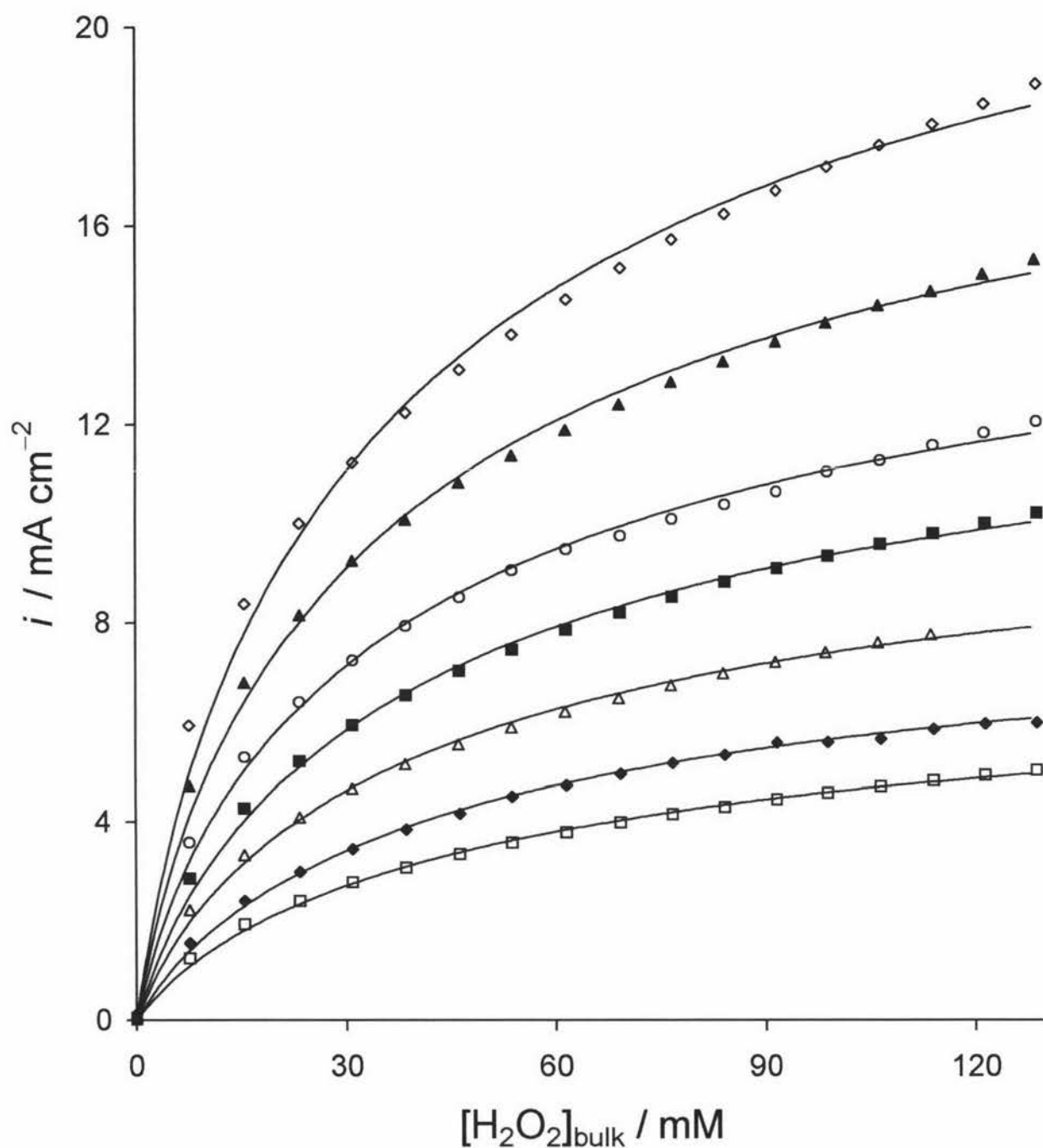
Fig. 4.3 Steady-state responses at 4000 rpm and +1036 mV vs Ag/AgCl as a function of $[H_2O_2]_{bulk}$ over a range of temperatures; □ 5°C, ◆ 10°C, △ 15°C, ■ 20°C, ○ 25°C, ▲ 30°C, and ◇ 35°C. Smooth solid curves are the model predicted response using the parameters developed in this study.

endothermic) then the rate would also increase. Whereas K_4, the inhibition by the complexation of dioxygen to the active nickel-binding site, might be expected to decrease (i.e. be exothermic). These changes in the equilibrium for the reaction Eqn. 3.6 will only have an effect when the electrode surface is not fully saturated and Fig. 4.3 indicates that the rate of saturation is faster at lower temperatures.

Another possibility, inferred from the rate equation, that may generate an increase in steady-state response at higher temperatures is that the nickel electrode's surface may become more catalytic. For example, through an increase in N, the number of active binding site available for the electrochemical oxidation of H_2O_2.

4.5   Changes in Optimised Parameters with Temperature.

The optimisation of the model parameters with temperature is an intrinsically more complicated procedure since it involves seven times the data used previously (n_p = 20286, c.f. Chapter 3 where n_p = 2898). The SIMPLEX optimisation must optimise the parameters, K_1, k_2N, K_4 and the k_2/k_3 ratio, over a similar data set to that involved in the optimisation explored in Chapter 3 (i.e. seven rotation rates from 630 to 10000 rpm and 23 potentials from +332 to +1100 mV all measured over the 0 to 130 mM $[H_2O_2]_{bulk}$ range) but for each of the seven temperatures. As before, the SIMPLEX program's goal seeking objective was to minimise the sum of residuals (r_s).

$$r_s = \Sigma(j - R_1) \tag{3.30}$$

and average deviation d_{av} given by

$$d_{av} = nF\sqrt{\frac{r_s}{n_p}} \tag{3.23}$$

In the first instance K_1, K_4 and k_3N were optimised as potential invariant parameters at each temperature, Table 4.3 lists these together with the sum of residuals and average deviation at each of the seven temperatures studied. Note that the 20°C data is that presented in Chapter 3. The sum of residuals, which indicates the quality of the model at each temperature, ranges from 8.78×10^{-9} mol m^{-2} s^{-1} at 5°C to 3.97×10^{-7} mol m^{-2} s^{-1} at 35°C. This is an expected trend since the relative differences between the model and the observed data would be magnified with the larger currents observed at high temperatures. Also, with

parameter	5°C	10°C	15°C	20°C	25°C	30°C	35°C
$\dfrac{K_1 \times 10^{-3}}{m^{-3}\ mol^{-1}}$	6.344	6.048	6.009	4.431	4.740	3.311	1.530
$\dfrac{K_4}{m^{-3}\ mol^{-1}}$	0.313	0.310	0.358	0.360	0.439	0.411	0.386
$\dfrac{k_3 N \times 10^{-3}}{mol\ m^{-2}\ s^{-1}}$	0.483	0.546	0.661	0.799	0.904	1.117	1.329
$\dfrac{r_s \times 10^{-7}}{mol\ m^{-2}\ s^{-1}}$	0.087	0.127	0.280	0.615	1.228	2.011	3.974
$\dfrac{d_{av}}{mA\ cm^{-2}}$	0.034	0.040	0.060	0.089	0.126	0.161	0.226

Table 4.3   Optimised potential invariant thermodynamic and rate parameters over the 5°C to 35°C temperature range together with the optimised sum of residuals r_s and average deviation calculated for each temperature (n_p = 2898).

higher currents, more dioxygen would be produced bubbles of which may adhere to the inverted electrode surface thus causing more dispersion in the data observed at these temperatures. However, Khudaish found this to not be a significant problem at the much higher rates on platinum [1,4]. The average deviation also increases with temperature from 0.034 to 0.226 mA cm^{-2} from 5°C to 35°C respectively. The fitness of the model to predict the expected responses over the entire temperature range can be examined by considering the sum of residuals over all the data points collected (n_p = 20286). This affords an r_s of 8.32 × 10^{-7} (mol m^{-2} s^{-1}) and a d_{av} of 0.124 mA cm^{-2} which is comparable to the fit obtained in the study of platinum [1,4].

Against the earlier predictions made from the rate equation (Eqn. 3.24), the equilibrium constant K_4, describing the inhibition by dioxygen binding to the active nickel-binding site, does not decrease with temperature but in fact exhibits a slight increase. K_4 changes from 0.313 to 0.386 m^3 mol^{-1} only a 23% rise over 5 to 35°C. This increase in the binding affinity of dioxygen would inhibit the binding of H$_2$O$_2$ and hence, inhibit the rate. However, the response observed, as shown in Fig. 4.3, increases with temperature. The change in K_4 with temperature suggests that the formation of the dioxygen bound nickel binding site complex is a slightly endothermic reaction. The enthalpy of formation, $\Delta H°$, of this complex was calculated employing the Arrhenius equation [78, 79].

$$\ln(K_i) = \frac{\Delta H°}{2.303R} \times \frac{1}{T} + const \tag{4.4}$$

as can be seen Fig. 4.4, a plot of the natural logarithm of K_4 versus the inverse of the temperature, renders a straight line the slope of which is

$$slope = \frac{\Delta H°}{2.303R} \tag{4.5}$$

This yields the enthalpy of formation of the dioxygen bound nickel complex of +16.5 kJ K^{-1} mol^{-1}, a slightly endothermic reaction.

The equilibrium constant K_1, describing the binding of H$_2$O$_2$ to the active nickel binding site to form a complex, surprisingly also goes against the earlier prediction made from the Model III rate equation that K_1 might increase with temperature. In contrast, K_1 decreases markedly with a four-fold decrease from 6.34 × 10^{-3} m^3 mol^{-1} to 1.53 × 10^{-3} m^3 mol^{-1} over
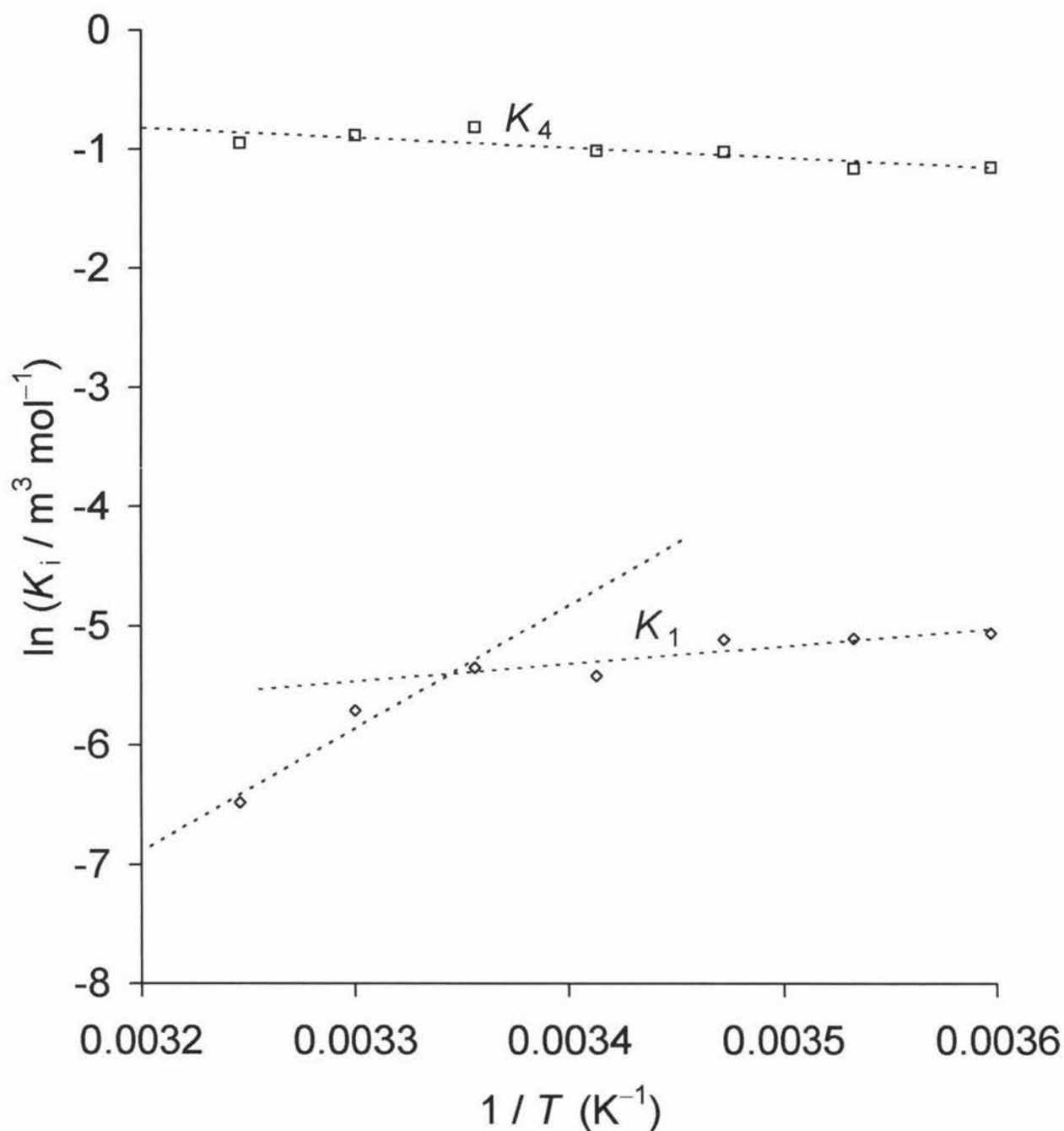
Fig. 4.4   A logarithmic plot of equilibrium constants K_1 (◇) and K_4 (□) versus the inverse on the temperature. Straight lines (----) are fitted to both sets of data. The K_1 data, however, is split into two regions; 5°C to 25°C and 25°C to 35°C.

the 5°C to 35°C range. Figure 4.4 shows that Eqn. 4.4 does not adequately describe the overall effect of temperature on K_1, however, between 5°C and 25°C K_1 does appear to exhibit a constant decrease giving an enthalpy of formation for the H_2O_2 bound nickel complex of -28.32 kJ K^{-1} mol^{-1}. Above 25°C, K_1 decreases markedly suggesting an enthalpy of formation of -198.33 kJ K^{-1} mol^{-1}, a much more exothermic complexing reaction.

Figures 4.5 and 4.6 show the surface coverage of electroactive nickel species on the electrode rotating at 4000 rpm displayed at +1036 mV of potential for 5°C and 35°C respectively. These figures show that the surface concentrations of nickel species at the temperature extremes follow the same trends versus the $[H_2O_2]_{bulk}$ as observed earlier at 20°C. The surface concentration of the active nickel binding site decreases exponentially with $[H_2O_2]_{bulk}$ with a coinciding build up of the nickel reduced site. Though the decline in Ni(OH)$_2$ is more severe at higher temperatures similarly the build up of Ni°. These are symptoms of higher rates of electrochemical oxidation of H_2O_2 as the reoxidation of the reduced site, k_3N, is a rate-limiting step. Significantly higher rates are observed at higher temperatures shown by the response observed in Fig. 4.3 and adequately reflected in the surface coverage trends of Figs. 4.5 and 4.6. One might expect the surface coverage of dioxygen bound nickel complexes to increase with the higher rate of H_2O_2 oxidation as more dioxygen would be produced. The slightly higher affinity for dioxygen that the active nickel-binding site exhibits would also contribute to the surface coverage. It is important to note that the relatively unusual profile of dioxygen species coverage with increasing $[H_2O_2]_{bulk}$, in which levels increase to a peak then slowly decline thereafter (discussed in Chapter 3 Section 3.6), remains unchanged. The dioxygen peak, which occurs at approximately 20 mM $[H_2O_2]_{bulk}$ at 35°C, decreases at lower temperatures and peaks later at 30 mM $[H_2O_2]_{bulk}$ at 5°C.

The surface coverage of the H_2O_2 bound nickel complex could be expected to decrease with temperature as the rate of oxidation of this site to its reduced state increases. The results of the optimisation show that as the temperature increases to 35°C from 5°C the extent of H_2O_2 binding decreases by a factor of four. Therefore, there is less H_2O_2 binding at 35°C, however, that which does is more rapidly oxidised. Both these factors contribute to the remarkable low surface coverage of this complex observed in Fig. 4.6 at 35°C. Should these
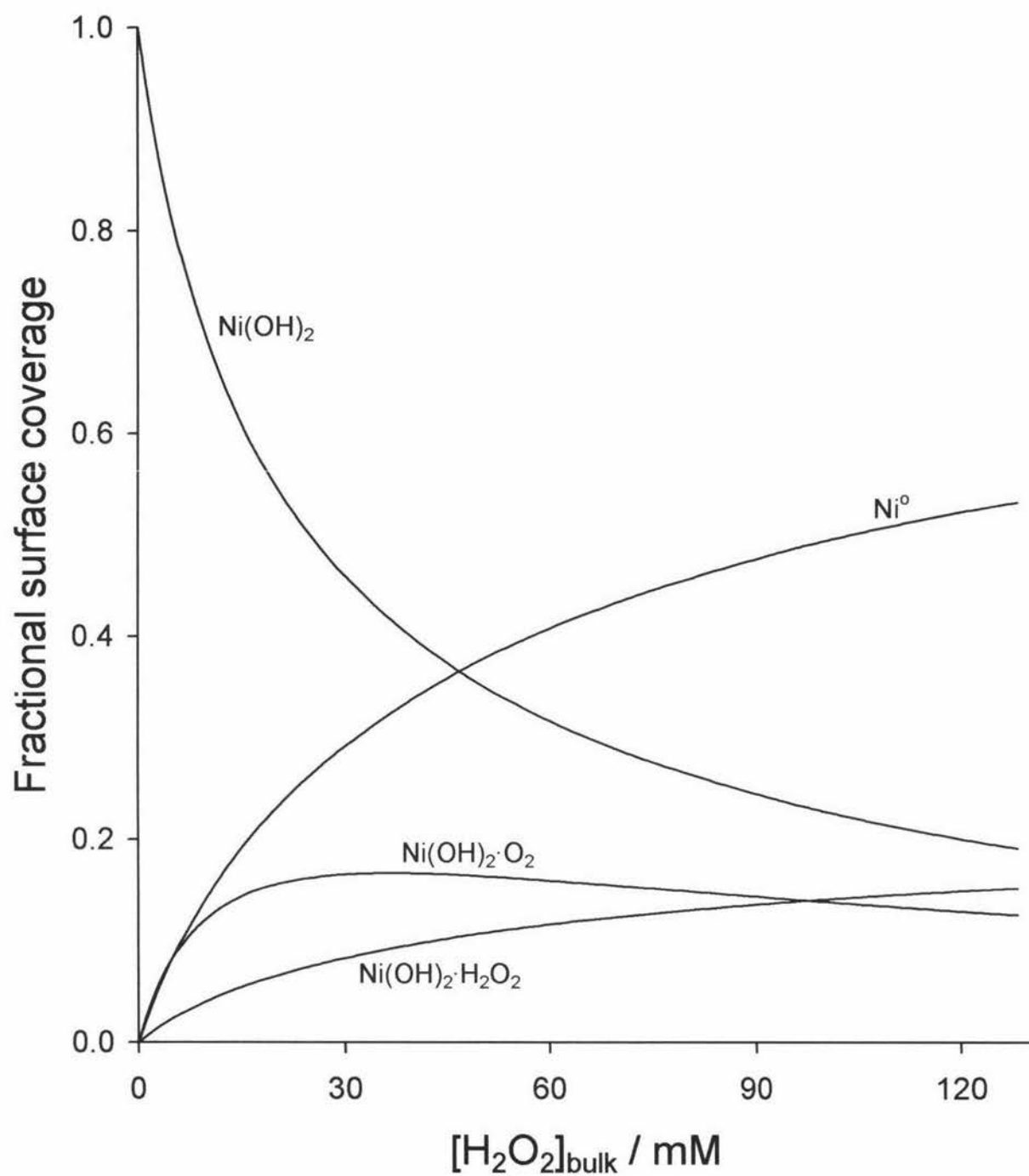
Fig. 4.5 The relative fractional surface coverage of the nickel species Ni(OH)$_2$, Ni(OH)$_2$·O$_2$, Ni(OH)$_2$·H$_2$O$_2$, and Ni^o on the nickel RDE surface at 5°C for E = +1036 mV vs Ag/AgCl and ω = 4000 rpm.
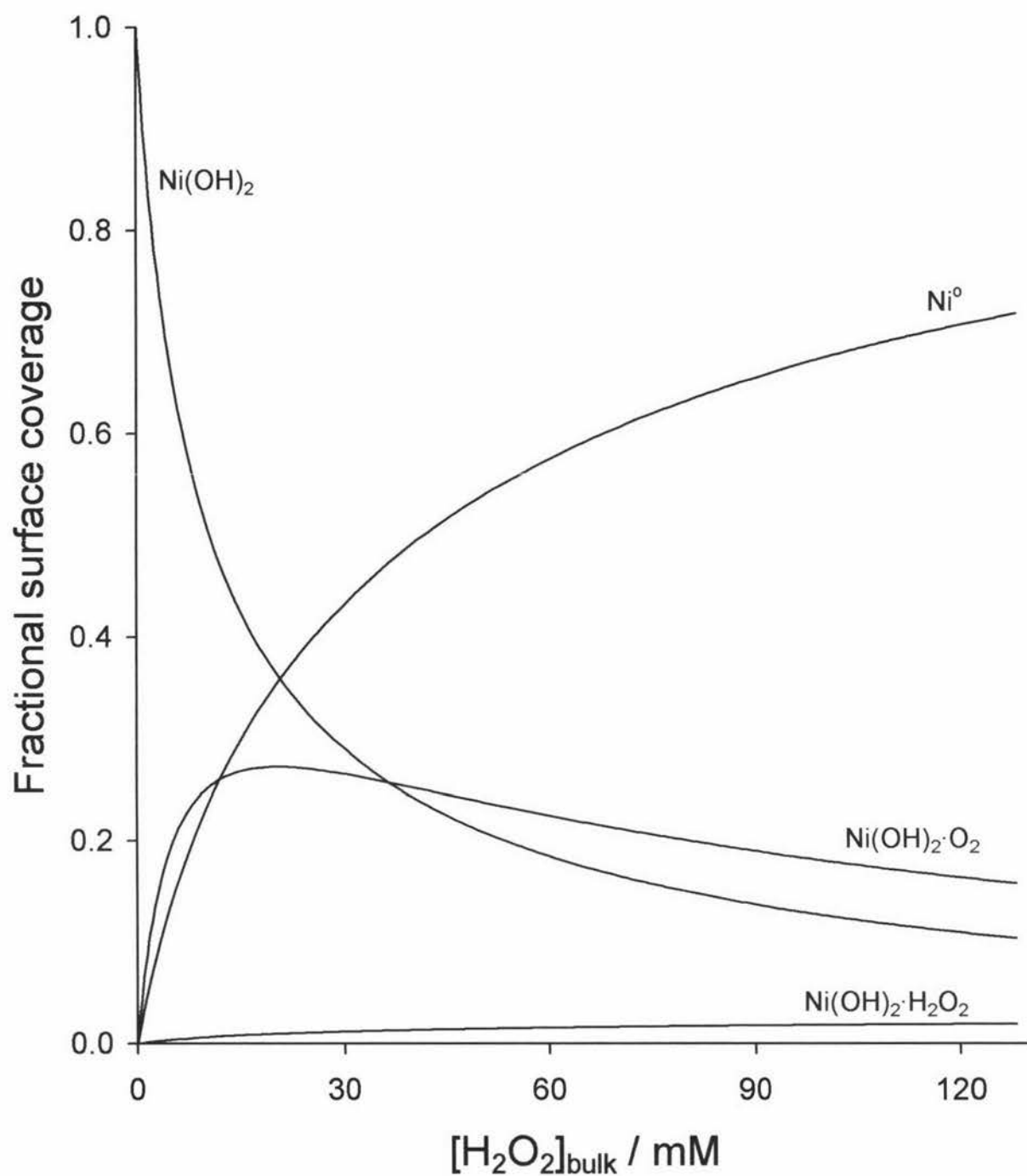
Fig. 4.6 The relative fractional surface coverage of the nickel species $Ni(OH)_2$, $Ni(OH)_2 \cdot O_2$, $Ni(OH)_2 \cdot H_2O_2$, and Ni^o on the nickel RDE surface at 35°C for $E = +1036$ mV vs Ag/AgCl and $\omega = 4000$ rpm.

trends continue it would suggest that at a temperature not much beyond 35°C the maximum rate for this system would be achieved. The rate of electrochemical oxidation would no longer be controlled by the rate that the bound H_2O_2 is oxidised. Both the rate at which the reduced site can be oxidised to liberate more active binding sites and the rate at which H_2O_2 can bind, would instead be the determining factors.

4.6   Variation of the Heterogeneous Rate Constants with Temperature

Changes in the equilibrium constants K_1 and K_4, as explained in the preceding section, could not alone account for the large increase in steady-state responses with temperature observed in Fig. 4.3. Indeed, the changes in both the equilibrium constants, brought about by increasing the temperature, effectively work to decrease the rate of electrochemical oxidation. The overall rate of reaction is given by

$$j = k_2 N \theta_{Ni(OH)_2 \cdot H_2O_2} \tag{4.6}$$

or

$$j = k_3 N \theta_{Ni^*} \tag{4.7}$$

Thus, the steady-state response observed is equal to the rate of the electrochemical oxidation of the bound H_2O_2 or to the rate of reoxidation of the reduced site liberating more active nickel binding sites for H_2O_2 complexation and oxidation. Therefore, as the other possibilities have been eliminated, the increase in rate observed must be caused by an increase in k_2, k_3, or indeed N (the number of available active nickel binding sites) with temperature. Moreover, these changes must account for the reduction in rate caused by an increase in inhibition from complexation of dioxygen and the reduction in H_2O_2 binding affinity.

Table 4.3 demonstrates how $k_3 N$, potential invariant in this Model III increases from 0.483×10^{-3} to 1.329×10^{-3} mol m^{-2} s^{-1} over 5°C to 35°C. However, despite the reduced site being reoxidised nearly 3 times faster at 35°C than at 5°C, Figs. 4.5 and 4.6 show that at +1036 mV vs Ag/AgCl there are 35% more reduced sites covering the surface at 35°C than at 5°C. This strongly indicates that at +1036 mV, at least, the electrochemical oxidation of complexed H_2O_2 shows a higher relative increase with temperature and is occurring much faster than the reoxidation of the reduced site. It is possible to perform an Arrhenius analysis

of both k_2N and k_3N on a nickel electrode. An Arrhenius analysis on k_3N was found to be unfeasible on platinum [1,4]. The slope of an Arrhenius plot may be related to the pseudo-activation energy of the process plotted using the logarithmic form of the Arrhenius equation [78, 79].

$$\ln(k_iN) = \frac{-E_{A,k_iN}}{R} \times \frac{1}{T} + \ln(A) \tag{4.8}$$

where E_{A,k_iN} is the pseudo-activation energy of the process k_iN. The pseudo-activation energy is so named since it encompasses changes to both k_i and N. These terms are inseparable. Therefore, an increase in the term with temperature may not be attributed solely to a faster electron transfer reaction that k_i describes but may also be attributed to an increase in N, the number of active nickel binding sites from a possible precursor site. Although k_3N is considered potential invariant for reasons discussed in Section 3.5.3, N may in fact be changing at lower potentials. Such a change in N may be described by

$$\text{Ni}_{PS} \underset{}{\overset{K_N}{\rightleftharpoons}} \text{Ni(OH)}_2 \tag{4.9}$$

where K_N is the equilibrium constant which may possibly be potential dependent, and Ni_{PS}, the nickel precursor site. N can therefore be written in terms of K_N and N^*, the total number of possible binding sites per m^2

$$N = \frac{N^*K_N}{1+K_N} \tag{4.10}$$

If it is assumed K_N obeys the Van't Hoff Equation [10, 80] at each potential and assuming that $K_N \ll 1$ then

$$N_E = N^*_E \exp\left(\frac{-\Delta H^\circ_{N,E}}{RT}\right) \tag{4.11}$$

where E denotes a fixed potential and $\Delta H^\circ_{N,E}$ is the enthalpy of formation of the binding site.

The Arrhenius expression solely for k_i at a fixed potential may be written

$$k_{i,E} = A_{k_i,E} \exp\left(\frac{-E_{A,k_i,E}}{RT}\right) \tag{4.12}$$

Therefore the pseudo-activation energy, $E_{A,k_iN,E}$ for the reaction described by k_iN now at a given potential E, may be a combination of the activation energy of the electron transfer process and the enthalpy of formation of the binding site. The enthalpy of formation of the binding site, $\Delta H^{\circ}_{N,E}$, may be either exothermic or endothermic.

A combination of the Eqns. 4.11 and 4.12 affords the expected temperature variation of k_iN at a fixed potential

$$\ln(k_iN) = \frac{-(E_{A,k_i,E} + \Delta H^{\circ}_{N,E})}{R} \times \frac{1}{T} + \ln(A_{k_i,E}N^*_E) \tag{4.13}$$

Figure 4.7 shows an Arrhenius plot for k_3N. The potential is irrelevant since k_3N is considered potential invariant. A straight line plotted through this data yields a relatively low pseudo-activation energy of $E_{A,k_3N} = +24.3 \pm 0.8$ kJ mol^{-1}.

The potential variance of k_2N presents a more complex situation. Figure 4.8 shows the change in k_2N with temperature and potential. The k_2N data shown in this plot do not have a common potential vs SHE since the potentials were interpolated for a series of set potentials vs Ag/AgCl at each temperature using the data in Table 4.1. k_2N is varying with potential in a similar manner at each temperature to that which was reported in the previous chapter. At +1036 mV vs Ag/AgCl there is a 30 fold increase in the rate of oxidation of bound H_2O_2 from 5°C to 35°C.

The Arrhenius plots shown in Fig. 4.9 are from a series of k_2N values interpolated from the data given in Fig. 4.8 for a range of potentials vs SHE (+550 mV to +1300 mV) using the relationship between $E_{Ag/AgCl}$ and temperature given in Table 4.1. For clarity, this plot only includes the potentials every 50 mV from +550 mV to +1250 mV vs SHE. However, at low potentials, close to the open circuit potentials, some degree of variation is shown which suggests that the number of available active nickel binding sites is changing with temperature.

Pseudo-activation energies, $E_{A,k_2N,E}$, obtained from the Arrhenius slopes are plotted in Fig. 4.10. This figure shows how initially the pseudo-activation energy decreases markedly with potential. This can be attributed to the decrease in the endothermic formation of
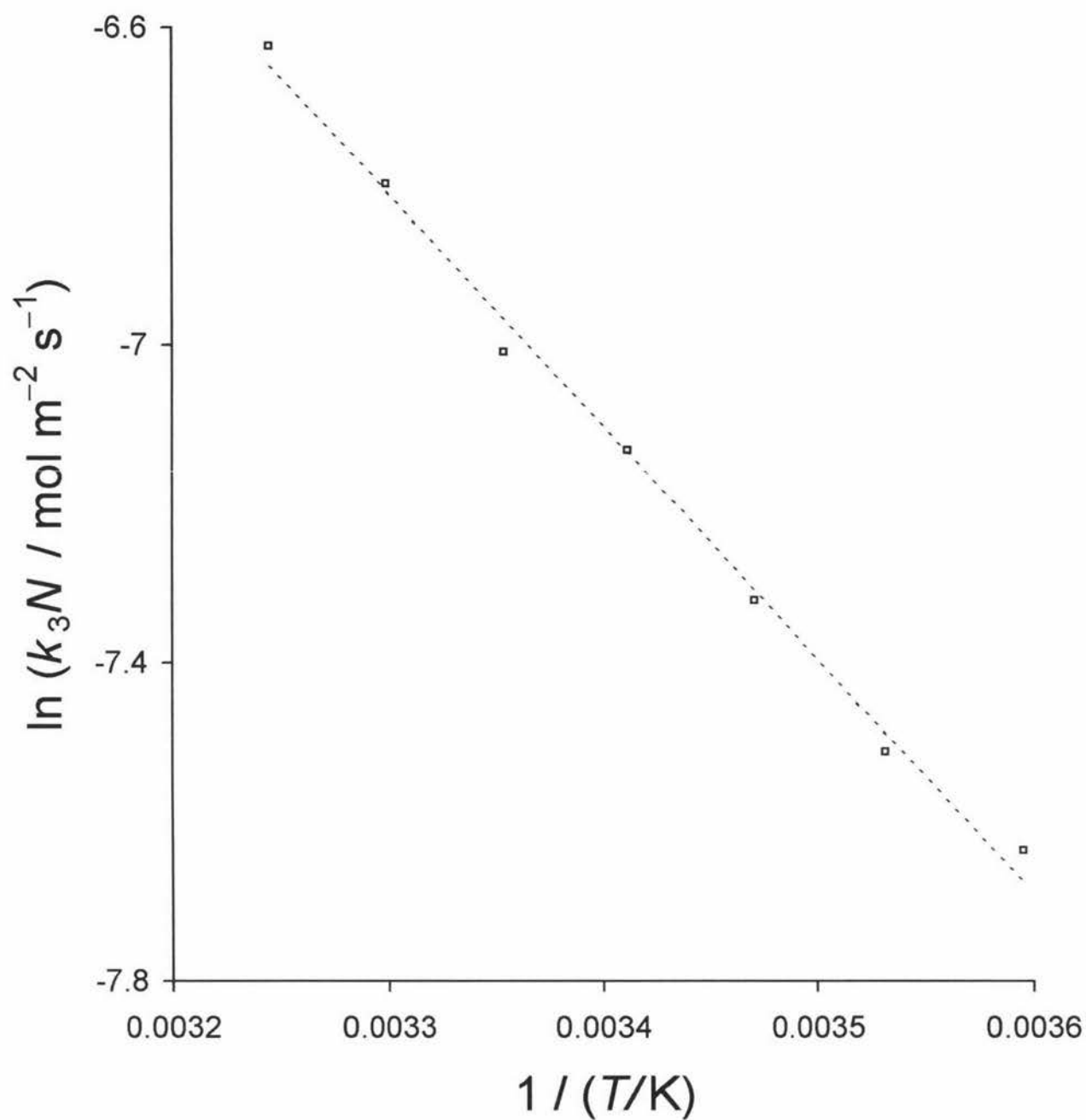
Fig. 4.7 An Arrhenius plot showing the effect of temperature on the rate constant for the reoxidation of the reduced binding site, k_3N.
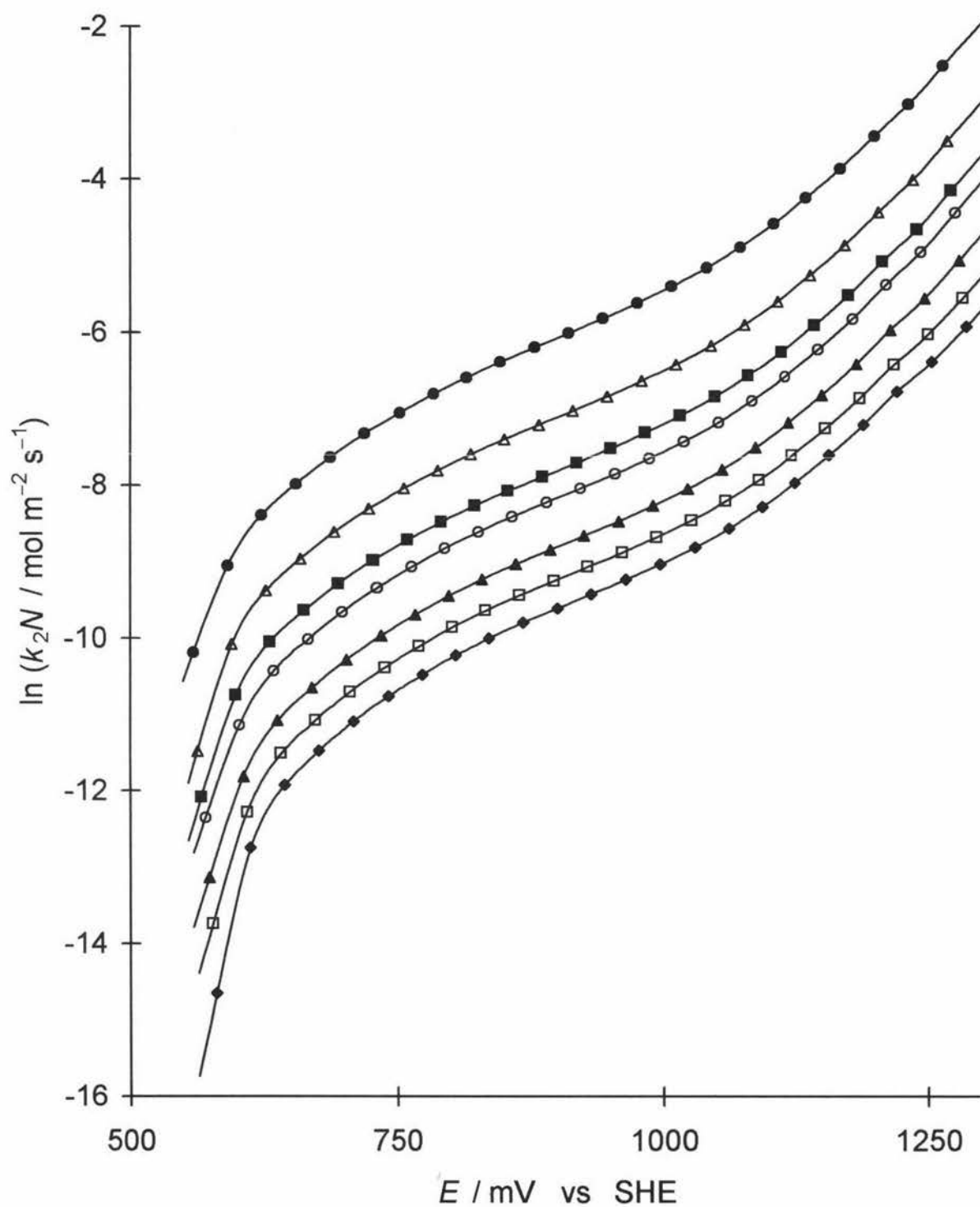
Fig. 4.8 A logarithmic plot of the optimised parameter k_2N, the rate constant for the reduction of the H_2O_2/nickel binding site complex, as a function of potential for each temperature; ♦ 5°C, □ 10°C, ▲ 15°C, ○ 20°C, ■ 25°C, △ 30°C, and ●35°C.
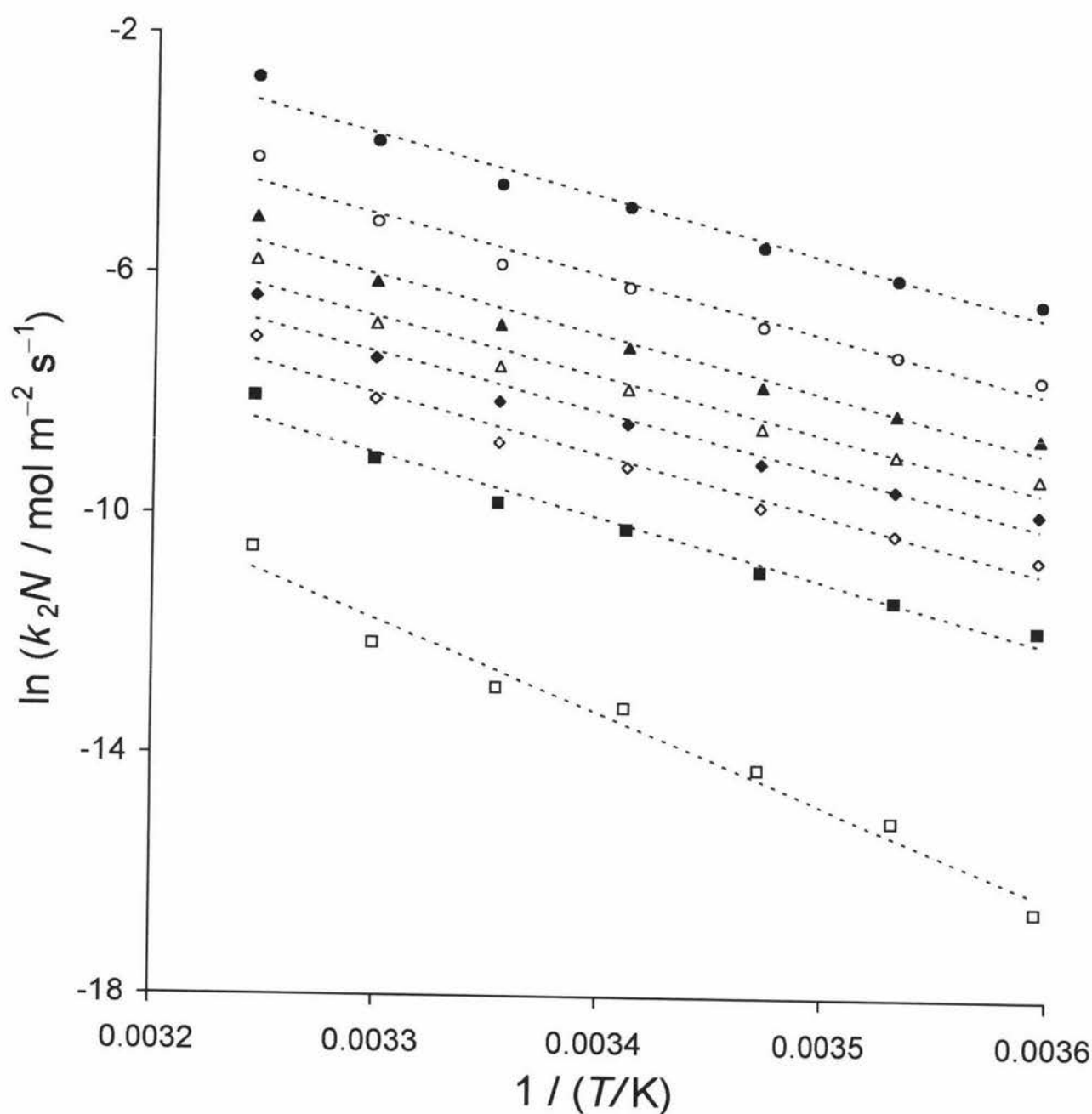
Fig. 4.9 An Arrhenius plot showing the effect of temperature on the rate constant for the reduction of the H_2O_2/nickel binding site complex, k_2N, for a selection of potentials vs SHE. Potentials were interpolated from potentials vs Ag/AgCl at each temperature using the data in Table 4.2; □ +550, ■ +650, ◇ +750, ◆ +850, △ +950, ▲ +1050, ○ +1150, and ● +1250 mV vs SHE.
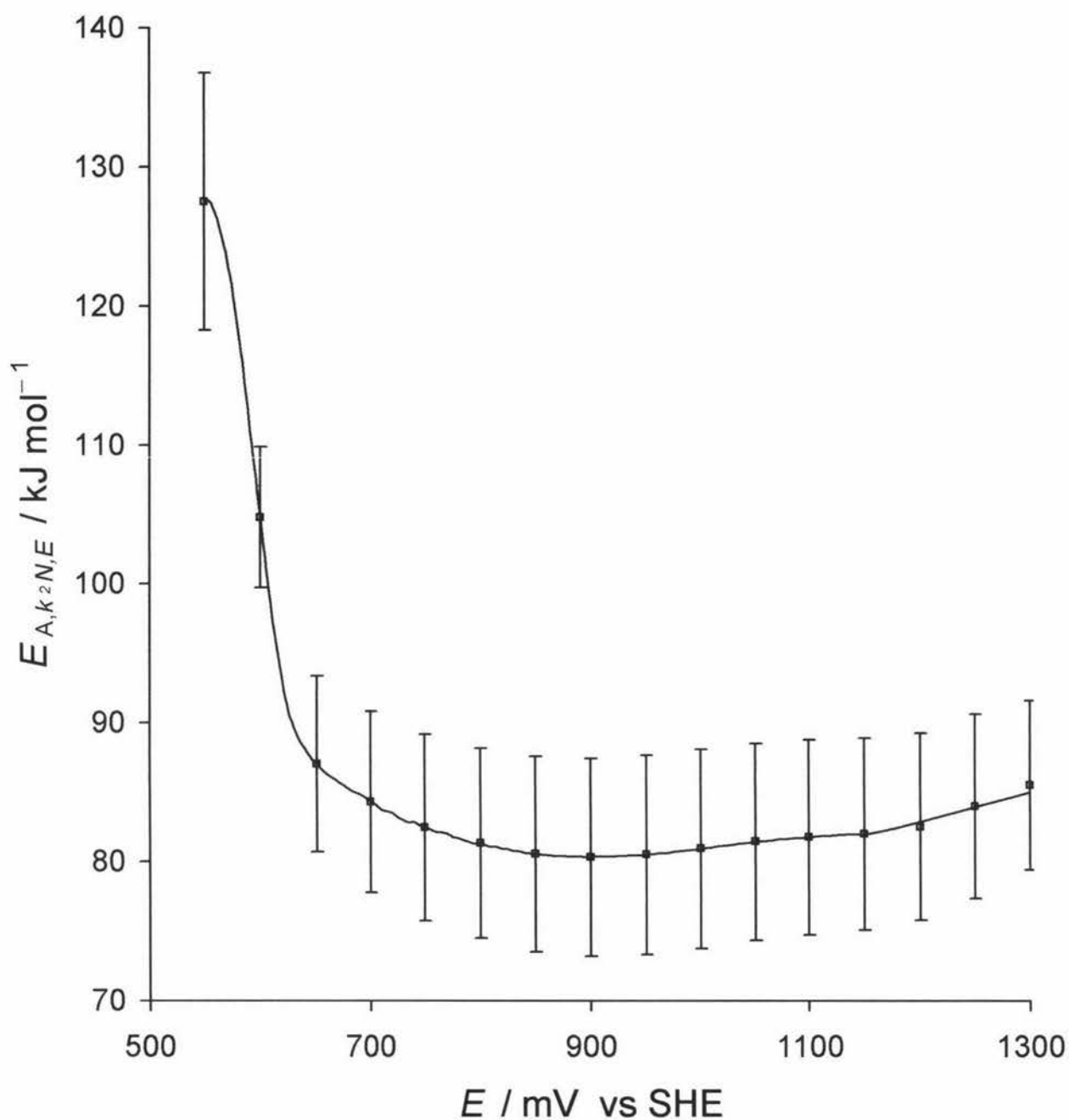
Fig. 4.10 A plot of the pseudo-activation energy, $E_{A,K_2N,E}$, for the kinetic parameter k_2N as a function of potential (E vs SHE). $E_{A,K_2N,E}$ values determined from the Arrhenius regression slopes and error bars created from the uncertainty in these slopes.

binding sites with potential. Above +700 mV vs SHE the pseudo-activation energy appears to adopt a constant value within the margins of error of about 82 ± 7 kJ mol^{-1}. This can be predominately attributed to the activation energy required to oxidise bound H_2O_2 (k_2) as at higher potentials the change in N with potential is insignificant.

Although the process of electrochemical oxidation of bound H_2O_2 has significantly higher activation energy than that of the reoxidation of the reduced site, the rate of the process is significantly faster. This has already been alluded to previously as an explanation for the backlog of reduced site remaining on the surface of the electrode. The pseudo-activation energy established by Khudaish [1,4] for the analogous electrochemical oxidation of bound H_2O_2 on a platinum electrode adopts a constant value between $E_{A,k_2N,E}$ 40 kJ mol^{-1} and 45 kJ mol^{-1} at higher potentials, this is approximately half that observed on nickel electrodes. However, one can not overlook the extremely slow rate of reoxidation of the reduced site back to the active nickel-binding site, k_3, which, especially at high temperatures, is a considerable hindrance to the overall rate.

The value established by Khudaish is comparable to the $\Delta H^{\ddagger}$ quoted by Koshino, Funahashi and Takagi [31] for the proposed H_2O_2 decomposition on a bis(1,4,7-triazacyclononane)-nickel(III) complex via a perhydroxyl ion (HO_2^-) intermediate. Here a rate constant at 298.2 K of 6.15×10^{-6} dm^3 mol^{-1} s^{-1} and a $\Delta H^{\ddagger} = 46.9$ kJ mol^{-1} was established. Koshino, Funahashi and Takagi also illustrate that it is not unexpected that a different metal or metal complex catalyst should yield different rates and enthalpies for analogous reactions. Since the identical reaction on a bis(1,4,7-trithiacyclononane)iron(III) complex had a different rate constant of 298.2 K of 2.63×10^{-9} dm^3 mol^{-1} s^{-1} with a $\Delta H^{\ddagger} = 26.7$ kJ mol^{-1}.

4.7   Conclusions

The model developed in Chapter 3 was indeed robust and model predictions, using the temperature optimised parameters, were found to satisfactorily match the observed steady-state responses over the wide range of temperatures studied without further modification. These observed steady-state responses increased quite markedly with temperature. This was partially attributable to enhanced mass transport at higher

temperatures of reactants to, and inhibiting products away from, the electrode surface brought about by increasing diffusion coefficients and decreasing buffer viscosity.

In depth analysis of the observed data in terms of the model parameters, optimised at each temperature, allowed the examination of the temperature variation of each reaction in the proposed model and how each individually influences the overall response. The reversible binding of H_2O_2 to the free nickel active site, K_1, was found to be an exothermic reaction. The reversible binding of the inhibiting by-product dioxygen to the free nickel active site was found to be slightly endothermic. This indicates that at higher temperatures more binding sites become blocked by dioxygen and with lower nickel active site affinity to bind H_2O_2. Therefore, less H_2O_2 will bind causing a coinciding decrease in the rate. Both these findings were unexpected (since the rate, as eluded earlier, in fact increases with temperature) and unprecedented, as Khudaish found the analogous reactions on a platinum electrode to be temperature invariant i.e. isothermic [1,4].

The oxidation of bound H_2O_2 and simultaneous reduction of the nickel-binding site, k_2N, is an endothermic reaction. So is the reoxidation of the reduced nickel site, k_3N. The rate of the latter reaction increased significantly, with a nearly three fold increase over the 5 to 35°C temperature range, whilst the rate of the former reaction increased even more markedly, by nearly 30 times over a similar range, causing a build up to 35% more reduced sites on the electrode surface. k_3N has a relatively low and k_2N a high pseudo-activation energy. The effect of higher temperatures on these two reactions dictates that bound H_2O_2 is oxidised significantly faster and more reduced sites are reoxidised liberating free binding sites for subsequent H_2O_2 binding and oxidation. These changes suitably account for the large increase in the rate observed while also counteracting the rate reducing effects of K_1 and K_4.

CHAPTER 5

THE EFFECT OF BUFFER COMPOSITION: pH AND CONCENTRATION

5.1   Introduction

In previous chapters the electrochemical oxidation of hydrogen peroxide on a nickel electrode was studied as a function of $[H_2O_2]_{bulk}$, rotation rate and potential (Chapter 3), and temperature (Chapter 4). A mechanism, Model III, was developed to mathematically account for the steady-state responses observed under these conditions. All experiments were conducted within a common pH 7.28 0.100 mol L^{-1} phosphate buffer. This specific buffer condition was employed in this study, due to its extensive use in enzyme-based biosensor devices [1-6,10-17].

In this chapter, the effect of the phosphate buffer concentration and pH may have on the electrochemical oxidation of hydrogen peroxide on nickel electrodes was studied. This investigation was undertaken to ascertain if the phosphate buffer has a more influential role in the electrochemical mechanism than merely acting as a supporting electrolyte. Khudaish found that the number of binding sites changed in proportion to the concentration of the species $H_2PO_4^-$, which was in turn controlled by both pH and phosphate buffer concentration.

5.2   Experimental Conditions

5.2.1   Reagents and Electrodes

All chemicals, reagents, electrodes and electrochemical equipment used during the experiments described in the following sections are outlined in Chapter 2. The preparation of phosphate buffer solutions of varying concentrations maintained at a constant pH and phosphate buffer solutions of varying pH maintained at a constant concentration are given in Sections 2.4.1 and 2.4.2.

5.2.2 Electrochemical Methodology

In this chapter, Sampled Current Polarography, SCP, was again employed to study the electrochemical oxidation of hydrogen peroxide (described in Section 2.5.2). The electrochemical steady-state measurements (n_p = 2898) were made at 20°C over the regimen for potential (+332 to +1100 mV vs Ag/AgCl), bulk H_2O_2 concentration (0 - 130 mM) and rotation rate (630 – 10000 rpm) established in the previous Chapters 3 and 4. A total of 40572 measurements were made for two series of buffer compositions. In the first series (n_p = 23184), buffers with the phosphate concentrations, 25, 50, 75, 100, 150, and 200 mM $[PO_4^{-3}]_{tot}$, maintained at *ca.* pH 7.28 were examined. In the second series (n_p = 17388), buffers of varying pH 4.07, 5.35, 6.09, 7.28, 8.20, 9.14, 10.28, and 11.51 all maintained at a constant 100 mM phosphate concentration were investigated.

5.3 Change in Steady-State Response with Phosphate Concentration

Figure 5.1 shows the steady-state responses for 127 mM $[H_2O_2]_{bulk}$ at each phosphate buffer concentration, 25, 50, 75, 100, 150, 200 mM, maintained at pH 7.23 – 7.32, over the potential range +332 to +1100 mV vs Ag/AgCl for a selection of data at 4000 rpm. At low potentials below +750 mV there is minimal phosphate dependence. However, in the high potential range, above +876 mV vs Ag/AgCl, the response has a clear dependence on the phosphate buffer concentration. The steady-state response, beyond +876 mV, increases markedly with phosphate concentration. With the response for 200 mM phosphate being 50% higher than 25 mM phosphate, at +876 mV. This rises to 150%, at 1100 mV. However, the relative increase with the concentration is diminished at higher concentrations. For example, an increase from 150 to 200 mM elicits a minimal change in response. The relationship between the limiting current density, i_L, and the electrolyte viscosity is given by the Levich equation

$$i_L = 0.62nFD^{2/3}v^{-1/6}\omega^{1/2}c_{bulk} \tag{2.4}$$

The likely small viscosity variation, from 25 mM to 200 mM, will have a minimal (to the sixth root) influence over the response observed. One might also expect the effect to be independent of the potential and show a consistent change with viscosity (over the potential
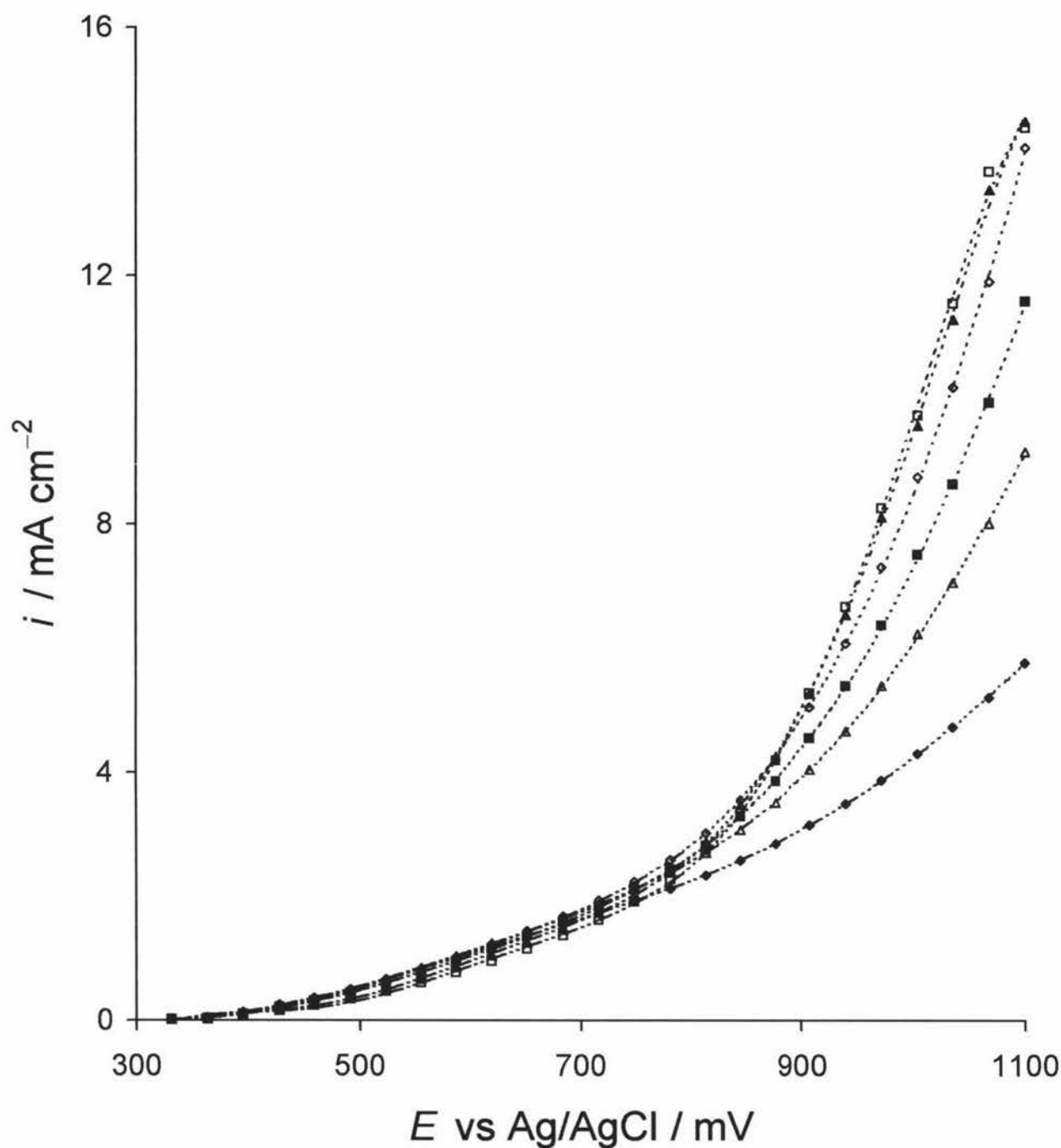
Fig. 5.1 Selected steady-state responses at 130 mM [H$_2$O$_2$]$_{bulk}$, ω = 4000 rpm at 20°C as a function of E vs Ag/AgCl for six different phosphate buffers of ($\blacklozenge$) 25 , ($\triangle$) 50, ($\blacksquare$) 75, ($\diamond$) 100, ($\blacktriangle$) 150, ($\square$) 200 mM concentration maintained at *ca.* pH 7.28. Smooth curves are trends not synthetic curves generated by Model III or any other model.

range) which is not observed. Therefore, the change in the steady-state responses with buffer concentration can not be attributed to increasing electrolyte viscosity. Once this physical parameter has been discounted, this only leaves only one option - that a phosphate species, general formula $H_xPO_4^{(x-3)}$ with x as yet unidentified, is involved in the mechanism of electrochemical oxidation of hydrogen peroxide on a nickel electrode. This is not an unexpected proposition since Khudaish found similar evidence for phosphate involvement where $H_2PO_4^-$ was the species responsible on platinum electrodes [1,5]. Hydrogen peroxide oxidising nickel tetraazamacrocyclic complexes incorporated into carbon paste electrode, were found to co-ordinate both HPO_4^- and $H_2PO_4^{-2}$ strongly [32]. The H_2O_2 oxidation on self-assembled monolayers (SAM) of Nickel (II) macrocyclic complexes in pH 2.7 Na_2SO_4 and $NaNO_3$ solutions was found to be influenced by buffer anions. This dependence of the rate of oxidation on $[NO_3^-]$ was attributed to stabilisation of the intermediates in the rate-determining step [50, 51]. Though the mechanism of involvement is not available in the nickel/H_2O_2 system it does highlight that solvent effects are possible.

Inspection of high, medium and low regions in detail (Figs. 5.2, 5.3, and 5.4 at +1036 mV, +780 mV and +364 mV vs Ag/AgCl respectively) as a function of $[H_2O_2]_{bulk}$ reveals a complex phosphate dependence which varies with potential. As discussed earlier, at high potentials, Fig. 5.1, the steady-state response increases with phosphate concentration. However, the relative increase with the concentration is diminished at the high phosphate concentrations. For example, changing from 25 to 50 mM phosphate concentration results in ca. 50% increase in rate, whereas, changing from 150 to 200 mM only elicits a 5% increase in rate.

In contrast, at the lowest potentials, shown in Fig. 5.3, whilst there is some data fluctuation at these low rates, there is an inversion of the buffer concentration dependence found at high potentials. At +364 mV vs Ag/AgCl the trend shows a uniform increase in steady-state response as the buffer phosphate concentration is decreased from 200 to 25 mM.

At the medium potentials, displayed in Fig. 5.4, although the responses at each phosphate concentration are very similar, a trend is evident. There appears to be a combination of both the high and low potential trends. At this, +780 mV vs Ag/AgCl, potential the phosphate concentration which produced the highest steady-state response was in the middle of the
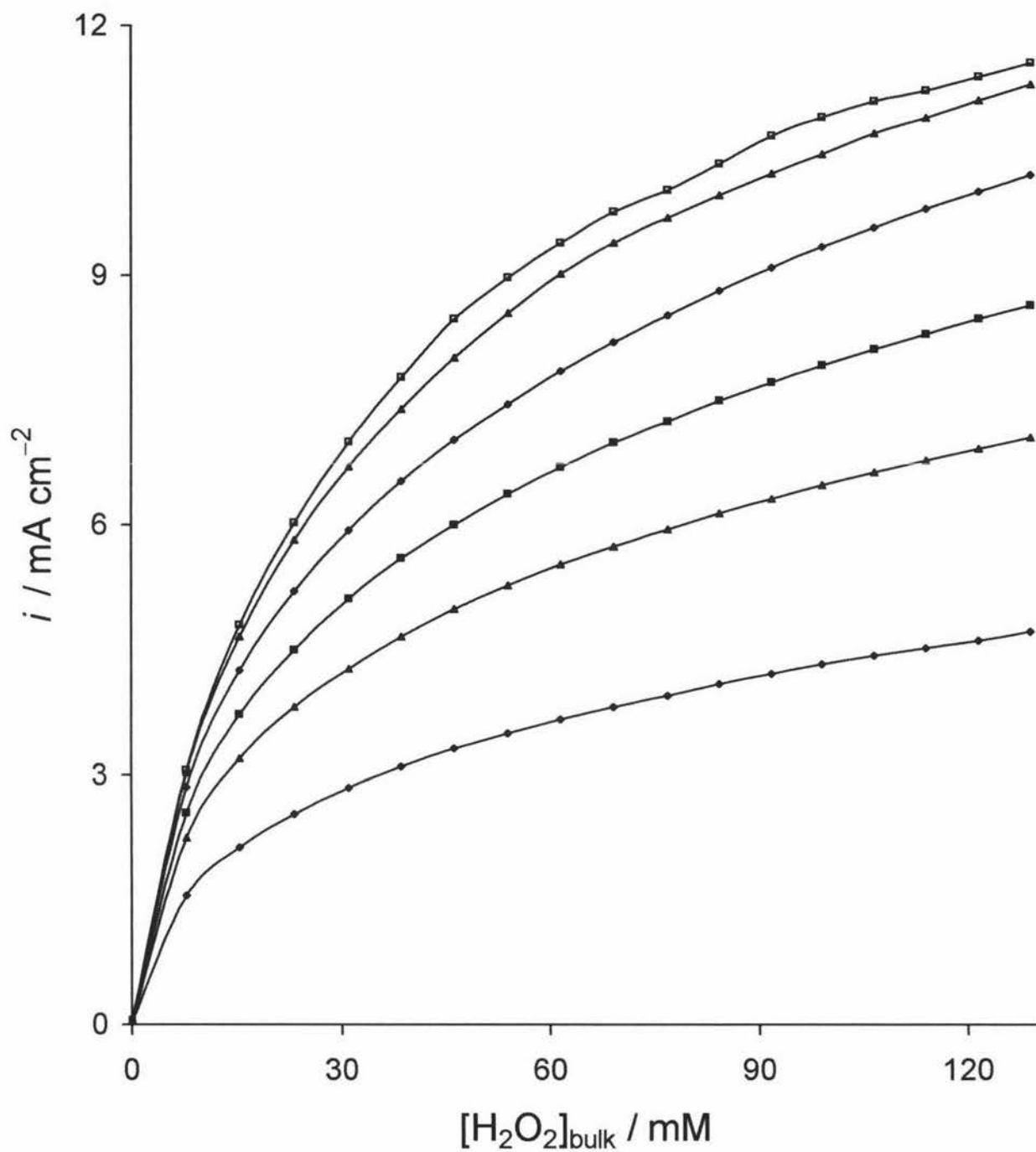
Fig. 5.2 Steady-state responses at E = +1036 mV vs Ag/AgCl, ω = 4000 rpm at 20°C as a function of $[H_2O_2]_{bulk}$ in six different phosphate buffers of ($\blacklozenge$) 25 , ($\triangle$) 50, ($\blacksquare$) 75, ($\diamond$) 100, ($\blacktriangle$) 150, ($\square$) 200 mM concentration maintained at *ca.* pH 7.28. Smooth curves are trends not synthetic curves generated by Model III or any other model.
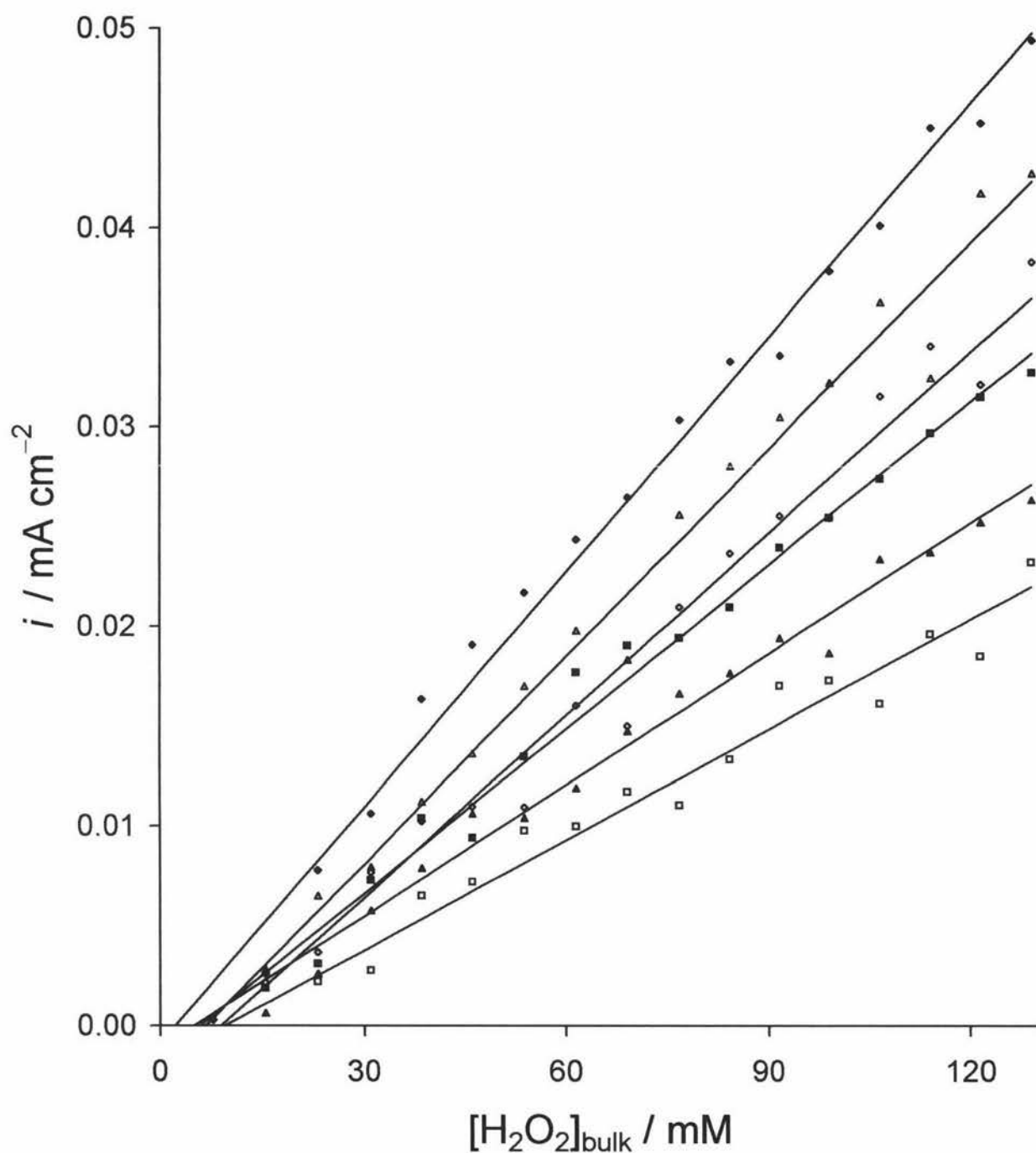
Fig. 5.3   Steady-state responses at $E = +364$ mV vs Ag/AgCl, $\omega = 4000$ rpm at 20°C as a function of $[H_2O_2]_{bulk}$ in six different phosphate buffers of ($\blacklozenge$) 25 , ($\triangle$) 50, ($\blacksquare$) 75, ($\diamond$) 100, ($\blacktriangle$) 150, ($\square$) 200 mM concentration maintained at *ca.* pH 7.28. Straight lines of best fit have been applied to the data.
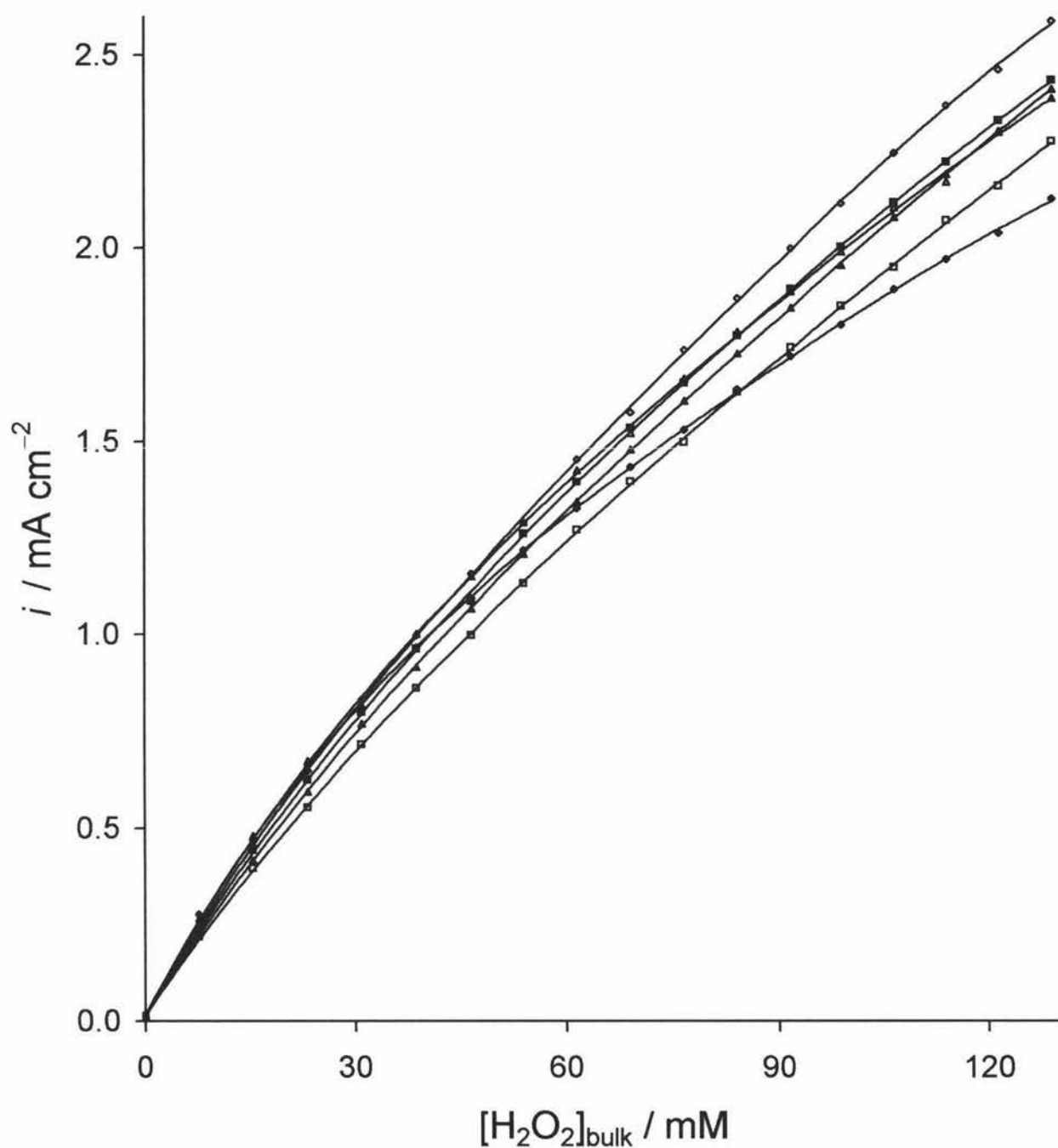
Fig. 5.4 Steady-state responses at $E = +780$ mV vs Ag/AgCl, $\omega = 4000$ rpm at 20°C as a function of $[H_2O_2]_{bulk}$ in six different phosphate buffers of ($\blacklozenge$) 25 , ($\triangle$) 50, ($\blacksquare$) 75, ($\diamond$) 100, ($\blacktriangle$) 150, ($\square$) 200 mM concentration maintained at *ca.* pH 7.28. Smooth curves are trends not synthetic curves generated by Model III or any other model.

phosphate concentration range at 100 mM (the primary buffer). As the phosphate concentration decreases from 100 to 25 mM the responses decrease in proportion with $[H_xPO_4]^{x-3}$. Conversely, the steady-state responses declined, as though reflected through 100 mM, as the phosphate concentration was increased from 100 to 200 mM.

All of these results suggest that the general response profiles, in relation to $[H_2O_2]_{bulk}$ and potential that were observed in the preceding chapters in the primary 100 mM buffer, do not significantly alter with changes in phosphate concentration, only the extent of saturation changes.

5.4   Change in Steady-State Response with Buffer pH

The steady-state responses for varying pH buffers with 100 mM phosphate concentration over 0 - 130 mM $[H_2O_2]_{bulk}$ at +1036 vs Ag/AgCl and ω = 4000 rpm are shown in Fig. 5.5. The response can be seen to increase sharply over this pH range. The increase is not uniform, with indications of a plateau forming below *ca.* pH 6 and between pH 7 and pH 10. The general response vs $[H_2O_2]_{bulk}$ saturation profile is identical to that previously observed in the primary phosphate buffer at pH 7.28 (Chapters 3 and 4) with one notable exception - that of pH 11.51. The steady-state response at pH 11.51 does not adhere to the standard response profile established in previous chapters and has a markedly high response even in the absence of H_2O_2. This is indicative of another current-producing process occurring at the electrode. Upon addition of H_2O_2 the response rises sharply from this initial current of 12.5 mA cm^{-2} to a $[H_2O_2]_{bulk}$ invariant value of 21 mA cm^{-2}. This rise is not attributable to the process of electrochemical oxidation of H_2O_2 due to the current being $[H_2O_2]_{bulk}$ invariant beyond 20 mM. Therefore, this new high pH electrochemical process occurring in the absence of H_2O_2 appears facilitated by small quantities of H_2O_2 ($[H_2O_2]_{bulk}$ < 20 mM). The process can be described by a Koutecky-Levich model, as shown in Fig. 5.6. This model is a modification of the Levich and permits the rate to be controlled by both mass transport and electron transfer processes. The Levich model is insufficient since a plot of the steady-state response vs $\omega^{\frac{1}{2}}$ fails to give a zero intercept. In the plateau region the current density depends only on the rate of mass transport and limiting current
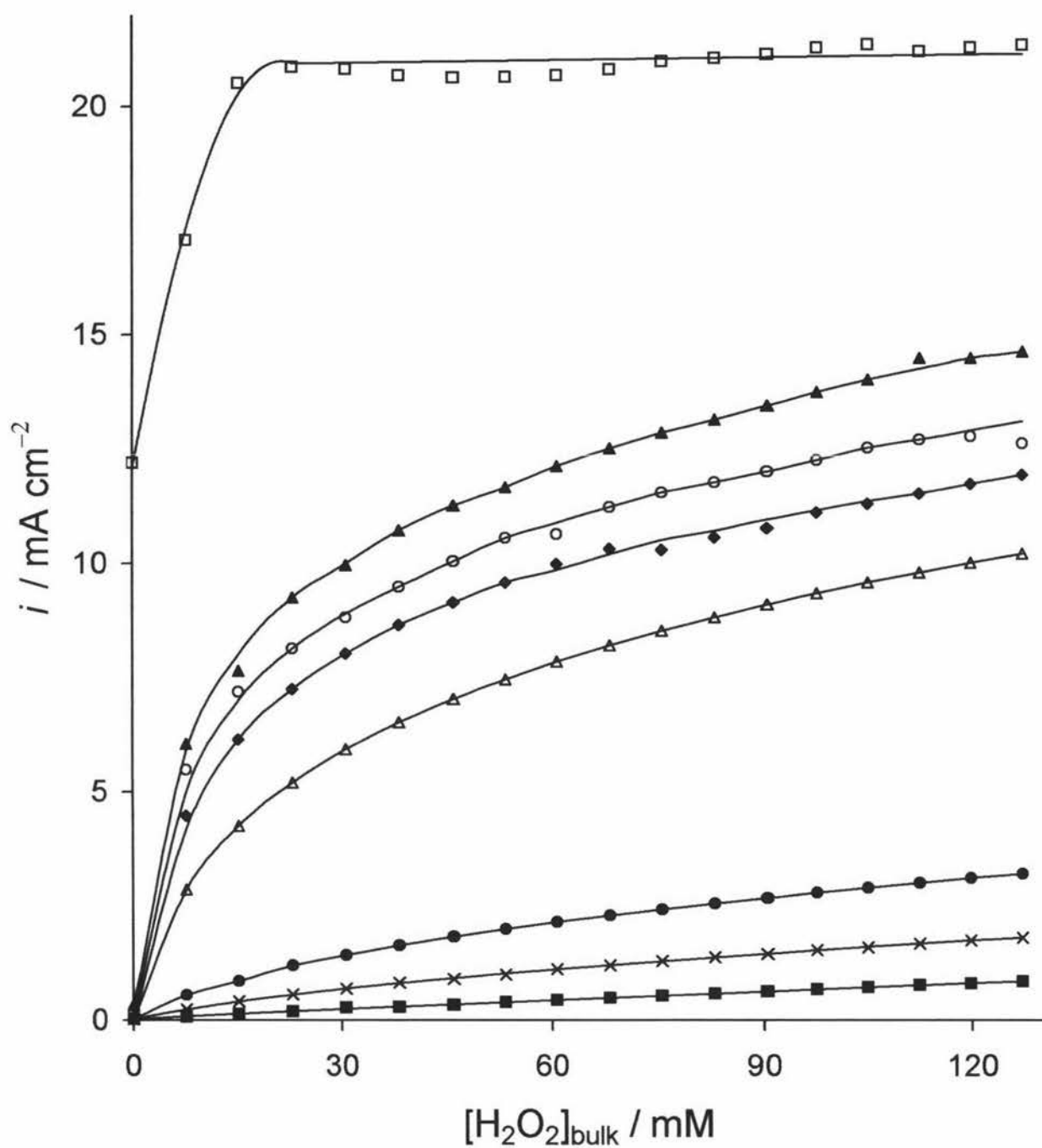
Fig. 5.5 Steady-state responses as a function of $[H_2O_2]_{bulk}$ at $E = +1036$ mV vs Ag/AgCl and $\omega = 4000$ rpm at 20°C in 100 mM phosphate buffers of pH 4.07 (■), 5.35 (×), 6.09 (●), 7.28 (△), 8.20 (◆), 9.14 (○), 10.28 (▲), and 11.51 (□). Smooth curves are trends not synthetic curves generated by Model III or any other model.
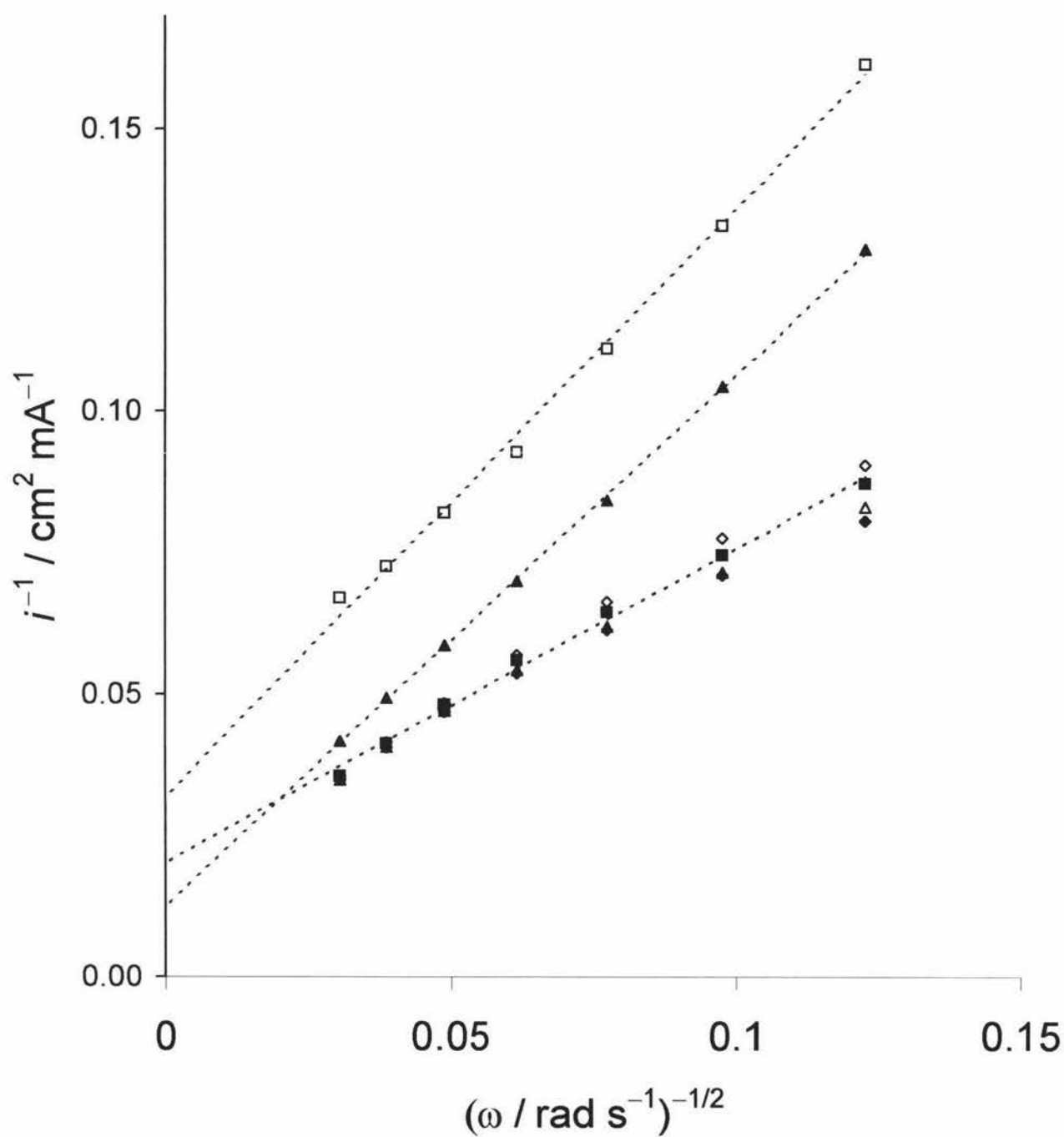
Fig. 5.6 Koutecky-Levich plots for a selection of steady-state responses at (□) 0, (▲) 7.7, (◇) 38.1, (■) 68.1, (△) 97.6, and (◆) 126.8 mM $[H_2O_2]_{bulk}$ at pH 11.52 and $E = +1036$ mV vs Ag/AgCl at 20°C. Straight lines of best fit have been applied to the data.

density will be proportional to square root of the rotation rate as observed in Fig. 5.6. The Koutecky-Levich relationship [1, 2, 53, 55] is given by

$$\frac{1}{i} = \frac{1}{nFk_f c_x} + \frac{1}{0.620FD^{2/3}v^{-1/6}\omega^{1/2}c_x}$$ (5.1)

where k_f is the heterogeneous electron transfer rate constant and c_x is the surface concentration of the electroactive species x, which is independent of the hydrogen peroxide concentration. Thus, the process occurring at pH 11.52 is a kinetic and mass controlled reaction as the Fig. 5.6 plotting $1/i$ vs $1/\omega^{1/2}$ shows linear relationship. The intercept, which is given by

$$\text{intercept} = \frac{1}{nFk_f c_x}$$ (5.2)

indicates that k_f for this process becomes constant above 20 mM $[H_2O_2]_{bulk}$, therefore, the reaction is entirely controlled by diffusion.

One possible process which may be occurring at this very high pH 11.51 is the direct oxidation of the nickel electrode surface to a higher oxidation state, soluble, nickel species. This process might involve the phosphate species PO_4^{-3}, as with a $pK_a = 12.32$ [54] this species becomes significant at this pH and is not significant at lower pH where this high pH process was not observed. The process is facilitated by low levels of either H_2O_2 or superhydroxide, HO_2^-, which also becomes prevalent at this pH, given the pK_a for H_2O_2 is 11.52 [31]. The nickel species may be free to diffuse into the bulk solution so the process described is the corrosion of the nickel electrode at high pH in phosphate buffer solutions facilitated by hydrogen peroxide or superhydroxide (Eqn. 5.2).

$$\text{Ni}_{PS\ (s)} + PO_4^{-3}{}_{(aq)} \xrightarrow{\ H_2O_2/HO_2^-\ } \text{Ni.PO}_4^{-3}{}_{(aq)}$$ (5.3)
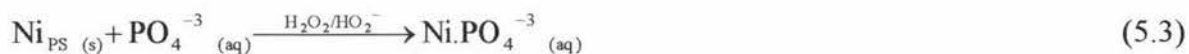
This process would be diffusion controlled as the oxidised nickel would have to be removed to allow expose a new metal surface. A similar mechanism was not observed to occur on platinum at high pH. This would appear to indicate that platinum is a more noble metal than nickel.

Another possible process that may result in the observed response is the oxidation of the electrolyte, which may be facilitated by small concentrations or hydrogen peroxide or

superhydroxide and possibly involves the PO_4^{-3} phosphate species.

$$Ni_{PS} + 2OH^- \xrightarrow{\quad H_2O_2/HO_2^-,PO_4^{-3} \quad} Ni_{PS\cdot red} + O_2 + 2H^+ + 3e^- \qquad (5.4)$$
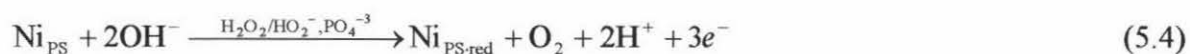
where $Ni_{PS\cdot red}$ refers to the reduced nickel precursor site. This process would also be diffusion controlled as the rate would depend on the mass transport of OH^- to and products away from the electrode surface.

When considering the effect of the phosphate buffer pH on the rate of electrochemical oxidation of H_2O_2 it is prudent to consider how the relative proportionations of the phosphate (pK_a =2.13, 7.21 and 12.32 [54]) and H_2O_2 (pK_a = 11.52 [31]) species vary in solution. These are shown in Fig. 5.7. At pH 11.51 it can be seen that approximately 50% of the bulk hydrogen peroxide has been deprotonated to HO_2^-, PO_4^{-3} is also present in reasonable quantities. These species, particularly PO_4^{-3}, may be involved in the process predominant at pH > 11 but not below.

The steady-state responses obtained above pH 11, for these reasons, are not directly attributable to the electrochemical oxidation of H_2O_2 on a nickel electrode surface, but rather another process not fully elucidated. The processes that may be occurring above pH 11.51 can not be substantiated within the bounds of this study and further high pH investigation would be required to defend these hypotheses. Due to this, regions beyond pH 11 are outside the scope of this study and are, therefore, not considered in all subsequent discussions.

Figure 5.8 shows the speciation profile for phosphate and H_2O_2 overlaid by the steady-state response obtained at +1036 mV vs Ag/AgCl, 130 mM $[H_2O_2]_{bulk}$ and $\omega = 4000$ rpm. It is apparent, at each pH, that the increase in the steady-state response, over the range of pH 4 to pH 9, coincides with the increase in the relative concentration of the phosphate species HPO_4^{-2}. Between pH 9 and 10, the response does not correspond to the HPO_4^{-2} profile but appears to correspond to the increase with the concentration of the superhydroxide (HO_2^-), with pH. The steady-state currents attributable to HO_2^- oxidation appear to constructively interfere with the currents already produced by the electrochemical oxidation of H_2O_2. Since superhydroxide is produced by the deprotonation of H_2O_2, the rise in $[HO_2^-]_{bulk}$ is matched by an equivalent drop in $[H_2O_2]_{bulk}$. Therefore, should superhydroxide oxidise at the same
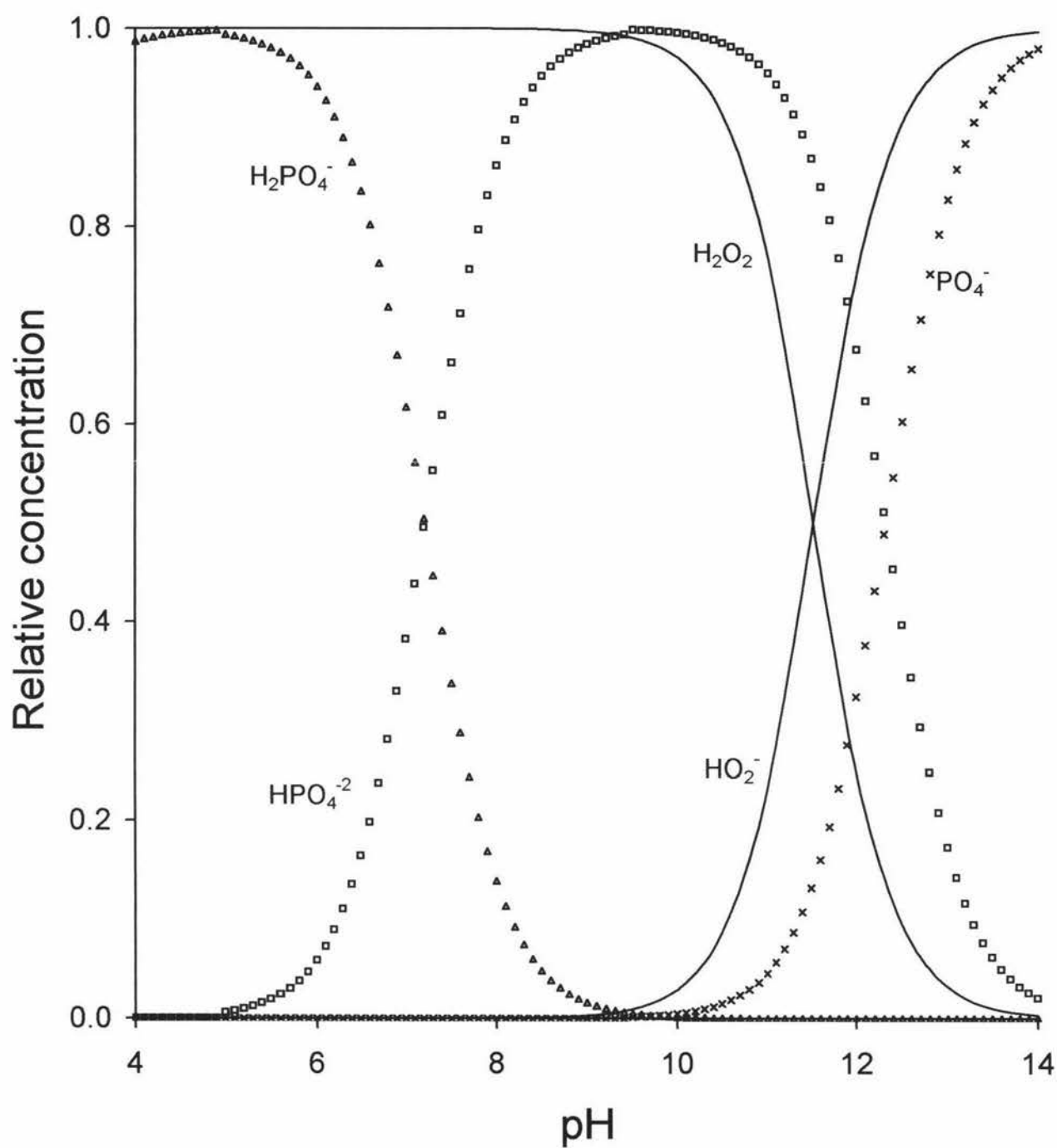
Fig. 5.7   Relative concentrations of phosphate as a function of pH $H_2PO_4^-$ ($\triangle$), HPO_4^{-2} ($\square$), and PO_4^{-3} ($\times$) and the hydrogen peroxide species H_2O_2 and HO_2^-, (—).
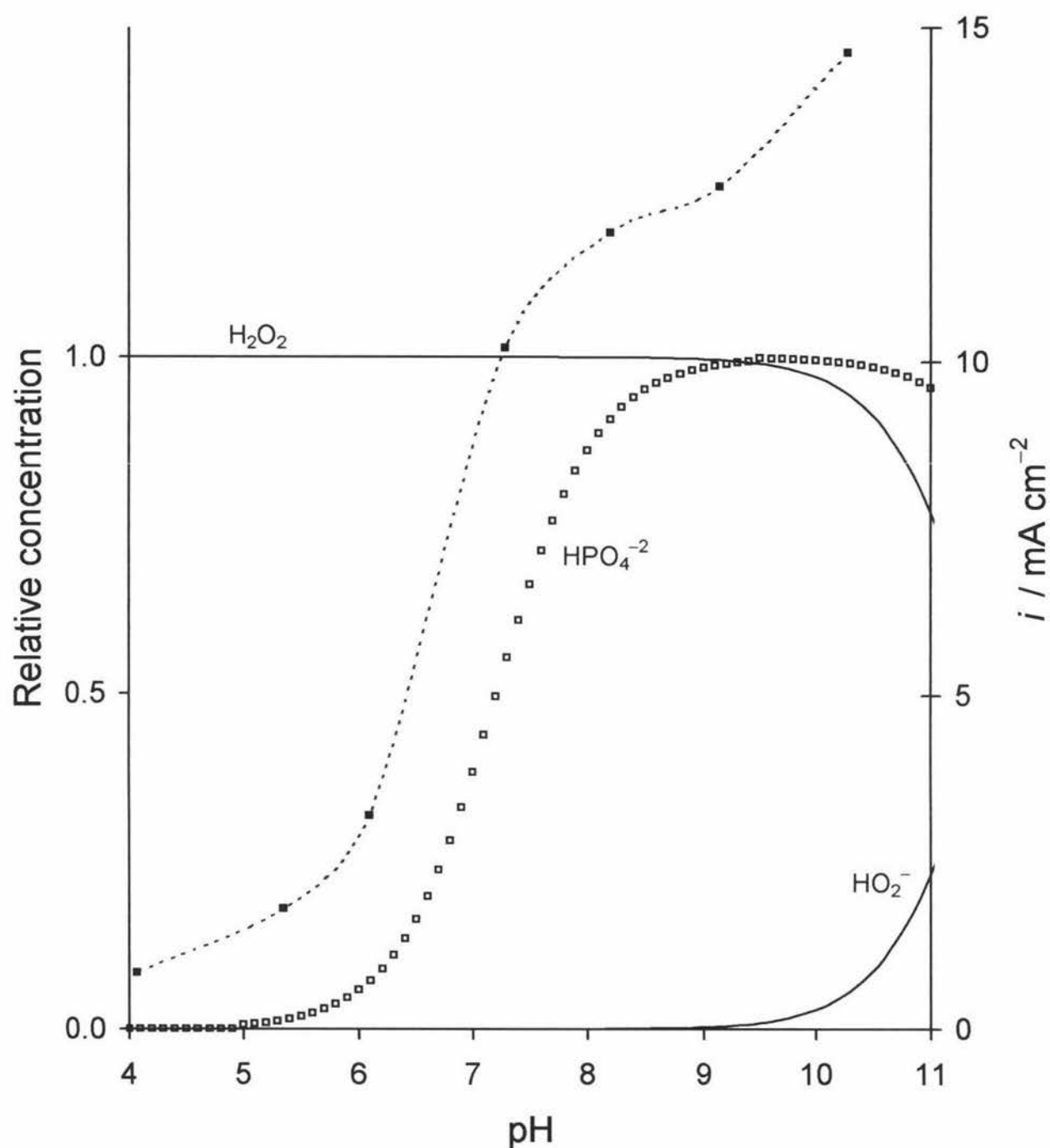
Fig. 5.8 Steady-state responses of 130 mM [H_2O_2]$_{bulk}$ at E = +1036 mV vs Ag/AgCl, ω = 4000 rpm at 20°C as a function of pH (right-axis). This is overlaid with the relative concentrations of electrochemically relevant phosphate HPO_4^{-2} ($\square$) and the hydrogen peroxide species H_2O_2 and HO_2^-, (—) as a function of pH (left-axis).

rate as hydrogen peroxide it would be expected that the current would be maintained. The steady-state response instead increases over the 9 to 10.3 pH range in correlation with $[HO_2^-]_{bulk}$. This leads to the conclusion that the oxidation of superhydroxide on a nickel electrode surface occurs at a significantly higher rate than that of H_2O_2, causing a corresponding increase in the steady-state response beyond that observed from H_2O_2. Superhydroxide is significantly more reactive than H_2O_2 in dissociation reactions [31, 34, 49] this trend may be also reflected in its electrochemical behaviour. Other hydrogen peroxide studies at high pH have identified superhydroxide as the major electroactive species [23, 31, 33, 46, 47]. One study went as far as to suggest that superhydroxide is the major electroactive species above pH 2 [31], which according to the findings of this study is debatable at least below pH 9. The electrochemical oxidation of superhydroxide on a nickel rotating disc electrode surface is not analogous to H_2O_2 and, therefore, would require further investigation in a similar manner to this study.

There appears to be some underlying activity occurring below pH 4, in the absence of HPO_4^{-2} to facilitate the mechanism. However, the rate of reaction, should the current trends continue, would become too slow to obtain viable results. This basil activity may be indicative of a novel phosphate free mechanism of significantly slower rates, occurring below pH 4. Above pH 9 a new constructive mechanism involving superhydroxide becomes prevalent to obscure the study of H_2O_2 and at higher pH > 11 an unidentified and potentially corrosive mechanism dominates.

The optimum pH region for studying the electrochemical oxidation of H_2O_2 on a nickel rotating disc electrode surface is, therefore, between pH 4 and 9. In this region all variation in steady-state response with pH can be attributed simply to changes in $[HPO_4]^{-2}$. Varying the pH simply changes the HPO_4^{-2} relative concentration in the phosphate buffer. Clearly, beyond these boundaries further investigation at both high and low pH would be necessary.

5.5   Phosphate in the Electrochemical Mechanism

In terms of the model developed earlier (Chapters 3 and 4), the phosphate dependence on pH and concentrations observed in Sections 5.3 and 5.4 could be accounted for by changes in the total number of nickel sites (free, complexed, and reduced) on the electrode surface.

This requires that the binding site model must be further altered to include terms for $[HPO_4^{-2}]$.

HPO_4^{-2} may be involved in the production of the active nickel-binding site from a precursor site Ni_{PS} (Section 4.6, Eqn. 4.9). Therefore, the equilibrium could be expressed

$$Ni_{PS} + HPO_4^{-2} \underset{}{\overset{K_{BS}}{\rightleftharpoons}} Ni_{BS \cdot HPO_4^{-2}} \qquad (5.5)$$
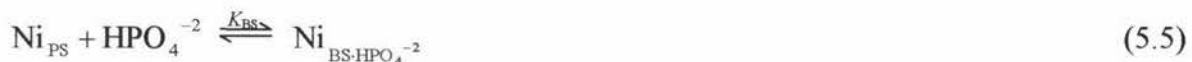
where $Ni_{BS \cdot HPO_4^{-2}}$ is the active nickel binding site

The active nickel binding site was formerly represented as $Ni(OH)_2$ in the previous models since formation of phase oxides such as $Ni(OH)_2$ have been well documented under anodic conditions alkaline solutions [23, 24, 27, 39, 41, 42]. It is likely that this oxide phase would be the basis of the active binding site since earlier research by others demonstrated that oxidation of H_2O_2 is favoured on oxidised metal surfaces [15, 23, 24, 27]. Chang *et al.* found that "the catalytic action of the nickel surface in alkaline media appears to be associated with the formation of a higher oxide, commonly termed NiOOH, from the $Ni(OH)_2$" [43]. It may be possible that the binding site and indeed the precursor site may have hydroxide ligands. However, no evidence of this is apparent from the present study. This would give the binding site a higher oxidation state than +2 once the phosphate is coordinated. Nickel oxidation states of +2, +3, or +4 are not uncommon in aqueous media [39, 40, 41, 43, 81]. One must also recognise that the binding site may be multinuclear in nature. The exact stoichiometrey and oxidation state of the nickel-binding site is unknown and, in part, irrelevant to this study, since the kinetic model can not be directly interpreted in terms of numbers of binding sites. Consequently our interest in the electrode lasts as far as to say that a H_2O_2 binding site exists and it involves the phosphate species HPO_4^{-2}.

Another possibility for HPO_4^{-2} involvement in the mechanism that should be considered is that HPO_4^{-2} facilitates the electrochemical oxidation of bound H_2O_2 and simultaneous reduction of the nickel binding site.

$$Ni(OH)_2 \cdot H_2O_2 \xrightarrow{\;HPO_4^{-2}\;} Ni^\circ + 2H_2O + O_2 \qquad (5.6)$$
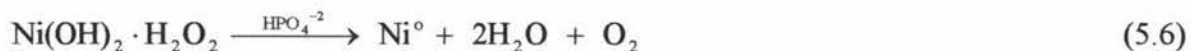
This reaction indicates that the electrochemical oxidation could be limited by HPO_4^{-2} quantities insufficient to meet the demands for H_2O_2 binding. Increasing $[HPO_4^{-2}]_{bulk}$ would therefore accelerate reaction 5.6, thereby increasing the steady-state response. This

relationship can be observed to occur at high potentials (Fig. 5.2). The response increase with phosphate concentration will plateau when sufficient binding sites are produced so that $[H_2O_2]_{bulk}$ or the rate of electrochemical oxidation becomes limiting (Section 5.3).

Equation 5.6 is not the favoured model since this reaction, k_2N, is not an elementary step but rather may involve many individual cascading reactions. Further study would be required to isolate the reactions and species involved in these elementary steps. The one-to-one binding site to phosphate species ratio described by Eqn. 5.5 is the simplest model and adequately explains the increase in response with $[HPO_4]^{-2}$ observed in the high potential region (Fig. 5.2).

It becomes apparent, at low potentials (Fig. 5.3), that excess $[HPO_4^{-2}]_{bulk}$ is rate inhibiting requiring even further modification to the binding site model. This inhibition may occur through secondary complexation of a phosphate species to the active binding site

$$Ni_{BS \cdot HPO_4^{-2}} + HPO_4^{-2} \overset{K_{PO_4}}{\rightleftharpoons} Ni_{BS \cdot HPO_4^{-2}} \cdot HPO_4^{-2} \tag{5.7}$$

where the incoming phosphate species, HPO_4^{-2}, prevents the binding of H_2O_2 to the binding site complex in either a competitive or a non-competitive manner. Competitive inhibition would arise from HPO_4^{-2} binding to the same point to which H_2O_2 binds. For non-competitive inhibition, HPO_4^{-2} might induce a conformational or electrostatic change denaturing the H_2O_2 binding site. These two models of inhibition would have quite different kinetics but cannot be differentiated in this present study.

There is strong indication that the phosphate species involved in the phosphate inhibiting reaction is HPO_4^{-2} as proposed in the inhibition modes that are presented here. The only other phosphate species present at pH 7.28, in significant concentrations, is $H_2PO_4^-$ (1 : 1.25 ratio to HPO_4^{-2}). Considering the speciation shown in Fig. 5.7, when the pH decrease from pH 9 to pH 4 $[HPO_4^{-2}]$ (required by the mechanism) decreases with a corresponding increase in $[H_2PO_4^-]$. Should $H_2PO_4^-$ be inhibiting as the pH decreases, from pH 9 to 4, both the rate reducing effects of increasing $[H_2PO_4^-]$ (inhibiting) and decreasing $[HPO_4^{-2}]$ would compound giving a sharp decline in response. The steady-state response over this range in fact has a slope very similar to that of the change in $[HPO_4^{-2}]$ with pH, as shown in Fig. 5.8. This strongly suggests that $H_2PO_4^-$ is not inhibiting. Whilst the particular phosphate species

involved in reaction 5.7, is yet unknown and further phosphate buffer concentration studies at higher and lower pH would be required, the initial indications point to the involvement of HPO_4^{-2}.

Other possible mechanisms for this phosphate inhibition include the non-competitive inhibition at the H_2O_2 bound nickel site

$$Ni_{BS \cdot HPO_4^{-2}} \cdot H_2O_2 + HPO_4^{-2} \overset{K_{PO_4}}{\rightleftharpoons} Ni_{BS \cdot HPO_4^{-2}} \cdot H_2O_2 \cdot HPO_4^{-2} \tag{5.8}$$
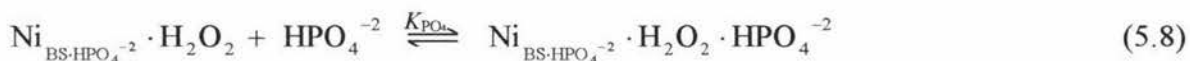
This mode of phosphate inhibition, which requires the prior binding of H_2O_2 to the nickel active site, provides an equally viable, but more complex, prospect for phosphate inhibition.

There is also a possibility that the phosphate inhibition may occur by decreasing the rate of reoxidation of the reduced nickel site liberating a free active nickel-binding site for subsequent H_2O_2 binding and oxidation.

$$Ni_{BS \cdot HPO_4^{-2} \cdot red} + HPO_4^{-2} \overset{K_{PO_4}}{\rightleftharpoons} Ni_{BS \cdot HPO_4^{-2} \cdot red} \cdot HPO_4^{-2} \tag{5.9}$$

where $Ni_{BS \cdot HPO_4^{-2} \cdot red}$ represents the reduced nickel binding site (previously identified as Ni°). This labelling demonstrates the lack of understanding as to the true nature of this site save that it is the reduced form of the binding site. Both the k_2N step and k_3N step (discussed in detail in Chapters 3 and 4), which produce and recycle the reduced nickel-binding site respectively, as stated earlier, are not elementary steps. They may involve many different reactions and species. The actual reactions occurring in these steps are irrelevant to this study, only the final conclusion is of importance. However, the inclusion of both these alternate phosphate inhibitions, Eqns. 5.8 and 5.9, should be avoided since they involve these complex and unresolved reactions. The simplest model involves the phosphate inhibition through binding site denaturation described by Eqn. 5.7.

Equations 5.3 and 5.5 in turn can satisfactorily account for increasing buffer concentration increasing the rate and for excess phosphate inhibiting the rate of electrochemical oxidation of H_2O_2. Figures 5.2, 5.3, and 5.4 show how the effect of phosphate buffer concentration varies over the +332 to +1100 mV vs Ag/AgCl potential range. These show that the optimal phosphate concentration becomes more concentrated the more anodic the potential. Above and below the optimum there is excess phosphate, which inhibits through Eqn. 5.7, and

insufficient phosphate, which limits the rate due to Eqn. 5.5, respectively. The shift in the optimal phosphate concentration with potential is highlighted by considering Figs. 5.9 and 5.10. Both of these figures are similar, save Fig. 5.9 which displays steady-state responses for a selection of highly anodic potentials, whereas, Fig. 5.10 displays steady-state responses for a selection of low anodic potentials. High and low potential regions have been separated to prevent the loss of information at low anodic potentials due to scaling effects. These figures show the phosphate concentration optimum shifting to higher concentrations with increasing potential. Optimums can be estimated and these are tabulated in Table 5.1.

These shifts in optimal phosphate concentrations with potential may, in terms of the electrochemical model, be attributable to one of two possibilities. First, the number of precursor sites, N^*, may increase with potential. Through consideration of Eqn. 5.5 an increase in the number of precursor sites would decrease the relative phosphate concentration required. Therefore, the optimum phosphate concentration would increase with potential, as is found in Table 5.1. Also, in terms of Eqn. 5.7, at higher potentials more binding sites would be produced, decreasing the effective phosphate concentration (already decreased due to phosphate removed during the binding site formation reaction Eqn. 5.5).

The second possible cause of increase in the optimal phosphate concentration with potential is that, as the rate of electrochemical oxidation of H_2O_2 increases with potential (Chapter 3, Section 3.6.2), the solution pH near the surface of the electrode decreases as a consequence of the oxidation by-product H^+. This low pH gradient near the surface causes the equilibrium

$$HPO_4^{-2} + H^+ \overset{K_{H^+}}{\rightleftharpoons} H_2PO_4^- \tag{5.10}$$

to shift according to the Henderson-Hasselbalch equation ($pK_a = 7.21$)

$$pH = pK_a + \log\left(\frac{[H_2PO_4]^-}{[HPO_4]^{-2}}\right) \tag{5.11}$$

At pH 7.28 the relative concentrations of the two phosphate species are approximately equal ($H_2PO_4^- : HPO_4^{-2} = 1 : 1.25$).

The shift in equilibrium induced by the lower surface pH, due to the build up of the oxidation by-product H^+, would effectively lower the surface concentration of electroactive phosphate species, HPO_4^{-2}, through protonation. Therefore, since the rate of H_2O_2
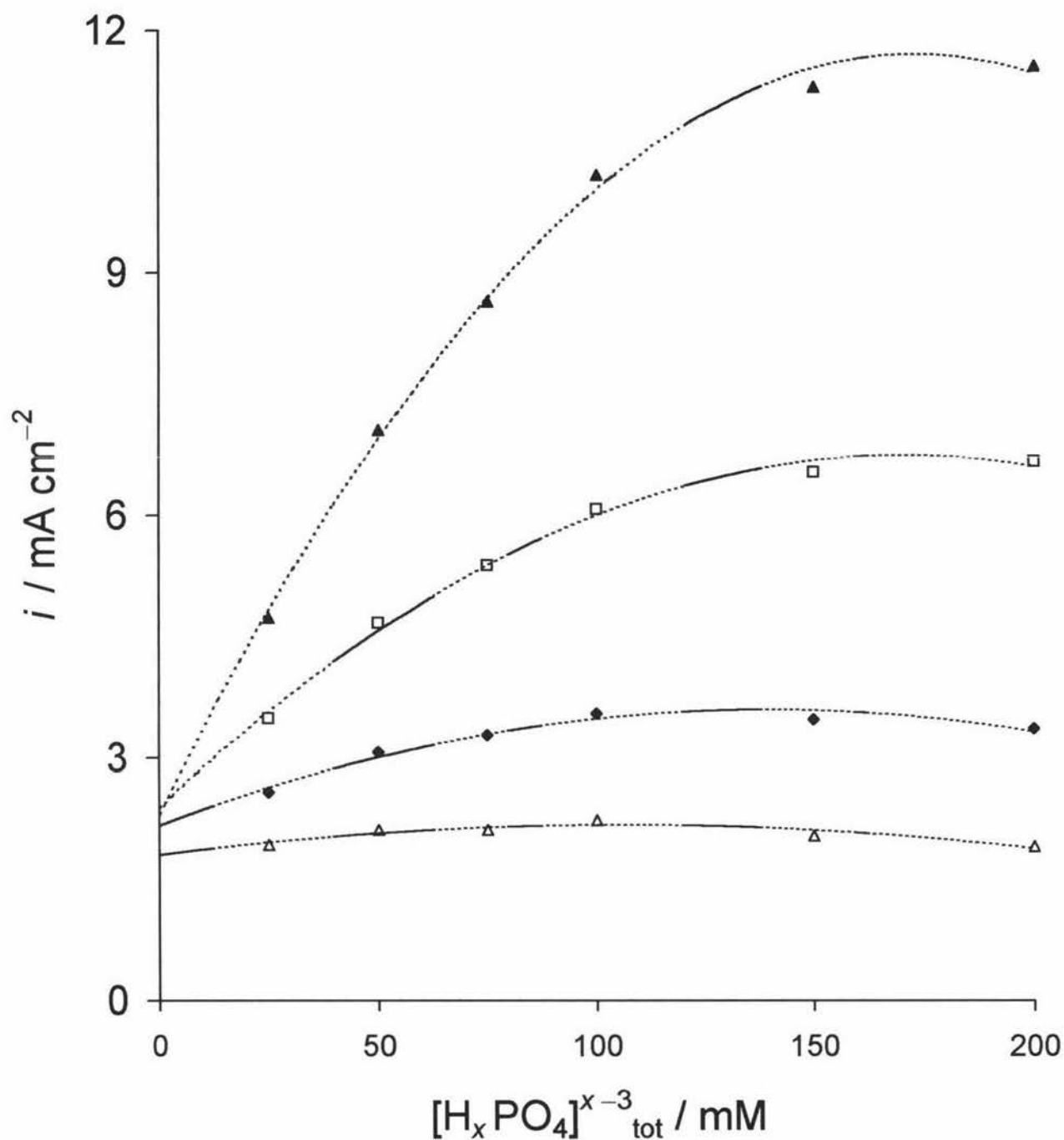
Fig. 5.9 Steady-state responses of 130 mM $[H_2O_2]_{bulk}$ as a function of $[H_xPO_4^{x-3}]$ at $\omega = 4000$ rpm and 20°C at a selection of high to medium potentials $E = +748$ ($\triangle$), $+844$ ($\blacklozenge$), $+940$ ($\square$), and $+1036$ ($\blacktriangle$) mV vs Ag/AgCl.
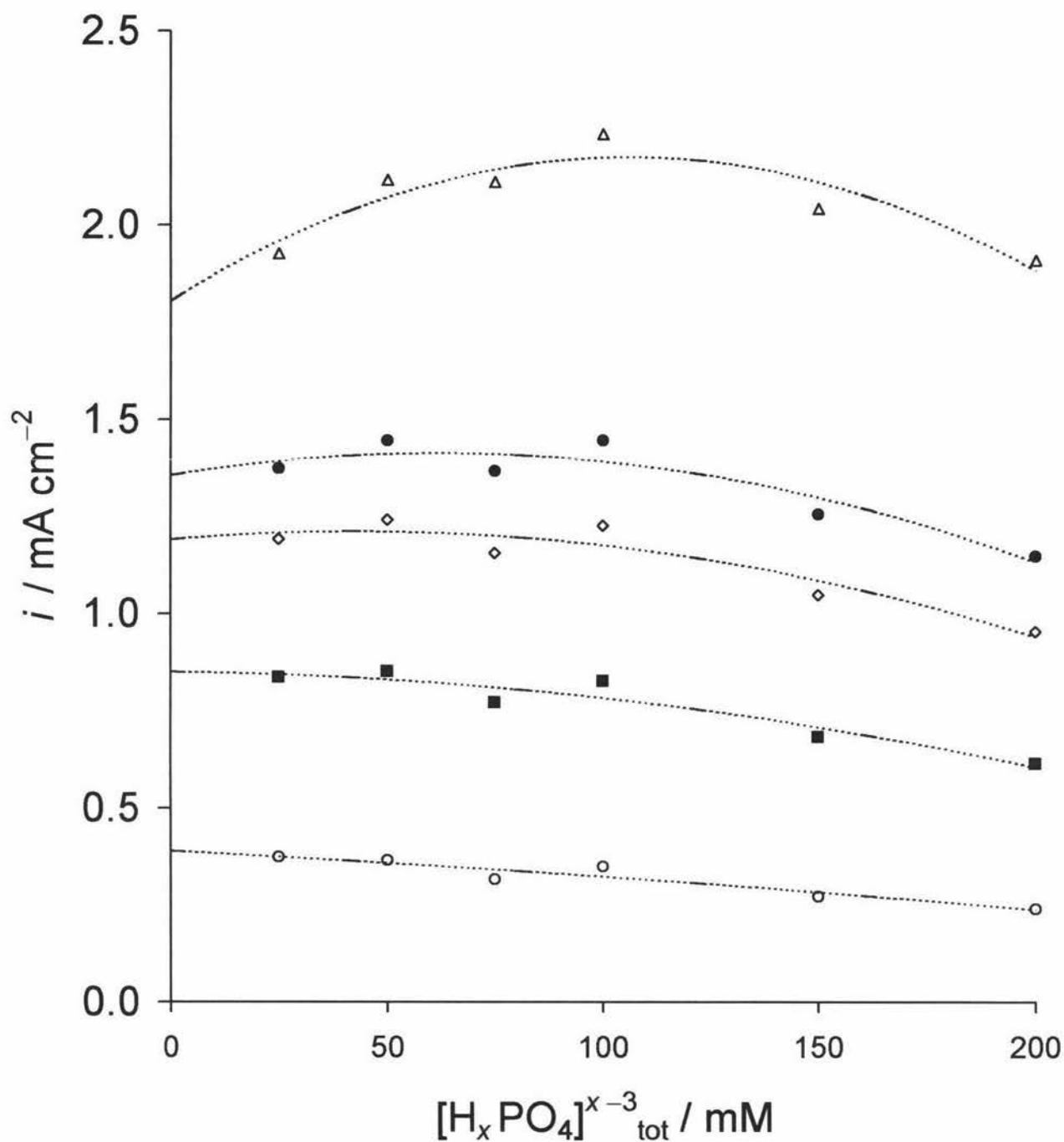
Fig. 5.10 Steady-state responses of 130 mM $[H_2O_2]_{bulk}$ as a function of $[H_xPO_4^{x-3}]$ at $\omega = 4000$ rpm and 20°C at a selection of medium to low potentials $E = +460$ (○), $+556$ (■), $+620$ (◇), $+652$ (●), $+748$ (△) mV vs Ag/AgCl.

| Optimal $[\text{HPO}_4^{-2}]$ | E vs Ag/AgCl |
mM	mV
25	+460
50	+620
75	+652
100	+748
150	+844
175	+1036

Table 5.1 Potentials at which the listed HPO_4^{-2} concentrations are estimated to elicit the maximum steady-state response.

oxidation increases with potential, the surface pH decreases and lowers the surface concentration of $HPO4^{-2}$. Consequently, higher concentrations of phosphate would be required to meet the demands of the rate according to Eqn. 5.5. Similarly, the lower surface pH at high potentials would reduce the effective excess phosphate, which in terms of Eqn. 5.7 would require a higher phosphate concentration to maintain a comparable level of phosphate inhibition.

Should the relationship between $[HPO_4^{-2}]$ and rate be caused by the lowering of the surface pH gradient, rotation-rate dependence would be exhibited. The rotation rate dependencies previously found in the primary pH 7.28 0.100 mol L^{-1} phosphate buffer are presented in Chapter 3, Section 3.4. The expected effect of raising the rotation rate would be to enhance the mass transportation of the hydrogen ion by-product away from the electrode surface thereby reducing the $[HPO_4^{-2}]$ dependence of the electrochemical mechanism. Figures 5.11 and 5.12 (similar to Fig. 5.2) show the phosphate concentration dependence of the steady-state responses over 0 – 130 mM $[H_2O_2]_{bulk}$ at +1036 mV vs Ag/AgCl for rotation rates 10000 and 630 rpm respectively. These figures clearly show that the $[HPO_4^{-2}]$ dependence of the system at +1036 mV is decreased at higher rotation rates with the data spread between 25 and 200 mM $[H_xPO_4^{x-3}]_{tot}$, the minima and optima respectively, at 630 rpm being 15% larger than that at 10000 rpm. This trend is reflected throughout the potential range with the differences between the optima (100 mM) and minima (25 mM) increasing by 5% at the medium potential +780 mV vs Ag/AgCl, which typically has the lowest data variation. Due to minimal rates occurring at low potentials combined with a low rotation rate the +364 mV data at 630 rpm is quite scattered (a problem previously encountered in Chapter 3). However, there is still an apparent trend whereby the data spread between the optima (25 mM) and minima (200 mM) is increased by *ca.* 40% by reducing the rotation rate from 10000 to 630 rpm.

The exact nature of the nickel precursor sites and nickel binding sites remain unknown. Therefore, the proposition that the number of precursor sites change with potential is a hypothesis that cannot be tested within this study. The second proposition that the surface pH gradient drops with potential and protonates the electroactive HPO_4^{-2} to form the
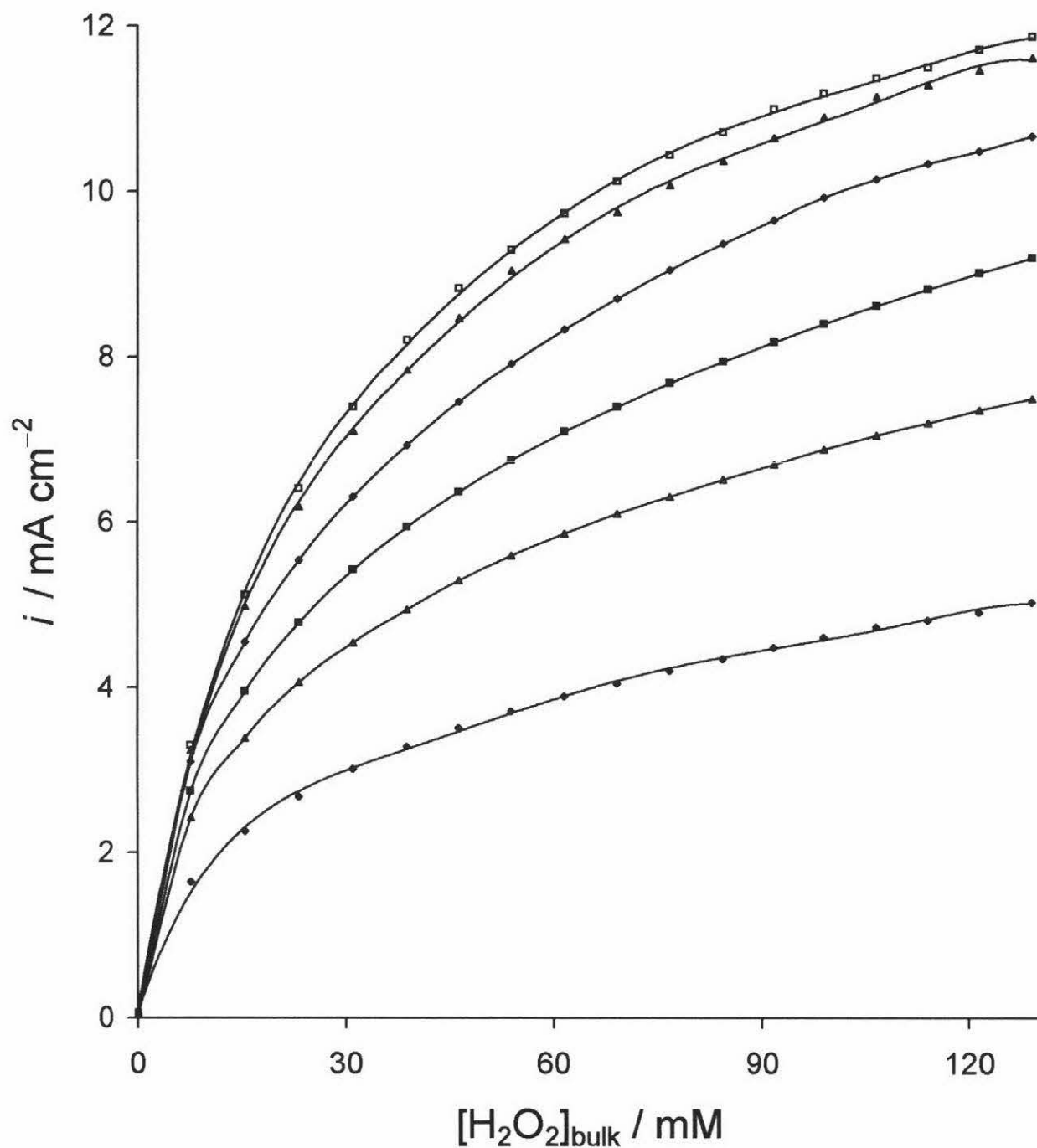
Fig. 5.11   Steady-state responses at $\omega = 10000$ rpm and $E = +1036$ mV vs Ag/AgCl at 20°C as a function of $[H_2O_2]_{bulk}$ in six different phosphate buffers of (♦) 25 , (△) 50, (■) 75, (◇) 100, (▲) 150, (□) 200 mM concentration maintained at *ca*. pH 7.28. Smooth curves are trends not synthetic curves generated by Model III or any other model.
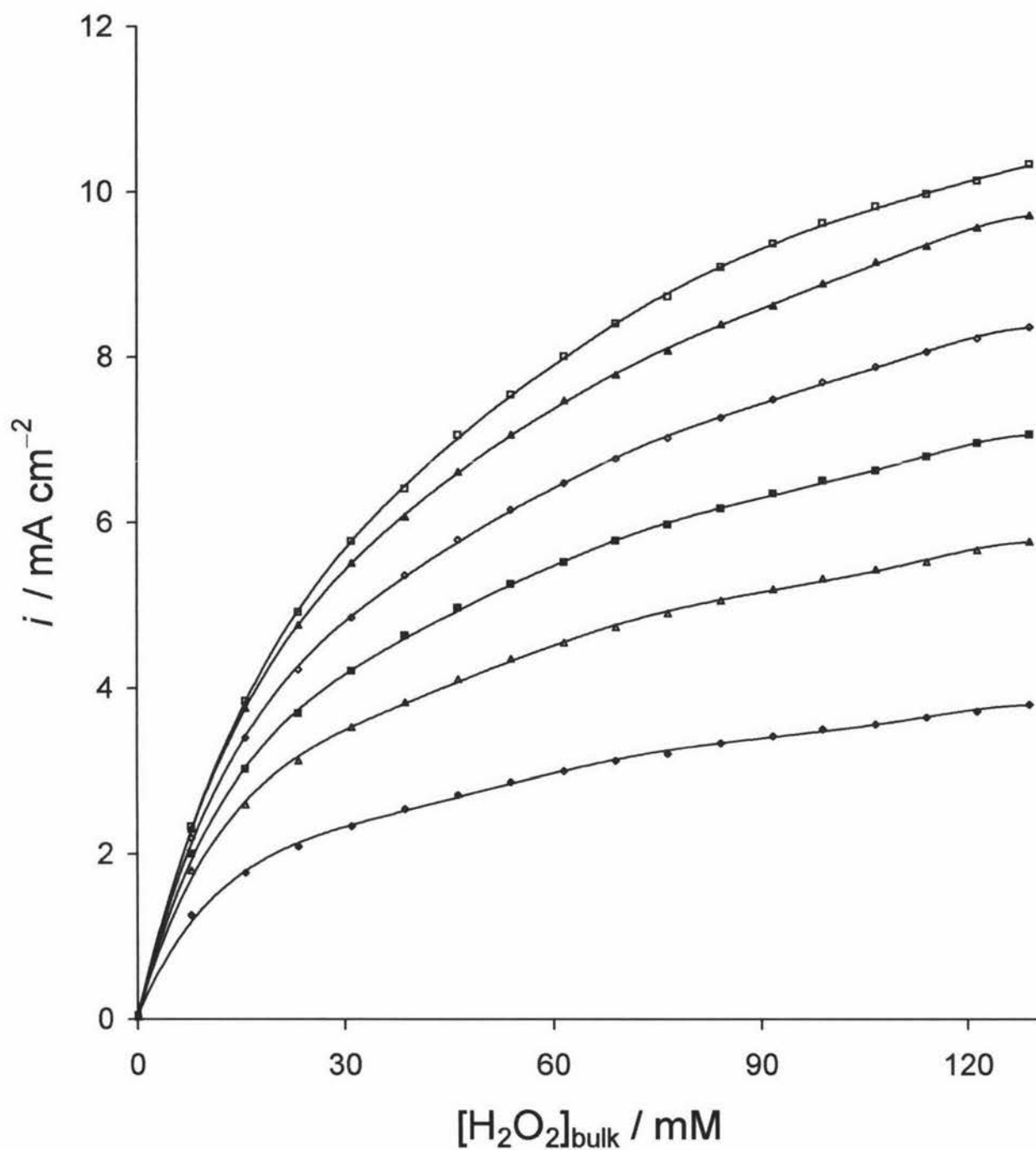
Fig. 5.12 Steady-state responses at $\omega = 630$ rpm and $E = +1036$ mV vs Ag/AgCl at 20°C as a function of $[H_2O_2]_{bulk}$ in six different phosphate buffers of ($\blacklozenge$) 25 , ($\triangle$) 50, ($\blacksquare$) 75, ($\diamond$) 100, ($\blacktriangle$) 150, ($\square$) 200 mM concentration maintained at *ca*. pH 7.28. Smooth curves are trends not synthetic curves generated by Model III or any other model.

inactive $H_2PO_4^-$ species provides an explanation of the observed trends. The first proposition that the number of precursor sites are changing with potential impacts on more than one reaction in the electrochemical mechanism. Due to this and the exact nature of the nickel precursor and binding sites remaining unknown, this proposition is unfavourable. This in conjunction with the support given from the rotation rate data renders the second proposition the favoured model. The overall model arising from this second proposition is described in the following Section 5.5.2.

5.6   Model IV

The simplest possible electrochemical mechanism to account for the effect of the buffer composition on the steady-state response involves the phosphate species, HPO_4^{-2}, in the formation of the active nickel binding site from a nickel precursor.

$$Ni_{PS} + HPO_4^{-2} \overset{K_{BS}}{\rightleftharpoons} Ni_{BS \cdot HPO_4^{-2}} \tag{5.5}$$

As in the models developed previously (Chapters 3 and 4) H_2O_2 reversibly binds to the active nickel binding site,

$$Ni_{BS \cdot HPO_4^{-2}} + H_2O_2 \overset{K_1}{\rightleftharpoons} Ni_{BS \cdot HPO_4^{-2}} \cdot H_2O_2 \tag{5.12}$$

an internal electron transfer occurs reducing the nickel site and oxidising the bound H_2O_2
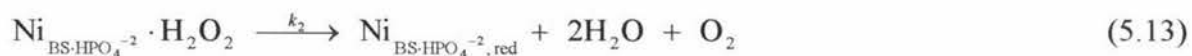
$$Ni_{BS \cdot HPO_4^{-2}} \cdot H_2O_2 \overset{k_2}{\longrightarrow} Ni_{BS \cdot HPO_4^{-2}, red} + 2H_2O + O_2 \tag{5.13}$$

followed by the regeneration of the active binding state to complete the catalytic cycle.

$$Ni_{BS \cdot HPO_4^{-2}, red} + 2H_2O \overset{k_3}{\longrightarrow} Ni_{BS \cdot HPO_4^{-2}} + 2H^+ + 2e^- \tag{5.14}$$
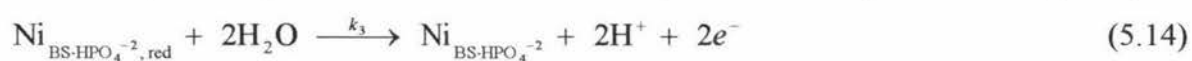
The mechanism is still inhibited by the reversible binding of the dioxygen by-product to the active nickel-binding site.

$$Ni_{BS \cdot HPO_4^{-2}} + O_2 \overset{K_4}{\rightleftharpoons} Ni_{BS \cdot HPO_4^{-2}} \cdot O_2 \tag{5.15}$$

The mechanism is further inhibited by the denaturation of the nickel binding site by the reversible binding of a second phosphate ion, HPO_4^{-2}, to form an inactive diphosphate complex.

$$Ni_{BS \cdot HPO_4^{-2}} + HPO_4^{-2} \overset{K_{PO_4}}{\rightleftharpoons} Ni_{BS \cdot HPO_4^{-2}} \cdot HPO_4^{-2} \tag{5.7}$$

This mechanism yields a complex rate equation expressed in terms of the surface concentrations of solution species $[H_2O_2]$, $[O_2]$, and $[HPO_4^{-2}]$.

$$j = \frac{k_2 N.K_1[H_2O_2]}{1 + K_4[O_2] + \dfrac{1}{K_{BS}[HPO_4^{-2}]} + K_{PO_4}[HPO_4^{-2}] + K_1[H_2O_2](1 + k_2/k_3)} \qquad (5.16)$$

To further complicate the issue, the surface concentration of the electroactive phosphate species, $[HPO_4^{-2}]$, is reduced by $[H^+]$ formed as a by-product of H_2O_2 oxidation.

$$HPO_4^{-2} + H^+ \overset{K_{H^+}}{\rightleftharpoons} H_2PO_4^{-} \qquad (5.10)$$

The surface concentration of H^+ is related to the rate and given by

$$[H^+] = [H^+]_{bulk} + 2jk_D D_{H^+}^{-2/3} \omega^{-1/2} \qquad (3.3)$$

This mechanism, Model IV, is schematically represented in Fig. 5.13.

A quantitative analysis of Model IV using the experimental data to SIMPLEX optimise the rate and equilibrium constants in the manner of the previous models (Chapters 3 and 4) was not considered feasible. In the previous chapters, SIMPLEX optimisation was used to obtain the solution to the rate polynomials created when diffusion effects are included. Whilst a similar polynomial expression could be developed for the rate equation of Model IV (Eqn. 5.16) which involves a phosphate species, it is believed that the results achieved would not be meaningful. Since the rate equation includes three more variables which, in conjunction with phosphate protonation effectively forcing $[HPO_4^{-2}]$ to vary with rate, makes the solving the polynomial vastly more complex. Due to the inseparable nature of k_2N and k_3N, and the binding site formation term, $(K_{BS}[HPO_4^{-2}])^{-1}$, influencing N would dominate over the rate constants of these reactions, Eqns. 5.13 and 5.14. It is believed that the influence of the phosphate species in forming the binding site, Eqn. 5.5, would dominate this analysis preventing reliable optimisation and lead to inaccurate and erratic results for the other constants involved. This situation could not be alleviated by varying the rotation rate due to phosphate being only circuitously influenced by mass-transport considerations in so far as it pertains to $[H^+]$, as shown by Eqn. 3.3. The findings of this chapter do not detract in any way from the models developed at the single pH and phosphate concentration conditions
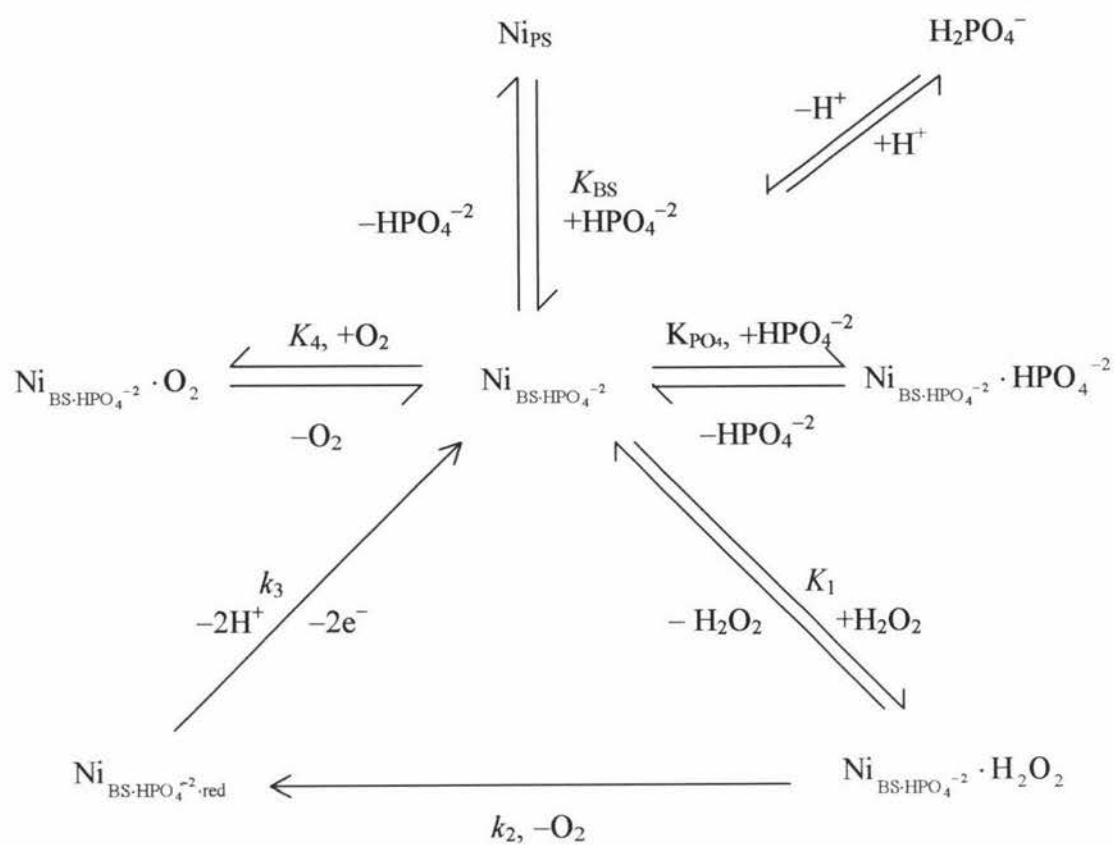
Fig. 5.13   A schematic representation of Model IV.

of the primary 7.28 pH 0.100 mol L^{-1} phosphate buffer in the previous chapters. It is simply an indication that our present optimisation techniques and knowledge of individual reactions involved are insufficient to advance this model without a significant amount of further research.

5.7   Conclusions

Preliminary studies of the phosphate buffer composition reveals the fundamental and complex role that phosphate species play in the electrochemical mechanism for the oxidation of H_2O_2 on a nickel electrode surface.

The experiments involving varying the pH from 4.0 to 11.5 at a sustained phosphate concentration demonstrated the optimum pH region to study this oxidative process was between pH 4 and 9. Investigation in this region revealed that the phosphate species involved in the electrochemical oxidation of hydrogen peroxide on a nickel electrode surface was HPO_4^{-2}. The pH bounds were established since above pH 9, evidence was found that the responses observed were not exclusively due the H_2O_2 oxidation but rather a combination of H_2O_2 and a superhydroxide oxidations. The superhydroxide oxidation was observed to proceed with significantly higher responses than that of a similar concentration of H_2O_2. At pH $\gg$ 9 another unresolved H_2O_2 or superhydroxide facilitated process yielding high currents began to occur. This behaviour was tentatively attributed to the corrosion of the electrode surface. At pH $<$ 4 insufficient HPO_4^{-2} is present to facilitate the oxidation of H_2O_2. The rates observed at pH 4 are minimal. However, there does appear to be some limited activity suggesting the presence of another auxiliary mechanism for H_2O_2 oxidation in the absence of the HPO_4^{-2} species.

Experiments involving phosphate buffer concentrations between 25 and 200 mM at a constant pH of 7.28 demonstrate the complex nature of the phosphate involvement in the oxidation of H_2O_2. There is not a simple relationship between the rate of oxidation and phosphate concentration. Whilst phosphate is required to facilitate the oxidative process excess phosphate levels were found to be inhibiting giving rise to an optimum phosphate concentration. This optimum phosphate concentration was found to be potential dependent.

Since the potential is fundamentally linked to the rate of electrochemical rate of H_2O_2 oxidation, a connection can be made between the rate and the phosphate optimum.

The data collected under varying phosphate buffer compositions serves to indicate that our present knowledge of the exact nature of the fundamental reactions described in Model III, developed through the previous chapters in uniform phosphate buffer conditions, is not complete. This does not undermine Model III, it is perfectly valid in describing the electrochemical oxidation of H_2O_2 at a constant concentration and pH. However, it does indicate that the model needs to be modified to include the involvement of a phosphate buffer species, HPO_4^{-2}. Two main consequences can be attributed to the complicated involvement of phosphate. First, that increasing $[HPO_4^{-2}]$, through either the pH or the over all phosphate concentration, enhances the rate. Secondly, that high $[HPO_4^{-2}]$ also suppresses the rate. A number of possible mechanisms for both of these conclusions were proposed, with the simplest and most plausible incorporated into Model IV.

Model IV employs HPO_4^{-2} in the formation of the active nickel-binding site from a hypothetical precursor site. This makes the earlier supposition, that the nickel-binding site species was $Ni(OH)_2$, obsolete. The species now is recognised to involve phosphate and formed $Ni_{BS\text{-}HPO_4}^{-2}$. The binding of H_2O_2 to the nickel-binding site once formed, while still inhibited by complexation of dioxygen, is further inhibited by the secondary complexation of another phosphate species. Once H_2O_2 binds to the nickel-binding site subsequent reactions are proposed to proceed in an identical manner to Model III, commencing with the electrochemical oxidation of the bound H_2O_2 and simultaneous reduction of the nickel site. Finally, the reduced nickel site is oxidised back to an active nickel-binding state completing the catalytic cycle. Further indirect inhibition of this mechanism occurs by high transient pH gradients near electrode surface due to the other by-product of H_2O_2 oxidation, H^+. This indirectly inhibits by protonating HPO_4^{-2}, required to form the nickel-binding site, to produce $H_2PO_4^-$ a species with little or no electroactivity.

CHAPTER 6

CONCLUSIONS

6.1 Introduction

This study presents fundamental research into the electrochemical oxidation of hydrogen peroxide on a nickel electrode surface in phosphate buffer solutions. An earlier study by Khudaish [1-6] investigated this reaction on platinum electrodes. This study applied the kinetic modelling techniques developed by Khudaish [1-6] to this nickel electrode study. A goal of this thesis was to develop a robust kinetic model to account for the electrochemical oxidation of hydrogen peroxide on nickel. Furthermore, the goal was also to interpret the thermodynamic and kinetic parameters to account for nickel electrodes having significantly lower rate of H_2O_2 oxidation than platinum.

The kinetic model for electrochemical oxidation of H_2O_2 on nickel was not found to be directly analogous to platinum. The sections that follow summarise the major findings of this research, demonstrate the key theories and concepts developed and how they pertain to the development of a viable kinetic model.

6.2 $[H_2O_2]_{bulk}$, Potential and Rotation Rate Dependence

6.2.1 *Potential*

A preliminary study was performed to ascertain the oxidation region of H_2O_2 on a nickel electrode (Fig. 3.1). The potential was cycled for two segments between +1300 and −1300 mV vs Ag/AgCl for 0.120 mol L^{-1} $[H_2O_2]_{bulk}$ and a blank control. This study showed that a significant oxidation wave occurred at $E > +300$ mV vs Ag/AgCl only in the presence of H_2O_2. The commencement of a solvent oxidation wave occurred at $E > +1100$ mV vs Ag/AgCl in the absence of H_2O_2 and thus set the upper bounds of potential for all subsequent experiments. These steady-state responses when compared to platinum deviate from the open circuit potential approximately +100 mV vs Ag/AgCl more anodic potential *c.f.* +275 mV vs Ag/AgCl for platinum [1,3].

SCP experiments over the potential range +332 to +1100 mV vs Ag/AgCl revealed that the steady-state responses observed increased exponentially with potential at every H_2O_2 concentration (Fig. 3.2). The response at platinum rises more rapidly with potential hence the oxidation was studied at lower potentials and over a smaller range c.f. +200 to +600 mV vs Ag/AgCl [1-6].

6.2.2 *Hydrogen Peroxide Concentration*

One of the most significant differences between platinum and nickel electrodes is the rates of oxidation at nickel are significantly slower, yielding approximately three fold lower currents for analogous H_2O_2 concentrations. Due to these relatively low rates, the surface H_2O_2 concentrations does not vary significantly from the $[H_2O_2]_{bulk}$ indicating limited mass-transport limitation. The steady-state response increases sharply with $[H_2O_2]_{bulk}$ but begins to approach a limiting current density plateau at higher concentrations (Fig. 3.3).

This behaviour is analogous to platinum although the response increase with $[H_2O_2]_{bulk}$ is significantly sharper on platinum and the limiting current density plateau is approached much more rapidly. Due to this, the steady-state response at nickel is studied over a much wider concentration range 0 – 130 mM $[H_2O_2]_{bulk}$ compared to 0 – 60 mM $[H_2O_2]_{bulk}$ at platinum [1,3].

6.2.3 *Rotation Rate*

Increasing the rotation of the RDE causes the bulk solution to be pumped faster towards the electrode surface. This solution flow improves the mass transportation of H_2O_2 to, and oxidation products away from, the electrode surface. Varying the rotation rate indicated moderate diffusion dependence, which became more pronounced at higher $[H_2O_2]_{bulk}$ (Fig. 3.4). Stronger rotation rate dependence was observed at platinum [1,3].

6.2.4 *Modelling at Constant Buffer Conditions*

A series of electrochemical models were developed in the course of this research. Initially, Model I was proposed to account for the steady-state responses collected as a function of $[H_2O_2]_{bulk}$, potential and rotation rate. Model I was based on the electrochemical model

developed by Khudaish [1-6], Eqns. 1.16-1.21, for the oxidation of H_2O_2 on a platinum electrode surface. This was a product inhibited Michaelis-Menten mechanism (Eqns. 3.6 to 3.9) including mass transport considerations (Eqns.3.1 to 3.4). The mechanism involved binding sites on the electrode surface and incorporated two feedback inhibition modes (Section 3.5), namely H^+ and O_2, the by-products of H_2O_2 oxidation. The steady-state responses collected were used to SIMPLEX (Section 2.6) optimise rate and equilibrium parameters (Table 3.1).

The unaltered Khudaish model, Model I, showed an unsatisfactory fit to the experimental data and required further refinement. Therefore, Model III was developed. This had one inhibition mode, that by H^+, removed (Section 3.5.1) and had the catalytic replenishment of the reduced nickel site constrained to be potential-invariant (Section 3.5.4). Model III was found to reliably account for the steady-state responses that occurred over the experimentally tested ranges of $[H_2O_2]_{bulk}$, potential and rotation rate under constant buffer conditions of pH 7.28 and 0.100 mol L^{-1} phosphate. The optimised kinetic parameter k_2N was found to increase exponentially with potential (Fig. 3.20) surpassing that of k_3N at $E > +844$ mV vs Ag/AgCl. The fractional surface coverage plots (Figs. 3.13 and 3.14) showed that dioxygen binds more strongly than H_2O_2 to the nickel binding site. The major effect of increasing the rotation rate was a marked drop in fractional surface coverage of dioxygen bound sites and a corresponding rise in H_2O_2 bound sites.

6.3   Temperature Dependence

The steady-state responses as a function of $[H_2O_2]_{bulk}$ were studied over the 5 to 35°C temperature range. Results indicated (Fig. 4.3) that the electrode reaction has strong temperature dependence that could not be attributed to viscosity changes in the supporting electrolyte. The increase in steady-state response with temperature at platinum electrodes was larger but not as smooth and regular as that observed at nickel. Platinum shows a regular increase with temperature from 5 to 20°C. However, after 20°C the increase with temperature becomes quite irregular.

6.3.1 *The Effect of Temperature on the Electrochemical Model*

Model III satisfactorily predicted the observed steady-state responses over the range of temperatures studied without further modifications. Kinetic and thermodynamic parameters of Model III were optimised at each of the seven temperatures studied (Table 4.3). The enthalpy of each reaction in the proposed mechanism was evaluated. This showed the reversible binding of H_2O_2 to the free nickel active site, K_1, was an exothermic reaction with $\Delta H = -28.32$ kJ K^{-1} between 5 and 25°C becoming significantly more exothermic between 25 and 35°C $\Delta H = -198.33$ kJ K^{-1}. The reversible binding of the inhibiting by-product dioxygen to the free nickel active site, K_4, in contrast, was slightly endothermic with $\Delta H = -16.5$ kJ K^{-1} (Fig. 4.4).

The rate constants, k_2N and k_3N, describe the oxidation of bound H_2O_2 and the oxidation of the reduced nickel site respectively. It was established by Arrhenius analysis that k_3N has a relatively low and k_2N a high pseudo-activation energy with $E_{A,k_3N} = 24.3$ kJ mol^{-1} and E_{A,k_2N} ranging from 80 to 130 mol^{-1} respectively (Figs. 4.7 and 4.10). The increase in k_2N with temperature as a function of potential (Fig. 4.8) was consistent with the overall increase in steady-state response Fig. 4.3. The pseudo-activation energies of k_2N were found to decrease at low potentials to achieve constant values at higher potentials. This behaviour was thought to be due to a combination of the activation energy for the formation of the reduced nickel site and the formation of the binding site (Eqn. 4.9). The large decrease in pseudo-activation energies at low potentials was attributed to the decrease in the endothermic formation of binding sites while the constant values observed at higher potential were predominantly due to k_2. This trend was not observed in k_3N since this reaction, in Model III, was considered potential-invariant.

The thermodynamic and kinetic constants, optimised by Khudaish [1,4], at platinum behave in a significantly different manner to the analogous reactions at nickel. Khudaish found the equilibrium constants K_1, K_4 and K_5 could be considered temperature-invariant with ΔH approaching 0 kJ K^{-1}. Of the heterogeneous rate constants k_2N and k_3N (potential-variant) only k_2N could be analysed by Arrhenius methods. This yielded a pseudo activation energy, E_{A,k_2N}, beginning at approximately 100 kJ mol^{-1} to decline in a similar manner to

nickel to a constant value of approximately 42 kJ mol^{-1} [1,4]. This constant region equates to approximately half of the pseudo activation energy at nickel. This lower energy barrier is one reason for the rate of H_2O_2 oxidation being faster at platinum electrodes.

6.4   Phosphate Buffer Dependence

6.4.1   *Buffer pH*

The steady-state data collected over the pH 4 to 11.5 range revealed two additional electrochemical processes occurring at the electrode surface (Fig. 5.5). The first, causing significant constructive interference at pH > 9, was the oxidation of superhydroxide. The second, an unidentified deleterious process occurring at pH > 11 which is facilitated by traces of H_2O_2 and prevents the oxidation of H_2O_2 on the electrode surface. Two possible processes were tentatively identified as occurring at this high pH. One was the corrosion of the nickel electrode surface involving the phosphate species PO_4^{-3} (Eqn. 5.3), the other the oxidation of the electrolyte (Eqn. 5.4).

The optimal pH range for studying the oxidation of H_2O_2 on a nickel electrode surface is between pH 4 and pH 9. Experiments within this range found that the steady-state response, which increased sharply with pH, was directly proportional to the relative concentration of HPO_4^{-2} (Fig. 5.8). Therefore, this species was identified as the phosphate species involved in binding site formation.

Both these additional high pH electrochemical processes, discussed previously, were not observed to occur on platinum electrodes. This suggests that platinum is more noble than nickel. The steady-state responses on platinum were found to have an optimum at approximately pH 7. Above and below this pH the steady-state responses steadily decline to approach zero. The rate optimum is strongly correlated with $[H_2PO_4^-]_{tot}$ indicating that $H_2PO_4^-$ was the phosphate species involved in platinum binding site formation [1,5].

6.4.2   *Buffer Concentration*

Experiments between 25 and 200 mM phosphate buffer concentration at pH 7.3 demonstrated the complex nature of the phosphate involvement in the oxidation of H_2O_2

(Fig. 5.1). Phosphate was found to facilitate the oxidative process but also inhibit when in excess. This relationship gave rise to optimum phosphate concentrations, which were potential dependent (Table 5.1 and Figs. 5.9 and 5.10).

Khudaish found that over the 0 to 100 mM range of phosphate concentrations not evidence of this potential-dependent phosphate optimum behaviour observed at nickel. The steady-state responses at platinum simply increase with phosphate concentration with a competing phosphate free mechanism at $[PO_3^{-3}]_{tot}$ approaching zero [1,5].

6.4.3 *A mechanism involving Buffer Composition*

The electrochemical mechanism, Model III, which successfully accounts for the H_2O_2 oxidation at constant phosphate conditions was altered to account for the participation of HPO_4^- in binding site formation (Eqn. 5.5) and the inhibition of H_2O_2 binding by complexation of a second HPO_4^- to this site (Eqn. 5.7). The rate equation for Model IV, therefore, included the surface concentration of HPO_4^-. This was decreased by the transiently high surface $[H^+]$ created as a product of H_2O_2 oxidation (Eqns. 5.10 and 5.14). Therefore, Model IV accounts for the effect of pH and phosphate concentration as well as the effect that the potential was observed to have on the steady-state response.

6.5 Summary of Differences between Pt and Ni Electrode Studies

The kinetic model for electrochemical oxidation of hydrogen peroxide on nickel was not found to be directly analogous to platinum.

i)   Significantly lower rates of reaction were observed at nickel.

ii)   Oxidation at nickel occurs at more anodic potentials.

iii)   Stronger rotation rate dependence was observed at platinum.

iv)   Less, but more consistent temperature dependence at nickel.

v)   Two high pH electrochemical processes; one involving superhydroxide oxidation and the other involving the corrosion of the electrode surface, occurring at nickel were not observed at platinum.

vi)   The steady-state response optimum that is attributable to H_2O_2 oxidation occurs at much higher pH on nickel and on Pt.

vii)   Nickel showed a rate optimum phosphate concentration, which varies with potential. Steady-state responses at platinum simply increase with phosphate concentration.
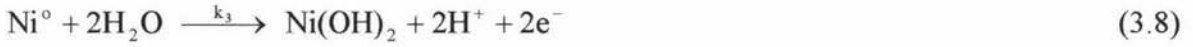
The electrochemical model developed for platinum was significantly modified in Model IV to apply to nickel. The key features are:

i)   The inhibition by protonation of the H_2O_2 bound binding site complex, Eqn. 1.20 found with platinum, was insignificant and removed.

ii)   The catalytic replenishment of the reduced nickel site, potential-variant at platinum, was significantly slower and could be constrained to be potential-invariant.

iii) k_2N increasing exponentially with potential surpassed k_3N at potentials significantly more anodic, $E > +844$ mV vs Ag/AgCl at nickel (c.f. $E > +271$ mV vs Ag/AgCl at platinum).

iv)   Fractional surface coverage plots show that dioxygen binds to a greater extent than H_2O_2 to the nickel binding site.

v) K_1 and K_4, temperature invariant for platinum, were exothermic and endothermic reactions respectively for nickel.

vi)   The reaction k_2N has a high pseudo-activation, approximately twice that at platinum.

vii)   pH/response profile indicates HPO_4^{-2} is the phosphate species involved in the formation of the binding site, not $H_2PO_4^{-}$ as in platinum.

viii) Two additional phosphate processes were recognised at nickel accounting for the complex phosphate dependence. The first involved inhibition by complexation of a second HPO_4^{-2} to the binding site. The second involved local depletion of surface phosphate concentrations by lower surface pH gradient due to proton by-products of H_2O_2 oxidation.
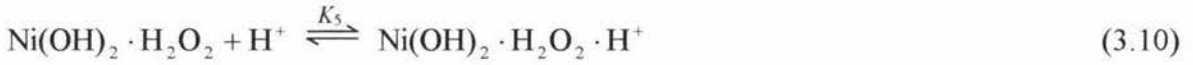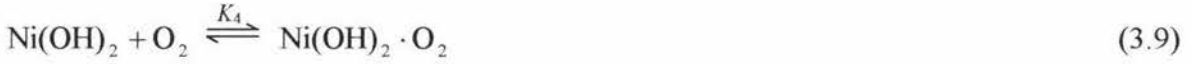
APPENDIX

Derivation of Model I

The mechanism for Model I: the electrochemical oxidation of hydrogen peroxide on a nickel electrode surface.

$$Ni(OH)_2 + H_2O_2 \overset{K_1}{\rightleftharpoons} Ni(OH)_2 \cdot H_2O_2 \tag{3.6}$$

$$Ni(OH)_2 \cdot H_2O_2 \overset{k_2}{\longrightarrow} Ni^\circ + 2H_2O + O_2 \tag{3.7}$$

$$Ni^\circ + 2H_2O \overset{k_3}{\longrightarrow} Ni(OH)_2 + 2H^+ + 2e^- \tag{3.8}$$

Overall

$$H_2O_2 \longrightarrow O_2 + 2H^+ + 2e^- \tag{1.15}$$

Inhibiting Reactions

$$Ni(OH)_2 + O_2 \overset{K_4}{\rightleftharpoons} Ni(OH)_2 \cdot O_2 \tag{3.9}$$

$$Ni(OH)_2 \cdot H_2O_2 + H^+ \overset{K_5}{\rightleftharpoons} Ni(OH)_2 \cdot H_2O_2 \cdot H^+ \tag{3.10}$$

The total surface coverage can be expressed in terms of each species

$$1 = \theta_{Ni(OH)_2} + \theta_{Ni^\circ} + \theta_{Ni(OH)_2 \cdot H_2O_2} + \theta_{Ni(OH)_2 \cdot H_2O_2 \cdot H^+} + \theta_{Ni(OH)_2 \cdot O_2} \tag{A.1}$$

The equilibrium reactions can be expressed as

$$K_1 = \frac{\theta_{Ni(OH)_2 \cdot H_2O_2}}{\theta_{Ni(OH)_2} + [H_2O_2]} \tag{A.2}$$

which can be rearranged to

$$\theta_{Ni(OH)_2} = \frac{\theta_{Ni(OH)_2 \cdot H_2O_2}}{K_1[H_2O_2]} \tag{A.3}$$

$$\theta_{Ni(OH)_2 \cdot O_2} = K_4[O_2]\theta_{Ni(OH)_2} \tag{A.4}$$

$$\theta_{Ni(OH)_2 \cdot H_2O_2 \cdot H^+} = K_5[H^+]\theta_{Ni(OH)_2 \cdot H_2O_2} \tag{A.5}$$

Substituting Eqns. A3, A.4 and A.5 into the surface coverage equation (Eqn. A.1)

$$1 = \frac{\theta_{\text{Ni(OH)}_2 \cdot \text{H}_2\text{O}_2}}{K_1[\text{H}_2\text{O}_2]} + \theta_{\text{Ni}^\circ} + \theta_{\text{Ni(OH)}_2 \cdot \text{H}_2\text{O}_2} + K_5[\text{H}^+]\theta_{\text{Ni(OH)}_2 \cdot \text{H}_2\text{O}_2} + K_4[\text{O}_2]\frac{\theta_{\text{Ni(OH)}_2 \cdot \text{H}_2\text{O}_2}}{k_1[\text{H}_2\text{O}_2]}$$ (A.6)

This can be rearranged to

$$1 = \theta_{\text{Ni}^\circ} + \theta_{\text{Ni(OH)}_2 \cdot \text{H}_2\text{O}_2}\left(1 + \frac{1}{K_1[\text{H}_2\text{O}_2]} + K_5[\text{H}^+] + K_4[\text{O}_2]\frac{1}{K_1[\text{H}_2\text{O}_2]}\right)$$ (A.7)

The rate, j, can be expressed

$$j = k_2 N\theta_{\text{Ni(OH)}_2 \cdot \text{H}_2\text{O}_2}$$ (4.6)

and

$$j = k_3 N\theta_{\text{Ni}^\circ}$$ (4.7)

Making the surface coverage of each species the subject

$$\theta_{\text{Ni(OH)}_2 \cdot \text{H}_2\text{O}_2} = \frac{j}{k_2 N}$$ (A.8)

and

$$\theta_{\text{Ni}^\circ} = \frac{j}{k_3 N}$$ (A.9)

Substituting these, Eqn. A.10 and A.11, into the surface coverage equation, Eqn. A.7, yields

$$1 = \frac{j}{k_3 N} + \frac{j}{k_2 N}\left(1 + \frac{1}{K_1[\text{H}_2\text{O}_2]} + K_5[\text{H}^+] + K_4[\text{O}_2]\frac{1}{K_1[\text{H}_2\text{O}_2]}\right)$$ (A.10)

rearranging to make $k_2 N.K_1[\text{H}_2\text{O}_2]$ the subject

$$\begin{aligned}k_2 N K_1[\text{H}_2\text{O}_2] &= j k_2/k_3\, K_1[\text{H}_2\text{O}_2] \\ &\quad + j\left(K_1[\text{H}_2\text{O}_2] + 1 + K_5[\text{H}^+]K_1[\text{H}_2\text{O}_2] + K_4[\text{O}_2]\right)\end{aligned}$$ (A.11)

which can be simplified to

$$k_2 N K_1[\text{H}_2\text{O}_2] = j\left(1 + K_4[\text{O}_2] + K_1[\text{H}_2\text{O}_2]\left(1 + K_5[\text{H}^+] + k_2/k_3\right)\right)$$ (A.12)

Finally rearranging to make the rate the subject gives the rate equation, for Model I, in terms of the surface concentration of H_2O_2, O_2 and H^+.

$$j = \frac{k_2 N.K_1[\text{H}_2\text{O}_2]}{1 + K_4[\text{O}_2] + K_1[\text{H}_2\text{O}_2]\left(1 + K_5[\text{H}^+] + k_2/k_3\right)}$$ (3.11)

REFERENCES

1. Emad A., Khudaish, *"Doctoral Thesis: The electrochemical oxidation of hydrogen peroxide on platinum electrodes at phosphate buffer solutions"* (1999).

2. S. B. Hall, E. A. Khudaish and A. L. Hart, *Electrochim. Acta*, 43 (1998) 579-588.

3. S. B. Hall, E. A. Khudaish and A. L. Hart, *Electrochim. Acta*, 43 (1998) 2015-2024.

3. S. B. Hall, E. A. Khudaish and A. L. Hart, *Electrochim. Acta*, 44 (1999) 2455-2462.

4. S. B. Hall, E. A. Khudaish and A. L. Hart, *Electrochim. Acta*, 44 (1999) 4573-4582.

5. S. B. Hall, E. A. Khudaish and A. L. Hart, *Electrochim. Acta*, (2000), in press

7. F. A. Lowenheim and M. K. Moran, *"Faith,Keyes and Clarks, Industrial Chemicals"*, 4th Edn., John Wiley & Sons Inc., New York.

8. D. T. Sawyer, *"Oxygen Chemistry"*, Oxford University Press, Oxford, (1991).

9. World Health Organisation, *"Milk Hygiene: Hygiene in Milk Production, Processing and Distribution"*, Published under the auspices of the Food and Agriculture Organisation of the United Nations and the World Health Organisation, Geneva, (1962).

10. G. G. Guilbault and G. J. Lubrano, *Anal. Chim. Acta*, 64 (1973) 439-455.

11. J. E. Frew, M. A. Harmer, A. H. O. Hill and S. I. Libor, *J. Electroanal. Chem.* 201 (1986) 1-10.

12. E. Csöregi, L. Gorton and G. Marko-Varga, *Anal. Chem.*, 66 (1994) 3604-3610.

13. I. Taniguchi, K. Matsushita, M. Okamoto, J. Collin and J. Sauvaye, *J. Electroanal. Chem.* 280 (1990) 221-226.

14. S. Milardović, I. Kruhak, D. Iveković, V. Rumenjak, M. Tkalčec, and B. S. Grabarić, *Anal. Chim. Acta*, 350 (1997) 91-96.

15. S. Berchmans, H. Gomathi, G. Prabhakara Rao, *Sensors and Actuators B*, 50 (1998) 156-163.

16. P. Vadgama, W. Mullen, S. Churchouse and C. Battersby, *"Implantable Glucose Sensors - The State of the Art"*, International Symposium, Vol. 20, New York, pp. 20-22.

17. S. P. Hendry and A. P. F. Tuner, *"Implantable Glucose Sensors - The State of the Art"*, International Symposium, Vol. 20, New York, 1988, pp. 37-40.

18. E. W. Kraegen and D. J. Chisholm, *"Implantable Glucose Sensors - The State of the Art"*, International Symposium, Vol. 20, New York, pp. 1-4.

19. K. Cammann, *"Implantable Glucose Sensors - The State of the Art"*, International Symposium, Vol. 20, New York, pp. 4-8.

20. T. Tallagrand, R. Sternberg, G. Reach and D. R. Thévenot, *"Implantable Glucose Sensors - The State of the Art"*, International Symposium, Vol. 20, New York, pp. 13-16.

21. T. Weiss and K. Cammann, *"Implantable Glucose Sensors - The State of the Art"*, International Symposium, Vol. 20, New York, 1988, pp. 23-25.

22. D. G. Bueck, *"Biosensors: Theory and applications"*, Technomic Publishing Co. Inc., (1993).

23. R. E. Carbono, V. A. Macayno and A. J. Arvia, *J. Electroanal. Chem*, 147 (1983) 139-156.

24. V. S. Bagotsky, N. A. Shumilova, G. P. Samoilov and E. I. Khrushcheva, *Electrochim. Acta.*, 17 (1972) 1625-1635.

25. N. Kobayashi, P. Janda, and A. B. P. Lever, *Inorg. Chem.*, 31 (1992) 5172-5177.

26. E. L. Littauer and K. C. Tsai, *Electrochim. Acta*, 24 (1979) 681-684.

27. S. Ceré, M. Vazquez, S. R. De Sánchez, D. S. Schiffin, *J. Electroanal. Chem*, 470 (1999) 31-38.

28. R. Garjonyté and A. Malinauskas, *Sensors and Actuators B*, 46 (1998) 236-241.

29. M. L. Bowers and F. C. Anson, *J. Electroanal. Chem.*, 216 (1987) 249-260.

30. N. Kobayashi, P. Sanda and B. P. Lever, *Inorg. Chem.*, 31 (1992) 5172-5177.

31. N. Koshino, S. Funahashi, and H. D. Takagi, *J. Chem. Soc. Dalton Trans.*, (1997) 4175-4180.

32. J. Taraszewska, G. Roslonek and W. Darlewski, *J. Electroanal. Chem.* 371 (1994) 223-230.

33. P. Westbroek and E. Temmerman, J. Electroanal. Chem. 482 (2000) 40-47.

34. D. H. Macartney, *Can. J. Chem*, 64 (1986) 1936-1942.

35. V. G. Prabhu, L. R. Zarapkar and R. G. Dhaneshwar, *Electrochim. Acta*, 26 (6) (1981) 725-729.

36. F. C. Anson and J. J. Lingane, *J. Am. Chem. Soc.*, 79 (1957) 4901-4903.

37. S. Lj. Gojković, S. K. Zečević and D. M. Dražić, *Electrochim. Acta*, 37 (10) (1992) 1845-1850.

38. C. R. Davidson and S. Srinivasan, *J. Electrochem. Soc.*, 127(5) (1980) 1060-1063.

39. N. A. Shumilova and V. S. Bagotzky, *Electrochim. Acta*, 13 (1968) 285-293.

40. X. Qian, H. Sambe, D. E. Ramaker, K. L. Pandya, and W.E. O'Grady, *J. Phys. Chem. B*, 101 (1997) 9441-9446.

41. R. S. Schrebler Guzmán, J. R. Vilche and A. J. Arvía, *J. Appl. Electrocem.*, 9 (1979) 183-189.

42. A. C. C. Tseung, B. S. Hobbs and A. D. S. Tantram, *Electrochim. Acta*, 15 (1970) 473.

43. S. Chang, Y. Ho, M. Weaver, *J. Am. Chem. Soc.* 113 (1991) 9506-9514.

44. A. A. Atia, N. R. E. Radwan, A. M. Donia, *Mansoura Sci. Bull. A: Chem.* 26 (1999) 1-18, as quoted Chem Abs. CAN 132: 171703.

45. N. D. Merkulova, G. V. Zhutaeva, N. A. Shumilova and V. S. Bagotzky, *Electrochim. Acta*, 18 (1973) 169-174.

46.   I. Morcos and E. Yeager, *Electrochim. Acta*, 15 (1970) 953.

47.   I. Morcos and E. Yeager, *Electrochim. Acta*, 15 (1970) 953-975.

48.   R. W. Zurilla. R. K. Sen and E. Yeager, J. Electrocehm. Soc., 125 (1978) 1103.

49.   C. F. Wells and D. Fox, *J. Chem. Soc. Dalton Trans.*, 15 (1977) 1498-1501.

50.   K. Vengatajalabathy Gobi, K. Tokuda and T. Ohsaka, *J. Electroanal. Chem.*,
        444 (1998) 145-150.

51.   K. Vengatajalabathy Gobi, F. Kitamura, K. Tokuda and T. Ohsaka,
        J. Phys. Chem. B, 103 (1999) 83-88.

52.   *"Digital Photo/Contact Tachometer: Operators Manual"*, EXTECH Instruments,
        Tawan.

53.   E. Gileadi, *"Electrode Kinetics for Chemists, Chemical Engineers, and Materials
        Scientists"*, VCH Publishers Inc., New York (1993).

54.   *"C.R.C: Handbook of Chemistry and Physics"*, 63rd Edn., (1982-1983).

55.   P. H. Rieger, *"Electrochemistry"*, 2nd Edn., Ghapman and Hall Inc., (1994) pp. 208.

56.   G. C. Barker, *Adv.Polarogr.*, 1 (1960) 144.

57.   J. A. Nedler, and R. Mead, *Computer J.*, 7 (1965) 308-313.

58.   L. A. Yarbro and S. N. Deming, *Anal. Chim. Acta*, 73 (1974) 391-398.

59.   G. E. P. Box and K. B. Wilson, *Roy. Statist. Soc. ser. B*, 13 (1951) 1.

60.   W. Spendley, G. R. Hext and F. R. Himsworth, *Technometric*, 4 (1962) 441.

61.   J. A. Nadler and R. Mead, *Computer J.*, 7 (1965) 308.

62.   S. B. Hall, J. R. Duffield, D. R. Williams, M. I. Barnett and A. G. Cosslett,
        Nutrition, 8 (1992) 167.

63.   A. K. Burrell, B. M. Jones, S. B. Hall, D. L. Officer, D. C. W. Reid and K. Y. Wild,
        J. Incl. Phenom., 35 (1999) 185-190.

64.	S. A. M. van Stroe-Biezen, F. M. Everaerts, L. J. J. Janssen and R. A. Tacken, *Anal. Chim. Acta*, 273 (1993) 553.

65.	P. W. Atkins, *"Physical Chemistry"*, Oxford University Press, Oxford (1978) pp. 836.

66.	R. P. Van Duyne and C. N. Reilly, *Anal. Chem.*, 44 (1972) 142.

67.	J. Kulys. J. A. Munk, T. Buch-Rasmussen, and H. E. Hansen, *Electroanalysis*, 6 (1993) 945-952.

68.	H. S. Harned and B. B. Owen *"The Physical Chemistry of Electrolytic Solutions"*, Reinhold Publishing Corporation, New York, 1943, P. 330.

69.	H. S. Harned and R. W. Ehlers, *J. Am. Chem. Soc.*, 55 (1933) 2179.

70.	R. G. Bates and V. E. Bower, *J. Research Nat. Bur. Standards*, 53 (1953) 282.

71.	 H. S. Harned and T. R. Paxton, *J. Phys. Chem.* 57 (1953) 1-5.

72.	R. A. Robinson, *Trans. Faraday Soc.*, 35 (1939) 1222.

73.	H. S. Harned and L. F. Nims, *J. Am. Chem. Soc.*, 54 (1932) 423.

74.	H. S. Harned and M. A. Cook, *J. Am. Chem. Soc.*, 61 (1939) 495.

75.	O. K. Borggaard, *Acta Chem. Scand.*, 26 (1972) 3393.

76.	A. Brestovisky, E. Kirowa-Eisner and J. Osteryoung, *Anal. Chem.*, 55 (1983) 2063.

77.	J. Clavilier, *Electroanal. Chem.*, 107 (1980) 211

78.	G. M. Barrow, *"Physical Chemistry"*, 2nd Edn., McGrow-Hill, New York (1966) pp. 486-490.

79.	R. P. Van Duyne and C. N. Reilley, *Anal. Chem.*, 44 (1) (1972) 153-169.

80.	P. W. Atkins, *"Physical Chemistry"*, 6th Edn, Oxford University Press, Oxford (1998) 225.

81.	F. A. Cotton and G. Wilkinson, *"Advanced Inorganic chemistry"*, 4th Edn., John Wiley Inc., (1980) pp. 783-784.